



SAPIENZA
Università di Roma

PhD Programme in Life Sciences

XXXII Cycle

New Tubulin and NHERF1 Targeting Anticancer Agents

Candidate
Valentina Naccarato

Supervisor:

Prof. Romano Silvestri

Coordinator:

Prof. Marco Tripodi

Table of Contents	<i>i</i>
<i>Abstract</i>	<i>iv</i>
<i>List of Abbreviations</i>	<i>v</i>
<i>1. Tubulin and Microtubules</i>	<i>1</i>
1.1 Microtubules structure and organization	1
1.2 Microtubules dynamics and GTP hydrolysis	2
1.3 Tubulin	3
1.4 Effects of microtubule dynamics on mitosis	4
1.5 Tubulin binding agents (TBAs) as anti-mitotic drugs	7
1.6 Multi-drug resistance (MDR) to TBAs	15
1.7 References	16
<i>2. New indole derivatives as potent tubulin assembly and cancer cell growth inhibitors</i>	<i>23</i>
2.1 Introduction	23
2.2 Arylthioindoles, Potent Inhibitors of Tubulin Polymerization	23
2.3 Objective of the Study	25
2.4 Chemistry	26
2.5 Results and Discussion	28
2.5.1 Inhibition of Tubulin Polymerization	29
2.5.2 Inhibition of MCF-7 Breast Cancer Cell Growth	30
2.5.3 Inhibition of the Binding of [³ H]Colchicine to Tubulin	30
2.5.4 Cell Growth Inhibition	30
2.5.5 Multi-Drug-Resistant (MDR) Cell Lines	33
2.5.6 Arrest of Mitotic Progression in HeLa Cells	33
2.5.7 Inhibition of Mitotic MT Assembly	34
2.5.8 Inhibition of HepG2 Cancer Cell Growth	35
2.6 Conclusions	36
2.7 Experimental Section	36
2.7.1 Chemistry	36
2.7.2 Molecular Modeling	47
2.7.3 Biological Assay	47
2.8 References	49
<i>3. New pyrrole derivatives inhibitors of chronic myeloid leukemia cell growth</i>	<i>53</i>
3.1 Introduction	53
3.1.1 Chronic myeloid leukemia (CML)	53
3.1.2 Characteristics and Diagnosis of CML	53
3.1.3 Current Drug Treatment	54
3.2 Objective of the study	55
3.3 Molecular Modeling	56
3.4 Chemistry	56
3.5 Results and Discussion	57
3.5.1 Inhibition of Tubulin Polymerization	58
3.5.2 Inhibition of MCF-7 Breast Cancer Cell Growth	58
3.5.3 Inhibition of the Binding of [³ H]Colchicine to Tubulin	58
3.5.4 Cell Growth Inhibition	59

3.5.5 Cytotoxicity on CML cells expressing the IM-sensitive KBM5-WT or its IM-resistant KBM5-T315I mutation	61
3.5.6 Induction of G2/M phase arrest and apoptosis via a mitochondria-dependent pathway	62
3.5.7 Strengthening of IM-mediated CML cell death by ARDAP 3.10	62
3.5.8 Morphological changes, altered tubulin immunostaining and mitotic arrest of KU812 cells by ARDAP 3.10	63
3.6 Conclusions	64
3.7 Experimental Section	64
3.7.1 Chemistry	64
3.7.2 Molecular Modeling	76
3.7.3 Biological assays	77
3.8 References	80
4. <i>Wnt/β-catenin Pathway in Human Colorectal Cancer (CRC)</i>	83
4.1 Introduction	83
4.1.1 Human Colorectal Cancer (CRC)	83
4.1.2 Epithelial-Mesenchymal-like Transition (EMT)	83
4.1.3 Role of E-Cadherin in EMT	84
4.1.4 Transcriptional Repressors of E-cadherin: Snail, Slug and Twist	85
4.2 Wnt/β-catenin Pathway	86
4.2.1 Wnt Protein Secretion	87
4.2.2 Wnt Receptors, Agonists, and Antagonists	88
4.2.3 β-catenin and The Cytoplasmic Destruction Complex	91
4.2.4 Nuclear β-Catenin in CRC	93
4.3 Role of NHERF1 (Na ⁺ /H ⁺ exchanger 3 regulating factor 1) in CRC	93
4.4 References	95
5. <i>NHERF1-Mediated Survival of CRC Cells After β-Catenin Knockdown</i>	102
5.1 Introduction	102
5.2 Objective of the Study	102
5.3 Results and Discussion	102
5.3.1 β-catenin represses NHERF1 expression by associating with TCF4	102
5.3.2 CRC Apoptosis after Genetic Targeting of β-catenin and NHERF1	106
5.3.3 Synthesis of a novel NHERF1/PDZ1-domain antagonist that synergizes with β-catenin inhibitors in promoting CRC apoptosis	110
5.4 Conclusions	114
5.5 Experimental Section	104
5.5.1 Cells Cultures and Reagents	116
5.5.2 RT-PCR	116
5.5.3 Chromatin Immunoprecipitation (ChIP) Assay	116
5.5.4 Immunofluorescence Staining	116
5.5.5 Staining of Monodansylcadaverine (MDC)-labeled Vacuoles	116
5.5.6 Cell Proliferation and Apoptosis Assays	116
5.5.7 Luciferase Reporter Assays, Flow Cytometry, and Soft Agar Clonogenic Analysis	117
5.5.8 Subcellular Fractionation Assays	117
5.5.9 Pulse-Chase Analysis, Immunoprecipitation, and Western Blotting	117
5.5.10 Sample Preparation and Mass Spectrometry Evaluation	117
5.5.11 Database Searching and Bioinformatics Analysis	118
5.5.12 Chemical Synthesis of Compound 5.3	118

5.5.13 Virtual Screening Studies	118
5.5.14 In Vitro Binding Studies	118
5.5.15 Statistical Analysis	118
5.6 References	119
6. <i>Synthesis of Novel NHERF1 PDZ1 Domain Inhibitors as Anticancer Agents</i>	122
6.1 Introduction	122
6.1.1 Molecular Dynamics (MD) Simulations of the PDZ1- β 2-AR and PDZ1-PTH1R Complexes	122
6.1.2 Objective of the Study	123
6.2 Chemistry	123
6.3 Results and Discussion	126
6.3.1 Inhibition of NHERF1	126
6.3.2 Molecular Modeling	128
6.3.3 Binding to NHERF1 PDZ1	129
6.3.4 Cell Growth Inhibition of DLD-1, SW480, and SW620 Cell Lines	130
6.3.5 Inhibition of the Wnt Pathway	131
6.3.6 Inhibition of Cancer Stem Cells	132
6.4 Conclusions	132
6.5 Experimental Section	132
6.5.1 Molecular Modeling Studies	132
6.5.2 Chemical Synthesis	133
6.5.3 NHERF1 PDZ1 Binding Studies	143
6.5.4 Wnt Reporter Assay	144
6.5.5 Cell Cultures	144
6.5.6 Determination of the IC ₅₀ by MTT Assay	144
6.5.7 CSC Inhibition Assay	145
6.6 References	145
<i>Other Collaborations</i>	148
7. <i>New Inhibitors of RNA-dependent RNA Polymerase (RdRp) of Norovirus</i>	148
7.1 Introduction	148
7.1.1 Norovirus RNA-dependent RNA polymerase (RdRp)	148
7.1.2 RdRp-Targeted Antivirals	149
7.2 Objective of the Study	150
7.3 Results and Discussion	150
7.4 Experimental Section	150
7.4.1 Chemistry	150
7.4.2 PicoGreen Assay	151
7.4.3 Gel Shift Assay	151
7.5 References	152
<i>General Conclusions</i>	153
<i>Acknowledgements</i>	155

Abstract

Microtubules (MTs) are key component of the cytoskeleton in most eukaryotic cells. One of the distinctive characteristics of MTs is the “dynamic instability” as their assembly is a dynamic process characterized by the continuous transitions between polymerization and depolymerization. Because of their dynamicity, MTs play a significant role in a number of essential cellular functions, such as maintenance of cell shape, cell motility, intracellular transport and cell division. Interfering with the dynamic MT equilibrium prevents proper cellular functions and ultimately leads to cell death. Since cancer cells are characterized by a high rate of cell division, the strategy of inducing cell death through an interference with the dynamics of MTs has proved successful for the design of effective antitumor drugs.

Nuclear activated β -catenin caused by Wnt-pathway mutations is the earliest driving event in hereditary (10%) and sporadic (90%) human colorectal cancers (CRC) ¹; despite its causative role in CRC, however, β -catenin remains an elusive therapeutic target. NHERF1 (Na⁺/H⁺ exchanger 3 regulating factor 1) is a membrane adaptor protein that contains two tandem PDZ (post-synaptic density 95/discs large/zona occludens 1) domains and physiologically recruits β -catenin underneath the plasma membrane to shape proper tissue morphogenesis and homeostasis.²

My thesis, arising from this background context, plans to synthesize and optimise new potential molecules with anticancer activity.

This thesis contains two sections: the first part is focused on the synthesis and biological evaluation of new indole and pyrrole derivatives with tubulin polymerization inhibiting activity while the second section discusses the synthesis of new NHERF1/PDZ1-domain antagonists in the treatment of colorectal cancer; in chapter 7, finally, are briefly described other research collaborations in which I have been involved:

(a) Synthesis of new inhibitors of Norovirus RNA-dependent RNA polymerase (RdRp).

(b) Biological evaluation of new inhibitors of Norovirus RNA-dependent RNA polymerase (RdRp) by PicoGreen assay and Gel Shift assay.

List of Abbreviations

(P(o-tol) ₃)	tri(o-tolyl)phosphine
(Pd(OAc) ₂)	palladium(II) acetate
(Pd ₂ dba ₃)	tris(dibenzylideneacetone)dipalladium(0)
+TIPs	microtubule plus end tracking proteins
°C	degree Celsius
μM	micromolar
2-HATI	2-heterocyclyl-3-arylthio-1 <i>H</i> -indole
Å	angstrom
ACN or CH ₃ CN	acetonitrile
ADR-RES	adriamycin-resistant
Ala	alanine
AlCl ₃	aluminum trichloride
APC	Adenomatous Polyposis Coli
ARAPs	3-aryl-1-arylpyrroles
ARDAP	3-aryl 1,4-diarylpyrrole
Arg	arginine
ARIs	arylindoles
Asn	asparagine
Asp	aspartic acid
ATCC	American Type Culture Collection
ATI	arylthioindole derivative
ATP	adenosine triphosphate
BSA	bovine serum albumin
BuOH	1-butanol
CDCl ₃	deuterated chloroform
CHCl ₃	chloroform
CK1γ	casein kinase I-γ
CLIP	cytoplasmic linker protein
cm	centimeter
CML	Chronic myeloid leukemia
Colch	colchicine
CRC	colorectal cancer
CRD	cysteine-rich domain
CSA4	combretastatinA-4
CSA4	combretastatin A-4
CSCs	cancer stem cells
Ctrl	control
Cys	cysteine
D ₂ O	deuterium oxide
Da	dalton
DAMA-colchicine	N-deacetyl-N-(2-mercaptoacetyl)colchicine
DAPI	4',6-diamidino-2-phenylindole
DCM or CH ₂ Cl ₂	dichloromethane
Dkk	Dickkopf
DMEM	Dulbecco's Modified Eagle Medium
DMF	<i>N,N</i> -dimethylformamide
DMSO	dimethyl sulfoxide
DMSO-d ₆	deuterated dimethyl sulfoxide

DNA	deoxyribonucleic acid
Dox	doxycycline
Dsh	Dishevelled
dsRNA	double-stranded RNA
DTT	dithiothreitol
EBD	Ezrin/Radixin/Moesin/Merlin-binding domain
EDTA	ethylenediaminetetraacetic acid
EGFR	epidermal growth factor receptor
EMT	Epithelial-Mesenchymal-like Transition
ER	endoplasmic reticulum
ERM	ezrin-radixin-moesin
E-site	exchangeable site
Et	ethyl
Et ₂ O	diethyl ether
EtOAc	ethyl acetate
EtOH	ethanol
evi	evenness interrupted
FBS	fetal bovine serum
FBS	fetal bovine serum
FISH	fluorescent-in-situ-hybridisation
FITC	fluorescein isothiocyanate
Fz	Frizzled
FZD	Frizzled
g	gram(s)
GDP	guanosine diphosphate
Glu	Glutamic acid
GSK3 β	glycogen synthase kinase 3 β
GTP	guanosine triphosphate
h	hours
HBF ₄	Tetrafluoroboric acid
H-bond	hydrogen bond
HCl	hydrochloric acid
HCV	hepatitis C virus
Het	heterocycle
HIF1 α	hypoxia-inducible factor 1 α
HIV	human immunodeficiency virus
HPLC	high-performance liquid chromatography
HSPG	heparan sulfate proteoglycans
HuNoV	human norovirus
Hz	herz
IC ₅₀	half maximal inhibitory concentration
IECs	intestinal epithelial cells
IF	Immunofluorescence
Ig	immunoglobulin
IM	imatinib mesylate
Inh. Colch. Bind.	inhibition of Colchicine binding
IR	Infrared
J	coupling constant in hertz
K ₂ CO ₃	Potassium carbonate
K ₃ PO ₄	potassium phosphate tribasic

Ka	acid dissociation constant
kcal	kilocalories
KCl	potassium chloride
Keq	equilibrium constants
Ki	inhibitory constant
LC-MS/MS	liquid chromatography–mass spectrometry
LEF	lymphoid enhancer factor
Leu	leucine
Leu	leucine
LiCl	lithium chloride
LRP	receptor-related proteins
LSM	laser scanning microscope
Lys	Lysine
M	molarity
MAP	microtubule-associated protein
MCF-7 cells	human breast adenocarcinoma cancer cells
MD	molecular dynamics
MDC	monodansylcadaverine
MDR	multi-drug resistance
Me	methyl
Me ₄ Si	tetramethylsilane
MeOH	Methanol
Met	methionine
MET	mesenchymal–epithelial transition
MgCl ₂	magnesium chloride
min	minutes
mL	millilitre
mm	millimetre
mmol	millimol
MOE	Molecular Operating Environment
mp	Melting point
mRNA	messenger ribonucleic acid
MT	microtubule
MTOC	microtubule organizing center
MTP	mitochondrial transmembrane potential
MTT	3-(4,5-dimethylthiazol-2-yl)-2,5-diphenyltetrazolium bromide
MW	micro-wave
N	normality
Na ₃ VO ₄	Sodium orthovanadate
NaCl	Sodium chloride
NaH	sodium hydride
NaNO ₂	Sodium nitrite
NAs	nucleoside analogues
ND	not determined
NHERF1/EBP50	Na ⁺ /H ⁺ exchanger 3 regulating factor 1
nM	nanomolar
nm	nanometer
NMR	nuclear magnetic resonance
NNIs	non-nucleoside inhibitors

ns	nanosecond
NTP	nucleoside triphosphates
OP	oncoprotein
PBMCs	peripheral blood mononuclear cells
PBS	phosphate-buffered saline
PCR	polymerase chain reaction
Pd/C	Palladium on carbon
PDB	Protein data bank
PDGFR	platelet-derived growth factor receptor
PDZ	postsynaptic density 95/discs large/ zona occludens 1
Pgp	P-glycoprotein
Ph	Philadelphia chromosome
ph	phenyl
pH	$-\log_{10}[\text{H}^+]$
Phe	phenylalanine
PHLPP	PH leucine-rich repeat protein phosphatase
PhMe	toluene
PI	propidium iodide
PM	plasma membrane
Pmax	maximum pressure
PPNDS	pyridoxal-5'-phosphate-6-(2'-naphthylazo-6'-nitro-4',8'-disulfonate) tetrasodium salt
psi	pound-force per square inch
PTEN	phosphatase and tensin homolog
PTHR	parathyroid hormone receptor
PTX	paclitaxel
PyBOP	(Benzotriazol-1-yloxy)tripyrrolidinophosphonium hexafluorophosphate
RdRp	RNA-dependent RNA polymerase
RNA	ribonucleic acid
rt	room temperature
SAR	structure-activity relationship
SD	Standard deviation
SEM	standard error of mean
SFRPs	Soluble Frizzled-Related Proteins
shCtr	control shRNA
shRNAs	small hairpin RNAs
siRNA	silencing RNA
SOCl ₂	thionyl chloride
SPhos	2-dicyclohexylphosphino-2',6'-dimethoxybiphenyl
TBA	tubulin-binding agent
TCF/ LEF	T-cell factor/lymphoid enhancing factor
TEA or Et ₃ N	triethylamine
THF	tetrahydrofuran
Thr	threonine
TKs	Tyrosine kinases
TLC	thin-layer chromatography
TosMIC	<i>p</i> -toluenesulfonylmethyl isocyanide
Trp	tryptophan
Tyr	tyrosine

UV	ultraviolet
Val	valine
VBL	vinblastine
VCR	vincristine
vol	volume
VRB	vinorelbine
W	watt
wls	wntless
Wnt	Wingless–Int
δ	chemical shift in parts per million
λ	wavelength
ν	frequency

1. Tubulin and Microtubules

1.1 Microtubules structure and organization

Microtubules (MTs) are essential for the mitotic division of cells and have been an attractive target for antitumour drugs due to the increased incidence of cancer and significant mitosis rate of tumour cells.³ Microtubules are components of the cytoskeleton and play several crucial roles in a diverse array of cellular processes such as morphogenesis, motility, organelle and vesicle trafficking, and chromosome segregation during mitosis.⁴ MTs are strictly organized to form hollow tubes that are composed of two polypeptides, denoted as α - and β -tubulin, which consist of about 450 aminoacid residues with a molecular mass of ~55 kDa. The two polypeptides interact non covalently to form a stable heterodimer of dimensions $4 \text{ nm} \times 5 \text{ nm} \times 8 \text{ nm}$ and 100,000 daltons in mass, and the association of tubulin heterodimers in a head-to-tail fashion create protofilaments, which in turn associate in a parallel manner to form sheets of tubulin (Figure 1.1).⁵

This arrangement of protofilaments imparts polarity to the final structure of the MT. The two MT poles differ in their dynamic properties, the plus end being more dynamic than the minus end. In eukaryotic cells, MTs form a well-organized network in which the minus ends are generally anchored at the centrosome or MT organizing center (MTOC) whereas the free plus ends probe the cytoplasm, in a search-andcapture-process, to reach specific targets. MT dynamics are tightly regulated both spatially and temporally. This regulation involves nucleotides, MT-associated proteins (MAPs), kinases and phosphatases as well as coordinated interactions with other cytoskeletal components, such as actin filaments, and integrin-containing adhesion sites. This intrinsic dynamic behaviour and its regulation are crucial for MT-specific functions.⁶

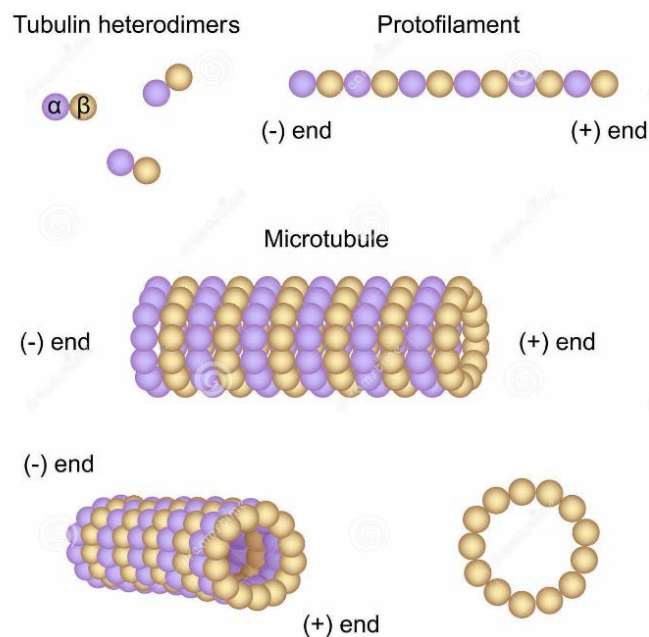


Figure 1.1. Schematic representation of the microtubule (MT) organization. Head-to-tail polymerization of α - and β -tubulin heterodimers results in protofilaments. Lateral interactions between protofilaments allow them to assemble into sheets of tubulin, which fold on themselves to form polarized hollow MT structures typically comprising 13 protofilaments per MT.

1.2 Microtubules Dynamics and GTP Hydrolysis

Polymerization of MTs occurs by a nucleation-elongation mechanism in which the formation of a short MT 'nucleus' is followed by elongation of the MT at its ends by reversible, non-covalent addition of α/β tubulin dimers. In 1984, Mitchison and Kirschner^{7,8} proposed the dynamic instability model of MT assembly, in which individual MTs exist either in an elongation state or a rapidly shortening state, with abrupt and apparently random transitions between these two states. Several studies performed *in vitro*, using purified tubulin^{9,10}, or in living cells¹¹ have confirmed this mechanism of MT assembly/disassembly. MTs are thus governed by an intrinsic property involving repetitive spurts of shortening from their plus ends, followed by periods of polymerization. This non-equilibrium behavior is based on the binding and hydrolysis of GTP at the nucleotide exchangeable site (E-site) in β tubulin. Only dimers that have GTP in their E-site can polymerize. This nucleotide is then hydrolyzed and becomes non-exchangeable. The GTP cap model proposes that the GDP-tubulin core of MT is stabilized at the plus end by a layer of GTP-tubulin subunits that may act to maintain association between protofilaments^{12,13}. When this cap is stochastically lost, the protofilaments peel outward and the MT rapidly depolymerizes (Figure 1.2). Although both MT ends can either grow or shorten, the changes in length at the plus end are much greater than at the minus end. MTs exhibit another important dynamic behavior called treadmilling or flux. It corresponds to a polymer mass steady state resulting from the net growth at one MT end and the net shortening at the opposite end¹⁴. In other words, treadmilling is a process by which tubulin subunits continuously flux from one end of the polymer to the other, due to net differences in the critical subunit concentrations at the opposite MT ends. Both dynamic instability and treadmilling can be produced as distinct phenomena *in vitro* using purified tubulin, and they have also been observed in living cells^{14,15}.

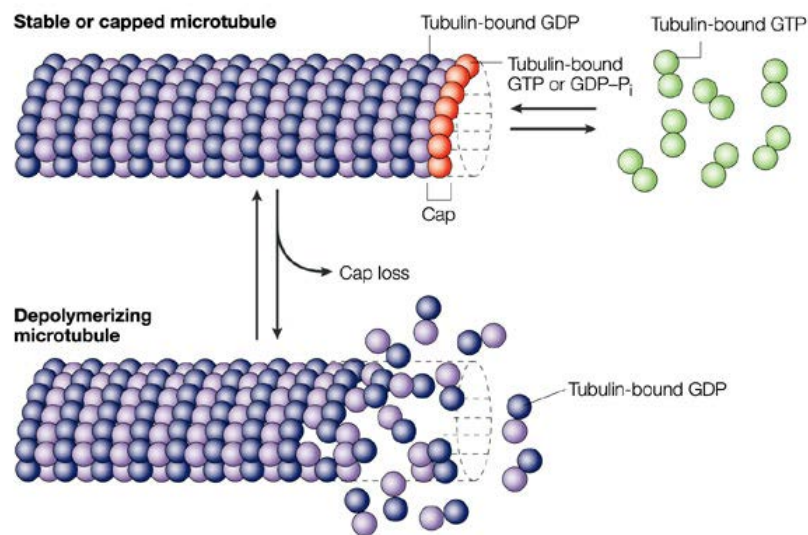


Figure 1.2. Schematic representation of the microtubule (MT) dynamics. During MT-polymerization, guanosine 5'-triphosphate (GTP)-bound α,β -tubulin heterodimers are added at the polymerizing end of the MT. Concomitantly or soon after incorporation into the MT, GTP-bound to β -tubulin is hydrolyzed to the corresponding diphosphate (GDP-MT).

1.3 Tubulin

Tubulin is a globular protein that exists as α - β heterodimers oriented in a polar fashion along the longitudinal protofilaments that make up a microtubule. It is the target of numerous small molecule ligands that interfere with microtubule dynamics, several of which are of clinical use, in particular for cancer treatment.

Most of them bind to one of three different sites: the colchicine, vinblastine and taxol sites.¹⁶ The atomic structure of tubulin in one assembled conformation is known from a 3.5 Å resolution map obtained by electron crystallography of zinc-induced polymers (Figure 1.3).^{17,18}

Each compact monomer contains an *N*-terminal, nucleotide-binding domain, comprising six parallel β -strands (S1-S6) alternating with helices (H1-H6).

The loops joining each strand with the beginning of the next helix are directly involved in binding the nucleotide (loops T1-T6). Within each monomer, nucleotide binding is completed by interaction with the *N*-terminal end of the core helix H7. The core helix connects the nucleotide binding domain with the smaller, second domain, formed by three helices (H8-H10) and a mixed beta sheet (S7-S10). The *C*-terminal region is formed by two antiparallel helices (H11-H12) that cross over the previous two domains. The *N*-site GTP in α -tubulin is buried at the monomer-monomer interface within the dimer, while the GDP at the E-site is exposed on the surface of the dimer, thus explaining the exchangeability of the nucleotides (Figure 1.4). The longitudinal contact between subunits, very similar between monomers within the dimer and between dimers, is very extensive (about 3000 Å² are buried with the formation of the dimer from the monomers, or in the contact between dimers).^{19,20}

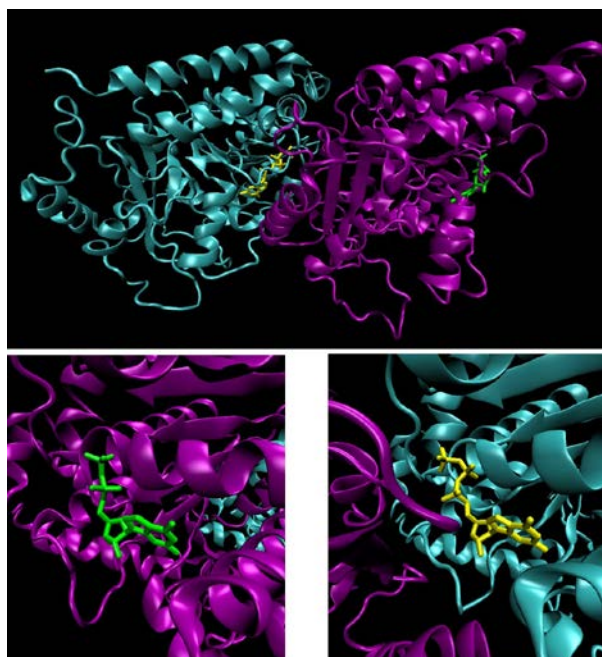


Figure 1.3. Ribbon diagram of the electron crystallography structure of zinc-induced $\alpha\beta$ - tubulin sheets (α -tubulin in cyan, β -tubulin in purple, GDP in green, GTP in yellow).¹⁸

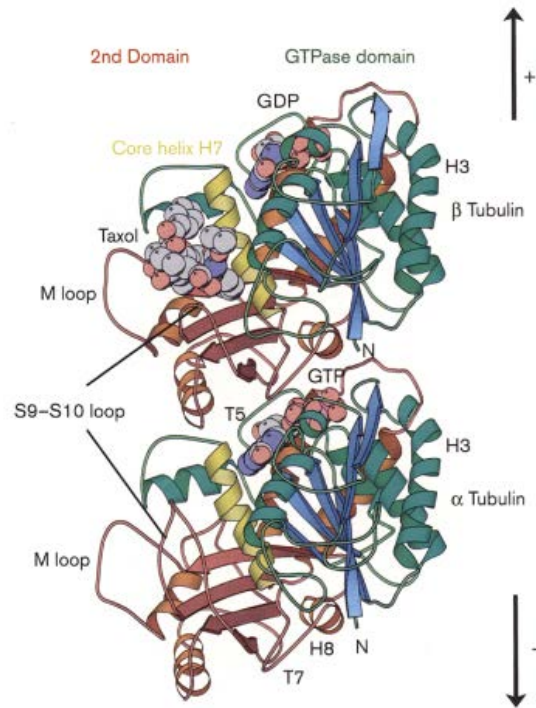


Figure 1.4. Three-dimensional conformation of cow tubulin dimers as predicted from a 3.7 Å resolution map determined using electron crystallography.¹⁷ Arrows show the orientation relative to the more dynamic (plus) and more stable (minus) ends of a microtubule.

About 52% of the residues at the intradimer interface are totally conserved across species, while about 40% are conserved at the interdimer contact.²¹

Of particular interest is the region of contact between the *N*-terminal and the second domain in β -tubulin.

A relative rotation of these domains has been proposed to be linked to microtubule depolymerization following nucleotide hydrolysis.²² Essential to this interface are residues 198 to 216 including strand S6 and helix H6.

This section of the *N*-terminal domain interacts with the core helix H7, and with several regions in the intermediate domain, specially strand S7 and the long loop following helix H9. Of particular interest is β Tyr202. The side-chain hydrogen bonds to Asn167 and Glu200 in an otherwise very hydrophobic region. In α -tubulin the tyrosine is substituted by a phenylalanine that makes non-polar interactions with Leu167 and Cys200. In fungi β -tubulin also has a phenylalanine at position 202, and accordingly residue 167 is an alanine while there is no consensus for position 200. In *Saccharomyces cerevisiae* mutation of Glu200 to alanine results in benomyl resistance,²³ suggesting that such change results in impaired drug binding or, more likely, in a gain in microtubule stability.

Interestingly, Antarctic Fish β -tubulin have a phenylalanine in position 202, in spite of the conservation of Asn167 and Glu200.²⁴

Microtubules from these species are cold resistant and have reduced dynamics, further suggesting the importance of this region in the stability of microtubules *via* its role at the domain boundary in β -tubulin. The two surfaces involved in the interfaces are convoluted in shape and highly complementary.

1.4 Effects of Microtubule Dynamics on Mitosis

Microtubules generate the mitotic spindle, a very important structure needed by eukaryotic cells to segregate their chromosomes correctly during cell division; in

particular MTs dynamic, characterized by non-covalent binding of tubulin dimers to a growing MT and subsequent depolymerization to return dimers, is essential for the process of mitosis.

Mitosis is a process of different stages in which duplicated chromosomes of a cell are separated into two identical sets before cleavage of the cell into two daughter cells.²⁵ Particularly during mitosis, the replicated chromosomes become equally segregated (via karyokinesis) into two identical twin sister nuclei, each of which then becomes enclosed (via cytokinesis) in its own separate cytoplasmic compartment.

The series of events that prepare the cell for mitosis are collectively termed *cell cycle*; it can be divided into four distinct phases “by means of the fact that S, the period of DNA synthesis (which can be recognized by radio-autographic determination of incorporated H3-thymidine) is separated from mitosis by an interval of several hours, which was called G2. Similarly, the period between the end of mitosis and the beginning of S was labeled G1.²⁶

Microtubule dynamics vary during the cell cycle (Figure 1.5), with the turnover of microtubules being slow in interphase cells and the duration of this turnover can be minutes or hours depending on the cell type.^{27,28}

At the onset of mitosis there are dramatic changes in the microtubule network in which the disassembly of microtubules is followed by the formation of a new network of spindle microtubules that can turnover 4–100 times more rapidly than interphase microtubules.^{29,30}

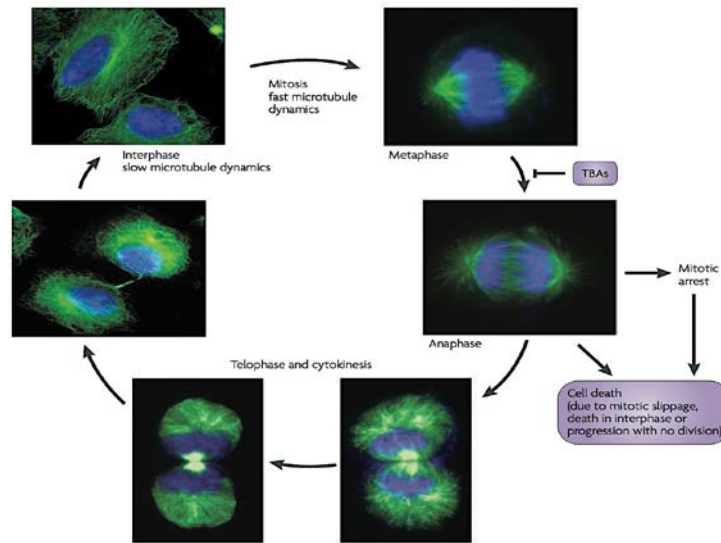


Figure 1.5. Microtubule changes during the cell cycle. Microtubule structures (shown in green) undergo marked morphological changes to mediate specific functions throughout the cell cycle. DNA is shown in blue. The formation of mitotic asters and kinetochore microtubules require tightly regulated microtubule dynamics to ensure the correct attachment and segregation of chromosomes during cell division.³¹ A large number of MT- or tubulin-interacting proteins play critical roles in regulation of the MT dynamic properties. These agents include the MT-associated proteins (MAPs), the MT plus end tracking proteins (+TIPs), minus end binding proteins, proteins that bind along the lengths of MTs, GTPases and guanine nucleotide exchange factors (Figure 1.6).

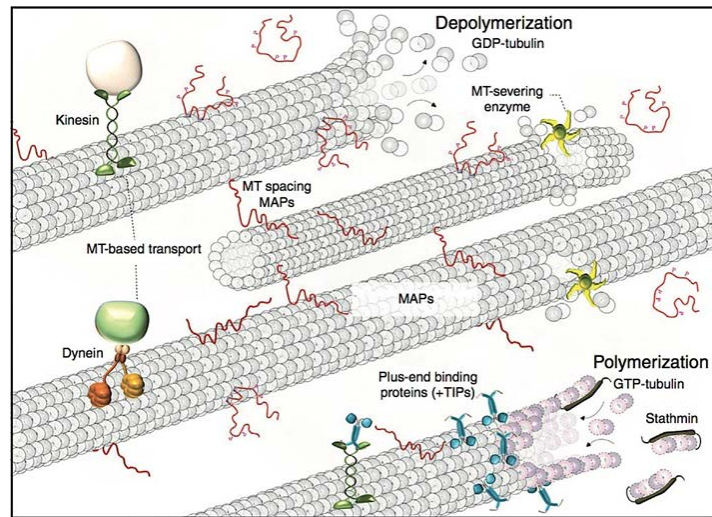


Figure 1.6. Schematic representation of MT dynamics and their regulation.³²

Among these agents, MAPs are primarily involved in modulating MT stability and dynamics. They were initially identified by their activity to copurify with tubulin through repetitive cycles of depolymerization and reassembly. A variety of structural MAPs can interact on the surface of MTs and reduce their dynamic behavior by stimulating tubulin polymerization and stabilization. The brain is a particularly rich source of MAPs and several structural MAPs such as tau, MAP1A, MAP1B, and MAP2 may play a central role in regulation of neuronal MT structure and function during development. As an example, MAP1A is abundant in the adult brain, whereas MAP1B is a neurogenesis-associated MAP predominantly expressed during the early stages of cell maturation, and tau and MAP2 are expressed in both immature and mature neurons.³³ Several MAPs also exhibit a pronounced compartment-specific distribution such as MAP2A and MAP2B, which preferentially locate in the cell bodies and dendrites in mature neurons,³⁴ whereas tau is mostly present in the axons,³⁵ although it can be found also in dendrites.³⁶ However, under physiological conditions, the vast majority of tau molecules are bound to MT with the primary function to promote MT stabilization.³⁷ The most abundant and ubiquitous MAP in non-neuronal cells is MAP4 that can localize both to interphase and mitotic MTs, which suggests that it may contribute to the role of MTs in proliferation and differentiation of cells.³⁸ In general, the activity of MAPs is regulated by phosphorylation that causes the dissociation of MAPs from MTs, hence, promoting depolymerization and increased dynamic instability. Furthermore, the stabilizing activity of MAPs is counteracted by proteins that bind to tubulin dimers and promote MT depolymerization. This class of proteins included, for example, the stathmin (also referred to as oncoprotein 18, OP18; metablastin; p19), which was first identified as a highly overexpressed protein in leukemia^{39,40} and as a protein that underwent phosphorylation in response to extracellular stimuli.⁴¹ Stathmin is a well-conserved, ubiquitous, cytosolic phosphoprotein that forms a specific complex with two tubulin dimers thereby preventing MT polymerization.^{42,43}

SCG10 belongs to the same gene family as stathmin and also promotes MT destabilization. However, while stathmin is expressed in a variety of cell types and shows a cytosolic distribution, SCG10 is neuron-specific and membrane-associated. Both stathmin and SCG10 are regulated by phosphorylation and have high expression in the developing nervous system, but persists in regions of synaptic plasticity of the adult brain.⁴⁴⁻⁴⁶ While MAPs such as tau and MAP2 localize to the entire MT surface, proteins like +TIPs, such as the cytoplasmic linker protein CLIP-170, the EB1, and others, bind to MT plus ends (Figure 1.6). +TIPs are involved in intracellular transport and crosstalk of

MTs with the actin cytoskeleton.⁴⁷ Furthermore, they participate in the establishment of neuron polarity, axon navigation, and spine growth and maintenance.⁴⁸ EB1 is a potent inducer of MT polymerization and plays an important role in anchoring the minus end of MTs to the centriole. Minus end binding proteins include the γ -TuRCs,⁴⁹ stathmin,⁵⁰ and possibly ninein.⁵¹ The GTPase Ran,⁵² and the chromatin-bound guanine nucleotide exchange factor RCC1 are additional recently discovered important MT regulatory proteins. Other important families of proteins involved in regulation of MT dynamics and function are the motor proteins, such as kinesins⁵³ and dyneins⁵⁴ (Figure 1.6).

Kinesins and dyneins are protein complexes that move along MTs (towards the plus and minus ends, respectively) by hydrolysing ATP. They generate forces that are used for various intracellular functions, especially for intracellular transport. For example, in neurons, these proteins allow the transport of cargoes over long distances from the cell body to the synapses.⁵⁵ Moreover, motor proteins generate forces for ciliary beating⁵⁶ and self-organization of the mitotic spindle, whereas specific kinesins catalyse the depolymerization of MTs,⁵⁷ thus participating in the complex network of interacting proteins that regulate MT dynamics. Most tubulin-binding agents (TBAs) act on spindle MT dynamics, which are important for normal spindle function.⁵⁸ Thus, disruption of spindle MTs results in mitotic arrest, which can lead to cell death through various mechanisms. Since cancer cells usually display higher proliferation rates than normal cells, drugs that interfere with the MT dynamic equilibrium, also known as antimitotic agents, have become a fruitful approach to develop anticancer agents in clinical use.

1.5 Tubulin Binding Agents (TBAs) as Anti-Mitotic Drugs

Tubulin is the primary target of an ever growing number of natural, semisynthetic and synthetic products as potential anticancer agents. The mechanisms of interaction of these molecules with tubulin are varied. The majority of these structurally different substances originate from natural sources and bind to tubulin and/or MTs altering MT dynamics in different ways.⁵⁹

These agents can be divided into two major classes: the MT-destabilizing agents and the MT-stabilizing agents, according to their effects on MT polymer mass at high concentration.

The MT-destabilizing agents bind preferentially to depolymerized MTs and inhibit MT assembly at high concentration, while the MT-stabilizing drugs bind to polymerized MTs and inhibit MT disassembly (Figure 1.7).

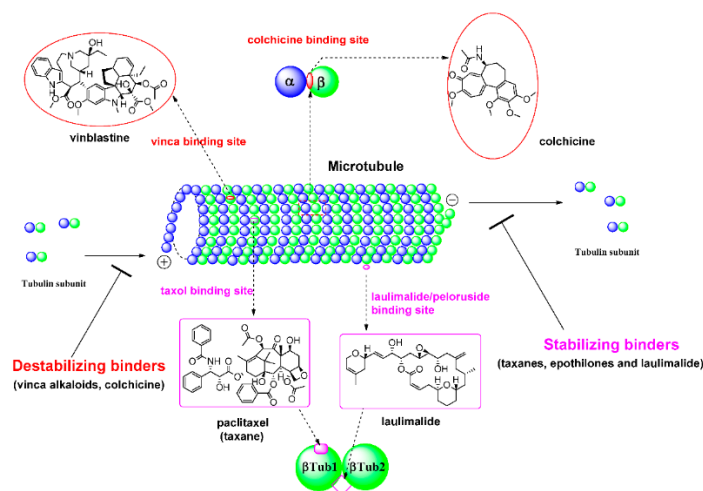


Figure 1.7. Tubulin binding sites and representative natural products of microtubule-targeted drugs.⁶⁰

The result of these interactions is inevitably the failure of the cell to undergo a normal mitosis. The first group includes compounds like the Vinca alkaloids (vinblastine, vincristine, vinorelbine, vindesine and vinflunine), cryptophycins, eribulin, halichondrins, estramustine, colchicine and combretastatins, which are mostly used for treatment of cancer.^{61,62} In addition, this group includes a large number of compounds that have not undergone clinical development for cancer therapy, including the anti-tussive noscapine,⁶³ maytansine, rhizoxin, spongistatins, podophyllotoxin, steganacins and curacins,⁶⁴ several herbicides;⁶⁵ antifungal and antihelmintic agents;⁶⁶ and some psychoactive drugs.^{61,62}

In contrast, the second group includes paclitaxel (Taxol), docetaxel (Taxotere; Sanofi-Aventis), the epothilones, discodermolide, the eleutherobins, sarcodictyins, dictyostatin, laulimalide, rhazinalam, peloruside A and certain steroids and polyisoprenyl benzophenones.^{61,67} The vast majority of the MT-binding agents act as antimetabolic drugs and interfere with the normal dynamic equilibrium of MTs, thereby disrupting the function of the mitotic apparatus. The suppression of MT dynamics, which are essential to proper spindle function, result in the slowing or blocking of mitosis at the metaphase/anaphase transition and induction of apoptotic cell death. Furthermore, these compounds can affect MTs in interphase cells and have the potential to inhibit cell motility and normal subcellular organization. Interestingly, the effects of the drugs on dynamics are often more powerful than their effects on polymer mass. Thus, they can modulate MT dynamics at 10- to 100-fold lower concentrations than those required to affect (increase or decrease) the MT polymer mass.

Vinca alkaloids

The naturally occurring members of this family, vinblastine (**1.1**, Figure 1.8) and vincristine (**1.2**, Figure 1.8), were originally isolated from the leaves of the periwinkle plant *Catharanthus roseus* (Figure 1.9).

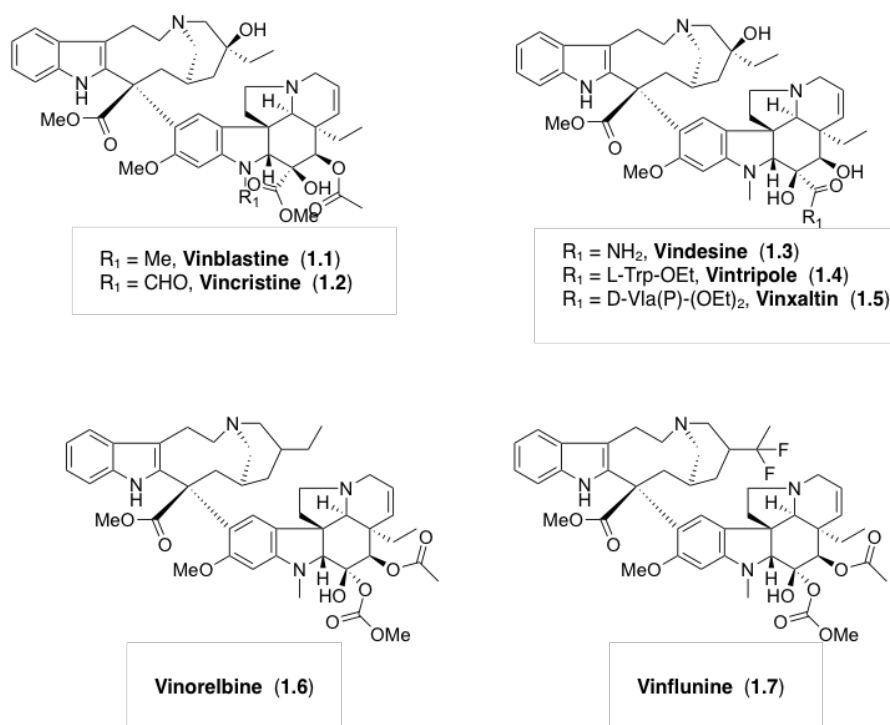


Figure 1.8. *Vinca alkaloid* site binding agents.



Figure 1.9. *Catharanthus roseus*.

In the late 1950s, the Eli Lilly Research Laboratories and the University of Western Ontario^{68,69} both discovered the antimitotic and, therefore, anticancer potential of these drugs that came into widespread use for the treatment of leukemias, lymphomas, and solid malignancies.⁷⁰⁻⁷² Since that time, the clinical efficacy of these drugs in several combination therapies has led to the development of various semi-synthetic analogues, including vindesine (**1.3**, Figure 1.8), vinorelbine (**1.6**, Figure 1.8) and vinflunine (**1.7**, Figure 1.8), with the principal aims to obtain more efficacious congeners with a broad spectrum of antitumor activity and to reduce neurotoxicities and myelosuppression, which are the principle side effects.⁷³ The main structure of Vinca alkaloids is composed of a catharenthine moiety and vindoline nucleus, which are not able to inhibit MT assembly when alone. Structural modifications of the vinblastine molecule led to the development of several non-naturally occurring analogues. For example, vindesine (**1.3**, Figure 1.8), the first semisynthetic derivative discovered, was developed by changing the acetyl group at C23 of vindoline moiety to an amide group,⁷⁴ whereas introduction at C23 of a L-tryptophane residue led to the development of vintripole (**1.4**, Figure 1.8).⁷⁵ Vinxaltin (**1.5**, Figure 1.8) is currently in phase II clinical trial for the treatment of advanced breast cancer showing an excellent antitumour profile. The semisynthetic analogue vinorelbine (**1.6**, Figure 1.8), showed promising activity against breast cancer⁷⁶ and is now in clinical trial for the treatment of other types of tumors.⁷⁷ Further structural modifications of vinorelbine led to the discovery of vinflunine (**1.7**, Figure 1.8), which showed significantly superior *in vivo* anticancer activity.⁷⁸ The interactions of Vinca alkaloids, especially vinblastine, with tubulin and MTs have been extensively studied.^{61,79-81} Vinblastine binds to the β -tubulin subunit at a distinct region, usually referred to as the “Vinca-binding domain”,^{82,83} which is located very close to the GTP site at the interface between β 1-tubulin subunit and the adjacent α 2-tubulin subunit. The binding of vinblastine to soluble tubulin is rapid and reversible, but relatively weak ($K_a \sim 2 \times 10^4$ M), and is not influenced by temperature.^{81,84,85} Remarkably, binding of vinblastine induces a conformational change in tubulin, which not only promotes tubulin self-association, but also results in an increased affinity of vinblastine for the tubulin.^{79,81,86} Vinblastine also binds directly to microtubules. *In vitro*, vinblastine binds to tubulin at the plus ends of the MT with very high affinity (1 μ M) (Figure 1.10) but it binds with markedly reduced affinity to tubulin that is buried in the tubulin lattice.^{87,88} The mechanism of action of the Vinca alkaloids on tubulin and MTs is highly dependent upon drug concentration.⁶¹ At substoichiometric concentrations (at concentrations well below the concentration of tubulin free in solution) these drugs bind to high-affinity sites at the ends of MTs ($K_a 5.3 \times 10^{-5}$ M) and do not decrease the polymer mass, but they prevent MT polymerization by blocking mitosis through the suppression of MT dynamics. At higher concentrations (for example, 10–100 nM in HeLa cells), these drugs bind to low affinity, high capacity sites ($K_a 3-4 \times 10^{-3}$ M)

and destroy mitotic spindles therefore leaving the dividing cancer cells blocked in mitosis with condensed chromosomes.

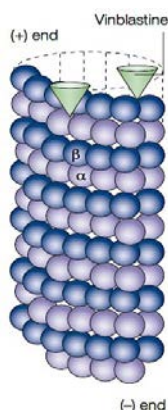


Figure 1.10. Binding of vinblastine to the MT plus end suffice.³¹

The structure of vinblastine bound to the tubulin/stathmin-like domain/vinblastine complex was determined at 4.1 Å resolution by X-ray diffraction (Figure 1.11).⁸⁹

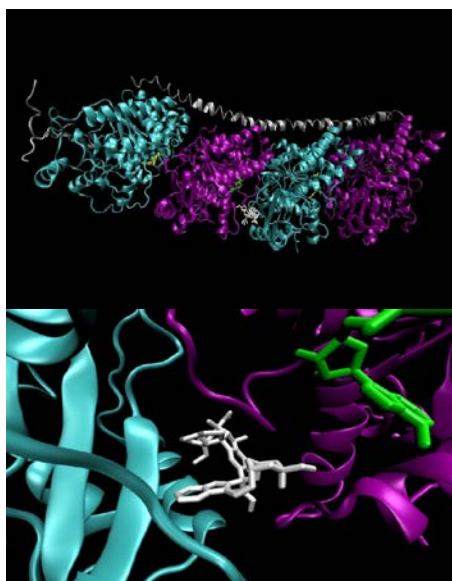


Figure 1.11. Ribbon diagram of the X-ray structure of tubulin($\alpha 1\beta 1\alpha 2\beta 2$)/stathmin-like domain/vinblastine complex ($\alpha 1$ -, $\alpha 2$ -tubulin in cyan, $\beta 1$ -, $\beta 2$ -tubulin in purple, GDP in green, GTP in yellow, stathmin-like in gray, vinblastine in white).^{89,90}

Colchicine

Colchicine (**1.8**, Figure 1.12) was originally isolated from the meadow saffron *Colchicum autumnale* (Figure 1.13) and it is used clinically in the treatment and prevention of gout,⁹¹ familial Mediterranean fever and liver cirrhosis.⁹² The toxicity profile of colchicine, as well as compounds that bind to the “colchicine site” on tubulin, prevented their use in other therapies, including cancer chemotherapy.

Because of the important toxicity profile of colchicine, hundreds of analogues have been discovered in the past decades. Thus, for example, colchicone (**1.9**, Figure 1.12), thicolchicine (**1.10**, Figure 1.12), allocalchicine, (**1.11**, Figure 1.12), cornigerine (**1.12**, Figure 1.12), podophyllotoxin (**1.13**, Figure 1.12), etoposide (**1.14**, Figure 1.12),

teniposide (**1.15**, Figure 1.12), combretastatin A-4 (**1.16**, Figure 1.12) and related congeners (**1.17-1.21**, Figure 1.12) are all derivatives of colchicine that share a common binding site on tubulin and mechanism of action together with a more favorable water solubility, more potent activity, and lower toxicity than colchicine.

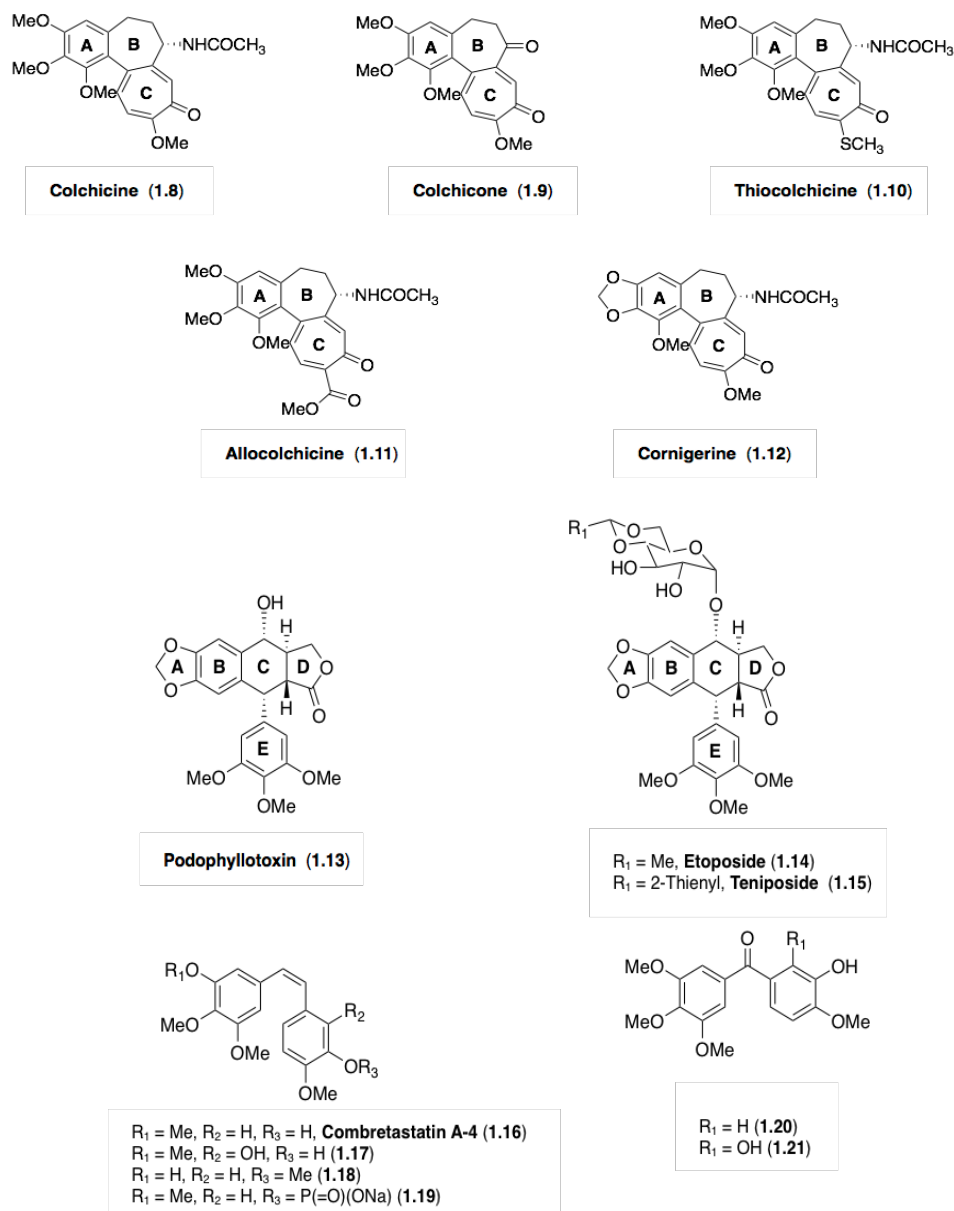


Figure 1.12. Colchicine binding site agents.

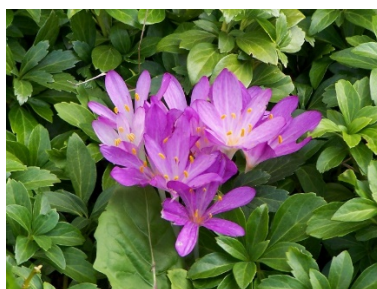


Figure 1.13. *Colchicum autumnale*.

The colchicine-binding site on tubulin has been extensively studied.^{93,94} It is located at the $\alpha\beta$ -tubulin heterodimer interface⁹⁵ and when colchicine is bound to tubulin, it forms complexes with tubulin dimers and copolymerizes into the MT lattice, suppressing MT dynamics (Figure 1.14).⁹⁶ As with the Vinca alkaloids, colchicine promotes MT depolymerization at high concentrations and powerfully suppresses MT dynamics at low concentrations, without appreciably affecting the mass of assembled MTs.^{96,97} Colchicine first binds to soluble tubulin, induces slow conformational changes in the tubulin, and ultimately forms a final-state tubulin–colchicine complex, which poorly dissociates.^{79,98} In contrast to vinblastine, which acts selectively at the plus ends, colchicine copolymerizes along with free tubulin into the MT at both ends,⁹⁹ which remain competent to grow but their dynamics are suppressed.¹⁰⁰

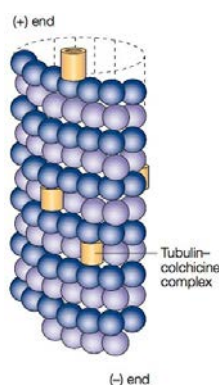


Figure 1.14. Binding of colchicine to MTs.³¹

The binding mode of colchicine was confirmed by the determination of a 3.58 Å X-ray structure of tubulin complexed with *N*-deacetyl-*N*-(2-mercaptoacetyl)colchicine (DAMA-colchicine), which is a close structural analogue of colchicine (Figure 1.15).⁹⁵

It has been reported that the β -tubulin subunit is mostly involved in colchicine binding. In particular, the A ring of colchicine (Figure 1.12) is involved in interactions with Cys-354 and Cys-239 residues and the C ring lying between the peptide region containing Cys-239, the terminal amino sequence, and the region containing aminoacids 1–36.^{101,102}

The seven membered B ring is not believed to be crucial for tubulin binding,^{103,104} while the trimethoxyphenyl group on A ring and the α -methoxytropolone ring C are important structural features essential for inhibition of MT assembly.

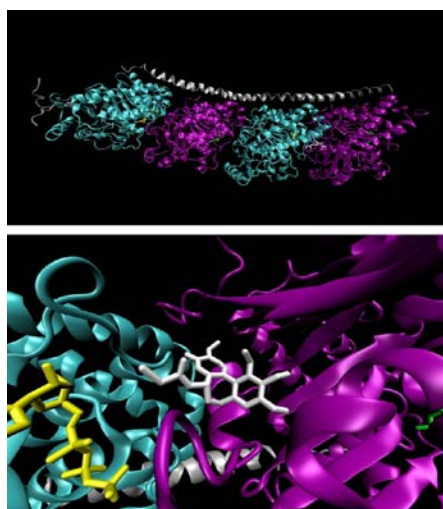


Figure 1.15. Ribbon diagram of the X-ray structure of tubulin($\alpha 1\beta 1\alpha 2\beta 2$)/stathmin-like domain/DAMA colchicine complex. $\alpha 1$ -, $\alpha 2$ -Tubulin in cyan, $\beta 1$ -, $\beta 2$ -tubulin in purple, GDP in green, GTP in yellow, stathmin-like in gray, DAMA-colchicine in white.^{95,105}

Taxanes

Paclitaxel (**1.22**, Figure 1.16) and its more potent, semisynthetic derivative docetaxel (**1.23**, Figure 1.16) are among the most important antimitotic agents with broad antitumor activity. Paclitaxel was isolated from the pacific yew, *Taxus brevifolia* (Figure 1.17), by Wani and Wall in 1971.¹⁰⁶ The difficulties in limited supplies of the natural compound, formulation, poorly solubility, and toxicities initially prohibited its clinical development.

The discovery by Peter Schiff and Susan Horwitz that, unlike the Vinca alkaloids, paclitaxel acts by stimulating MT polymerization,¹⁰⁷ encouraged the development of procedures for its semi-synthesis and a more practical formulation that allowed paclitaxel to be approved for clinical purposes by 1995. Paclitaxel is now semisynthesized from baccatin III (**1.24**, Figure 1.16), which is isolated from *Taxus baccata*,¹⁰⁸ or fully synthesized¹⁰⁹ and it is widely used to treat breast and ovarian cancer, non-small-cell lung cancer and Kaposi's sarcoma. Principal side effects are represented by neurotoxicity and myelosuppression.^{110,111} Extensive structure-activity relationship (SAR) studies provided the structural determinants responsible for the activity of paclitaxel. It is now established that the side chain at C13 bearing a C2'-OH, as well as the benzoyl group at C2 and the oxetane ring at C4-C5 are essential for both cytotoxicity and stabilization of MTs.^{112,113}

Remarkably, the oxetane ring appeared to be an important feature, as analogues that bear an open oxetane ring showed a greatly reduced activity. The acetyl group at C4 did not appear to play a significant role in the biological activity, but it may contribute to the final conformation of the molecule. Finally, the C1-OH group imparts a significant contribution to the overall bioactivity.¹¹²

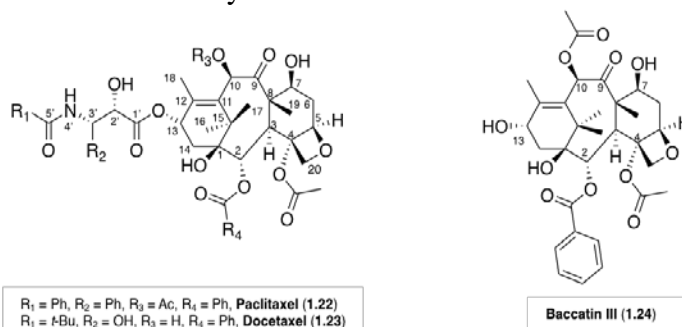


Figure 1.16. Taxane site binding agents.



Figure 1.17. *Taxus brevifolia*.

Paclitaxel binds poorly to soluble tubulin itself, while binds directly with high affinity to tubulin along the length of the MT (Figure 1.18). In detail, paclitaxel acts on MTs by binding within the lumen of the MT at a site in the β -tubulin subunit on the inside surface of the MT, which is commonly referred to as the “taxane site”.

Although the binding site is on the inside surface of the MT, paclitaxel is thought to gain access to its binding site by diffusing through small openings in the MT or fluctuations of the MT lattice.¹¹⁴ The interaction with β -tubulin results in conformational changes in the M-loop of β -tubulin that ultimately stabilize lateral interactions of adjacent protofilaments.¹¹⁵

Like the Vinca alkaloids, the mechanism of action of paclitaxel, and taxanes in general, is dose-dependent.¹¹⁶ At low concentrations, taxanes induce a mitotic block without a significantly increase in MT polymer mass. These effects are associated with abnormalities in the metaphase plate and mitotic asters. At higher concentrations, taxanes induce polymerization of stable MTs.

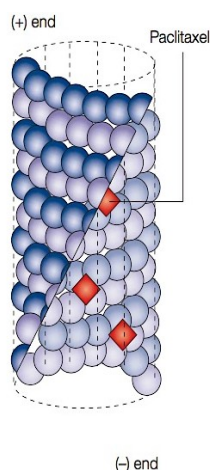


Figure 1.18. A MT cut away to Taxol binding along the interior surface of the MT.³¹

The structure of the tubulin-paclitaxel complex has been solved at 3.5 Å by electron crystallography (Figure 1.19).¹⁸



Figure 1.19. Ribbon diagram of the X-ray structure of α,β -tubulin/paclitaxel complex (α - tubulin in cyan, β -tubulin in purple, GDP in green, GTP in yellow, stathmin-like in gray, paclitaxel in white).¹⁸

The clinical success of the taxanes has led to a search for other drugs that enhance MT polymerization, yielding several promising compounds, including the epothilones, discodermolide, the sarcodictyins, eleutherobin and laulimalide.

Some of these compounds compete with paclitaxel for binding to MTs and are said to bind at or near the taxane site (epothilones, discodermolide, eleutherobins and sarcodictyins), but others, such as laulimalide, seem to bind to unique sites on MT.¹¹⁷

1.6 Multi-drug resistance (MDR) to TBAs

The ability of malignant cells to develop resistance to tubulin binding agents (TBAs) poses a major obstacle to the ultimate success of cancer therapy. While some mechanisms of resistance allow cells to survive exposure to a single agent, the phenomenon of multidrug resistance (MDR) confers upon cells the ability to withstand exposure to lethal doses of many structurally unrelated antineoplastic agents.

MDR has been strongly linked to the overexpression of a membrane-associated glycoprotein, P-glycoprotein, which appears to play a role in drug efflux. However, several lines of evidence suggest that other mechanisms of resistance are involved in MDR.¹¹⁸ These mechanisms can be broadly divided into five categories¹¹⁹ (Figure 1.20):

- a) Decreased cellular drug accumulation owing to the overexpression of membrane-bound drug efflux proteins such as P-glycoprotein.
- b) A direct alteration in the drug target through mutation, as is evident in drug-resistant cell lines.
- c) Altered expression of tubulin isotypes or microtubule associated protein (MAP) expression that reduces drug efficacy, as is evident in drug-resistant cell lines and clinical samples.
- d) Changes to the microtubules induced by interactions with or regulation by other cytoskeletal proteins, such as γ -actin or actin-regulating proteins, that can affect the ability of TBAs to induce mitotic arrest and cell death.¹²⁰⁻¹²²
- e) Defects in apoptotic pathways also influence resistance to TBAs.¹²³

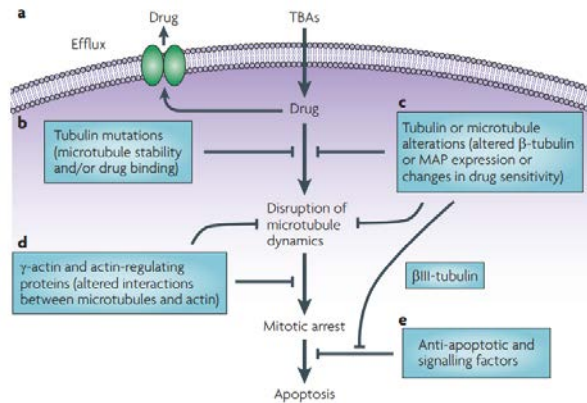


Figure 1.20. Mechanisms of tubulin-binding agent resistance.¹¹⁹

1.7 References

1. Frattini, M.; Balestra, D.; Suardi, S.; Oggionni, M.; Alberici, P.; Radice, P. et al. Different genetic features associated with colon and rectal carcinogenesis. *Cancer Res.* **2004**, *10*, 4015–21
2. Vaquero, J.; Nguyen Ho-Bouloires, T.H.; Claperon, A.; Fouassier, L. Role of the PDZ-scaffold protein NHERF1/EBP50 in cancer biology: from signaling regulation to clinical relevance. *Oncogene* **2017**, *36*, 3067–79.
3. Duan, Y.; Liu, W.; Tian, L.; Mao, Y.; Song, C. Targeting tubulin-colchicine site for cancer therapy: inhibitors, antibody-drug conjugates and degraders. *Curr Top Med Chem.* **2019**, DOI: 10.2174/1568026619666190618130008. [Epub ahead of print].
4. The Role of Microtubules in Cell Biology, Neurobiology, and Oncology (Ed.: T. Fojo), Humana Press, Totowa, NJ (USA), **2008**.
5. Bryan, J.; Wilson, L. Are cytoplasmic microtubules heteropolymers? *Proc. Natl. Acad. Sci. USA.* **1971**, *68*, 1762–1766.
6. Honore, S.; Pasquier, E.; Braguer, D. Understanding microtubule dynamics for improved cancer therapy. *Cell. Mol. Life Sci.* **2005**, *62*, 3039–3056.
7. Mitchison, T.; Kirschner, M. Dynamic instability of microtubule growth. *Nature* **1984**, *312*, 237–242.
8. Mitchison, T.; Kirschner, M. Microtubule assembly nucleated by isolated centrosomes. *Nature* **1984**, *312*, 232–237.
9. Panda, D.; Miller, H.P.; Banerjee, A.; Luduena, R.F.; Wilson, L. Microtubule dynamics in vitro are regulated by the tubulin isotype composition. *Proc. Natl. Acad. Sci. USA.* **1994**, *91*, 11358–11362.
10. Billger, M.A.; Bhattacharjee, G.; Williams, R.C.Jr. Dynamic instability of microtubules assembled from microtubule-associated protein-free tubulin: neither variability of growth and shortening rates nor “rescue” requires microtubule-associated proteins. *Biochemistry* **1996**, *35*, 13656–13663.
11. Joshi, H.C. Microtubule dynamics in living cells. *Curr. Opin. Cell Biol.* **1998**, *10*, 35–44.
12. Chretien, D.; Jainosi, I.; Taveau, J.C.; Flyvbjerg, H. Microtubule’s conformational cap. *Cell. Struct. Funct.* **1999**, *24*, 299–303.
13. Panda, D.; Miller, H.P.; Wilson, L. Determination of the size and chemical nature of the stabilizing “cap” at microtubule ends using modulators of polymerization dynamics. *Biochemistry* **2002**, *41*, 1609–1617.
14. Margolis, R.L.; Wilson, L. Microtubule treadmilling: what goes around comes around. *Bioessays* **1998**, *20*, 830–836.

15. Waterman-Storer, C.M.; Salmon, E.D. Microtubule dynamics: treadmilling comes around again. *Curr. Biol.* **1997**, *7*, 369–372.
16. Ravelli, R.; Gigant, B.; Curmi, P.; Jourdain, I.; Lachkar, S.; Sobel, A.; Knossow, M. Insight into tubulin regulation from a complex with colchicine and a stathmin-like domain. *Nature* **2004**, *428*, 198-202.
17. Nogales, E.; Wolf, S.; Downing, K.H. Structure of the tubulin dimer by electron crystallography. *Nature* **1998**, *391*, 199–203.
18. Löwe, J.; Li, H.; Downing K.H.; Nogales, E. Refined structure of tubulin at 3.5Å resolution. *J. Mol. Biol.* **2001**, *313*, 1045–1057.
19. Nogales, E., Downing, K.H., Amos, L. A. & Löwe, J. Tubulin and FtsZ form a distinct family of GTPases. *Nature Struct. Biol.* **1998**, *5*, 451-458.
20. Nogales, E.; Whittaker, M.; Milligan, R.A.; Downing, K.H. High resolution structure of the microtubule. *Cell* **1999**, *96*, 79-88.
21. Nogales, E. A structural view of microtubuledynamics. *Cell. Mol. Life Sci.* **1999**, *56*, 133-142.
22. Amos, L.A.; Löwe, J. How taxol stabilizes microtubule structure. *Chem. Biol.* **1999**, *6*, R65-R69.
23. Richards, K. L.; Anders, K. R.; Nogales, E.; Schwartz, K.; Downing, K.H.; Botstein, D. Structure-function relationships in yeast tubulins. *Mol. Biol. Cell.* **2000**, *11*, 1887-1903.
24. Detrich, H.W.; Parker, S.K.; Williams, R.C.; Nogales, E.; Downing, K.H. Cold adaptation of microtubule assembly and dynamics. Structural interpretation of primary sequence changes present in the alpha- and beta-tubulins of Antarctic fishes..*J. Biol. Chem.* **2000**, *275*, 37038-37047.
25. Kaur, R.; Kaur, G.; Gill, K.R.; Soni, R.; Bariwal, J. Recent developments in tubulin polymerization inhibitors: an overview. *Eur. J. Med. Chem.* **2014**, *87*, 89–124.
26. Puck, T.T.; Steffen, J. Life cycle analysis of mammalian cells. I. a method for localizing metabolic events within the life cycle, and its application to the action of colcemid and sublethal doses of X-irradiation. *Biophys J.* **1963**, *3*, 379–397.
27. Pepperkok, R.; Bre, M.H.; Davoust, J.; Kreis, T.E. Microtubules are stabilized in confluent epithelial cells but not in fibroblasts. *J. Cell Biol.* **1990**, *111*, 3003–3012.
28. Saxton, W.M. et al. Tubulin dynamics in cultured mammalian cells. *J. Cell Biol.* **1984**, *99*, 2175–2186.
29. Rusan, N.M.; Fagerstrom, C.J.; Yvon, A.M.; Wadsworth, P. Cell cycle-dependent changes in microtubule dynamics in living cells expressing green fluorescent protein- α tubulin. *Mol. Biol. Cell.* **2001**, *12*, 971–980.
30. Zhai, Y.; Kronebusch, P.J.; Simon, P.M.; Borisy, G.G. Microtubule dynamics at the G2/M transition: abrupt breakdown of cytoplasmic microtubules at nuclear envelope breakdown and implications for spindle morphogenesis. *J. Cell Biol.* **1996**, *135*, 201–214.
31. Jordan, M.A.; Wilson, L. Microtubules as a target for anticancer drugs. *Nature Rev. Cancer* **2004**, *4*, 253–265.
32. Penazzi, L.; Bakota, L.; Brandt, R. Chapter Three-Microtubule Dynamics in Neuronal Development, Plasticity, and Neurodegeneration. *Int. Rev. Cell Mol. Biol.* **2016**, *321*, 89–169.
33. Tucker, R.P. The roles of microtubule-associated proteins in brain morphogenesis: a review. *Brain Res. Rev.* **1990**, *15*, 101–120.
34. Sanchez, C.; Diaz-Nido, J.; Avila, J. Phosphorylation of microtubule-associated protein 2 (MAP2) and its relevance for the regulation of the neuronal cytoskeleton function. *Prog. Neurobiol.* **2000**, *61*, 133–168.
35. Dehmelt, L.; Halpain, S. The MAP2/Tau family of microtubule-associated proteins. *Genome Biol.* **2005**, *6*, 204.

36. Chen, Q.; Zhou, Z.; Zhang, L.; Wang, Y.; Zhang, Y.W.; Zhong, M.; Xu, S. C.; Chen, C.H.; Li, L.; Yu, Z.P. Tau protein is involved in morphological plasticity in hippocampal neurons in response to BDNF. *Neurochem. Int.* **2012**, *60*, 233–242.
37. Drechsel, D.N.; Hyman, A.A.; Cobb, M.H.; Kirschner, M.W. Modulation of the dynamic instability of tubulin assembly by the microtubule-associated protein tau. *Mol. Biol. Cell* **1992**, *3*, 1141–1154.
38. Chapin, S.J.; Bulinski, J.C. Cellular microtubules heterogeneous in their content of microtubule-associated protein 4 (MAP4). *Cytoskeleton* **1994**, *27*, 133–149.
39. Hanash, S.M.; Baier, L.J.; McCurry, L.; Schwartz, S.A. Lineage-related polypeptide markers in acute lymphoblastic leukemia detected by two-dimensional gel electrophoresis. *Proc. Natl. Acad. Sci. USA* **1986**, *83*, 807–811.
40. Melhem, R.F.; Zhu, X.X.; Hailat, N.; Strahler, J.R.; Hanash, S.M. Characterization of the gene for a proliferation-related phosphoprotein (oncoprotein 18) expressed in high amounts in acute leukemia. *J. Biol. Chem.* **1991**, *266*, 17747–17753.
41. Sobel, A.; Tashjian, A.H. Jr. Distinct patterns of cytoplasmic protein phosphorylation related to regulation of synthesis and release of prolactin by GH cells. *J. Biol. Chem.* **1983**, *258*, 10312–10324.
42. Sobel, A. Stathmin: a relay phosphoprotein for multiple signal transduction? *Trends Biochem. Sci.* **1991**, *16*, 301–305.
43. Belmont, L.; Mitchison, T. Identification of a protein that interacts with tubulin dimers and increases the catastrophe rate of microtubules. *Cell* **1996**, *84*, 623–631.
44. Grenningloh, G.; Soehman, S.; Bondallaz, P.; Ruchti, E.; Cadas, H. Role of the microtubule destabilizing proteins SCG10 and stathmin in neuronal growth. *J. Neurobiol.* **2004**, *58*, 60–69.
45. Koppel, J.; Boutterin, M.C.; Doye, V.; Peyro-Saint-Paul, H.; Sobel, A. Developmental tissue expression and phylogenetic conservation of stathmin, a phosphoprotein associated with cell regulations. *J. Biol. Chem.* **1990**, *265*, 3703–3707.
46. Sobel, A.; Boutterin, M.C.; Beretta, L.; Chneiweiss, H.; Doye, V.; Peyro-Saint-Paul, H. Intracellular substrates for extracellular signaling. Characterization of a ubiquitous, neuron-enriched phosphoprotein (stathmin). *J. Biol. Chem.* **1989**, *264*, 3765–3772.
47. Lansbergen, G.; Akhmanova, A. Microtubule plus end: a hub of cellular activities. *Traffic* **2006**, *7*, 499–507.
48. Akhmanova, A.; Hoogenraad, C.C. Microtubule plus-end-tracking proteins: mechanisms and functions. *Curr. Opin. Cell Biol.* **2005**, *17*, 47–54.
49. Job, D.; Valiron, O.; Oakley, B. Microtubule nucleation. *Curr. Opin. Cell Biol.* **2003**, *15*, 111–117.
50. Manna, T.; Thrower, D.; Miller, H.P.; Curmi, P.; Wilson, L. Stathmin strongly increases the minus end catastrophe frequency and induces rapid treadmilling of bovine brain microtubules at steady state in vitro. *J. Biol. Chem.* **2006**, *281*, 2071–2078.
51. Wittmann, T.; Bokoch, G.M.; Waterman-Storer, C.M. Regulation of microtubule destabilizing activity of Op18/stathmin downstream of Rac1. *J. Biol. Chem.* **2004**, *279*, 6196–6203.
52. Wilde, A.; Lizarraga, S.B.; Zhang, L.; Wiese, C.; Gliksman, N.R.; Walczak, C.E.; Zheng, Y. Ran stimulates spindle assembly by altering microtubule dynamics and the balance of motor activities. *Nat. Cell Biol.* **2001**, *3*, 221–227.
53. Verhey, K.J.; Hammond, J.W. Traffic control: regulation of kinesin motors. *Nature Rev. Mol. Cell Biol.* **2009**, *10*, 765–777.
54. Vallee, R.B.; Williams, J.C.; Varma, D.; Barnhart, L.E. Dynein: an ancient motor protein involved in multiple modes of transport. *J. Neurobiol.* **2004**, *58*, 189–200.

55. Sheetz, M.P.; Steuer, E.R.; Schroer, T. A. The mechanism and regulation of fast axonal transport. *Trends Neurosci.* **1989**, *12*, 474–478.
56. Lindemann, C.B.; Lesich, K.A. Flagellar and ciliary beating: the proven and the possible. *J. Cell Sci.* **2010**, *123*, 519–528.
57. Howard, J.; Hyman, A.A. Microtubule polymerases and depolymerases. *Curr. Opin. Cell Biol.* **2007**, *19*, 31–35.
58. Kermack, W.O.; Perkin, W.H., Jr.; Robinson, R. Harmine and harmaline. V. Synthesis of norharman. *J. Chem. Soc., Trans.* **1921**, *119*, 1602–1642.
59. Dumontet, C.; Jordan, M.A. Microtubule-binding agents: a dynamic field of cancer therapeutics. *Nature* **2010**, *9*, 790–803.
60. Banerjee, S.; Hwang, D.; Li, W.; Miller, D. Current Advances of Tubulin Inhibitors in Nanoparticle Drug Delivery and Vascular Disruption/Angiogenesis. *Molecules* **2016**, *21*, 1468.
61. Jordan, M. A. Mechanism of action of antitumor drugs that interact with microtubules and tubulin. *Curr. Med. Chem. Anticancer Agents* **2002**, *2*, 1–17.
62. Hamel, E.; Covell, D.G. Antimitotic peptides and depsipeptides. *Curr. Med. Chem. Anticancer Agents* **2002**, *2*, 19–53.
63. Zhou, J.; Gupta, K.; Aggarwal, S.; Aneja, R.; Chandra, R.; Panda, D.; Joshi, H.C. Brominated derivatives of noscapine are potent microtubule-interfering agents that perturb mitosis and inhibit cell proliferation. *Mol. Pharmacol.* **2003**, *63*, 799–807.
64. Hoffman, J.C.; Vaughn, K.C. Mitotic disrupter herbicides act by a single mechanism but vary in efficacy. *Protoplasma* **1994**, *179*, 16–25.
65. Lacey, E.; Gill, J.H. Biochemistry of benzimidazole resistance. *Acta Trop.* **1994**, *56*, 245–262.
66. Cann, J.R.; Hinman, N.D. Interaction of chlorpromazine with brain microtubule subunit protein. *Mol. Pharmacol.* **1975**, *11*, 256–267.
67. Jimenez-Barbero, J.; Amat-Guerri, F.; Snyder, J.P. The solid state, solution and tubulin-bound conformations of agents that promote microtubule stabilization. *Curr. Med. Chem. Anticancer Agents* **2002**, *2*, 91–122.
68. Johnson, I.S.; Wright, H.F.; Svoboda, G.H. Experimental basis for clinical evaluation of anti-tumor principles derived from *Vinca rosea* Linn. *J. Lab. Clin. Med.* **1959**, *54*, 830–837.
69. Noble, R.L.; Beer, C.T.; Cutts, J.H. Further biological activities of vincalkebostine: an alkaloid isolated from *Vinca rosea* (L.). *Biochem. Pharmacol.* **1958**, *1*, 347–348.
70. Mukherjee, A.K.; Basu, S.; Sarkar, N.; Ghosh, A.C. Advances in cancer therapy with plant based natural products. *Curr. Med. Chem.* **2001**, *8*, 1467–1486.
71. Svoboda, G.H. Alkaloids of *Vinca rosea*. IX. Extraction and characterization of leurosine and leurocristine. *Lloydia* **1961**, *24*, 173–178.
72. Neuss, N.; Gorman, M.; Svoboda, G.H.; Maciak, G.; Beer, C.T. *Vinca* alkaloids. III. Characterization of leurosine and vincalkebostine, new alkaloids from *Vinca rosea*. *J. Am. Chem. Soc.* **1959**, *81*, 4754–4755.
73. Gidding, C.E.; Kellie, S.J.; Kamps, W.A.; de Graaf, S.S. Vincristine revisited. *Crit. Rev. Oncol. Hematol.* **1999**, *29*, 267–287.
74. Barnett, C.J.; Cullinan, G.J.; Gerzon, K.; Hoying, R.C.; Jones, W.E.; Newlon, W.M.; Poore, G.A.; Robison, R.L.; Sweeney, M.J. Structure activity relationships of dimeric *Catharanthus* alkaloids. 1. Deacetyl vinblastine amide (vindesine) sulfate. *J. Med. Chem.* **1978**, *21*, 88–96.
75. Budman, D.R. New *vinca* alkaloids and related compounds. *Sem. Oncol.* **1992**, *19*, 639–645.

76. Canobbio, L.; Boccardo, F.; Pastorino, G.; Brema, F.; Martini, C.; Resasco, M.; Santi, L. Phase-II study of Navelbine in advanced breast cancer. *Sem. Oncol.* **1989**, *16*, 33–36.
77. Martins, R. G.; Dienstmann, R.; de Biasi, P.; Dantas, K.; Santos, V.; Toscano, E.; Roriz, W.; Zamboni, M.; Sousa, A.; Small, I. A.; Moreira, D.; Ferreira, C.G.; Zukinb, M. Phase II trial of neoadjuvant chemotherapy using alternating doublets in non-small-cell lung cancer. *Clin. Lung Cancer* **2007**, *8*, 257–263.
78. Kruczynski, A.; Etievant, C.; Perrin, D.; Chansard, N.; Duflos, A.; Hill, B. T. Characterization of cell death induced by vinflunine, the most recent Vinca alkaloid in clinical development. *Br. J. Cancer* **2002**, *86*, 143–150.
79. Wilson, L.; Jordan, M.A. Pharmacological probes of microtubule function. Microtubules. *Modern Cell Biol.* **1994**, *13*, 59–83.
80. Jordan, M. A.; Wilson, L. Use of drugs to study the role of microtubule assembly dynamics in living cells. *Meth. Enzymol.* **1998**, *298*, 252–276.
81. Lobert, S.; Correia, J. Energetics of Vinca alkaloid interactions with tubulin. *Meth. Enzymol.* **2000**, *323*, 77–103.
82. Bai, R.B.; Pettit, G.R.; Hamel E. Dolastatin 10. A powerful cytostatic peptide derived from a marine animal. Inhibition of tubulin polymerization mediated through the vinca alkaloid binding domain. *Biochem. Pharmacol.* **1990**, *39*, 1941–1949.
83. Bai, R.B.; Pettit, G.R.; Hamel E. Binding of dolastatin 10 to tubulin at a distinct site for peptide antimetabolic agents near the exchangeable nucleotide and vinca alkaloid sites. *J. Biol. Chem.* **1990**, *265*, 17141–17149.
84. Wilson, L.; Jordan, M.A.; Morse, A.; Margolis, R.L. Interaction of vinblastine with steady-state microtubules in vitro. *J. Mol. Biol.* **1982**, *159*, 129–149.
85. Correia, J.J.; Lobert, S. Physicochemical aspects of tubulin-interacting antimetabolic drugs. *Curr. Pharm. Des.* **2001**, *7*, 1213–1228.
86. Na, G.C.; Timasheff, S.N. Thermodynamic linkage between tubulin self-association and the binding of vinblastine. *Biochemistry* **1980**, *19*, 1347–1354.
87. Jordan, M.A.; Margolis, R.L.; Himes, R.H.; Wilson, L. Identification of a distinct class of vinblastine binding sites on microtubules. *J. Mol. Biol.* **1986**, *187*, 61–73.
88. Singer, W.D.; Jordan, M.A.; Wilson, L.; Himes, R.H. Binding of vinblastine to stabilized microtubules. *Mol. Pharmacol.* **1989**, *36*, 366–370.
89. Gigant, B.; Wang, C.; Ravelli, R.B.G.; Roussi, F.; Steinmetz, M.O.; Sobel, A.; Knossow, M. Structural Basis for the Regulation of Tubulin by Vinblastine. *Nature* **2005**, *435*, 519–522.
90. Protein Data Bank, <http://www.rcsb.org/>, PDB code: 1Z2B.
91. Jordan, A.; Hadfield, J. A.; Lawrence, N.J.; McGown, A.T. Tubulin as a target for anticancer drugs: agents which interact with the mitotic spindle. *Med. Res. Rev.* **1998**, *18*, 259–296.
92. Niel, E.; Scherrmann, J.M. Colchicine today. *Joint Bone Spine* **2006**, *73*, 672–678.
93. Hamel, E. Interactions of tubulin with small ligands. *Microtubule Proteins*. (J. Avila, ed.); CRC Press: Boca Raton, FL, **1990**, *4*, 89–192.
94. Uppuluri, S.; Knipling, L.; Sackett, D.L.; Wolff, J. Localization of the colchicine-binding site of tubulin. *Proc. Natl. Acad. Sci. USA* **1993**, *90*, 11598–11602.
95. Ravelli, R.B.; Gigant B.; Curmi, P.A.; Jourdain, I.; Lachkar, S.; Sobel, A.; Knossow, M. Insight into tubulin regulation from a complex with colchicine and a stathmin-like domain. *Nature* **2004**, *428*, 198–202.
96. Skoufias, D.A.; Wilson L. Mechanism of inhibition of microtubule polymerization by colchicine: inhibitory potencies of unliganded colchicine and tubulin colchicine complexes. *Biochemistry* **1992**, *31*, 738–746.

97. Wilson, L.; Farrell, K. W. Kinetics and steady-state dynamics of tubulin addition and loss at opposite microtubule ends: the mechanism of action of colchicine. *Ann. NY Acad. Sci.* **1986**, *466*, 690–708.
98. Hastie, S.B. Interactions of colchicine with tubulin. *Pharmacol. Ther.* **1991**, *512*, 377–401.
99. Margolis, R.L.; Rauch, C.T.; Wilson, L. Mechanism of colchicine dimer addition to microtubule ends: Implications for the microtubule polymerization mechanism. *Biochemistry* **1980**, *19*, 5550–5557.
100. Farrell, K.W.; Wilson, L. The differential kinetic stabilization of opposite microtubule ends by tubulin-colchicine complexes. *Biochemistry* **1984**, *23*, 3741–3748.
101. Bai, R.; Pei, X. F.; Boye, O.; Getahun, Z.; Grover, S.; Bekisz, J.; Nguyen, N.Y.; Brossi, A.; Hamel, E. Identification of cysteine 354 of β -tubulin as part of the binding site for the A ring of colchicine. *J. Biol. Chem.* **1996**, *271*, 12639–12645.
102. Dumortier, C.; Gorbunoff, M.J.; Andreu, J.M.; Engelborghs, Y. Different kinetic pathways of the binding of two biphenyl analogs of colchicine to tubulin. *Biochemistry* **1996**, *35*, 4387–4395.
103. Andreu, J.M.; Perez-Ramirez, B.; Gorbunoff, M.J.; Ayala, D.; Timasheff, S.N. Role of the colchicine ring A and its methoxy groups in the binding to tubulin and microtubule inhibition. *Biochemistry* **1998**, *37*, 8356–8368.
104. Andreu, J.M.; Timasheff, S.N. Conformational states of tubulin liganded to colchicine, tropolone methyl ether, and podophyllotoxin. *Biochemistry* **1982**, *21*, 6465–6476.
105. Protein Data Bank, <http://www.rcsb.org/>, PDB code: 1SA0.
106. Wall, M.E.; Wani, M.C. Camptothecin and taxol: discovery to clinic--thirteenth Bruce F. Cain Memorial Award Lecture. *Cancer Res.* **1995**, *55*, 753–760.
107. Schiff, P.B.; Fant, J.; Band Horwitz, S. Promotion of microtubule assembly in vitro by taxol. *Nature* **1979**, *277*, 665–667.
108. He, L.; Jagtap, P.G.; Kingston, D.G.I.; Shen, H.J.; Orr G.A.; Band Horwitz, S. A common pharmacophore for taxol and the epothilones based on the biological activity of a taxane molecule lacking a C-13 side chain. *Biochemistry* **2000**, *39*, 3972–3978.
109. Nicolaou, K.C.; Yang, Z.; Liu, J.J.; Ueno, H.; Nantermet, P.G.; Guy, R. K.; Claiborne, C.F.; Renaud, J.; Couladouros, E.A.; Paulvannan, K.; Sorensen, E.J. Total synthesis of taxol. *Nature* **1994**, *367*, 630–634.
110. Von Hoff, D.D. The taxoids: same roots, different drugs. *Semin. Oncol.* **1997**, *24*, S13.3–S13.10.
111. Markman, M. Managing taxane toxicities. *Support Care Cancer* **2003**, *11*, 144–147.
112. Gueritte-Voegelein, F.; Guenard, D.; Lavelle, F.; Le Goff, M.T.; Mangatal, L.; Potier, P. Relationships between the structure of taxol analogs and their antimitotic activity. *J. Med. Chem.* **1991**, *34*, 992–998.
113. Saicic, R.N.; Matovic, R. An efficient semisynthesis of 7-deoxypaclitaxel from taxine. *J. Chem. Soc. Perkin Trans.* **2000**, *1*, 59–65.
114. Nogales, E. Structural insights into microtubule function. *Annu. Rev. Biophys. Biomol. Struct.* **2001**, *30*, 397–420.
115. Amos, L.A.; Löwe, J. How Taxol stabilises microtubule structure. *Chem. Biol.* **1999**, *6*, R65–R69.
116. Huizing, M.T.; Giaccone, G.; van Warmerdam, L.J.; Rosing, H.; Bakker, P.J.; Vermorken, J.P.; Postmus, P.E.; van Zandwijk, N.; Koolen, M.G.; ten Bokkel Huinink, W.W.; van der Vijgh, W.J.; Bierhorst, F.J.; Lai, A.; Dalesio, O.; Pinedo, H.M.; Veenhof, C.H.; Beijnen, J.H. Pharmacokinetics of paclitaxel and carboplatin in a dose-escalating

and dose-sequencing study in patients with non-small-cell lung cancer. The European Cancer Centre. *J. Clin. Oncol.* **1997**, *15*, 317–329.

117. Pryor, D.E.; O'Brate, A.; Bilcer, G.; Díaz, J.F.; Wang, Y.; Wang, Y.; Kabaki, M.; Jung, M.K.; Andreu, J.M.; Ghosh, A.K.; Giannakakou, P.; Hamel, E. The microtubule stabilizing agent laulimalide does not bind in the taxoid site, kills cells resistant to paclitaxel and epothilones, and may not require its epoxide moiety for activity. *Biochemistry* **2002**, *41*, 9109–9115.

118. Moscow, J.A.; Cowan, K.H. Multidrug resistance. *J. Natl. Cancer Inst.* **1988**, *80*, 14–20.

119. Kavallaris, M. Microtubules and resistance to tubulin-binding agents. *Nature Rev. Cancer* **2010**, *10*, 194–204.

120. Verrills, N.M. et al. Proteomic analysis reveals a novel role for the actin cytoskeleton in vincristine resistant childhood leukemia - An in vivo study. *Proteomics* **2006**, *6*, 1681–1694.

121. Verrills, N.M. et al. Alterations in γ -actin and tubulin-targeted drug resistance in childhood leukemia. *J. Natl Cancer Inst.* **2006**, *98*, 1363–1374.

122. Po'uha, S.T.; Shum, M.S.; Goebel, A.; Bernard, O.; Kavallaris, M. LIM-kinase 2, a regulator of actin dynamics, is involved in mitotic spindle integrity and sensitivity to microtubule-destabilizing drugs. *Oncogene* **2010**, *29*, 597–607.

123. Bhalla, K.N. Microtubule-targeted anticancer agents and apoptosis. *Oncogene* **2003**, *22*, 9075–9086.

2. New Indole Derivatives as Potent Tubulin Assembly and Cancer Cell Growth Inhibitors

2.1 Introduction

MTs regulate key cellular functions, such as cell growth and division, intracellular trafficking, preservation of the architecture of the cell, and motility. Due to these key roles, disrupting the dynamic equilibrium of MTs at either the tubulin assembly or MT disassembly level, results in a fatal cellular event.

Cancer cells are characterized by a high rate of cell division: hence, the strategy of inducing cell death through an interference with the dynamics of MTs has proved successful for the design of effective antitumor drugs.^{1,5}

MT binding agents fall into two main groups: (i) inhibitors of tubulin polymerization, including colchicine,^{6,7} combretastatinA-4 (CSA4),⁸ vincristine (VCR), vinorelbine (VRB) and vinblastine (VBL); and (ii) MT stabilizers, including taxoids and epothilones. The stabilizers stimulate MT polymerization and stabilization at high concentrations, whereas at lower concentrations paclitaxel (PTX) inhibits MT dynamics with little effect on the proportion of tubulin in polymer.⁹

Taxoids and epothilones bind at a luminal site on the β -subunit^{10,11} following entry into the MT through pores in its wall¹² that are shaped by various tubulin subunits on the MT surface. Some evidence indicates a transient binding of MT stabilizers at a specific pore site.

Despite considerable clinical successes,^{13,14} the anticancer therapies based on tubulin binding agents still have limitations perhaps due to multi-drug resistance (MDR), toxicity and unwanted side effects.^{15,16}

Therefore, there is a quest for new effective MT inhibitors with fewer side effects to become components of improved anticancer treatments.^{17,18}

2.2 Arylthioindoles, Potent Inhibitors of Tubulin Polymerization

In the past few years, a series of indole derivatives were found to be able to inhibit tubulin assembly.¹⁹⁻²¹ In this context, Prof. Silvestri and coworkers have recently described arylthioindole derivatives (ATIs) as a new class of potent inhibitors of tubulin polymerization and the growth of MCF-7 human breast carcinoma cells.²² In their studies, many of the new indole derivatives showed to be more potent than other chemotypes so far presented, thus confirming their potential as new candidate drugs in cancer chemotherapy.^{23,24} These molecules act through the binding at the colchicine site on β -tubulin, hampering mitotic progression, thus causing cells to undergo apoptosis. ATIs inhibit [³H]colchicine binding in the β -tubulin site close to its interface with α -tubulin within the α,β -dimer.²⁵ Structure–activity relationship (SAR) studies of previous reported ATIs highlighted three essential structural requirements: (a) aromatic ring at position 2 of the indole, which is important for activity and improves metabolic stability (b) 3,4,5-trimethoxyphenyl moiety; (c) sulfur, ketone, or methylene bridging group at position 3. As tubulin polymerization inhibitors, 2-heterocycl-3-arylthio-1*H*-indole (2-HATI) derivatives were found to be more effective than the corresponding 2-aryl-3-arylthio-1*H*-indole counterparts.

For example, 2-(thiophen-2-yl)-3-[(3,4,5-trimethoxyphenyl)thio]-1*H*-indole (**2.1**, Figure 2.1) inhibited tubulin assembly with an IC₅₀ of 0.74 μ M and MCF-7 cancer cell growth with an IC₅₀ of 39 nM.²⁶ Compound **2.1** was superior to VRB, VBL, and PTX as an inhibitor of the P-glycoprotein (Pgp) overexpressing NCI/adriamycin-resistant (ADR-RES) MDR cell line and showed satisfactory metabolic stability.

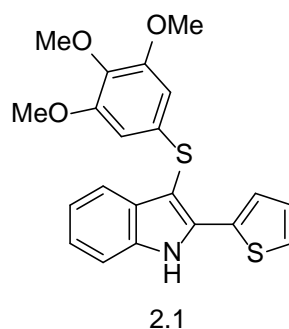


Figure 2.1. Structure of 2-(thiophen-2-yl)-3-[(3,4,5-trimethoxyphenyl)thio]-1*H*-indole (2.1)

Preliminary modeling studies showed that the five-membered heterocycle at position 2 of the indole nucleus could form hydrophobic interactions with Lys254 and Leu248 of the colchicine site of tubulin.

The molecular modeling approach was based on the combination of molecular docking and molecular dynamics that was able to estimate the binding energies of ATIs to tubulin with a good accuracy, showing a correlation value of $r^2 = 0.74$ between the experimental data observed and the in silico calculation.

Compounds **2.1** and its analogues were designed using this approach. The results obtained from modeling calculations showed that the trimethoxyphenyl group lay in proximity to the β Cys241, β Met259 and β Leu255 residues, the indole NH established a H-bond with α Thr179 and hydrophobic interaction between β Lys254 and β Leu248 residues with the carbon atoms of heterocyclic rings (Figure 2.2.).²⁶

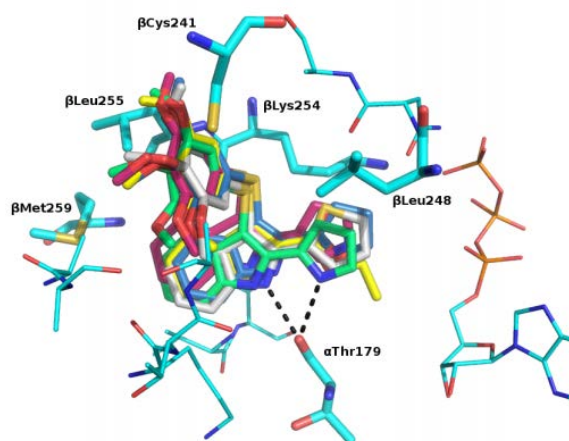


Figure 2.2 Binding mode proposed by PLANTS for **2.1** (white) and its analogues into the colchicine site. H-bond is shown as a dashed line. Residues of the β -tubulin binding site and the nonexchangeable GTP, which is on α -tubulin, α -Thr179 are shown stick rendition.²⁶

All molecular modeling studies were performed on a MacPro dual 2.66 GHz Xeon running Ubuntu 9. The tubulin structure was downloaded from the PDB data bank (<http://www.rcsb.org/> - PDB code: 1SA0). Hydrogen atoms were added to the protein, using Molecular Operating Environment (MOE) 2007.09 and minimized keeping all the heavy atoms fixed until a RMSD gradient of $0.05 \text{ kcal mol}^{-1} \text{ \AA}^{-1}$ was reached. Ligand structures were built with MOE and minimized using the MMFF94x forcefield until a

RMSD gradient of $0.05 \text{ kcal mol}^{-1} \text{ \AA}^{-1}$ was reached. The docking simulations were performed using FlexX4S with the MOE interface. The RMSD of the trimethoxyphenyl moiety for each of the results obtained was calculated in comparison with ring A of DAMA-colchicine, and the results from the docking were scored using this value.²⁶

2.3 Objective of the Study

In contrast to the other region of the ATI molecule, chemical modification of positions 5-7 of the indole nucleus have been not yet exhaustively explored.

Docking studies suggested that five-membered heterocyclic rings at position 5, 6 or 7 of the indole nucleus could enhance the binding to tubulin.

Three representative compounds bearing a thiophene ring at position 5-, 6- or 7- of the indole nucleus, were docked into the tubulin-DAMA-colchicine complex (PDB code 1SA0)²⁷ by following a previously reported procedure.²⁸ The docking studies were also performed for five newly available tubulin crystal structures.²⁹

The docking results in the different tubulin structures revealed a consistent binding mode for compounds bearing the heterocyclic ring at position 5-, 6- or 7- of the indole: (i) the 3,4,5-trimethoxyphenyl moiety formed an H-bond with the Cys241 β side chain and hydrophobic contacts with Leu248 β and Leu255 β ; (ii) the indole established hydrophobic contacts with Asn258 β and Met259 β ; (iii) the heterocyclic ring at position 5, 6 or 7 of the indole, arranged hydrophobic interactions with Met259 β (for compound bearing a thiophen-3-yl ring at position 5); Lys353 β (for compound bearing a thiophen-3-yl ring at position 6); Ala180 α and Val181 α (for compound bearing a thiophen-2-yl ring at position 7) in the same cleft of the colchicine site (Figures 2.3 and 2.4).

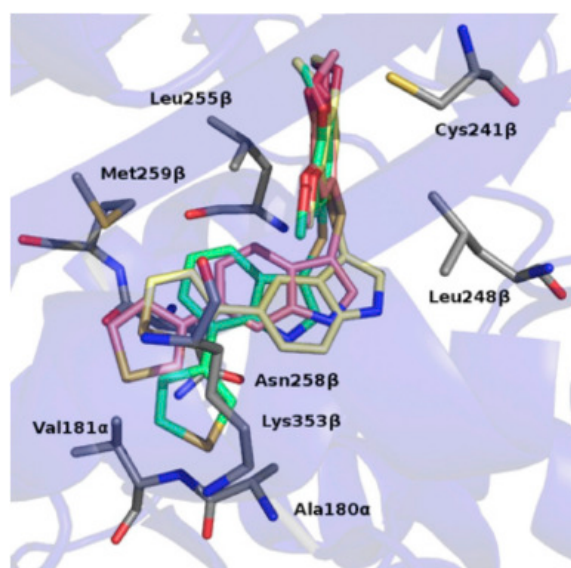


Figure 2.3. Plants proposed binding mode for derivatives bearing a thiophen-3-yl ring at position 5 (yellow), a thiophen-3-yl ring at position 6 (pink) and a thiophen-2-yl ring at position 7 (green) into the 1SA0 tubulin structure. Residues involved in interactions are shown as stick diagrams. The tubulin polypeptide chains are shown as ribbon cartoons.

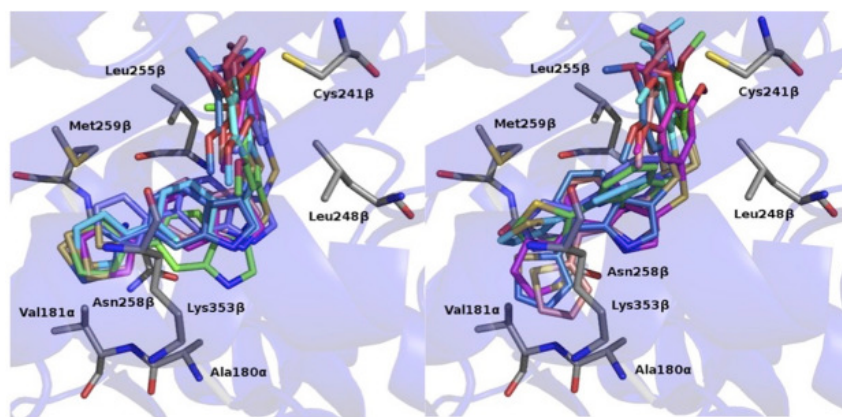


Figure 2.4. Plants proposed binding mode for derivatives bearing a thiophen-3-yl ring at position 6 (left panel) or a thiophen-2-yl ring at position 7 (right panel) for the studied tubulin structures: 1SA0 (green), 3HKC (cyan), 4O2B (magenta), 5CA0 (purple), 5CB4 (sky blue), 5LYJ (pink). Residues involved in interactions are shown as stick diagrams. The tubulin polypeptide chains are shown as ribbon cartoons. Residues and cartoon are from 1SA0.

Starting from these observations and from the good biological activity showed by previously reported 2-heterocycl-3-arylthio-1*H*-indole (2-HATI) derivatives we decided to shift the heterocycle from position 2 to positions 5, 6 and 7 of the indole (Figure 2.5).

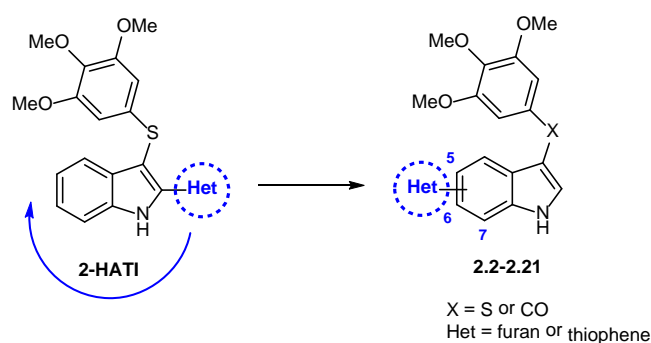


Figure 2.5. Design of new ATI derivatives **2.2–2.21**.

So we conducted SAR investigations of new indole derivatives bearing five-membered heterocyclic rings at position 5, 6 or 7 of the indole nucleus. We maintained the trimethoxyphenyl moiety at position 3, because of its important role in binding at the colchicine site. Accordingly, we designed and synthesised 20 new ATI derivatives that were evaluated as inhibitors of tubulin polymerization, the growth of MCF-7 human breast cancer cells, and the binding of [³H]colchicine to tubulin.

As a Ph.D. student of Prof. R. Silvestri's research group, I participated to the synthesis and characterization of compounds **2.2–2.21** (see Experimental Section, Chemistry 2.7.1).³⁰

2.4 Chemistry

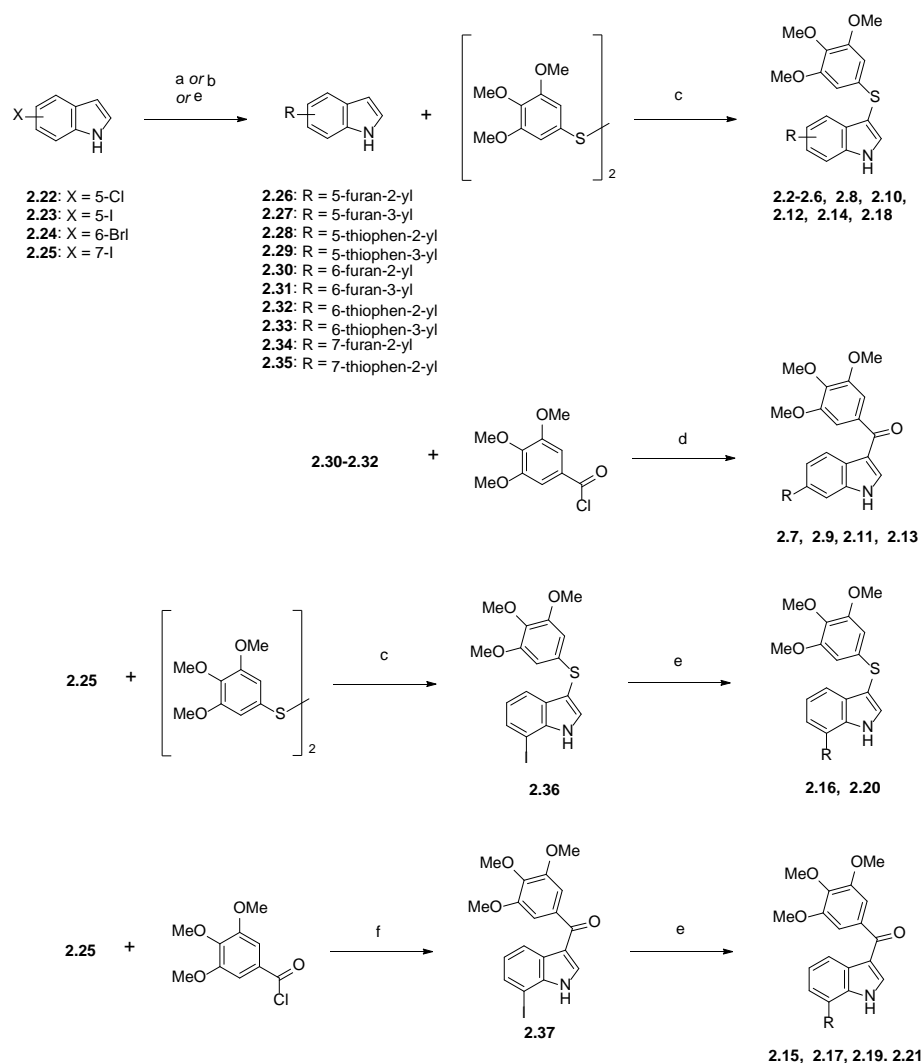
Arylthioindoles **2.2-2.6**, **2.8**, **2.10**, **2.12**, **2.14**, **2.18**, and **2.36** were synthesized using a previously reported venting-while-heating micro-wave (MW)-assisted procedure³¹ by treating the appropriate indole with bis(3,4,5-trimethoxyphenyl)disulfide³² in the presence of sodium hydride in anhydrous *N,N*-dimethylformamide (DMF) at 130 °C for 2 min (120 W) (Scheme 2.1).

Methanones **2.7**, **2.9**, **2.11** and **2.13** were prepared by reaction of the appropriate indole with 3,4,5-trimethoxybenzoyl chloride in the presence of diethylaluminum chloride in dichloromethane at 100 °C for 2 h.

Derivatives **2.15-2.17**, **2.19-2.21**, **2.29-2.31**, **2.34** and **2.35** were synthesized by a coupling reaction of the appropriate indole with the boronic derivative in the presence of tris(dibenzylideneacetone)dipalladium(0)(Pd₂dba₃), 2-dicyclohexylphosphino-2',6'-dimethoxybiphenyl (SPhos) and potassium phosphate tribasic in 1-butanol at 100 °C for 15 h. A palladium(II) acetate (Pd(OAc)₂)-catalyzed reaction of 5-iodo-1*H*-indole (**2.23**) with 2-furanboronic or 2-thienylboronic acid in the presence of tri(*o*-tolyl)phosphine (P(*o*-tol)₃) and potassium phosphate tribasic in ethanol/toluene at 80 °C for 2 h gave the corresponding heteroaryl indoles **2.26** and **2.28**, respectively.

MW-assisted treatment of indole **2.23** with 3-furanboronic acid pinacol ester in the presence of Pd(OAc)₂ and potassium carbonate in methylpyrrolidone/water at 110 °C for 15 min (200 W) furnished 5-(furan-2-yl)-1*H*-indole (**2.27**).

Compound **2.37** was prepared by MW-assisted Friedel-Crafts acylation of 7-iodo-1*H*-indole (**2.25**) with 3,4,5-trimethoxybenzoyl chloride in the presence of anhydrous aluminum chloride in 1,2-dichloroethane at 110 °C for 2 min (150 W).



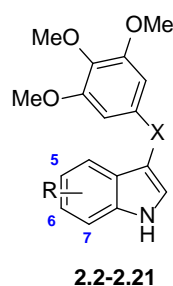
Scheme 2.1. Synthesis of Compounds **2.2-2.21** and **2.26-2.36**. Reagents and reaction conditions: (a) (**2.26**, **2.28**) boronic derivate, Pd(OAc)₂,P(*o*-tol)₃,K₃PO₄, EtOH/PhMe, 80 °C, 2 h, 73-87%; (b) (**2.27**) 3-furanboronic acid pinacol ester, Pd(OAc)₂,K₂CO₃, methylpyrrolidone/water, closed vessel, 200 W, 110 °C, 15 min, 45%; (c) (**2.2-2.6**, **2.8**,

2.10, 2.12, 2.14, 2.18 and **2.36**) bis(3,4,5-trimethoxyphenyl)disulfide, NaH, anhydrous DMF, closed vessel, 120 W, 130 °C, 2 min, 5-50%; (d) (**2.7, 2.9, 2.11, 2.13**) (i) diethylaluminum chloride, CH₂Cl₂, -78 °C, Ar stream; (ii) 3,4,5-trimethoxybenzoyl chloride, -10 °C → 25 °C within 2 h, 14-69%; (e) (**2.15-2.17, 2.19-2.21, 2.29-2.32, 2.34** and **2.35**) boronic derivative, Pd₂dba₃, SPhos, K₃PO₄, BuOH, 100 °C, 15 h, 5-75%; (f) (**2.37**) 3,4,5-trimethoxybenzoyl chloride, CH₂Cl₂, anhydrous AlCl₃, closed vessel, 150 W, 110 °C, 2 min, 51%.

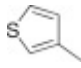
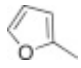
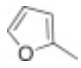
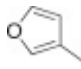
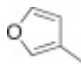
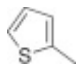
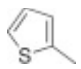
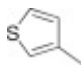
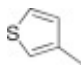
2.5 Results and Discussion

Arylthioindole and aroylindole derivatives **2.2-2.21** have been synthesized to investigate the effects of the introduction of five-membered heterocyclic rings at position 5, 6 or 7 of the indole nucleus on the inhibition of tubulin polymerization, binding of colchicine to tubulin and growth of MCF-7 cancer cells (Table 2.1).

Table 2.1. Inhibition of tubulin polymerization, growth of MCF-7 human breast carcinoma cells, and colchicine binding by compounds **2.2-2.21**.^a



Compd	R	X	IC ₅₀ ± SD	IC ₅₀ ± SD	Inh. Colch. Bind. ^d	
			(μM)	(nM)		
			Tubulin ^b	MCF-7 ^c		
2.2	5-		S	0.87 ± 0.1	70 ± 10	81 ± 1
2.3	5-		S	1.8 ± 0.1	200 ± 100	63 ± 1
2.4	5-		S	1.3 ± 0.09	150 ± 70	76 ± 2
2.5	5-		S	1.7 ± 0.03	200 ± 0	72 ± 3
2.6	6-		S	0.59 ± 1	10 ± 3	97 ± 1
2.7	6-		CO	0.76 ± 0.04	4.7 ± 0.6	96 ± 0.1
2.8	6-		S	2.3 ± 0.04	10 ± 0	90 ± 2
2.9	6-		CO	0.61 ± 0.06	4.3 ± 0.6	96 ± 0.1
2.10	6-		S	0.47 ± 0.05	6.0 ± 1	95 ± 1
2.11	6-		CO	0.38 ± 0.1	9.6 ± 0.6	96 ± 0.8
2.12	6-		S	0.58 ± 0.06	4.5 ± 1	97 ± 0.3

2.13	6-		CO	0.60 ± 0.04	18 ± 4	94 ± 0.6
2.14	7-		S	0.64 ± 0.06	15 ± 4	95 ± 0.6
2.15	7-		CO	1.9 ± 0.03	320 ± 10	70 ± 1
2.16	7-		S	1.3 ± 0.1	24 ± 2	86 ± 1
2.17	7-		CO	3.0 ± 0.3	1300 ± 0	29 ± 0.6
2.18	7-		S	0.57 ± 0.03	29 ± 1	89 ± 1
2.19	7-		CO	2.6 ± 0.04	550 ± 70	48 ± 0.5
2.20	7-		S	1.3 ± 0.01	38 ± 10	77 ± 0.1
2.21	7-		CO	6.2 ± 1	1400 ± 100	Nd ^e
2.1	–	–	–	0.74 ± 0.05	39 ± 10	88 ± 2
Colch.	–	–	–	3.2 ± 0.4	5 ± 1	–
CSA4 ^f	–	–	–	1.0 ± 0.1	13 ± 3	98 ± 0.6

^fCSA4 yielded IC₅₀ of 0.65 ± 0.03 μM in the assay with **2.4-2.6**, **2.9**, **2.11**, **2.14** and **2.16**, and IC₅₀ of 0.64 ± 0.01 μM in the assay with **2.8** and **2.16**, in which different tubulin preparations were used. ^aExperiments were performed in duplicate or triplicate. ^bInhibition of tubulin polymerization. Tubulin was at 10 μM in the assembly assay. ^cInhibition of growth of MCF-7 human breast carcinoma cells. ^dInhibition of [³H]colchicine binding: tubulin, [³H]colchicine, inhibitor at 1:5:5 μM. ^eNd, not done.

2.5.1 Inhibition of Tubulin Polymerization

Ten new derivatives (**2.2**, **2.6**, **2.7**, **2.9-2.14**, and **2.18**) were able to inhibit tubulin polymerization with IC₅₀ values at submicromolar concentrations, six compounds (**2.3-2.5**, **2.15**, **2.16** and **2.20**) were in the 1.0-2.0 μM range, as compared with colchicine (IC₅₀ = 3.2 μM) and CSA4 (IC₅₀ = 1.0 μM). Except for compound **2.3**, the most potent tubulin polymerization inhibitors (**2.6**, **2.7** and **2.9-2.13**) were characterized by the presence of the heterocyclic ring at position 6 of the indole; among others, compound **2.2**, bearing the heterocyclic ring at position 5 of the indole, and **2.15**, **2.16** and **2.20**, with the heterocyclic ring at position 7, showed IC₅₀ values < 1.0 μM. In general, derivatives characterized by the presence of a furan-2-yl or thiophen-2-yl ring showed to be more active as tubulin polymerization inhibitors than the corresponding furan-3-yl- and thiophen-3-yl derivatives (compare **2.2** with **2.3**, **2.4** with **2.5**, **2.6** with **2.8**, **2.14** with **2.16**, and **2.18** with **2.20**).

Replacement of the sulfur bridging atom at position 3 of the indole nucleus with the carbonyl group also provided potent inhibitors of tubulin assembly. Compounds bearing the heterocycle at position 7 of the indole nucleus showed significant differences in the inhibition of tubulin assembly depending on the bridging atom at position 3 (compare **2.14** with **2.15**, **2.16** with **2.17**, **2.18** with **2.19**, and **2.20** with **2.21**), while compounds **2.6-2.13** bearing the heterocycle at position 6 of the indole nucleus showed almost similar activities, with the exception of compounds **2.8** and **2.9**, with **2.11** (IC₅₀ = 0.38 μM) being

the most potent inhibitor of tubulin polymerization among the newly synthesized compounds.

2.5.2 Inhibition of MCF-7 Breast Cancer Cell Growth

The majority of the newly synthesized indole derivatives were able to inhibit the growth of human MCF-7 nonmetastatic breast cancer epithelial cells at nanomolar concentrations (Table 2.1). From structure-activity relationship (SAR) studies it was clear that (i) the introduction of the heterocyclic ring at position 5 of the indole nucleus furnished relatively weak inhibitors of MCF-7 cell growth, with IC₅₀ values ranging from 70 (**2.2**) to 200 nM (**2.3**, **2.5**); (ii) compounds characterized by the presence of the heterocyclic ring at position 6 of the indole (**2.6-2.13**), proved to be all potent MCF-7 cell growth inhibitors, with IC₅₀ values ranging from 4.3 (**2.9**) to 18 (**2.13**) nM, with five compounds (**2.7** and **2.9-2.12**) having single digit nanomolar IC₅₀ values; (iii) the derivatives bearing the heterocycle at position 7 of the indole nucleus showed different behavior, depending on the bridging atom at position 3: the 7-heterocyclyl-3-arylthio-1*H*-indoles **2.14**, **2.16**, **2.18** and **2.20** (IC₅₀s ranging from 15 to 38 nM) were more than one order of magnitude superior to the corresponding aryl derivatives **2.15**, **2.17**, **2.19** and **2.21**.

2.5.3 Inhibition of the Binding of [³H]Colchicine to Tubulin

The majority of the newly synthesized compounds showed good activity as inhibitors of the binding of [³H]colchicine to tubulin (Table 2.1). Compounds **2.2**, **2.4**, **2.6-2.16** and **2.18**, in fact, yielded > 75% inhibition of the binding reaction. From structure-activity relationship (SAR) studies it was clear that all the indoles with the heterocycle at position 7 were strong inhibitors of [³H]colchicine binding, with **2.12** (97% inhibition) nearly as potent as CSA4 (98% inhibition). The data presented in Table 2.1 reveal that inhibition of the growth of MCF7 cancer cells is in good agreement with inhibition of colchicine binding, as demonstrated by comparing the MCF7 cells growth inhibitory concentrations with the percent inhibition of colchicine binding, which provide an indirect measure of the affinity of the compounds for the colchicine site. In general compounds which inhibited [³H]colchicine binding > 90%, inhibited the growth of the MCF-7 cancer cell with IC₅₀s ≤ 15 nM; compounds with 80-90% inhibition of [³H]colchicine binding inhibited the growth of the MCF-7 cancer cell line with IC₅₀s in the range of 24-70 nM; except for compound **2.20**, compounds with 70-80% inhibition of [³H]colchicine binding inhibited the growth of the MCF-7 cancer cells with IC₅₀s in the range of 150-350 nM.

2.5.4 Cell Growth Inhibition

Two representative members of the 6- and 7-heterocyclyl series, **2.12** and **2.18**, were found to uniformly inhibit the growth of a large panel of cancer cells, including T98G (human glioblastoma), U87MG (humanglioblastoma-astrocytoma) and U343MG (human glioblastoma-astrocytoma) cells; the human cell lines HT29 (colon adenocarcinoma), HCT116 (colonic carcinoma), and HepG2 (hepatocellular carcinoma); MV4-11 (leukemia, acute myeloid), THP1 (leukemia, acute monocytic), A549 (lung carcinoma) and PC3 (prostate carcinoma) cancer cells. Treatments of T98G (human glioblastoma), U87MG (humanglioblastoma-astrocytoma) and U343MG (human glioblastoma-astrocytoma) cells with increasing concentrations of compounds **2.12** and **2.18** significantly inhibited cell growth in a dose-dependent manner (Table 2.2 and Figures 2.6-2.8). The IC₅₀ values were calculated taking into account the relative cellular doubling times^{31,32} of 48 h for the T98G and U87MG cells and of 72 h for the U343MG cells. Compound **2.12** potently inhibited the glioblastoma cells at nanomolar concentrations. Arylthioindoles with the imidazole-1-yl or pyridin-4-yl heterocyclic ring at position 2 of the indole nucleus were weaker

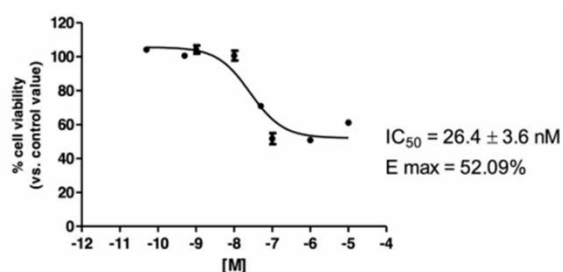
inhibitors of glioblastoma U87MG cells than **2.12** and **2.18**, even though such compounds exhibited potent inhibition of the MCF-7 cancer cell growth.²⁶

Table 2.2. Growth Inhibition of HT29, HCT116, HepG2, T98G, U87MG, U343G, MV4-11, THP-1, A-549 and PC3 cells by **2.12** and **2.18**.^{a,b}

Cpd	IC ₅₀ ± SD (nM)									
	HT29	HCT116	HepG2	T98G	U87 MG	U343G	MV4-11	THP-1	A-549	PC3
2.12	10 ± 1.4	21 ± 1.5	20 ± 1.1	26 ± 3.6	16 ± 2.0	31 ± 4.3	6 ± 2.0	2 ± 1	2 ± 0.1	3.5 ± 2
2.18	69 ± 1.4	70 ± 1.7	80 ± 1.2	211 ± 20	96 ± 14	154 ± 6.9	70 ± 16	20 ± 2	58 ± 1	39 ± 4

^aCytotoxic concentrations for the indicated cell lines; cytostatic concentrations for A-549 and PC3 cells. ^bIncubation time was 48 h; for U343G, MV4-11 and PC3 cells, incubation was 72 h.

2.12 (T98G cells)



2.18 (T98G cells)

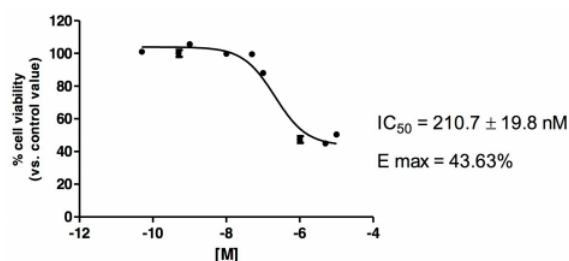
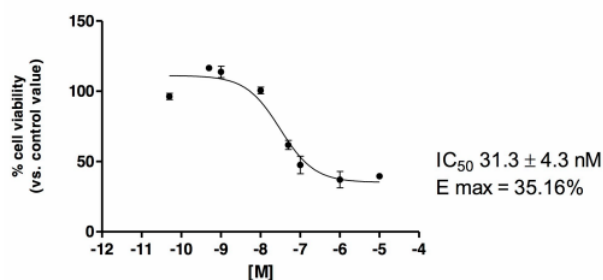


Figure 2.6 Effect of **2.12** and **2.18** on cell viability of T98G cells.

2.18 (U343 cells)



2.18 (U343 cells)

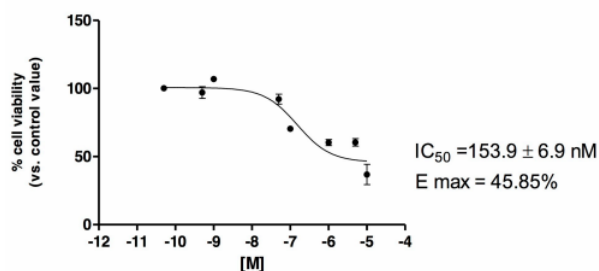
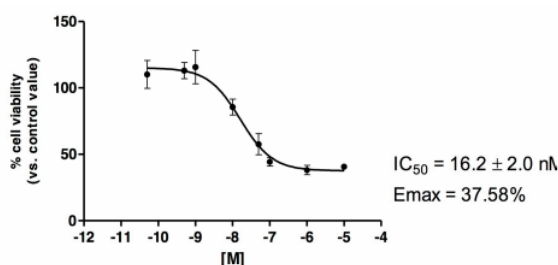


Figure 2.7 Effect of **2.12** and **2.18** on cell viability of U343 cells.

2.12 (U87MG cells)



2.18 (U87MG cells)

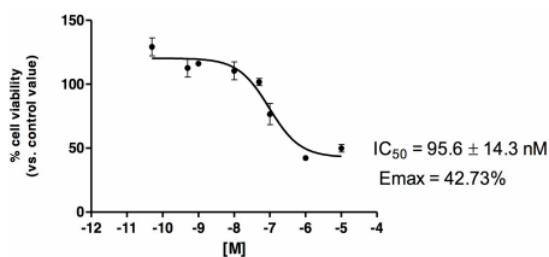


Figure 2.8 Effect of **2.12** and **2.18** on cell viability of U87MG cells.

In addition compounds **2.12** and **2.18** were evaluated as growth inhibitors of the human cell lines HT29 (colon adenocarcinoma), HCT116 (colocarcinoma), and HepG2 (hepatocellular carcinoma) using PTX as reference compound (Table 2.2).

These two compounds proved to be good inhibitors of the HT29 and HCT116 cell lines. Interestingly, as inhibitors of the HepG2 cells, **2.12** and **2.18** results even more effective than PTX ($IC_{50} = 2660$ nM). Compounds **2.12** and **2.18** were evaluated as inhibitors of MV4-11 (leukemia, acute myeloid), THP1 (leukemia, acute monocytic), A549 (lung carcinoma) and PC3 (prostate carcinoma) cancer cells.

Compound **2.12** inhibited MV4-11, THP-1, A-549 and PC3 cells at single digit nanomolar concentration, while **2.18** was consistently less active (Table 2.2).

2.5.5 Multi-Drug-Resistant (MDR) Cell Lines

Compounds **2.12** and **2.18** were compared with CSA4, VRB, VLB and PTX in the ovarian carcinoma cell lines OVCAR-8 and its cognate Pgp overexpressing line NCI/ADR-RES (Table 2.3). In contrast to CSA4, the standard agents VRB, VLB and PTX showed weak inhibition of the MDR line NCI/ADR-RES. The IC₅₀ values of **2.12** and **2.18** for the MCF-7 cells, repeated in this study, resembled those obtained in the studies summarized in Table 2.1.

Table 2.3 Growth Inhibition of the OVCAR-8 and NCI/ADR-RES cells by compounds **2.12** and **2.18** and reference compounds CSA4, VRB, VLB and PTX.^a

Compd	IC ₅₀ ± SD (nM) ^a		
	OVCAR-8	NCI/ADR_RES	MCF-7
2.12	9.3 ± 2	7.5 ± 2	6.7 ± 2
2.18	58 ± 8	34 ± 8	55 ± 7
CSA4	4.0 ± 0 ^b	3.5 ± 0.7	5.0 ± 1
PTX	4.0 ± 1	3100 ± 600	5.5 ± 0.7
VRB	300 ± 0	5000 ± 1000	Nd ^c
VBL	15 ± 7	200 ± 0	Nd ^c

^aInhibition of growth of the indicated cell lines. ^bSame value obtained in all experiments. ^cNd, not done.

2.5.6 Arrest of Mitotic Progression in HeLa Cells

To assess whether the growth-suppressive effect of **2.12** and **2.18** reflected their antimitotic activity, we evaluated their ability to induce mitotic arrest. In previous studies we found that treatment with 20 nM vinblastine effectively arrested the cell cycle of HeLa cells in mitosis;³³ at lower concentrations vinblastine did not completely prevent mitotic progression, such that cells assemble defective mitotic spindles, “slip” through the mitotic checkpoint, and progress toward aberrant chromosome segregation. We examined HeLa cell cultures after treatment with increasing concentrations of 20, 50, and 100 nM **2.12** and **2.18** in DMSO, 20 nM vinblastine, and DMSO vehicle. Treatments were carried out for 24 h, allowing all cells to enter mitosis during the treatment. Cell cultures were then harvested, incubated with propidium iodide (PI) and analyzed for their genomic content by FACS analysis. Representative cell cycle profiles are shown in Figure 2.9 A, left panel; in the right panel of the same figure data from three experiments are quantified. A dose-dependent inhibition of cell cycle progression was obtained with both compounds both with different effectiveness: treatment with 100 nM **2.18** yielded over 71% of the cell population in the G2/M phase, whereas lower doses had no significant effect; compound **2.12** was already partly effective at 20 nM and induced substantial G2/M arrest at 50 nM (77% arrest). Immunofluorescence (IF) analysis of **2.12** and **2.18**- treated HeLa cell cultures confirmed that treatment with 20 nM **2.12** (24 h) induced stable arrest in mitosis in over 50% of all cells, similar to the effect of VBL; only 15% of the cell population, in fact, included multinucleated cells, resulting from mitotic “slippage” and interphase re-entry with unsegregated, or randomly segregating, chromosomes. Compound **2.18** showed a lower ability to inhibit mitotic arrest than **2.12**: (i) 100 nM **2.18** arrested 50% of the cell population in mitosis, compared with 20 nM **2.12** or VBL; (ii) the induction of mitotic progression by **2.18** was not fully sustained. The higher accumulation of cells in mitosis observed with 100 nM **2.18** was accompanied by induction of a relevant fraction (around 32%) of multinucleated cells (MN): this suggests that cells that reached mitosis arrested only transiently, and eventually resumed mitotic progression with an inefficient mitotic apparatus, generating multi-nucleated cellular offspring (Figure 2.9 B). Furthermore, to assess whether G2/M-arrested cells underwent cell death over time, cultures were

incubated for 24 h with annexin V to identify cells with damaged plasma membranes committed to death. Annexin V, in fact, reacts with phosphatidylserine residues on the outer cell membrane during early apoptosis; PI, to which viable cells are not spontaneously permeable, instead, discriminates early and late stages of apoptotic cell death from necrotic cells, which are permeable to PI but do not react with annexin V. Both compounds **2.12** and **2.18** activated cell death parallel to arresting cell cycle progression; again, **2.18** was effective when used at 100 nM, whereas 20 nM **2.12** was already partly effective and reached the same death-inducing capacity as VBL at the 50 nM dose (Figure 2.9 C).

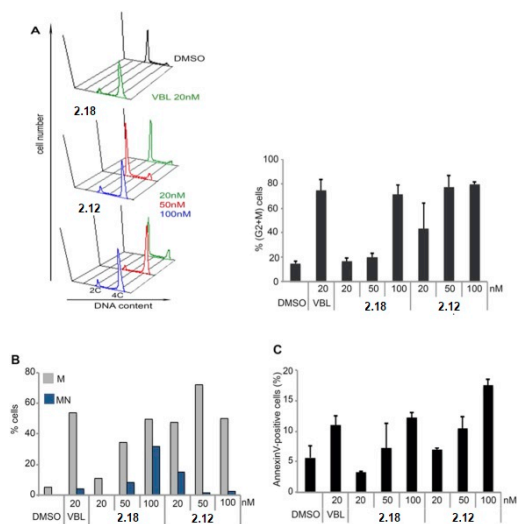


Figure 2.9. FACS analysis of the cell cycle and cell death in HeLa cell populations treated with **2.12** and **2.18**. Panel A left: distribution of cells after a 24 h treatment with **2.12** and **2.18** or VBL (DMSO as control). The DNA content indicates the cell cycle phase (2C: G1; 4C: G2+M; intermediate values between 2C and 4C: S phase). The panel shows a representative analysis of the cell cycle phase distribution, arranged according to the compound concentration (on the z axis). In the lower two diagrams, instead. In the lower two diagrams, 20 nM, green curves; 50 nM, red curves; 100 nM; blue curves. The profiles illustrate that **2.18** only induces 4C cell accumulation when used at 100 nM, whereas **2.12** is fully effective at 50 nM. Panel A right: the histograms show the mean % values SD of 4C cells (G2+M phases) counted in 3 independent experiments. Panel B: the graph represents the frequency of mitotic figures (grey bars) and multinucleated cells (blue bars) in cell populations treated for 24 h under the indicated conditions, processed for immunofluorescence and scored by microscopy. Between 300 and 650 cells were counted for each condition in 2 independent experiments. Panel C: FACS analysis of cell populations treated for 24 h under the indicated conditions and stained with annexin V. Mean \pm SD values were calculated from three experiments.

2.5.7 Inhibition of Mitotic MT Assembly

Immunofluorescence (IF) was employed to evaluate the effect of these newly synthesized indoles derivatives on tubulin and MTs and determine the correlation between the cell cycle arrest and cell death induction with inhibition of MT dynamics. 20 or 50 nM of compound **2.18** induced a mixture of apparently normal, or fragmented or multipolar spindles in variable proportions (Figure 2.10); 100 nM **2.18** largely induced small formations of radially arranged short microtubules that failed to elongate (labeled as “MTasters”, Figure 2.10 A). Compound **2.12** had a more pronounced effect at all tested concentrations, and no cell showed a normal or only weakly affected spindle. Even with **2.18** at 20 nM, most mitotic cells displayed multipolar (Figure 2.10 B, top row) or

fragmented spindles (Figure 2.10 B, central row); at higher concentration, 50 nM or above, **2.12** inhibited MT formation with sparse tubulin foci in virtually all treated cells (Figure 2.10 B, bottom row). Representative phenotypes are shown in Figure 2.10 A and B and quantified in Figure 2.10 C. In summary, both **2.12** and **2.18** arrested cells in mitosis, with formation of a defective mitotic apparatus, however, compound **2.12** induced the inhibition of MT polymerization to a greater extent than **2.18**, and it showed a full inhibitory effect on tubulin polymerization in cells at 50 nM, comparable to the effect of VBL. Compound **2.18** induced milder inhibition: it essentially affected the mitotic spindle structural organization but did not fully inhibit tubulin polymerization in cells below 100 nM. The parallel observation that **2.12** was a more effective inducer of cell death than **2.18** correlated with cellular data on microtubule disruption and with inhibition of [³H]colchicine binding.

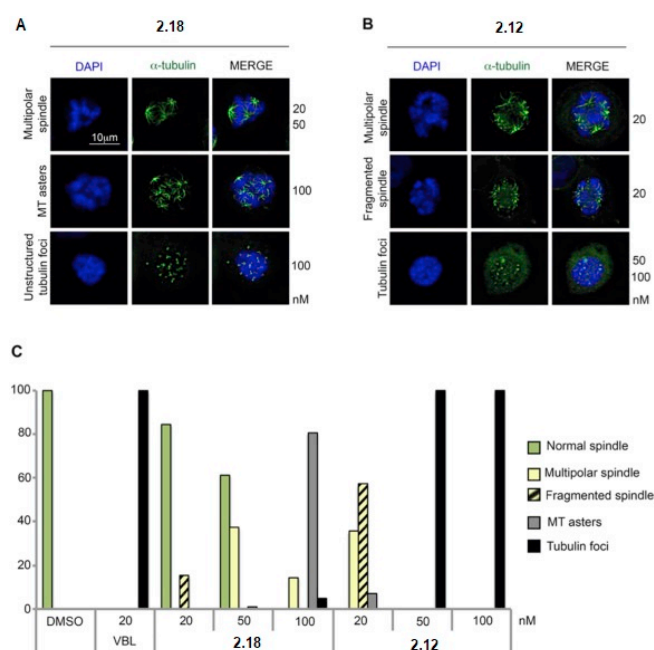


Figure 2.10 IF analysis of mitotic cells in HeLa cultures treated with **2.12** or **2.18**. Panel A: representative phenotypes induced by **2.18**: all cells were arrested in prometaphase (compare the configuration of chromosomes in DAPI panels); the green channel shows the extent of inhibition of tubulin polymerization at increasing compound concentrations (indicated at the right of the panels in nM). Panel B: representative phenotypes induced by **2.12**: the DAPI panels show the prometaphase configuration of chromosomes; the green channel shows the extent of inhibition of tubulin polymerization at the indicated concentrations. Panel C: Distribution of tubulin cytological phenotypes under the indicated conditions. The histograms represent the frequency of the indicated phenotypes (n, 100 to 250 prometaphase-arrested cells per condition).

2.5.8 Inhibition of HepG2 Cancer Cell Growth

Compounds **2.12** and **2.18** were evaluated as growth inhibitors of human liver hepatocellular carcinoma HepG2 cell lines. After 48 h incubation in the presence of test compounds, **2.12** and **2.18** strongly inhibited the growth of these cells. Compound **2.18** caused a dose-dependent decrease of cell viability: at 80 nM nearly 30% of cells displayed reduced viability as compared to untreated cells (Figure 2.11 A). The dose-dependent decrease of cell viability on treatment with **2.12** became significant at 20 nM (Figure 2.11 B).

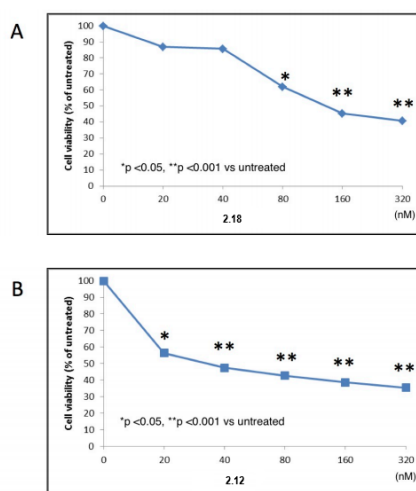


Figure 2.11 Effect of **2.12** and **2.18** on cell viability of HepG2 cells. Dose-dependence effect of **2.18** treatment (Panel A) and **2.12** treatment (Panel B) on cell viability of HepG2 cells; viability was determined by the MTT assay. Cell viability is expressed as the percentage (%) of untreated cells. The data shown are means \pm SEM of 6 independent experiments.

2.6 Conclusions

Our synthetic effort led to the preparation and SAR description of 20 new indole derivatives bearing a 3,4,5-trimethoxyphenyl moiety with a sulfur or ketone bridging group at position 3 of the indole and a heterocyclic ring at position 5, 6 or 7. As inhibitors of tubulin polymerization, ten new derivatives inhibited polymerization of purified tubulin with IC_{50} values at submicromolar concentrations. Seven of the new indole derivatives inhibited the growth of MCF-7 cells with IC_{50} values ≤ 10 nM. Inhibition of cell growth showed good correlation with inhibition of [3H]colchicine binding to tubulin. Two representative highly potent members of the 6- and 7-heterocyclyl-1*H*-indoles, **2.12** and **2.18**, inhibited a large panel of cancer cell lines and the NCI/ADR-RES multidrug resistant cell line at low nanomolar concentrations. Compound **2.12** at 50 nM induced 77% G2/M in HeLa cells, and at 20 nM caused 50% stable arrest of mitosis. As an inhibitor of HepG2 cells ($IC_{50} = 20$ nM), **2.12** was 4-fold superior to **2.18**.

Compound **2.12** was a potent inhibitor of the human U87MG glioblastoma cells at nanomolar concentrations, being nearly one order of magnitude superior to previously reported arylthioindoles. The present results highlight **2.12** as a robust scaffold for the design of new anticancer agents.

2.7 Experimental Section

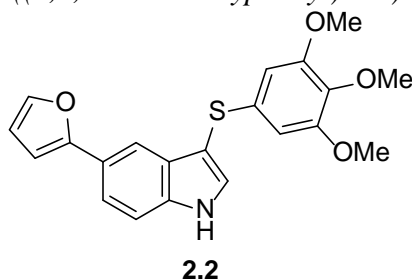
2.7.1 Chemistry

All reagents and solvents were handled according to the material safety data sheet of the supplier and were used as purchased without further purification. 5-Chloro-1*H*-indole (**2.22**), 5-iodo-1*H*-indole (**2.23**), 6-bromo-1*H*-indole (**2.24**), 7-iodo-1*H*-indole (**2.25**), 6-(thiophen-2-yl)-1*H*-indole (**2.32**) and 6-(thiophen-3-yl)-1*H*-indole (**2.33**) were commercially available. MW-assisted reactions were performed on a CEM Discover SP single-mode reactor equipped with an Explorer 72 autosampler, controlling the instrument settings by PC-running CEM Synergy 1.60 software. Closed vessel experiments were carried out in capped MW-dedicated vials (10 mL) with a cylindrical stirring bar (length 8 mm, diameter 3 mm). Stirring, temperature, irradiation power, maximum pressure (Pmax), pressure set point, times at set point, delta pressure, PowerMAX (simultaneous cooling-while-heating), ActiVent (simultaneous venting-while-heating), and ramp and

hold times were set as indicated. Reaction temperature was monitored by an external CEM fiber optic temperature sensor. After completion of the reaction, the mixture was cooled to 25 °C via airjet cooling. Organic solutions were dried over anhydrous sodium sulfate. Evaporation of solvents was carried out on a Büchi Rotavapor R-210 equipped with a BüchiV-850 vacuum controller and a Büchi V-700 vacuum pump. Column chromatography was performed on columns packed with silica gel from Macherey-Nagel (70-230 mesh). Silica gel thin layer chromatography (TLC) cards from Macherey-Nagel (silica gel precoated aluminum cards with fluorescent indicator visualizable at 254 nm) were used for TLC. Developed plates were visualized with a Spectroline ENF 260C/FE UV apparatus. Melting points (mp) were determined on a Stuart Scientific SMP1 apparatus and are uncorrected. Infrared (IR) spectra were recorded on a PerkinElmerSpectrum 100 FT-IR spectrophotometer equipped with a universal attenuated total reflectance accessory and IR data acquired and processed by PerkinElmer Spectrum 10.03.00.0069 software. Band position and absorption ranges are given in cm⁻¹. Proton nuclear magnetic resonance (¹H NMR) spectra were recorded with a VarianMercury (300 MHz) or a Bruker Avance (400 MHz) spectrometer in the indicated solvent, and the corresponding fid files were processed by MestreLab Research SL MestreReNova 6.2.1-769 software. Chemical shifts are expressed in δ units (ppm) from tetramethylsilane. Mass spectra were recorded on a Bruker Daltonics MicroTOF LC/MS mass spectrometer equipped with a positive ion ESI source. Compound purity was checked by high pressure liquid chromatography (HPLC). Purity of tested compounds was found to be > 95%. The HPLC system used (Thermo Fisher Scientific Inc. Dionex UltiMate 3000) consisted of an SR-3000 solvent rack, a LPG-3400SD quaternary analytical pump, a TCC-3000SD column compartment, a DAD-3000 diode array detector, and an analytical manual injection valve with a 20 mL loop. Samples were dissolved in acetonitrile (1 mg/mL). HPLC analysis was performed by using a Thermo Fisher Scientific Inc. Acclaim 120C18 column (5μm, 4.6 mm x 250 mm) at 25±1 °C with an appropriate solvent gradient (acetonitrile/water), flow rate of 1.0 mL/min and signal detector at 206, 230, 254 and 365 nm. Chromatographic data were acquired and processed by Thermo Fisher Scientific Inc. Chromeleon 6.80 SR15 Build 4656 software.

General procedure for the synthesis of derivatives 2.2-2.6, 2.8, 2.10, 2.12, 2.14, 2.18 and 2.36.

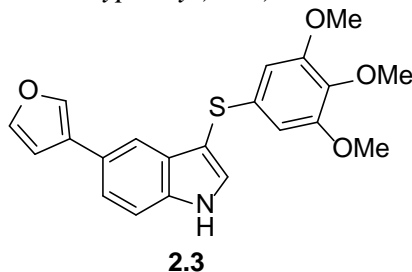
Example. 5-(Furan-2-yl)-3-((3,4,5-trimethoxyphenyl)thio)-1H-indole (2.2).



A mixture of indole **2.26** (183 mg, 1 mmol), bis(3,4,5-trimethoxyphenyl)disulfide²² (438 mg, 1.1 mmol), and sodium hydride (88 mg, 2.2 mmol; 60% in mineral oil) in anhydrous DMF(3 mL) was placed into the MW cavity (closed vessel mode, Pmax = 250 psi). Starting MW irradiation of 120 W was used, the temperature being ramped from 25 to 130 °C, while rapidly stirring and venting (pressure set point: 100 psi; times at set point: 100; delta pressure: 20 psi). Once 130 °C was reached, taking about 1 min, the reaction mixture was held at this temperature for 2 min. The mixture was diluted with water and extracted with ethyl acetate. The organic layer was washed with brine and dried. Removal of the solvent gave a residue that was purified by column chromatography (silica gel, *n*-

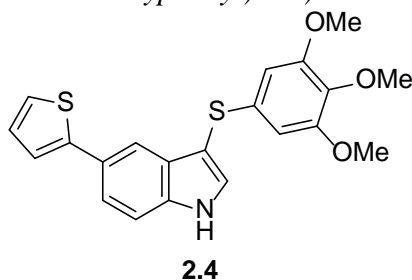
hexane:ethyl acetate = 3:2 as eluent) to give **2.2** (122 mg, yield 32%), mp 118-120 °C (from ethanol). ¹H NMR (DMSO-d₆, 400 MHz): δ 3.98 (s, 9H), 6.82 (s, 2H), 6.95 (s, 1H), 7.22 (d, *J* = 1.7 Hz, 1H), 7.93-7.96 (m, 2H), 8.07 (s, 1H), 8.17 (s, 1H), 8.22 (s, 1H), 12.20 ppm (br s, disappeared after treatment with D₂O, 1H). IR: ν 3448 cm⁻¹.

5-(Furan-3-yl)-3-((3,4,5-trimethoxyphenyl)thio)-1H-indole (2.3).



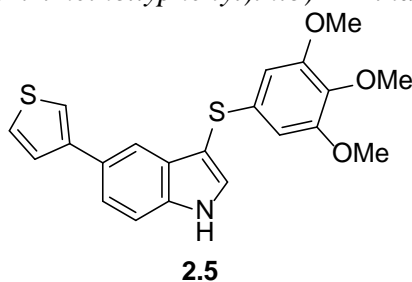
Synthesized as **2.2** starting from **2.27**. Yield 20%, mp 125-130 °C (from ethanol). ¹H NMR (DMSO-d₆, 400 MHz): δ 3.57 (s, 3H), 3.59 (s, 6H), 6.44 (s, 2H), 6.89-6.91 (m, 1H), 7.45-7.47 (m, 2H), 7.61-7.65 (m, 1H), 7.70 (d, *J* = 1.7 Hz, 1H), 7.77 (s, 1H), 8.05-8.10 (m, 1H), 11.70 ppm (br s, disappeared after treatment with D₂O, 1H). IR: ν 3425 cm⁻¹.

5-(Thiophen-2-yl)-3-((3,4,5-trimethoxyphenyl)thio)-1H-indole (2.4).



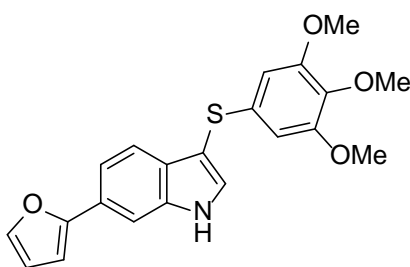
Synthesized as **2.2** starting from **2.28**. Yield 31%, mp 115-120 °C (from ethanol). ¹H NMR (CDCl₃, 400 MHz): δ 3.69 (s, 6H), 3.78 (s, 3H), 6.44 (s, 2H), 7.00-7.07 (m, 1H), 7.24 (dd, *J* = 2.9 and 7.1 Hz, 1H), 7.28 (s, 1H), 7.44 (d, *J* = 8.5 Hz, 1H), 7.52 (d, *J* = 2.6 Hz, 1H), 7.55-7.60 (m, 1H), 7.89 (s, 1H), 8.49 ppm (br s, disappeared after treatment with D₂O, 1H). IR: ν 3439 cm⁻¹.

5-(Thiophen-3-yl)-3-((3,4,5-trimethoxyphenyl)thio)-1H-indole (2.5).



Synthesized as **2.2** starting from **2.29**. Yield 40%, mp 116-120 °C (from ethanol). ¹H NMR (DMSO-d₆, 400 MHz): δ 3.57 (s, 3H), 3.58 (s, 6H), 6.44 (s, 2H), 7.49-7.51 (m, 1H), 7.53 (s, 1H), 7.55 (d, *J* = 1.3 Hz, 1H), 7.59-7.62 (m, 1H), 7.72-7.74 (m, 2H), 7.79 (d, *J* = 2.4 Hz, 1H), 11.71 ppm (br s, disappeared after treatment with D₂O, 1H). IR: ν 3448 cm⁻¹.

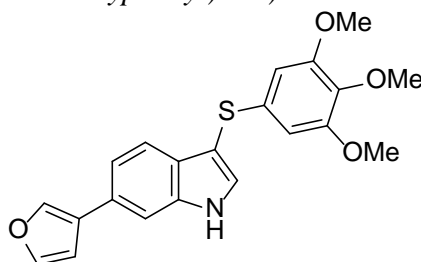
6-(Furan-2-yl)-3-((3,4,5-trimethoxyphenyl)thio)-1H-indole (2.6).



2.6

Synthesized as **2.2** starting from **2.30**. Yield 44%, mp 164-169 °C (from ethanol). ¹H NMR (DMSO-d₆, 300 MHz): δ 3.56 (s, 9H), 6.37 (s, 2H), 6.56-6.60 (m, 1H), 6.85 (d, *J* = 3.2 Hz, 1H), 7.45 (s, 2H), 7.70-7.74 (m, 3H), 11.74 ppm (br s, disappeared after treatment with D₂O, 1H). IR: ν 3179 cm⁻¹.

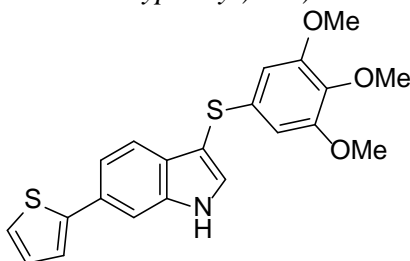
6-(Furan-3-yl)-3-((3,4,5-trimethoxyphenyl)thio)-1H-indole (2.8).



2.8

Synthesized as **2.2** starting from **2.31**. Yield 4%, slurry. ¹H NMR (DMSO-d₆, 400 MHz): δ 3.57 (s, 9H), 6.39 (s, 2H), 6.90-6.95 (m, 1H), 7.34-7.36 (m, 1H), 7.40-7.43 (m, 1H), 7.63 (s, 1H), 7.70-7.73 (m, 2H), 8.14 (s, 1H), 11.66 ppm (br s, disappeared after treatment with D₂O, 1H). IR: ν 3401 cm⁻¹.

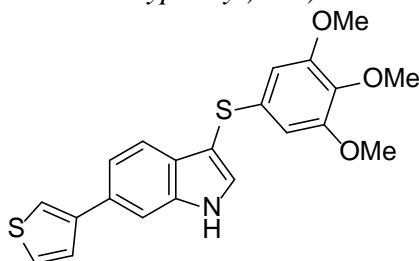
6-(Thiophen-2-yl)-3-((3,4,5-trimethoxyphenyl)thio)-1H-indole (2.10).



2.10

Synthesized as **2.2** starting from **2.32**. Yield 50%, mp 158-161 °C (from ethanol). ¹H NMR (DMSO-d₆, 400 MHz): δ 3.58 (s, 3H), 3.59 (s, 6H), 6.41 (s, 2H), 7.10-7.13 (m, 1H), 7.41-7.43 (m, 1H), 7.44-7.48 (m, 3H), 7.70-7.72 (m, 1H), 7.82 (s, 1H), 11.74 ppm (br s, disappeared after treatment with D₂O, 1H). IR: ν 3372 cm⁻¹.

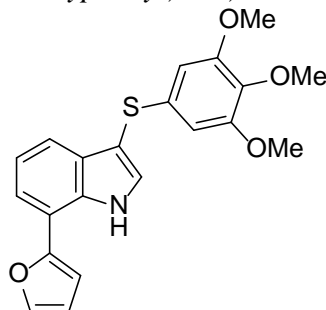
6-(Thiophen-3-yl)-3-((3,4,5-trimethoxyphenyl)thio)-1H-indole (2.12).



2.12

Synthesized as **2.2** starting from **2.38**. Yield 30%, mp 188-190 °C (from ethanol). ¹H NMR (DMSO-d₆, 400 MHz): δ 3.58 (s, 3H), 3.59 (s, 6H), 6.40 (s, 2H), 7.45-7.47 (m, 2H), 7.52-7.57 (m, 1H), 7.60-7.64 (m, 1H), 7.76 (s, 1H), 7.79 (s, 1H), 7.77-7.81 (m, 1H), 11.72 ppm (br s, disappeared after treatment with D₂O, 1H). IR: ν 3376 cm⁻¹.

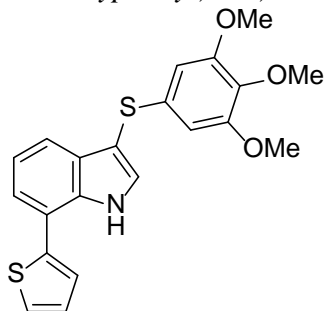
7-(Furan-2-yl)-3-((3,4,5-trimethoxyphenyl)thio)-1H-indole (2.14).



2.14

Synthesized as **2.2** starting from **2.34**. Yield 15%, mp 80-83 °C (from ethanol). ¹H NMR (DMSO-d₆, 400 MHz): δ 3.58 (s, 9H), 6.42 (s, 2H), 6.71-6.75 (m, 1H), 7.16-7.21 (m, 2H), 7.44-7.50 (m, 1H), 7.59-7.63 (m, 1H), 7.80-7.83 (m, 2H), 11.59 ppm (br s, disappeared after treatment with D₂O, 1H). IR: ν 3351 cm⁻¹.

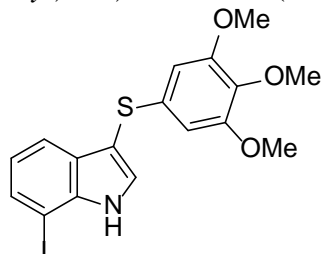
7-(Thiophen-2-yl)-3-((3,4,5-trimethoxyphenyl)thio)-1H-indole (2.18).



2.18

Synthesized as **2.2** starting from **2.35**. Yield 29%, mp 153-155 °C (from ethanol). ¹H NMR (DMSO-d₆, 300 MHz): δ 3.56 (s, 3H), 3.58 (s, 6H), 6.43 (s, 2H), 7.14 (t, *J* = 5.8 Hz, 1H), 7.24 (t, *J* = 3.8 Hz, 1H), 7.32 (d, *J* = 5.5 Hz, 1H), 7.46 (d, *J* = 5.9 Hz, 1H), 7.56 (d, *J* = 2.7 Hz, 1H), 7.64 (d, *J* = 3.8 Hz, 1H), 7.76 (s, 1H), 11.57 ppm (br s, disappeared after treatment with D₂O, 1H). IR: ν 3322 cm⁻¹.

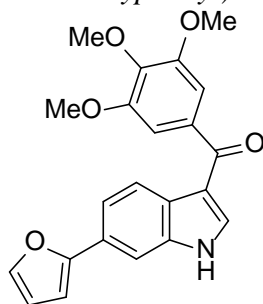
7-Iodo-3-((3,4,5-trimethoxyphenyl)thio)-1H-indole (2.36).



2.36

Synthesized as **2.2** starting from **2.25**. Yield 27%, mp 100-103 °C (from ethanol). ¹H NMR (DMSO-d₆, 400 MHz): δ 3.56 (s, 3H), 3.57 (s, 6H), 6.40 (s, 2H), 6.90 (t, *J* = 7.6 Hz, 1H), 7.46 (d, *J* = 7.8 Hz, 1H), 7.58 (d, *J* = 7.4 Hz, 1H), 7.77 (s, 1H), 11.61 ppm (br s, disappeared after treatment with D₂O, 1H). IR: ν 3270 cm⁻¹.

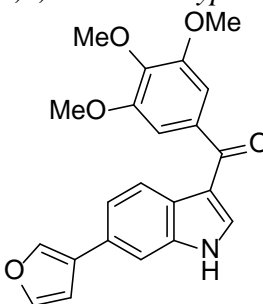
General procedure for the synthesis of derivatives **2.7**, **2.9**, **2.11** and **2.13**. Example. (6-(Furan-2-yl)-1H-indol-3-yl) (3,4,5-trimethoxyphenyl)methanone (**2.7**).



2.7

Diethylaluminum chloride (120 mg, 1 mmol; 1.0 M in hexanes) was added to a -78 °C solution of indole **2.30** (183 mg, 1 mmol) in dichloromethane (2.5 mL). The reaction mixture was warmed to -10 °C, and 3,4,5-trimethoxybenzoyl chloride (276 mg, 1.2 mmol) was added. The reaction mixture was stirred for 2 h, and the temperature rose to 25 °C. Water and chloroform were added, and the layers were separated. The organic phase was washed with brine, dried and filtered. Evaporation of the solvent gave a residue that was purified by column chromatography (silica gel, *n*-hexane:acetone = 7:3 as eluent) to give **2.7** (53 mg, yield 14%), mp 190-195 °C (from ethanol). ¹H NMR (DMSO-*d*₆, 400 MHz): δ 3.75 (s, 3H), 3.85 (s, 6H), 6.58-6.62 (m, 1H), 6.88-6.92 (m, 1H), 7.10 (s, 2H), 7.61 (dd, *J* = 1.4 and 8.4 Hz, 1H), 7.74-7.78 (m, 2H), 8.13 (s, 1H), 8.20-8.24 (m, 1H), 12.11 ppm (br s, disappeared after treatment with D₂O, 1H). IR: ν 1573 and 3192 cm⁻¹.

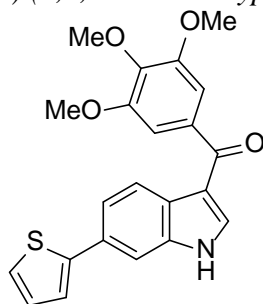
(6-(Furan-3-yl)-1H-indol-3-yl) (3,4,5-trimethoxyphenyl)methanone (**2.9**)



2.9

Synthesized as **2.7** starting from **2.31**. Yield 17%, mp 180-185 °C (from ethanol). ¹H NMR (DMSO-*d*₆, 300 MHz): δ 3.75 (s, 3H), 3.85 (s, 6H), 6.95-6.98 (m, 1H), 7.09 (s, 2H), 7.50-7.55 (m, 1H), 7.66 (s, 1H), 7.75 (t, *J* = 1.4 Hz, 1H), 8.07 (s, 1H), 8.18-8.20 (m, 2H), 12.04 ppm (br s, disappeared after treatment with D₂O, 1H). IR: ν 1576 and 3238 cm⁻¹.

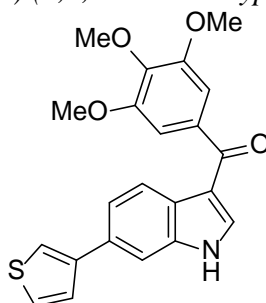
(6-(Thiophen-2-yl)-1H-indol-3-yl) (3,4,5-trimethoxyphenyl)methanone (**2.11**)



2.11

Synthesized as **2.7** starting from **2.32**. Yield 68%, mp 200-205 °C (from ethanol). ¹H NMR (DMSO-d₆, 300 MHz): δ 3.75 (s, 3H), 3.85 (s, 6H), 7.09 (s, 2H), 7.14-7.20 (m, 1H), 7.45-7.50 (m, 2H), 7.56 (dd, *J* = 1.5 and 8.3 Hz, 1H), 7.73-7.76 (m, 1H), 8.12 (s, 1H), 8.23 (d, *J* = 8.2 Hz, 1H), 12.04 ppm (br s, disappeared after treatment with D₂O, 1H). IR: ν 1575 and 3219 cm⁻¹.

(6-(Thiophen-3-yl)-1H-indol-3-yl) (3,4,5-trimethoxyphenyl)methanone (**2.13**)

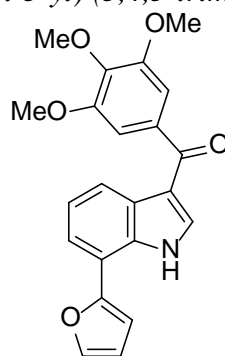


2.13

Synthesized as **2.7** starting from **2.33**. Yield 69%, mp 188-192 °C (from ethanol). ¹H NMR (DMSO-d₆, 400 MHz): δ 3.74 (s, 3H), 3.84 (s, 6H), 7.08 (s, 2H), 7.60-7.65 (m, 3H), 7.72-7.76 (m, 1H), 7.82-7.85 (m, 1H), 8.10 (s, 1H), 8.22 (d, *J* = 8.3 Hz, 1H), 12.05 ppm (br s, disappeared after treatment with D₂O, 1H). IR: ν 1733 and 3113 cm⁻¹.

General procedure for the synthesis of derivatives **2.15-2.17**, **2.19-2.21**, **2.29-2.31**, **2.34** and **2.35**.

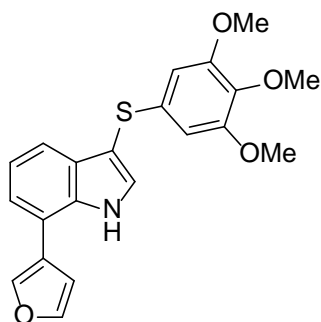
Example (7-(Furan-2-yl)-1H-indol-3-yl) (3,4,5-trimethoxyphenyl)methanone (**2.15**).



2.15

A mixture of derivative **2.37** (437 mg, 1 mmol), tris(dibenzylideneacetone)dipalladium (0) (20 mg, 0.022 mmol), 2-dicyclohexylphosphino-2',6'-dimethoxybiphenyl (3.2 mg, 0.008 mmol) and potassium phosphate tribasic (435 mg, 2.05 mmol) was degassed for 20 min. 1-Butanol (2.2 mL) and a solution of (2-(furan-2-yl)-6-methyl-1,3,6,2-dioxazaborocane-4,8-dione) (334 mg, 1.5 mmol) in the same solvent (4.4 mL) were added. The reaction mixture was heated at 100 °C for 15 h. After cooling, the mixture was treated dropwise with 1N HCl and extracted with ethyl acetate. The organic layer was washed with brine, dried and filtered. Evaporation of the solvent gave a residue that was purified by column chromatography (silica gel, *n*-hexane:acetone = 2:1 as eluent) to give **2.15** (124 mg, yield 33%), mp 221-224 °C (from ethanol). ¹H NMR (DMSO-d₆, 400 MHz): δ 3.76 (s, 3H), 3.85 (s, 6H), 6.71-6.75 (m, 1H), 7.12 (s, 2H), 7.15 (d, *J* = 3.4 Hz, 1H), 7.31 (t, *J* = 7.7 Hz, 1H), 7.63 (dd, *J* = 1.1 and 7.5 Hz, 1H), 7.80-7.85 (m, 1H), 7.98 (s, 1H), 8.23 (dd, *J* = 1.1 and 8.0 Hz, 1H), 11.85 ppm (br s, disappeared after treatment with D₂O, 1H). IR: ν 1623 and 3427 cm⁻¹.

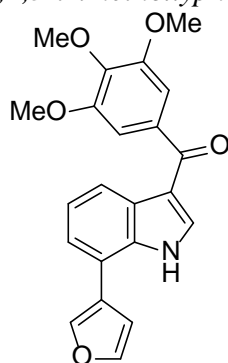
7-(Furan-3-yl)-3-((3,4,5-trimethoxyphenyl)thio)-1H-indole (**2.16**).



2.16

Synthesized as **2.15** from **2.36** and furan-3-boronic acid pinacol ester. Yield 58%, mp 156-160 °C (from ethanol). ¹H NMR (DMSO-d₆, 400 MHz): δ 3.57 (s, 3H), 3.58 (s, 6H), 6.42 (s, 2H), 7.04 (m, 1H), 7.15 (t, *J* = 7.7 Hz, 1H), 7.40 (m, 2H), 7.78 (s, 1H), 7.85 (t, *J* = 1.8 Hz, 1H), 8.31 (t, *J* = 1.3 Hz, 1H), 11.39 ppm (br s, disappeared after treatment with D₂O, 1H). IR: ν 3318 cm⁻¹.

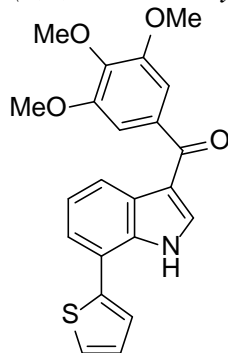
(7-(Furan-3-yl)-1H-indol-3-yl) (3,4,5-trimethoxyphenyl)methanone (**2.17**)



2.17

Synthesized as **2.15** starting from **2.37** and furan-3-boronic acid pinacol ester. Yield 46%, mp 215-220 °C (from ethanol). ¹H NMR (DMSO-d₆, 400 MHz): δ 3.76 (s, 3H), 3.85 (s, 6H), 7.00-7.05 (m, 1H), 7.11 (s, 2H), 7.29 (t, *J* = 7.9 Hz, 1H), 7.42 (dd, *J* = 1.1 and 7.4 Hz, 1H), 7.86 (t, *J* = 1.8 Hz, 1H), 7.97 (s, 1H), 8.21 (dd, *J* = 1.2 and 8.0 Hz, 1H), 8.25-8.30 (m, 1H), 11.76 ppm (br s, disappeared after treatment with D₂O, 1H). IR: ν 1568 and 3285 cm⁻¹.

(7-(Thiophen-2-yl)-1H-indol-3-yl) (3,4,5-trimethoxyphenyl)methanone (**2.19**)

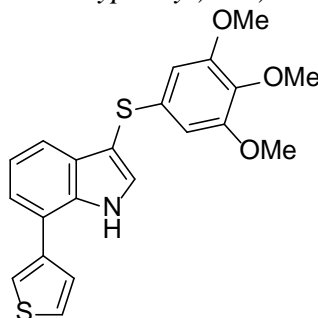


2.19

Synthesized as **2.15** starting from **2.37** and 2-thienylboronic acid. Yield 6%, mp 209-211 °C (from ethanol). ¹H NMR (DMSO-d₆, 400 MHz): δ 3.76 (s, 3H), 3.85 (s, 6H), 7.11 (s, 2H), 7.28-7.33 (m, 2H), 7.38 (dd, *J* = 1.2 and 7.4 Hz, 1H), 7.56 (dd, *J* = 1.2 and 3.6

Hz,1H), 7.68 (dd, $J = 1.1$ and 5.1 Hz, 1H), 7.95 (s, 1H), 8.25 (dd, $J = 1.2$ and 7.9 Hz, 1H), 11.94 ppm (br s, disappeared after treatment with D_2O ,1H). IR: ν 1573 and 3263 cm^{-1} .

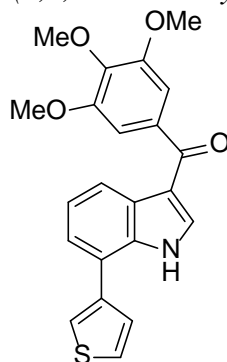
7-(Thiophen-3-yl)-3-((3,4,5-trimethoxyphenyl)thio)-1H-indole (**2.20**)



2.20

Synthesized as **2.15** starting from **2.36** and 3-thienylboronic acid. Yield 75%, mp 147-150 °C (from ethanol). 1H NMR (DMSO- d_6 , 400 MHz): δ 3.57 (s, 3H), 3.58 (s, 6H), 6.43 (s, 2H), 7.15 (t, $J = 7.8$ Hz, 1H), 7.35 (dd, $J = 1.1$ and 7.4 Hz, 1H), 7.44 (dd, $J = 1.1$ and 7.9 Hz, 1H), 7.54 (dd, $J = 1.4$ and 5.0 Hz, 1H), 7.70-7.75 (m, 2H), 7.80-7.85 (m, 1H), 11.52 ppm (br s, disappeared after treatment with D_2O , 1H). IR: ν 3327 cm^{-1} .

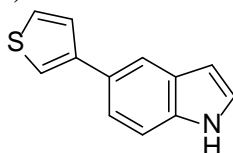
(7-(Thiophen-3-yl)-1H-indol-3-yl) (3,4,5-trimethoxyphenyl)methanone (**2.21**)



2.21

Synthesized as **2.15** starting from **2.37** and 3-thienylboronic acid. Yield 5%, slurry. 1H NMR (DMSO- d_6 , 400 MHz): δ 3.76 (s, 3H), 3.84 (s, 6H), 7.10 (s, 2H), 7.30 (t, $J = 7.8$ Hz, 1H), 7.40 (dd, $J = 1.1$ and 7.4 Hz, 1H), 7.52 (dd, $J = 1.3$ and 5.0 Hz, 1H), 7.70-7.75 (m, 1H), 7.80-7.86 (m, 1H), 7.93 (s, 1H), 8.23 (dd, $J = 1.1$ and 7.8 Hz, 1H), 11.86 ppm (br s, disappeared after treatment with D_2O , 1H). IR: ν 1580 and 2925 cm^{-1} .

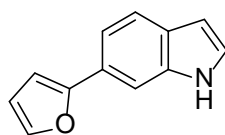
5-(Thiophen-3-yl)-1H-indole (**2.29**)



2.29

Synthesized as **2.15** starting from **2.22** and 3-thienylboronic acid. Yield 40%, mp 80-83 °C (from *n*-hexane), lit. 80-82 °C.³⁴

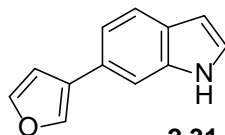
6-(Furan-2-yl)-1H-indole (**2.30**)



2.30

Synthesized as **2.15** starting from **2.24** and furan-2-boronic acid MIDA ester. Yield 19%, mp 90-96 °C (from *n*-hexane). ¹H NMR (DMSO-d₆, 400 MHz): δ 6.38-6.42 (m, 1H), 6.50-6.56 (m, 1H), 6.81 (dd, *J* = 0.8 and 3.4 Hz, 1H), 7.32-7.36 (m, 2H), 7.55 (d, *J* = 8.3 Hz, 1H), 7.69-7.71 (m, 2H), 11.17 ppm (br s, disappeared after treatment with D₂O, 1H). IR: ν 3388 cm⁻¹.

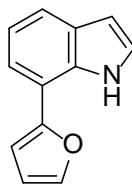
6-(Furan-3-yl)-1H-indole (2.31)



2.31

Synthesized as **2.15** starting from **2.24** and furan-3-boronic acid MIDA ester. Yield 7%, mp 155-158 °C (from *n*-hexane). ¹H NMR (DMSO-d₆, 400 MHz): δ 6.37-6.40 (m, 1H), 6.90-6.95 (m, 1H), 7.25 (dd, *J* = 1.6 and 8.2 Hz, 1H), 7.30-7.32 (m, 1H), 7.50-7.53 (m, 2H), 7.77 (t, *J* = 1.8 Hz, 1H), 8.08-8.12 (m, 1H), 11.07 ppm (br s, disappeared after treatment with D₂O, 1H). IR: ν 3384 cm⁻¹.

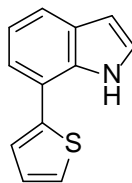
7-(Furan-2-yl)-1H-indole (2.34)



2.34

Synthesized as **2.15** starting from **2.25** and 2-furanyl boronic acid MIDA ester. Yield 21% as an oil.³⁵

7-(Thiophen-2-yl)-1H-indole (2.35)

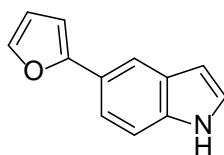


2.35

Synthesized as **2.15** starting from **2.25** and 2-thienyl boronic acid. Yield 67% as an oil.³⁶

General procedure for the synthesis of derivatives 2.26 and 2.28.

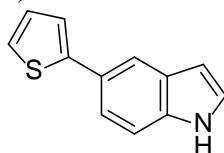
Example. 5-(Furan-2-yl)-1H-indole (2.26)



2.26

A mixture of **2.23** (243 mg, 1 mmol), 2-furan boronic acid (223 mg, 2 mmol), palladium(II) acetate (11 mg, 0.05 mmol), tri(o-tolyl)phosphine (30 mg, 0.1 mmol), potassium phosphate tribasic (745 mg, 3.5 mmol) in ethanol (10 mL) and toluene (5 mL) was heated at 80 °C for 2 h. After cooling, the reaction mixture was diluted with a saturated aqueous solution of sodium hydrogen carbonate and extracted with ethyl acetate. The organic layer was washed with brine, dried and filtered. Evaporation of the solvent gave a residue that was purified by column chromatography (silicagel, *n*-hexane:ethyl acetate = 5:1 as eluent) to give **2.26** (159 mg, yield 87%), mp 108-110 °C (from ethanol), lit. 110-111 °C.

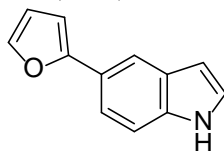
5-(Thiophen-2-yl)-1H-indole (2.28)



2.28

Synthesized as **2.26** starting from 2-thienyl boronic acid. Yield 73%, mp 50-51 °C (from *n*-hexane), lit. 53-54 °C.³⁷

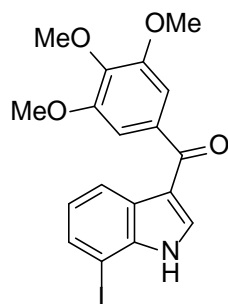
Synthesis of 5-(furan-2-yl)-1H-indole (2.27)



2.27

A mixture of **2.23** (243 mg, 1 mmol), 3-furan boronic acid pinacol ester (253 mg, 1.3 mmol), potassium carbonate (179 mg, 1.3 mmol) in methylpyrrolidone (2 mL) and water (0.15 mL) was degassed for 15 min. Palladium(II) acetate (30 mg, 0.13 mmol) was added, and the reaction mixture was placed into the MW cavity (closed vessel mode, Pmax = 250 psi). Starting MW irradiation of 200 W was used, the temperature being ramped from 25 to 110 °C. Once this was reached, taking around 2 min, the mixture was held at this temperature for 15 min with rapid stirring. The reaction mixture was diluted with water and extracted with ethyl acetate. The organic layer was washed with brine, dried and filtered. Evaporation of the solvent gave a residue that was purified by column chromatography (silica gel, *n*-hexane:ethyl acetate = 5:1 as eluent) to give **2.27** (82 mg, yield 45%) mp 89-90 °C (from *n*-hexane), lit. 89-91 °C.³⁸

Synthesis of (7-iodo-1H-indol-3-yl)(3,4,5-trimethoxyphenyl)methanone (2.37)



2.37

A mixture of **2.25** (243 mg, 1 mmol), 3,4,5-trimethoxybenzoylchloride (230 mg, 1 mmol) and anhydrous aluminum chloride (133 mg, 1 mmol) in *1,2*-dichloroethane (2 mL) was placed into the MW cavity (closed vessel mode, $P_{max} = 250$ psi). A starting MW irradiation of 150 W was used, the temperature being ramped from 25 to 110 °C with rapid stirring. Once 110 °C was reached, taking around 1 min, the reaction mixture was held at this temperature for 2 min, diluted with water, treated with 1N HCl and extracted with chloroform. The organic layer was washed with brine, dried and filtered. Evaporation of the solvent gave a residue that was purified by column chromatography (silica gel, *n*-hexane:ethyl acetate = 1:1 as eluent) to give **2.37** (223 mg, yield 51%, mp 148-153 °C (from ethanol). $^1\text{H NMR}$ (DMSO- d_6 , 400 MHz): δ 3.76 (s, 3H), 3.85 (s, 6H), 7.04 (t, $J = 7.6$ Hz, 1H), 7.09 (s, 2H), 7.66 (dd, $J = 1.0$ and 7.6 Hz, 1H), 7.98 (s, 1H), 8.23 (dd, $J = 1.0$ and 7.96 Hz, 1H), 11.86 ppm (br s, disappeared after treatment with D_2O , 1H). IR: ν 1577 and 3112 cm^{-1} .

2.7.2 Molecular Modeling

All molecular modeling studies were performed on a MacPro dual 2.66 GHz Xeon running Ubuntu 14LTS. The tubulin structures were downloaded from the PDB data bank (<http://www.rcsb.org/>), PDB code: 1SA0,²⁸ 4O2A,³⁹ 4O2B,³⁹ 5CA0,⁷ 5CB4,⁷ 5LYJ,⁴⁰ and 3HKC.⁴¹ Ligand structures were prepared with Maestro.⁴² Proteins were prepared by the protein preparation wizard⁴³ of Maestro. The docking simulations were performed using Plants⁴⁴ and Autodock.⁴⁵ Images shown in the manuscript were prepared with Pymol.⁴⁶

2.7.3 Biological assays

Tubulin assembly. The reaction mixtures contained 0.8 M monosodium glutamate (pH 6.6 with HCl in a 2 M stock solution), 10 μM tubulin, 4% (v/v) DMSO, and varying concentrations of drug. Following a 15 min preincubation at 30 °C, samples were chilled on ice, GTP to 0.4 μM was added, and turbidity development was followed at 350 nm in a temperature-controlled recording spectrophotometer for 20 min at 30 °C. The extent of reaction was measured. Full experimental details were previously reported.⁴⁷

[^3H]Colchicine binding assay. The reaction mixtures contained 1.0 μM tubulin, 5.0 μM [^3H]colchicine, and 5.0 μM inhibitor and were incubated for 10 min at 37 °C. Complete details were described previously.⁴⁸

Cell cultures. Cell lines were obtained from the American Type Culture Collection (ATCC), unless otherwise specified. MCF-7 breast carcinoma, OVCAR-8, and NCI/ADR-RES cells were obtained from the National Cancer Institute drug screening laboratory. U87MG and U343MG cell lines were obtained from the National Institute for Cancer Research of Genoa (Italy) and Cell Lines Service GmbH (Germany), respectively. All cell lines, except as indicated, were grown in Dulbecco's modified Eagle's medium (DMEM) supplemented with 10% fetal bovine serum (FBS), 20 mM HEPES, 100 U/mL penicillin, 100 mg/mL streptomycin, and 1% L-glutamine; specific requirements include the addition of glucose (4.5 g/L for HT29 and HCT116 cells; 1 g/L for HepG2). Cell lines

were cultured at 37 °C in 5% CO₂ / 95% air in a humidified incubator. Treatments were initiated 24 h after cell seeding using compound **2.12** or **2.18** diluted in 0.1% DMSO, the indicated reference compound, or 0.1% DMSO vehicle, for 24-72 h as indicated. T98G and U87MG cells were cultured in RPMI medium and minimum essential medium Eagle, respectively, supplemented with 10% FBS, 2 mM L-glutamine, 100 U/mL penicillin, 100 mg/mL streptomycin and 1% non-essential amino acids at 37 °C in 5% CO₂. The U343MG cells were cultured in minimum essential medium Eagle with 2 mM L-glutamine and Earle's BSS adjusted to contain 1.5 mg/mL sodium bicarbonate and supplemented with 10% FBS, 100 U/mL penicillin, 100 mg/mL streptomycin, 1% non-essential amino acids and 1.0 mM sodium pyruvate at 37 °C in 5% CO₂.

Cell viability assays. The methodology for the evaluation of the growth of human MCF-7 breast carcinoma, OVCAR-8, and NCI/ADR-RES cells, obtained from the National Cancer Institute drug screening laboratory, was previously described, except that cells were grown for 96 h for IC₅₀ determinations.⁴⁹ Cell viability of HT29, HCT116 and HepG2 cells was determined using the MTT colorimetric assay. HT29, HepG2 and HCT116 cells were seeded into 24-well plates to a density of 15 x 10³/mL in each well. After 24 h of growth to allow attachment of cells to the wells, test compounds were added at 20-320 nM. After 48 h of growth and removal of the culture medium, 500 µL/well of PBS containing 500 µM MTT was added. Cell cultures were further incubated at 37 °C for 2 h in the dark. The solutions were then gently aspirated from each well, and the formazan crystals within the cells were dissolved in propan-2-ol and 0.04N HCl (200 µL). Optical densities were read at 550 nm using a Multiskan Spectrum Thermo Electron Corporation reader. The results were expressed as % relative to vehicle-treated control (0.1% DMSO), and IC₅₀ values were calculated by non linear regression analysis (GraphPad Prism statistics software). The effect of the treatment with compounds **2.12** or **2.18** on the T98G, U87MG and U343MG cell lines was estimated using the colorimetric MTS conversion assay, as previously reported.³³ After compound incubations, the MTS reagent was added, and the absorbance at 590 nm was measured by a microplate reader (Wallac, Victor 2, 1420 Multilabel Counter, PerkinElmer). The percentage of proliferating cells after compound exposure was calculated with respect to control cells (100%). The effect of treatment with compounds **2.12** or **2.18** on MV4-11, THP-1, A-549 and PC3 cell was determined by CellTiter-Fluor™ (Promega cod. G6082). The cells were seeded in 96 multiwell plates at the indicated densities (MV-4: 5000 cells/50 µL/well; THP-1: 2000 cells/50 µL/well; A549: 3500 cells/50 µL/well; MDA-MB-231: 3500 cells/50 µL/well; PC-3: 2000 cells/50 µL/well). 24 h after plating, compound **2.12** or **2.18** was added to the cells, and the effect on cell proliferation was determined after 72 h by the CellTiter-Fluor™ assay. After adding the reagents to the cell plates, the cells were incubated for 90 min at 37 °C, and the fluorescent signal was read by using a TECAN reader. The IC₅₀ and GI₅₀ results were obtained by analysis with GraphPad Prism and Assay Explorer software.

Statistical analyses. Graph-Pad Prism 5 software (GraphPad Software Inc, San Diego, CA) was used for data analysis and graphic presentations. Statistical analysis was performed by non-linear regression fitting; sigmoidal-dose response curves were performed using the log(i-nhibitor) vs response analyses. The IC₅₀ value and the maximal efficacy of compounds in inhibiting cell viability (E max) were derived.

Immunofluorescence and microscopy. After treatment, HeLa cells directly grown on sterile poly-L-lysine (Sigma P4832) coated coverslips were fixed in methanol for 6 min at -20 °C and processed for IF using mouse α-tubulin antibody (Sigma clone B-5-1-2, 1:3000 dilution) followed by FITC-conjugated anti-mouse secondary antibody (Jackson ImmunoResearch Laboratories). Slides were counterstained with 0.05 µg/mL DAPI (Sigma) and mounted in Vectashield (Vector). IF-processed cells were examined under an epifluorescence Nikon Eclipse 90i with a QICAM Fast 1394 (QImaging) camera and

using the NIS-Elements AR 4.0 software (Nikon). Single cell images were routinely taken using immersion oil 100 x objectives with NA 1.3.

Flow cytometric analysis. Cell cycle phase distribution was analyzed after incubation with PI (Sigma P4170). All parameters (FS, SS and FL-3) were acquired in a linear amplification scale. Cell aggregates were gated out on the bi-parametric graph FL-3 lin/ratio. Cell death was analyzed using annexin V-FITC (Immunological Sciences, IK-11120). Cell samples were analyzed in a Coulter Epics XL cytofluorometer (Beckman Coulter) equipped with EXPO 32 ADC software. Data from at least 10.000 cells per sample were acquired and processed using Win MDI software.

RNA extraction, reverse transcription and real-time polymerase chain reaction analysis. Total cellular RNA was processed, and 1 µg of total RNA was retro-transcribed. The cDNA was used to perform a real-time PCR using p21^{Cip1/Waf1} and GAPDH primers as indicated in Table 2.4. For p21^{Cip1/Waf1} and GAPDH genes, the following protocols were used for the PCRs: initialization at 95 °C for 3 min, followed by 40 cycles of 95 °C for 10 s, 60 °C for 10 s, 72 °C for 10 s. The melting program was 95 °C for 5 s, 65 °C for 1 min and 97 °C for 10 s. The rate of temperature increase was 1 °C/s, and fluorescence data were continuously acquired. The relative amounts of target genes were normalized to GAPDH expression by Light Cycler[®] 480 Software version 1.5 (Roche Diagnostics) using the $2^{-\Delta\Delta Ct}$ method.

Table 2.4. Features of the primers used for real-time polymerase chain reaction.

Transcript	T _{ann} (°C)	NCBI Ref Seq. ^a
P21 ^{Cip1/Waf1}	60	Fw:GGACAGCAGAGGACCATGT
		Rw:TGGAGTGGTAGAAATCTGTCATGC
GAPDH	60	Fw:AGGCTGAGAAACGGGAAGC
		Rw:CCATGGTGGTGAAGACGC

^a NCBI Ref Seq: National Center for Biotechnology Information Reference Sequence (<http://www.ncbi.nlm.nih.gov/RefSeq/>) identifier.

2.8 References

- Jordan, M.A.; Wilson, L. Microtubules as a target for anticancer drugs. *Nat. Rev. Canc.* **2004**, *42*, 53,265.
- Florian, S.; Mitchison, T.J. Anti-microtubule drugs. *Methods Mol. Bioogy* **2016**, *1413*, 403, 421.
- Marzo, I.; Naval, J. Antimitotic drugs in cancer chemotherapy: promises and Pitfalls. *Biochem. Pharmacol.* **2013**, *86*, 703, 710.
- Mukhtar, E.; Adhami, V.M.; Mukhtar, H. Targeting microtubules by natural agents for cancer therapy. *Mol. Canc. Therapeut.* **2014**, *13*, 275, 284.
- Chandrasekaran, G.; Tatrai, P.; Gergely, F. Hitting the brakes: targeting microtubule motors in cancer. *Br. J. Canc.* **2015**, *113*, 693, 698.
- Bhattacharyya, B.; Panda, D.; Gupta, S.; Banerjee S. Anti-mitotic activity of colchicine and the structural basis for its interaction with tubulin. *Med. Res. Rev.* **2008**, *28*, 155,183.
- Hong, Y.; Zhao, Y.; Yang L.; Gao, M.; Li, L.; Man, S.; Wang, Z.; Guan, Q.; Bao, K.; Zuo, D.; Wu, Y.; Zhang, W. Design, synthesis and biological evaluation of 3,4-diaryl-1,2,5-oxadiazole-2/5-oxides as highly potent inhibitors of tubulin polymerization. *Eur. J. Med. Chem.* **2019**, *178*, 287–296.

8. Lin, C.M.; Ho, H.H.; Pettit, G.R.; Hamel, E. Antimitotic natural products combretastatin A-4 and combretastatin A-2: studies on the mechanism of their inhibition of the binding of colchicine to tubulin. *Biochemistry* **1989**, *28*, 6984, 6991.
9. Beckers, T.; Mahboobi, S. Natural, semisynthetic and synthetic microtubule inhibitors for cancer therapy. *Drugs Future* **2003**, *28*, 767,785.
10. Nogales, E.; Whittaker, M.; Milligan, R.A.; Downing, K.H. High-resolution model of the microtubule. *Cell* **1999**, *96*, 79, 88.
11. Nettles, J.H.; Li, H.; Cornett, B.; Krahn, J.M.; Snyder, J.P.; Downing, K.H. The binding mode of epothilone A on alpha, beta-tubulin by electron crystallography. *Science* **2004**, *305*, 866, 869.
12. Buey, R.M.; Calvo, E.; Barasoain, I.; Pineda, O.; Edler, M.C.; Matesanz, R.; Cerezo, G.; Vanderwal, C.D.; Day, B.W.; Sorensen, E.J.; Lopez, J.A.; Andreu, J.M.; Hamel, E.; Diaz, J.F. Cyclostreptin binds covalently to microtubule pores and luminal taxoid binding sites. *Nat. Chem. Biol.* **2007**, *3*, 117,125.
13. Liu, Y.M.; Chen, H.L.; Lee, H.Y.; Liou, J.P. Tubulin inhibitors: a patent review. *Expert Opin. Ther. Pat.* **2014**, *24*,69,88.
14. Field, J.J.; Kanakkanthara, A.; Miller, J.H. Microtubule-targeting agents are clinically successful due to both mitotic and interphase impairment of microtubule function. *Bioorg. Med. Chem.* **2014**, *22*, 5050, 5059.
15. Wu, X.; Wang, Q.; Li, W. Recent advances in heterocyclic tubulin inhibitors targeting the colchicine binding site. *Anti Canc. Agents Med. Chem.* **2016**, *16*, 1325, 1338.
16. Cella, D.; Peterman, A.; Hudgens, S.; Webster, K.; Socinski, M.A.; Measuring the side effects of taxane therapy in oncology: the functional assesment of cancer therapy-taxane (FACT-taxane). *Cancer* **2003**, *98*, 822, 831.
17. Kumar, B.; Kumar, R.; Skvortsova, I.I.; Kumar, V. Mechanisms of tubulin binding ligands to target cancer cells: updates on their therapeutic potential and clinical trials. *Curr. Cancer Drug Targets*, **2017**, *17*, 357,375.
18. Fanale, D.; Bronte, G.; Passiglia, F.; Calo, V.; Castiglia, M.; Di Piazza, F.; Barraco, N.; Cangemi, A.; Catarella, M.T.; Insalaco, L.; Listi, A.; Maragliano, R.; Massihnia, D.; Perez, A.; Toia, F.; Cicero, G.; Bazan, V. Stabilizing versus Destabilizing the Microtubules: a Double-edge Sword for an Effective Cancer Treatment Option? *Analytical Cellular Pathology*, Amsterdam, **2015**, pp. 690, 916.
19. Gastpar, R.; Goldbrunner, M.; Marko, D.; von Angerer, E. Methoxy-substituted 3-formyl-2-phenylindoles inhibit tubulin polymerization. *J. Med. Chem.* **1998**, *41*, 4965–4972.
20. Medarde, M.; Ramos, A.; Caballero, E.; Peláz-Lamamié de Clairac, R.; López, J.L.; García Grávalos, D.; San Feliciano, A. Synthesis and antineoplastic activity of combretastatin analogues: heterocombretastatins. *Eur. J. Med. Chem.* **1998**, *33*, 71–77.
21. Flynn, B.L.; Hamel, E.; Jung, M. K. One-pot synthesis of benzo-[b]furan and indole inhibitors of tubulin polymerization. *J. Med. Chem.* **2002**, *45*, 2670–2673.
22. De Martino, G.; La Regina, G.; Coluccia, A.; Edler, M. C.; Barbera, M. C.; Brancale, A.; Wilcox, E.; Hamel, E.; Artico, M.; Silvestri, R. Arylthioindoles, potent inhibitors of tubulin polymerization. *J. Med. Chem.* **2004**, *47*, 6120–6123.
23. La Regina, G.; Sarkar, T.; Bai, R.; Edler, M. C.; Saletti, R.; Coluccia, A.; Piscitelli, F.; Minelli, L.; Gatti, V.; Mazzocchi, C.; Palermo, V.; Mazzoni, C.; Falcone, C.; Scovassi, A. I.; Giansanti, V.; Campiglia, P.; Porta, A.; Maresca, B.; Hamel, E.; Brancale, A.; Novellino, E.; Silvestri, R. New arylthioindoles and related bioisosteres at the sulfur bridging group. 4. Synthesis, tubulin polymerization, cell growth inhibition, and molecular modeling studies. *J. Med. Chem.* **2009**, *52*, 7512–7527.
24. La Regina, G.; Bai, R.; Rensen, W. M.; Di Cesare, E.; Coluccia, A.; Piscitelli, F.; Famigliani, V.; Reggio, A.; Nalli, M.; Pelliccia, S.; Da Pozzo, E.; Costa, B.; Granata, I;

Porta, A.; Maresca, B.; Soriani, A.; Iannitto, M. L.; Santoni, A.; Li, J.; Cona, M. M.; Chen, F.; Ni, Y.; Brancale, A.; Dondio, G.; Vultaggio, S.; Varasi, M.; Mercurio, C.; Martini, C.; Hamel, E.; Lavia, P.; Novellino, E.; Silvestri, R. Towards highly potent cancer agents by modulating the C-2 group of the arylthioindole class of tubulin polymerization inhibitors. *J. Med. Chem.* **2013**, *56*, 123–149.

25. De Martino, G.; La Regina, G.; Coluccia, A.; Edler, M. C.; Barbera, M. C.; Brancale, A.; Wilcox, E.; Hamel, E.; Artico, M.; Silvestri, R. Arylthioindoles, potent inhibitors of tubulin polymerization. *J. Med. Chem.* **2004**, *47*, 6120–6123.

26. La Regina, G.; Bai, R.; Rensen, W.M.; Coluccia, A.; Piscitelli, F.; Gatti, V.; Bolognesi, A.; Lavecchia, A.; Granata, I.; Porta, A.; Maresca, B.; Soriani, A.; Iannitto, M.L.; Mariani, M.; Santoni, A.; Brancale, A.; Ferlini, C.; Dondio, G.; Varasi, M.; Mercurio, C.; Hamel, E.; Lavia, P.; Novellino, E.; Silvestri, R. Design and synthesis of 2-heterocyclyl-3-arylthio-1*H*-indoles as potent tubulin polymerization and cell growth inhibitors with improved metabolic stability. *J. Med. Chem.* **2011**, *54*, 8394, 8406.

27. Ravelli, R.B.; Gigant, B.; Curmi, P.A.; Jourdain, I.; Lachkar, S.; Sobel, A.; Knossow, M. Insight into tubulin regulation from a complex with colchicine and a stathmin-like domain. *Nature* **2004**, *428*, 198, 202.

28. Coluccia, A.; Sabbadin, D.; Brancale, A. Molecular modelling studies on arylthioindoles as potent inhibitors of tubulin polymerization. *Eur. J. Med. Chem.* **2011**, *46*, 3519, 3525.

29. Wang, Y.; Zhang, H.; Gigant, B.; Yu, Y.; Wu, Y.; Chen, X.; Lai, Q.; Yang, Z.; Chen, Q.; Yang, J. Structures of a diverse set of colchicine binding site inhibitors in complex with tubulin provide a rationale for drug discovery. *FEBS J.* **2016**, *283*, 102, 111.

30. La Regina, G.; Bai, R.; Coluccia, A.; Naccarato, V.; Famigliani, V.; Nalli, M.; Masci, D.; Verrico, A.; Rovella, P.; Mazzoccoli, C.; Da Pozzo, E.; Cavallini, C.; Martini, C.; Vultaggio, S.; Dondio, G.; Varasi, M.; Mercurio, C.; Hamel, E.; Lavia, P.; Silvestri, R. New 6- and 7-heterocyclyl-1*H*-indole derivatives as potent tubulin assembly and cancer cell growth inhibitors. *Eur J Med Chem.* **2018**, *152*, 283-297.

31. Simonart, T.; Andrei, G.; Parent, D.; Van Vooren, J.P.; De Clercq, E.; Snoeck, R., In vitro sensitivity of Kaposi's sarcoma cells to various chemotherapeutic agents including acyclic nucleoside phosphonates. *Antiviral Chem. Chemother.* **1999**, *10*, 129-134.

32. H.H. Ryu, S. Jung, T.Y. Jung, K.S. Moon, I.Y. Kim, Y.L. Jeong, S.G. Jin, J. Pei, M. Wen, W.Y. Jang, Role of metallothionein 1E in the migration and invasion of human glioma cell lines. *Int. J. Oncol.* **2012**, *41*, 1305-1313.

33. La Regina, G.; Bai, R.; Coluccia, A.; Famigliani, V.; Pelliccia, S.; Passacantilli, S.; Mazzoccoli, C.; Ruggieri, V.; Verrico, A.; Miele, A.; Monti, L.; Nalli, M.; Alfonsi, R.; Di Marcotullio, L.; Gulino, A.; Ricci, B.; Soriani, A.; Santoni, A.; Caraglia, M.; Porto, S.; Da Pozzo, E.; Martini, C.; Brancale, A.; Marinelli, L.; Novellino, E.; Vultaggio, S.; Varasi, M.; Mercurio, C.; Bigogno, C.; Dondio, G.; Hamel, E.; Lavia, P.; Silvestri, R. New indole tubulin assembly inhibitors cause stable arrest of mitotic progression, enhanced stimulation of natural killer cell cytotoxic activity, and repression of Hedgehog-dependent cancer. *J. Med. Chem.* **2015**, *58*, 5789-5807.

34. Billingsley, K.; Buchwald, S.L. Highly efficient monophosphine-based catalyst for the palladium-catalyzed suzuki–miyaura reaction of heteroaryl halides and heteroaryl boronic acids and esters. *J. Am. Chem. Soc.* **2007**, *129*, 11, 3358-3366.

35. Read, M. L.; Krapp, A.; Miranda, P.O.; Gundersen, L.L. Synthesis of complex fused polycyclic heterocycles utilizing IMDAF reactions of allylamino- or allyloxy-furyl(hetero)arenes. *Tetrahedron.* **2012**, *68*, 7, 1869-1885.

36. Wesemann, L.; Kleih, M.; Mayer, H.A. Aromatic aza-bicyclic compounds containing Cu, Ag, Au, Zn, Al for use in electroluminescent devices. *PCT Int. Appl.* **2013**, WO 2014067598 A1.

37. Tsuchimoto, T.; Iketani, Y.; Sekine, M. Zinc-catalyzed dehydrogenative N-silylation of indoles with hydrosilanes. *Chem. Eur J.* **2012**, *18*, 9500-9504.
38. Oberli, M.A.; Buchwald, S.L. A general method for Suzuki-Miyaura coupling reactions using lithium triisopropyl borates. *Org. Lett.* **2012**, *14*, 4606-4609.
39. Prota, A. E.; Danel, F.; Bachmann, F.; Bargsten, K.; Buey, R. M. Pohlmann, J.; Reinelt, S.; Lane, H.; Steinmetz, M. O. The novel microtubule-destabilizing drug BAL27862 binds to the colchicine site of tubulin with distinct effects on microtubule organization. *J. Mol. Biol.* **2014**, *426*, 1848-1860.
40. Gaspari, R.; Prota, A.E.; Bargsten, K.; Cavalli, A.; Steinmetz, M.O. Structural basis of cis- and trans-combretastatin binding to tubulin, *Inside Chem.* **2017**, *2*, 102-113.
41. Dorleans, B.; Gigant, R.B.G.; Ravelli, P.; Mailliet, V.; Mikol, M.; Knossow, Variations in the colchicine-binding domain provide insight into the structural switch of tubulin, *Proc. Natl. Acad. Sci. U.S.A.* **2009**, *106*, 13775-13779.
42. Schrodinger Release 2017-3, Maestro, Schrodinger, LLC, New York, NY, 2017.
43. Sastry, G.M.; Adzhigirey, M.; Day, T.; Annabhimoju, R.; Sherman, W. Protein and ligand preparation: parameters, protocols, and influence on virtual screening enrichments. *J. Comput. Aided Mol. Des.* **2013**, *27*, 221-234.
44. Korb, O.; Stutzle, T.; Exner, T.R. Plants: application of ant colony optimization to structure-based drug design, in: M. Dorigo, L.M. Gambardella, M. Birattari, A. Martinoli, R. Poli, T. Stutzle (Eds.), *Ant Colony Optimization and Swarm Intelligence. Proceedings of the 5th International Workshop, Ants*, Springer, Berlin, 2006, pp. 247-258. *Lecture Notes in Computer Science, Series 4150*.
45. Morris, G.M.; Huey, R.; Lindstrom, W.; Sanner, M.F.; Belew, R.K.; Goodsell, D.S.; Olson, A.J. Autodock4 and AutoDockTools4: automated docking with selective receptor flexibility, *J. Comput. Chem.* **2009**, *16*, 2785-2791.
46. The Pymol Molecular Graphics System, Version 2.0 Schrodinger, (LLC).
47. Hamel, E. Evaluation of antimitotic agents by quantitative comparisons of their effects on the polymerization of purified tubulin, *Cell Biochem. Biophys.* 2003, *38*, 1-21.
48. Verdier-Pinard, P.; Lai, J.-Y.; Yoo, H.-D.; Yu, J.; Marquez, B.; Nagle, D. G.; Nambu, M.; White, J. D.; Falck, J. R.; Gerwick, W. H.; Day, B. W.; Hamel, E. Structure-activity analysis of the interaction of curacin A, the potent colchicine site antimitotic agent, with tubulin and effects of analogs on the growth of MCF-7 breast cancer cells. *Mol. Pharmacol.* 1998, *35*, 62-76.
49. Ruan, S.; Okcu, M.F.; Pong, R.C.; Andreeff, M.; Levin, V.; Hsieh, J. T.; Zhang, W. Attenuation of WAF1/Cip1 expression by an antisense adenovirus expression vector sensitizes glioblastoma cells to apoptosis induced by chemotherapeutic agents 1,3-bis(2-chloroethyl)-1-nitrosourea and cisplatin. *Clin. Canc. Res.* **1999**, *5*, 197-202.

3. New Pyrrole Derivatives Inhibitors of Chronic Myeloid Leukemia Cell Growth

3.1 Introduction

3.1.1 Chronic Myeloid Leukemia (CML)

Approximately 1.6 percent of men and women will be diagnosed with leukemia at some point during their lifetime.¹ Chronic myeloid leukemia (CML) is a myeloproliferative disease characterised by the reciprocal translocation $t(9;22)(q34;q11)$ (named Philadelphia chromosome, Ph) encoding for the hybrid protein BCR/ABL, a tyrosine kinase with leukemogenic potential² (Figure 3.1).

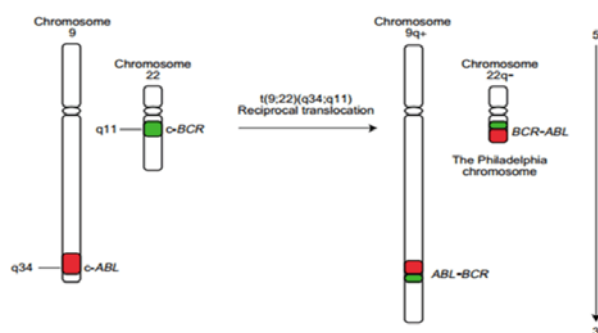


Figure 3.1 The $t(9;22)(q34;q11)$ translocation.

ABL1 encodes a non-receptor tyrosine kinase that phosphorylates substrate proteins via its SH1 domain, and affects crucial cellular activities, such as increased proliferation, loss of stromal adhesion, and resistance to apoptosis. Through the loss of upstream control elements in the creation of the fusion gene, Bcr-Abl1 is capable of autophosphorylation and uncontrolled signalling to a large number of downstream proteins, activating these effector pathways. A BCR-ABL1 fusion gene is present in all cases of chronic myeloid leukemia and results in two critical events in the disease. First, the gene provides a unique biomarker for diagnosis and monitoring response to treatment, and second, the fusion tyrosine kinase is susceptible to drug targeting.

3.1.2 Characteristics and Diagnosis of CML

Chronic myeloid leukemia is characterized by a biphasic or triphasic clinical course in which a terminal blastic phase follows an initial chronic phase and an intermediate accelerated phase of variable duration. In most patients (85%), the disease is diagnosed in the chronic phase. Accelerated and blastic phase presentations occur in only 5% to 10% of patients. Up to half of the patients in recent studies were asymptomatic, and the disease was diagnosed by routine blood tests³. Among symptomatic patients, instead, fatigue, weight loss, abdominal fullness, bleeding, and sweats are common; also purpura and splenomegaly are frequent findings on physical examination, while leukocytosis, anemia, and thrombocytosis are typical laboratory features at presentation.⁴ The blastic phase is usually defined by the presence of extramedullary blastic infiltrates or 30% or more leukemic blasts in peripheral blood or marrow.⁵⁻⁷ In one third of patients, blasts have a lymphoid structure and express lymphoid markers, such as terminal deoxynucleotidyl transferase, CD19, CD20, or CD10 (common acute lymphoblastic leukemia antigen). The diagnostic work-up for chronic myeloid leukemia consists of a complete blood count, including a differential and a platelet count; marrow aspiration, with measurement of the percentage of blasts and the percentage of basophils; marrow biopsy; and cytogenetic studies for Ph and markers of karyotypic evolution.² Conventional cytogenetics occasionally fails for technical reasons in which case the BCR-ABL1 fusion gene can be identified by fluorescent-in-situ-hybridisation (FISH) using specific chromosome

markers. In a small proportion of cases, the BCR-ABL1 fusion gene can be present without t(9;22) being detectable by conventional cytogenetics: this situation can be identified by FISH, reverse transcriptase PCR (RT-PCR), or both.

This extensive investigation not only confirms the diagnosis, but also allows disease staging and prognostic scoring.⁸

3.1.3 Current Drug Treatment

In vitro studies and studies in animal models have established that BCR-ABL alone is sufficient to cause CML, and mutational analysis has established that the tyrosine kinase activity of the protein is required for its oncogenic activity.⁹⁻¹² Tyrosine kinases (TKs), in fact, are enzymes that catalyze the transfer of phosphate from ATP to tyrosine residues on a protein substrate. Through this phosphorylation reaction and via modulation of substrate activity, TKs act as crucial mediators of cellular signal transduction; they regulate diverse cellular processes such as cell-cycle progression, metabolism, transcription and apoptosis. Dysregulation of tyrosine kinase signaling, through either mutation or amplification, can lead to malignant transformation, proliferation of cells and the promotion of tumor angiogenesis.¹³ For these reasons, inhibitors of the BCR-ABL tyrosine kinase should be an effective and selective treatment for CML.

Tyrosine Kinase Inhibitors (TKIs) act through different mechanisms such as: direct competition for ATP binding to the tyrosine kinase (genistein, lavendustin, imatinib, erlotinib, gefitinib; allosteric inhibition of the tyrosine kinase (lavendustin A); inhibition of ligand binding to receptor tyrosine kinases (cetuximab); inhibition of tyrosine kinase interaction with other proteins (e.g., UCS15A, p60-v-Src inhibitor peptide) or destabilization of the tyrosine kinase (e.g., herbimycin A and radicicol).¹⁴

At present, imatinib mesylate (IM, Gleevec), an inhibitor of both the BCR/ ABL and c-ABL tyrosine kinases, represents the treatment of choice for CML, inducing stable clinical remissions in more than 80% of newly diagnosed patients; it acts by blocking the ATP binding pocket of Abl1 kinase domain, inhibiting phosphorylation, and resulting in cell death.¹⁵ (Figure 3.2).

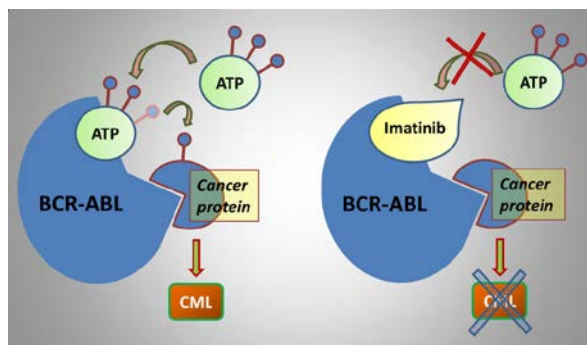


Figure 3.2 Mechanism of action of Imatinib.

However, point mutations in the catalytic domain of the BCR/ABL oncoprotein^{16,17} or bcr/abl gene amplification¹⁸ can select IM-resistant clones in CML patients leading to a fatal blast crisis phase. Among the reported BCR/ABL point mutations, T315I (resulting in substitution of a threonine for an isoleucine residue at the “gatekeeper” position 315) is the most interesting one because it also provides resistance to clinically useful second-generation tyrosine kinase inhibitors (TKIs) such as nilotinib, dasatinib, and bosutinib.¹⁹ Therefore, there is a pressing need for devising novel combination regimens aimed at overcoming TKI-resistance in CML cells.

3.2 Objective of the Study

Since evidence has accumulated correlating inhibition of tubulin polymerization and leukemic cell proliferation,²⁰⁻²⁴ in continuing our studies on tubulin targeting agents, we designed and synthesized new 3-aroyl 1,4-diarylpyrrole (ARDAP) derivatives. Starting from previously reported aroylindoles (ARIs, **3.1**)²⁵ Prof. Silvestri and co-workers developed a class of 3-aroyl-1-arylpyrroles (ARAPs, **3.2**) via benzocracking approach by shifting the indole benzene moiety to position 1 of the pyrrole ring (Figure 3.3).²⁶ ARAPs proved to be potent inhibitors of both tubulin assembly and cancer cells growth, by binding the colchicine binding site.

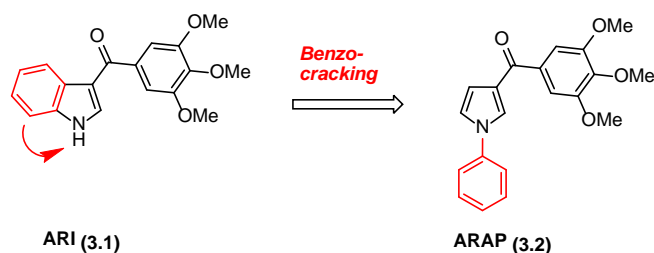


Figure 3.3 Design of ARAP through benzocacking approach

Pursuing our studied on tubulin targeting agents, we designed and syntesized 3-aroyl-1,4-diarylpyrroles (ARDAPs, **3.3-3.16**) as potential anticancer agents bearing different substituents at the 1- or 4-phenyl ring (Figure 3.4, Table 3.1).²⁷

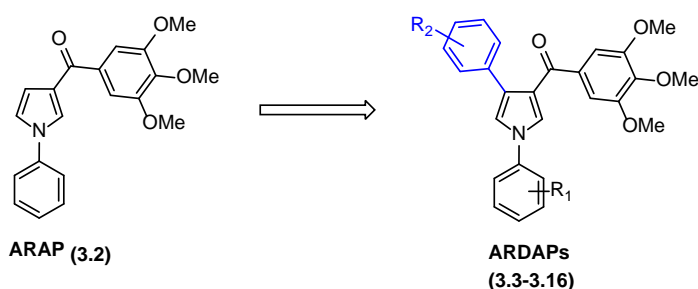
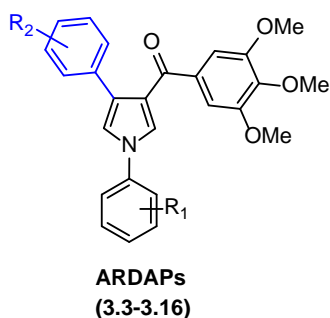


Figure 3.4 Design of new ARDAPs derivatives

Table 3.1 Structures of ARDAPs **3.3-3.16**



Compd	R ₁	R ₂
3.4	H	2-F
3.5	H	3-Me
3.6	H	3-F
3.7	H	3-NH ₂
3.8	H	4-Me
3.9	H	4-F
3.10	H	4-NH ₂

3.11	2-F	H
3.12	3-Me	H
3.13	3-F	H
3.14	3-NH ₂	H
3.15	4-Me	H
3.16	4-F	H

3.3 Molecular Modeling

Molecular docking studies revealed that the proposed binding mode of selected representative examples of these ARDAP derivatives, such as **3.3**, was significantly different from those of its parent compounds ATI **3.1**²⁵ and ARAP **3.2**.⁶ However, the three compounds all shared the key interactions of the trimethoxyphenyl moiety with the β Cys241 of tubulin (Figure 3.5).

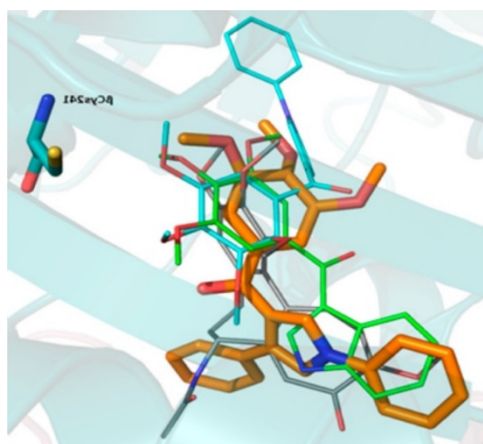


Figure 3.5 Proposed binding modes for **3.3** (orange stick), **3.1** (green), **3.2** (cyan), and colchicine (gray) in the colchicine site.

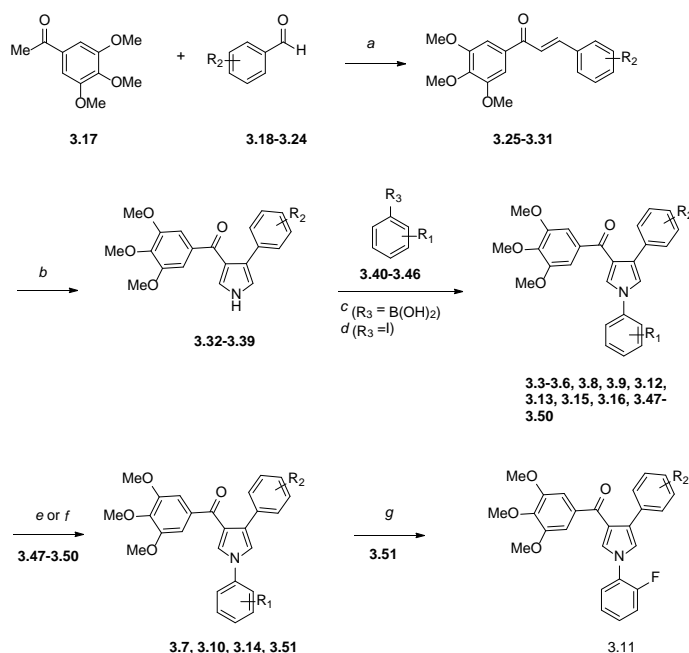
Analyzing the binding mode of ARDAP **3.3**, it is clear that its *N*-phenyl pyrrole group was placed in the same position as the indole ring of **3.1**, while the other ARDAP phenyl ring occupied the same area as colchicine ring B.²⁸ Starting from these observations we conducted SAR investigations on this new scaffold in search of novel tubulin binding agents. As a Ph.D. student of Prof. R. Silvestri's research group, I participated in the synthesis and characterization of a group of new ARDAP derivatives bearing phenyl or substituted-phenyl groups at positions 1 and 4 of the pyrrole nucleus (**3.3–3.16**, Table 3.1).

In this study, we introduced on the phenyl rings substituents that were associated with the best biological activity in the ARAP series previously developed by our research group.⁶

3.4 Chemistry

The first step of the preparation of new ARDAP compounds **3.3–3.16** was the synthesis of chalcones **3.25–3.31** which were subsequently converted to the corresponding pyrrole derivatives **3.32**²⁶ or **3.33–3.39** by reacting with *p*-toluenesulfonylmethyl isocyanide (TosMIC). ARDAP compounds **3.3–3.6**, **3.8**, **3.9**, **3.12**, **3.13**, **3.15**, and **3.16** were obtained by reacting **3.32**²⁶ or **3.33–3.39** with the appropriate boronic acid **3.40**, **3.42**, **3.43**, **3.45** or **3.46**. ARDAP derivative **3.7** was finally obtained by reduction of **3.47** with Pd/C–H₂ (1 atm). Nitro derivatives **3.48–3.50** were treated with Tin(II) chloride to furnish respectively ARDAP compounds **3.10**, **3.14** and **3.51**. Compound **3.51** was converted to ARDAP **3.11** by reaction with sodium nitrite in tetrafluoroboric acid (Scheme 3.1; see Experimental Section, Chemistry 3.7.1).

Scheme 3.1 Synthesis of Compounds 3.3-3.16^a

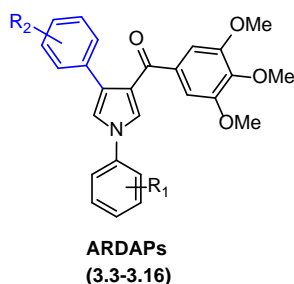


^aReagents and conditions: a) NaOH, EtOH 99%; rt, 24h, 59-89%; b) NaH, Et₂O, TOSMIC, DMSO/Et₂O; rt, 4h, Ar, 21-84%; c) (13.3-3.5, 3.8, 3.9, 3.12, 3.13, 3.15, 3.16, 3.47 and 3.48) boronic acid 3.40, 3.42, 3.43, 3.45 or 3.46 ; Copper(II) acetate, Triethylamine, 1,2-dichloroethane, reflux, Ar, 4-72%; d) (3.49 and 3.50) 3.41 or 3.44, Copper(I) bromide, 8-quinolinol *N*-oxide, cesium carbonate, DMSO, 65 °C, 6 h, Ar, 9 and 34%; e) (3.7) H₂, Pd/C, MeOH, 1 atm, rt, 2 h, 82%; f) (3.10, 3.14 and 3.51) tin(II) chloride dehydrate, methyl acetate, reflux, 6 h, 47-60% ;g) NaNO₂, HBF₄, 0 °C, 1 h, 13%.

3.5 Results and Discussion

Pyrrole derivatives **3.3-3.16** have been synthesized to investigate the effects of the introduction of phenyl or substituted-phenyl groups at positions 1 and 4 of the pyrrole nucleus on the inhibition of tubulin polymerization, binding of colchicine to tubulin and growth of MCF-7 cancer cells (Table 3.2). Besides the ability to inhibit tubulin polymerization, for which they were originally designed, we found that ARDAP compounds augment Imatinib-mediated apoptotic effects in BCR/ABL⁺ CML cells obtained from patients in blast crisis.

Table 3.2 Inhibition of Tubulin Polymerization, Growth of MCF-7 Human Breast Carcinoma Cells, and Colchicine Binding by ARDAPs **3.3-3.16** and Reference **3.2**, Colchicine, and CSA4^a



Compd	R ₁	R ₂	tubulin ^b IC ₅₀ ± SD (μM)	MCF-7 ^c IC ₅₀ ± SD (nM)	inh. colch. binding ^d (% ± SD)
3.4	H	2-F	0.58 ± 0.02	30 ± 7	72 ± 4
3.5	H	3-Me	1.6 ± 0.04	450 ± 70	5.7 ± 5
3.6	H	3-F	0.63 ± 0.004	57 ± 2	53 ± 0.7
3.7	H	3-NH ₂	0.39 ± 0.005	28 ± 3	57 ± 0.7
3.8	H	4-Me	2.2 ± 0.1	280 ± 40	24 ± 0.07
3.9	H	4-F	0.76 ± 0.1	78 ± 4	47 ± 4
3.10	H	4-NH ₂	1.2 ± 0.1	9.0 ± 2	81 ± 2
3.11	2-F	H	2.0 ± 0.1	85 ± 7	29 ± 5
3.12	3-Me	H	1.7 ± 0.09	120 ± 0	82 ± 2
3.13	3-F	H	2.9 ± 0.3	350 ± 90	42 ± 0.5
3.14	3-NH ₂	H	1.1 ± 0.08	74 ± 6	82 ± 4
3.15	4-Me	H	0.88 ± 0.03	30 ± 0	79 ± 0.1
3.16	4-F	H	1.3 ± 0.1	15 ± 5	62 ± 2
3.2 ^e			1.5 ± 0.2	700 ± 200	80 ± 2
Colch			3.2 ± 0.4	5 ± 1	
CSA4			1.0 ± 0.1 ^{f,g}	13 ± 3	98 ± 0.6
3.4	H	2-F	0.58 ± 0.02	30 ± 7	72 ± 4
3.5	H	3-Me	1.6 ± 0.04	450 ± 70	5.7 ± 5
3.6	H	3-F	0.63 ± 0.004	57 ± 2	53 ± 0.7

^aExperiments were performed in triplicate. ^bInhibition of tubulin polymerization. Tubulin was at 10 μM in the assembly assay. ^cInhibition of growth of MCF-7 human breast carcinoma cells. ^dInhibition of [³H]colchicine binding: tubulin, [³H]colchicine, inhibitor at 1:5:5 μM. ^eReference 26. ^fCSA4 yielded an IC₅₀ of 0.65 μM in an assay contemporaneous with the evaluations of ARDAPs 3.5 and 3.7, in which a different tubulin preparation was used. ^gCSA4 yielded an IC₅₀ of 0.79 μM in an assay contemporaneous with the evaluations of 3.4, 3.6, and 3.9, in which a different tubulin preparation was used.

3.5.1 Inhibition of Tubulin Polymerization

In general all newly synthesized compounds proved to be potent inhibitors of tubulin polymerization (Table 3.2). In detail, five new derivatives (**3.4**, **3.6**, **3.7**, **3.9** and **3-15**) were able to inhibit tubulin polymerization with IC₅₀ values at micro- or submicromolar concentrations and seven compounds (**3.3**, **3.5**, **3.10-3.12**, **3.14** and **3.16**) were in the 1.0-2.0 μM range, as compared with colchicine (IC₅₀ = 3.2 μM) and CSA4 (IC₅₀ = 1.0 μM).

In general, the introduction of phenyl or substituted-phenyl groups at positions 1 and 4 of the pyrrole nucleus furnished potent tubulin assembly inhibitors with compound **3.7** (IC₅₀ = 0.39 μM), characterized by a phenyl ring at position 1 and a 3-aminophenyl ring at position 4 of the pyrrole nucleus, being the most potent inhibitor of tubulin polymerization among the newly synthesized compounds.

3.5.2 Inhibition of MCF-7 Breast Cancer Cell Growth

Most of the newly synthesized pyrrole derivatives were able to inhibit the growth of human MCF-7 nonmetastatic breast cancer epithelial cells at nanomolar concentrations (Table 3.2). In particular ARDAPs **3.4**, **3.7**, **3.10**, **3.15**, and **3.16** exhibited IC₅₀ values ≤ 30 nM. Compound **3.10**, bearing a *p*-aminophenyl ring at position 4 of the pyrrole nucleus and a non substituted phenyl group at positions 1 was the most potent MCF-7 cell growth inhibitor within the series with an IC₅₀ of 9 nM.

3.5.3 Inhibition of the Binding of [³H]Colchicine to Tubulin

The majority of the newly synthesized compounds showed good activity as inhibitors of the binding of [³H]colchicine to tubulin (Table 3.2). Seven compounds **3.3**, **3.4**, **3.10**, **3.12** and **3.14-3.16**, infact, yielded > 60% inhibition of the binding reaction. The data

presented in Table 3.2 reveal that inhibition of the growth of MCF7 cancer cells and inhibition of tubulin polymerization are, in most cases, in good agreement with inhibition of colchicine binding, as demonstrated by comparing the MCFT cells growth inhibitory concentrations and the tubulin assembly inhibitory activity with the percent inhibition of colchicine binding, which provide an indirect measure of the affinity of the compounds for the colchicine site. The best tubulin assembly inhibitor **3.7** ($IC_{50} = 0.39 \mu\text{M}$) inhibited the growth of MCF-7 cells with an IC_{50} of 28 nM and colchicine binding by 57%. The best MCF-7 cell growth inhibitor **3.10** ($IC_{50} = 9 \text{ nM}$) inhibited tubulin polymerization with an IC_{50} of 1.2 μM and colchicine binding by 81%.

3.5.4 Cell Growth Inhibition

Representative members of the ARDAP series were found to uniformly inhibit the growth of a large panel of cancer cells. In particular compounds **3.7** and **3.16**, were found to strongly inhibit the growth of the ovarian carcinoma cell lines OVCAR-8 and its cognate P-glycoprotein (Pgp) overexpressing line NCI/ADR-RES. In detail compound **3.7** yielded IC_{50} values of 190 and 110 nM, and compound **3.16** of 180 and 110 nM, respectively. With the exception of CSA-4, the reference compounds colchicine, vinorelbine, vinblastine, and paclitaxel were quite weak inhibitors of the MDR cell line (Table 3.3).

Table 3.3 Inhibition of Growth of the OVCAR-8 and NCI/ADR-RES Cell Line Pair by Compounds **3.7** and **3.16**, and Reference Compounds Colch., CSA-4, VRB, VBL and PTX^a

Compd	$IC_{50} \pm SD$ (nM)	
	OVCAR-8	NCI/ADR-RES
3.7	190 \pm 30	110 \pm 10
3.16	180 \pm 30	110 \pm 20
Colch.	30 \pm 1	420 \pm 100
CSA-4	4.0 \pm 1	3.0 \pm 0.5
VRB	300 \pm 0	5000 \pm 1000
VBL	15 \pm 7	200 \pm 0
PTX	3.0 \pm 2	11000 \pm 2000

^aInhibition of growth of the indicated cell lines. Colch., colchicine; CSA-4, combretastatin A4; VRB, vinorelbine; VBL, vinblastine; PTX, paclitaxel.

Compounds **3.7**, **3.10**, and **3.16** were also evaluated as growth inhibitors of the KYSE150 (esophageal squamous cell), THP-1 (acute monocytic leukemia), NB4 (acute promyelocytic leukemia), HT-29 (human colorectal adenocarcinoma), HCT116 (colon cancer), and HepG2 (liver hepatocellular) cell lines (Table 3.4); the most potent compound was derivative **1.10**, showing IC_{50} values ranging from 20 nM (KYSE150 and HCT116) to 46 nM (HepG2).

Table 3.4 Growth Inhibition of the KYSE150, THP-1, NB4, HT29, HCT116 and HepG2 Cell Lines by Compounds **3.7**, **3.10** and **3.16**^a

Compd	$IC_{50} \pm SD$ (nM)					
	KYSE150 ^b	THP-1 ^b	NB4 ^c	HT29 ^c	HCT116 ^c	HepG2 ^c
3.7	80 \pm 31	46 \pm 16	96 \pm 50	63 \pm 1.8	56 \pm 1.5	70 \pm 1
3.10	20 \pm 5	22 \pm 8	33 \pm 5	nd ^d	20 \pm 1.7	46 \pm 1.2
3.16	73 \pm 28	50 \pm 14	68 \pm 38	116 \pm 0.3	120 \pm 1.3	130 \pm 1.4
CSA4	2.0 \pm 0.2	3.1 \pm 0.02	1.2 \pm 0.2	31 \pm 0.7	121 \pm 1.2	120 \pm 1.4
PTX	2.0 \pm 0.2	1.4 \pm 0.2	1.4 \pm 0.2	8.0 \pm 1.5	4.0 \pm 0.4	2660 \pm 1.5

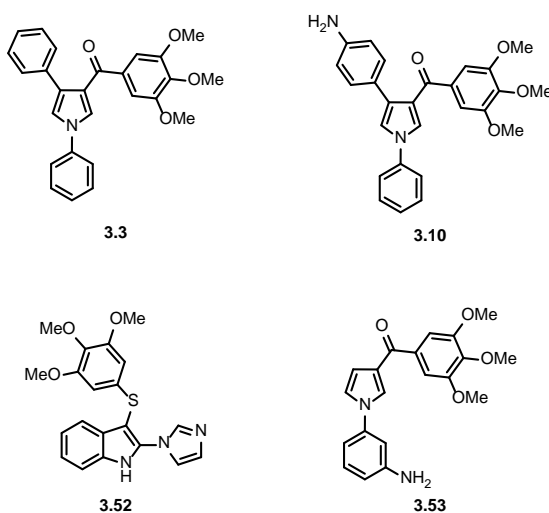
^aInhibition of growth of the indicated cell lines. Experiments were performed in triplicate. ^bIncubation time 96 h. ^cIncubation time 48 h. ^dNot determined.

In addition the most potent ARDAP derivative **1.10** was investigated for efficacy with BCR/ABL-expressing cells established in vitro from CML patients in blast crisis (KU812 and LAMA 84) compared with previously reported colchicine site binders 2(1*H*-imidazol-1-yl)-3-((3,4,5-trimethoxyphenyl)thio)-1*H*-indole²⁹ (**3.52**) and (1-(3-aminophenyl)-1*H*-pyrrol-3-yl)(3,4,5-trimethoxyphenyl) methanone (**3.53**).²⁶

Compounds **3.52** and **3.53** were able to inhibit CML cell growth (IC₅₀) at concentrations ranging from 28 to 35 nM, while ARDAP derivative **1.10** appeared to be the most potent compound showing IC₅₀ of 12 and 14 nM, respectively (Table 3.5, and Figure 3.6).

These results demonstrate that high cytotoxicity can occur with compounds belonging to this new class of compounds.

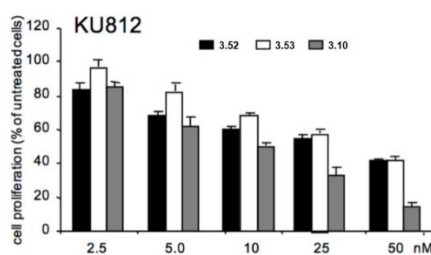
Table 3.5 Inhibition of Growth of the KU812 and LAM84 CML Cell Lines by Compounds **3.3**, **3.10**, **3.52** and **3.53**.



Compd	IC ₅₀ ± SD (nM) ^a	
	OVCAR-8	NCI/ADR-RES
3.3	26 ± 8	22 ± 5
3.10	12 ± 6	14 ± 5
3.52	35 ± 11	32 ± 8
3.53	32 ± 10	28 ± 16

^aInhibition of growth of the indicated cell lines.

A



B

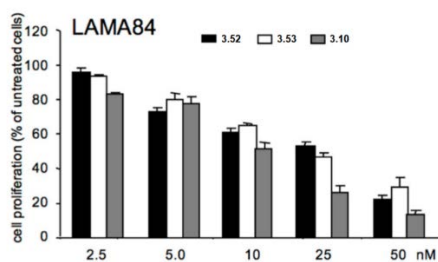


Figure 3.6 Growth inhibition of CML KU812 (A) and LAMA84 (B) cells by compounds **3.10**, **3.52** and **3.53**.

A dose-dependent inhibition of proliferation was observed for KU812 and LAMA84 cells exposed to increasing doses of **3.10** for 48 h, as assessed by MTT assays. Derivative **3.10** was able to inhibit CML cell growth by 50% at 12 nM and, most importantly, at such nanomolar concentrations, it minimally affected normal blood cells. Interestingly, peripheral blood mononuclear cells (PBMCs) isolated from healthy donors remained substantially insensitive to **3.10** up to 1 μ M (Figure 3.7).

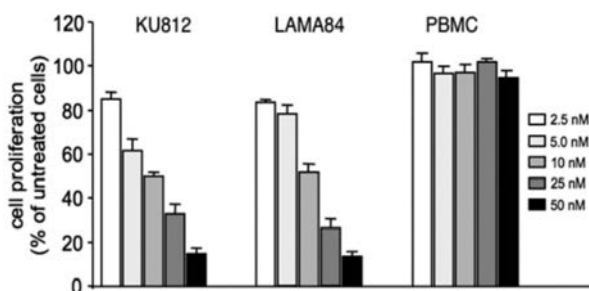


Figure 3.7 Compound **3.10** decreased CML cell proliferation at nanomolar concentrations without affecting normal PBMCs. Experiments were performed in triplicate.

3.5.5 Cytotoxicity on CML cells expressing the IM-sensitive KBM5-WT or its IM-resistant KBM5-T315I mutation

Based on the previous illustrated results, compound **3.10** was investigated for efficacy with hematopoietic cells ectopically expressing the IM-sensitive KBM5-WT or IM-resistant KBM5-T315I mutation (Figure 3.8).

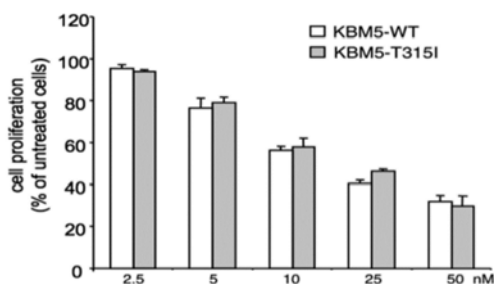


Figure 3.8 Cytotoxicity of **3.10** on CML cells ectopically expressing the IM-sensitive wild type KBM5-WT or its IM-resistant KBM5-T315I mutation. Experiments were performed in triplicate.

Compound **3.10** resulted able to dose-dependently block the growth of KBM5 and KBM5-T315I cells with similar average IC₅₀ values of 15 and 18 nM, respectively, as assessed by MTT assays. The antileukemic activity of **3.10** in BCR/ABL⁺ cells expressing the T315I gatekeeper mutation suggested that the drug may be a promising agent to overcome broad TKI-resistance in relapsed/refractory CML patients.

3.5.6 Induction of G2/M phase arrest and apoptosis via a mitochondria-dependent pathway

The CML cell inhibition went through G2/M phase arrest and apoptosis via a mitochondria-dependent pathway. Infact, KU812 cells exposed to 100 nM **3.10** for 8 h showed a rapid collapse of mitochondrial transmembrane potential in to a greater extent as compared with those exposed to IM (100 nM for 8 h), as a consequence of the opening of permeability transition pores that accumulate a fluorescent dye from its red-aggregated to its green-monomeric forms (Figure 3.9 A, left panels).

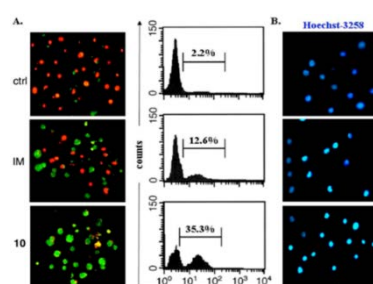


Figure 3.9 Compound **3.10** promotes CML cell death via mitochondria dependent pathways; comparison with IM. Experiments were performed in triplicate.

In detail, the majority (97.8%) of solvent-treated KU812 cells showed a bright red fluorescence, indicative of intact mitochondria, while 35.3% of **3.10**-treated KU812 cells at 100 nM for 8 h exhibited a marked green fluorescence indicative of damaged mitochondria. Hoechst-3258 staining helped to study the nuclear morphology of **3.10**-treated KU812 cells (Figure 3.9 B, right panels); a blue-to-cyan fluorescence was detected in most of the nuclei of **3.10**-treated vs DMSO-control cells indicating their apoptotic morphology. All these data indicated that **3.10** significantly decreased CML proliferation by inducing G2/M phase arrest and apoptosis via a mitochondria-dependent pathway.

3.5.7 Strengthening of IM-mediated CML cell death by ARDAP 3.10

LAMA84 cells were incubated for 48 h with increasing doses of IM (range 1– 1000 nM) in the absence or presence of compound (100 nM) and then analyzed by MTT assay in order to check the ability of **3.10** to augment the cytotoxic effects of IM in human CML cells (Figure 3.10 A).

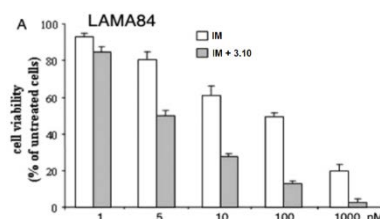


Figure 3.10 Compound **3.10** potentiates IM-mediated cell death of CML cells, including those expressing the T315I mutation. Experiments were performed in triplicate.

IM and ARDAP derivative **3.10** in combination improved the effectiveness of IM alone in reducing CML cell growth, leading to a 10-fold reduction of the IC₅₀ value for IM from 100 nM to less than 10 nM. It had been reported previously that the average IC₅₀ value for IM in LAMA84 cells overexpressing BCR-ABL is 100 nM,¹⁶ and this was also observed here. In addition, the IM-resistant KBM5-T315I cells showed the same susceptibility to **3.10**-induced cell death as well as IM-sensitive KBM5-WT cells, reaching, respectively, 58.2 ± 4.5% and 62.6 ± 5.4% of annexin V⁺ cells at 48 h of drug exposure as compared to 2.2 ± 1.8% for control cells. Moreover, using annexin V-FITC staining to detect early cell death at 24 h, it was evident that 100 nM **3.10** significantly augmented the pro-apoptogenic effects of IM (Figure 3.10 B).

3.5.8 Morphological changes, altered tubulin immunostaining and mitotic arrest of KU812 cells by ARDAP 3.10

Assessed that ARDAP compound **3.10** interferes with tubulin function, phase contrast microscopy and flow cytometry were used to study the cell morphological features and the cell cycle distribution, respectively (Figure 3.11).

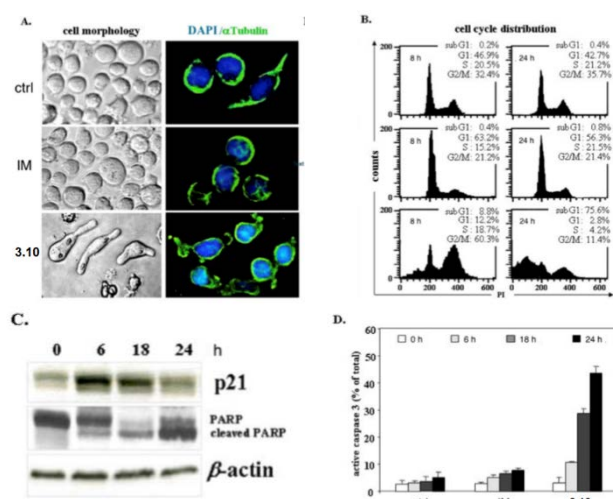


Figure 3.11 Compound 3.10 induces morphological changes, altered tubulin immunostaining and mitotic arrest of KU812 cells in a time-dependent manner.

KU812 cells were so treated with 100 nM **3.10** and then compared to cell cultures incubated with DMSO as vehicle control (ctrl); the result was an elongated shape and multiple centrosomes typical of giant cells with failed cytokinesis and altered tubulin immunostaining (Figure 3.11, Panel A).

These characteristics, typically resembling those referred to as mitotic catastrophe, occurred at relatively early (2 to 8 h) exposure intervals correlating with a net mitotic arrest of **3.10**-treated cells accumulated in the G2/M cell cycle phase (60.3 ± 3.4% of treated vs 35.7 ± 2.8% of control cells), whereas apoptotic cells in the subG1 phase did not exceed 10%. After a 24 h treatment, cell mitotic abnormalities disappeared in keeping with a reduced G2/M fraction reaching 11.4 ± 8.3%, while a massive apoptosis induction (peaking at 75.6 ± 11.4% of 10-treated cells vs 0.4 ± 0.8% of control cells) indicated a greater susceptibility to death following the initial mitotic arrest²⁷ (Figure 3.11, Panel B). Imatinib alone at 100 nM, was ineffective in altering CML KU812 cell shape or viability, causing only a weak antiproliferative effect at 24 h (56.3 ± 3.4% in IM-treated vs 42.7 ± 6.2% in DMSO-treated cells arrested in the G1 phase of the cell cycle).

In Figure 3.11 C, it is evident that the levels of the growth inhibitory protein p21Cip/WAF1 were rapidly up-regulated after 6 h of **3.10** treatment and decreased after 24 h when the cleavage of the pro-apoptotic protein PARP indicated prominent activation; moreover treatment with **3.10** also increased caspase-3 activation in a time-dependent manner, as assessed by flow cytometry (Figure 3.11 D).

3.6 Conclusions

In continuing our studies on tubulin targeting agents, we designed and synthesized 16 new 3-aryl 1,4-diarylpyrrole (ARDAP) derivatives starting from previously reported arylindoles via benzoclocking approach by shifting the indole benzene moiety to position 1 of the pyrrole ring. Additional phenyl or substituted-phenyl groups were added at positions 4 of the pyrrole nucleus in order to improve their biological activity as inhibitors of tubulin polymerization, binding of colchicine to tubulin and growth of MCF-7 cancer cells. As inhibitors of tubulin polymerization, five new derivatives (**3.4**, **3.6**, **3.7**, **3.9** and **3-15**) were able to inhibit tubulin polymerization with IC_{50} values at micro- or submicromolar concentrations and seven compounds (**3.3**, **3.5**, **3.10-3.12**, **3.14** and **3.16**) were in the 1.0-2.0 μ M range, as compared with colchicine ($IC_{50} = 3.2 \mu$ M) and CSA4 ($IC_{50} = 1.0 \mu$ M). Most of the newly synthesized pyrrole derivatives were able to inhibit the growth of human MCF-7 nonmetastatic breast cancer epithelial cells at nanomolar concentrations; compound **3.10** was the most potent MCF-7 cell growth inhibitor within the series with an IC_{50} of 9 nM. The majority of the newly synthesized compounds showed good activity as inhibitors of the binding of [3 H]colchicine to tubulin; seven of them, in fact, yielded > 60% inhibition of the binding reaction; it was evident that inhibition of the growth of MCF7 cancer cells and inhibition of tubulin polymerization are, in most cases, in good agreement with inhibition of colchicine binding. The best tubulin assembly inhibitor **3.7** ($IC_{50} = 0.39 \mu$ M) inhibited the growth of MCF-7 cells with an IC_{50} of 28 nM and colchicine binding by 57%. The best MCF-7 cell growth inhibitor **3.10** ($IC_{50} = 9$ nM) inhibited tubulin polymerization with an IC_{50} of 1.2 μ M and colchicine binding by 81%. The most potent MCF-7 cell growth inhibitor **3.10** was also able to inhibit BCR/ABL-expressing KU812 and LAMA84 cells from CML patients in blast crisis and hematopoietic cells ectopically expressing the IM-sensitive KBM5-WT or its IM-resistant KBM5-T315I mutation. The CML cell inhibition went through G2/M phase arrest and apoptosis via a mitochondria-dependent pathway; in addition compound **3.10** augmented the cytotoxic effects of IM leading to a 10-fold decrease in the IC_{50} value for IM as inhibitor of CML cell growth. All together, our results indicate that compound **3.10** represents a robust lead compound to develop tubulin inhibitors with potential as novel treatments for CML.

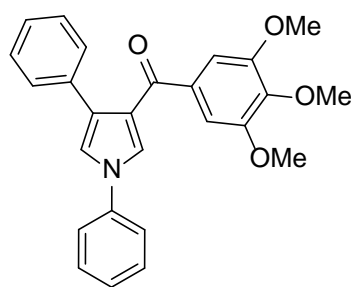
3.7 Experimental Section

3.7.1 Chemistry

All reagents and solvents were handled according to the material safety data sheets of the supplier and were used as purchased without further purification. 3,4,5-Trimethoxyacetophenone (**3.17**), 2-fluorobenzaldehyde (**3.18**), 3-methylbenzaldehyde (**3.19**), 3-fluorobenzaldehyde (**3.20**), 3-nitrobenzaldehyde (**3.21**), 4-methylbenzaldehyde (**3.22**), 4-fluorobenzaldehyde (**3.23**), 4-nitrobenzaldehyde (**3.24**), phenylboronic acid (**3.40**), 1-iodo-2-nitrobenzene (**3.41**), *m*-tolylboronic acid (**3.42**), (3-fluorophenyl)boronic acid (**3.43**), 1-iodo-3-nitrobenzene (**3.44**), *p*-tolylboronic acid (**3.45**), and (4-fluorophenyl) boronic acid (**3.46**) were commercially available. Organic solutions were dried over anhydrous sodium sulfate. Evaporation of the solvents was carried out on a Büchi Rotavapor R-210 equipped with a Büchi V-850 vacuum controller and a Büchi V-700 vacuum pump. Column chromatography was performed on columns packed with silica

gel from Macherey-Nagel (70–230 mesh). Silica gel thin layer chromatography (TLC) cards from Macherey-Nagel (silica gel precoated aluminum cards with fluorescent indicator visualizable at 254 nm) were used for TLC. Developed plates were visualized with a Spectroline ENF 260C/FE UV apparatus. Melting points (mp) were determined on a Stuart Scientific SMP1 apparatus and are uncorrected. Infrared spectra (IR) were recorded on a PerkinElmer Spectrum 100 FT-IR spectrophotometer equipped with universal attenuated total reflectance accessory, and IR data acquired were processed by PerkinElmer Spectrum 10.03.00.0069 software. Band position and absorption ranges are given in cm^{-1} . Proton nuclear magnetic resonance (^1H NMR) spectra were recorded with a Varian Mercury (300 MHz) or a Bruker Avance (400 MHz) spectrometer in the indicated solvent. Carbon (^{13}C) NMR spectra were recorded with a Varian Mercury (75 MHz) spectrometer in the indicated solvent. Fid files were processed by MestreLab Research SL MestreReNova 6.2.1–769 software. Chemical shifts are expressed in δ units (ppm) from tetramethylsilane. Mass spectra (MS) were recorded on AB Sciex API-2000 equipped with an ESI source. Elemental analyses of biologically evaluated compounds were found to be within $\pm 0.4\%$ of the theoretical values, and their purity was found to be $>95\%$ by high performance liquid chromatography (HPLC). The HPLC system used (Thermo Fisher Scientific Inc. Dionex UltiMate 3000) consisted of a SR-3000 solvent rack, a LPG-3400SD quaternary analytical pump, a TCC3000SD column compartment, a DAD-3000 diode array detector, and an analytical manual injection valve with a 20 μL loop. Samples were dissolved in acetonitrile (1 mg/mL). HPLC analysis was performed by using a Thermo Fisher Scientific Inc. Acclaim 120 C18 column (5 μm , 4.6 mm \times 250 mm) at 25 ± 1 $^\circ\text{C}$ with an appropriate solvent gradient (acetonitrile/water), flow rate of 1.0 mL/min and signal detector at 206, 230, 254 and 365 nm. Chromatographic data were acquired and processed by a Thermo Fisher Scientific Inc. Chromeleon 6.80 SR15 Build 4656 software. ATI 23S and ARAP 32S were prepared as previously reported.

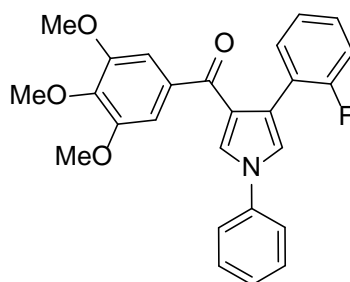
General Procedure for the Preparation of Compounds 3.3-3.6, 3.8, 3.9, 3.12, 3.13, 3.15, 3.16, 3.47 and 3.48. Example: (1,4-diphenyl-1H-pyrrol-3-yl)(3,4,5-trimethoxyphenyl)methanone (**3.3**).



3.3

A mixture of **3.32**²⁶ (0.10 g, 0.30 mmol), **3.40** (0.08 g, 0.66 mmol), copper(II) acetate (0.09 g, 0.47 mmol) and triethylamine (0.07 g, 0.10 mL, 0.70 mmol) in 1,2-dichloroethane (2.0 mL) was heated at reflux for 18 h under an Ar stream, cooled, diluted with water and extracted with chloroform. The organic layer was washed with brine, dried and filtered. Evaporation of the solvent gave a residue that was purified by column chromatography (silica gel, ethyl acetate:n-hexane = 1:1 as eluent) to furnish **3.3** (0.04 g, 0.097 mmol, 37 %), oil. ^1H NMR (DMSO- d_6 , 400 MHz): δ 3.71 (s, 3H), 3.77 (s, 6H), 7.11 (s, 2H), 7.19-7.26 (m, 1H), 7.27-7.29 (m, 2H), 7.33-7.39 (m, 3H), 7.51 (t, $J = 7.6$ Hz, 2H), 7.73-7.78 (m, 3H), 7.93 ppm (d, $J = 2.4$ Hz, 1H). IR: ν 1615 cm^{-1} .

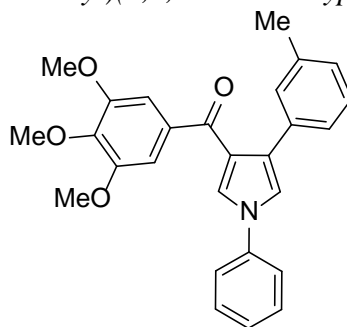
(4-(2-Fluorophenyl)-1-phenyl-1H-pyrrol-3-yl)(3,4,5-trimethoxyphenyl) methanone (3.4).



3.4

Synthesized as **3.3**, starting from **3.33** and **3.40**. Yield 14%, 0.18 g, 0.41 mmol, mp 138-140 °C (from ethanol/n-hexane). ¹H NMR (CDCl₃, 300 MHz): δ 3.81 (s, 9H), 6.96 (t, *J* = 9.3 Hz, 1H), 7.10 (s, 3H), 7.11-7.20 (m, 1H), 7.21-7.40 (m, 3H), 7.49-7.70 (m, 4H), 7.72 ppm (d, *J* = 3.3 Hz, 1H). ¹³C NMR (CDCl₃): δ 56.52, 61.10, 107.95, 115.83, 116.12, 121.55, 121.89, 122.23, 124.64, 124.68, 125.19, 127.03, 127.96, 129.20, 129.31, 130.66, 131.63, 131.68, 135.02, 140.21, 142.36, 153.49 ppm. IR: ν 1639 cm⁻¹.

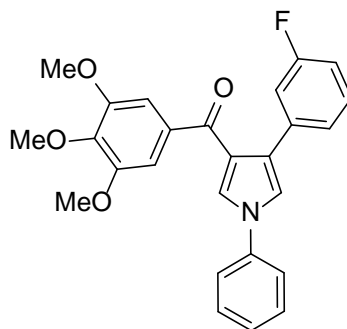
(1-Phenyl-4-(*m*-tolyl)-1H-pyrrol-3-yl)(3,4,5-trimethoxyphenyl)methanone (3.5).



3.5

Synthesized as **3.3**, starting from **3.34** and **3.40**. Yield 6%, 0.06 g, 0.13 mmol, mp 137-139 °C (from ethanol/n-hexane). ¹H NMR (CDCl₃, 400 MHz): δ 2.26 (s, 3H), 3.79 (s, 6H), 3.85 (s, 3H), 6.99 (d, *J* = 6.4 Hz, 1H), 7.0-7.15 (m, 6H), 7.35 (s, 1H), 7.40-7.46 (m, 4H), 7.60 ppm (s, 1H). ¹³C NMR (DMSO-*d*₆): δ 21.43, 56.33, 60.48, 107.39, 120.37, 120.50, 123.42, 125.89, 126.67, 127.02, 127.21, 128.02, 128.20, 129.45, 130.20, 134.34, 134.67, 137.22, 139.20, 152.85, 189.65 ppm. IR: ν 1639 cm⁻¹.

(4-(3-Fluorophenyl)-1-phenyl-1H-pyrrol-3-yl)(3,4,5-trimethoxyphenyl) methanone (3.6).

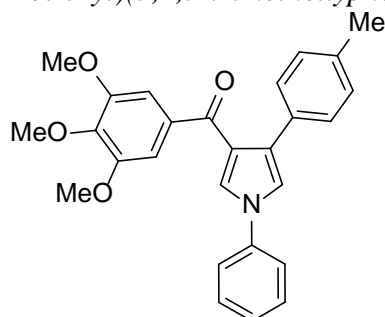


3.6

Synthesized as **3.3**, starting from **3.35** and **3.40**. Yield 44%, 0.29 g, 0.67 mmol, mp 119-121 °C (from ethanol/n-hexane). ¹H NMR (CDCl₃, 300 MHz): δ 3.83 (s, 6H), 3.88

(s, 3H), 6.87-6.93 (m, 1H), 7.107.24 (m, 6H), 7.35-7.40 (m, 1H), 7.45-7.53 (m, 4H), 7.57 ppm (d, $J = 2.4$ Hz, 1H). ^{13}C NMR (CDCl_3): δ 56.24, 60.91, 107.18, 113.25, 113.53, 115.18, 115.47, 120.08, 120.87, 123.65, 124.24, 124.028, 126.75, 127.27, 127.43, 127.46, 129.45, 129.56, 129.94, 134.34, 136.45, 136.56, 139.31, 141.66, 152.73, 164.25, 190.15 ppm. IR: ν 1638 cm^{-1} .

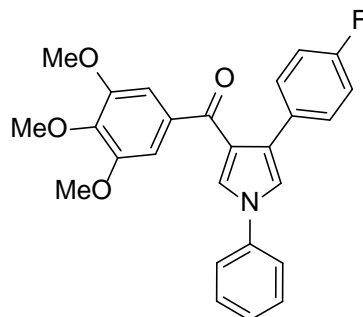
(1-Phenyl-4-(*p*-tolyl)-1*H*-pyrrol-3-yl)(3,4,5-trimethoxyphenyl)methanone (**3.8**).



3.8

Synthesized as **3.3**, starting from **3.37** and **3.40**. Yield 8%, 0.04 g, 0.1 mmol, mp 125-130 °C (from ethanol/*n*-hexane). ^1H NMR (DMSO-d_6 , 400 MHz): δ 2.27 (s, 3H), 3.72 (s, 6H), 3.77 (s, 3H), 7.10-7.11 (m, 4H), 7.27 (d, $J = 8.4$ Hz, 2H), 7.34 (t, $J = 7.0$ Hz, 1H), 7.50 (t, $J = 7.6$ Hz, 2H), 7.69 (d, $J = 4.6$ Hz, 1H), 7.76 (d, $J = 7.9$ Hz, 2H), 7.91 ppm (d, $J = 2.3$ Hz, 1H). ^{13}C NMR (DMSO-d_6): δ 21.14, 56.35, 60.54, 107.40, 120.25, 120.52, 123.22, 126.72, 127.00, 127.90, 128.60, 128.92, 130.20, 131.85, 134.50, 135.66, 139.22, 152.88, 189.56 ppm. IR: ν 1636 cm^{-1} .

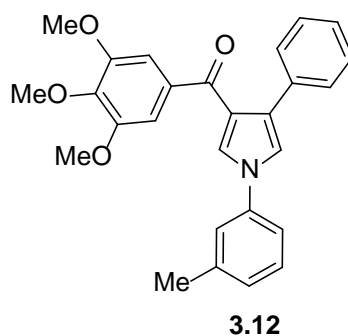
(4-(4-Fluorophenyl)-1-phenyl-1*H*-pyrrol-3-yl)(3,4,5-trimethoxyphenyl) methanone (**3.9**).



3.9

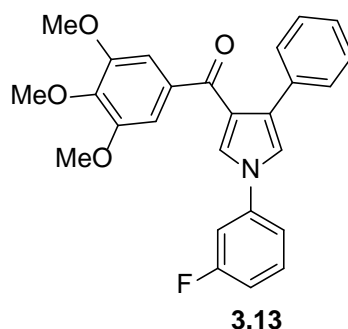
Synthesized as **3.3**, starting from **3.38** and **3.40**. Yield 35%, 0.33 g, 0.76 mmol, mp 131-133 °C (from ethanol/*n*-hexane). ^1H NMR (CDCl_3 , 300 MHz): δ 3.83 (s, 6H), 3.89 (s, 3H), 6.97 (t, $J = 8.7$ Hz, 2H), 7.13 (s, 2H), 7.19 (d, $J = 2.1$ Hz, 1H), 7.35-7.39 (m, 3H), 7.44-7.52 (m, 4H), 7.56 ppm (d, $J = 2.4$ Hz, 1H). ^{13}C NMR (CDCl_3): δ 56.27, 60.93, 107.15, 114.84, 115.12, 119.77, 120.81, 123.50, 126.73, 127.18, 127.64, 129.92, 130.03, 130.14, 130.30, 130.34, 134.43, 139.36, 141.60, 152.71, 160.19, 163.45, 190.20 ppm. IR: ν 1635 cm^{-1} .

(4-Phenyl-1-(*m*-tolyl)-1*H*-pyrrol-3-yl)(3,4,5-trimethoxyphenyl)methanone (**3.12**).



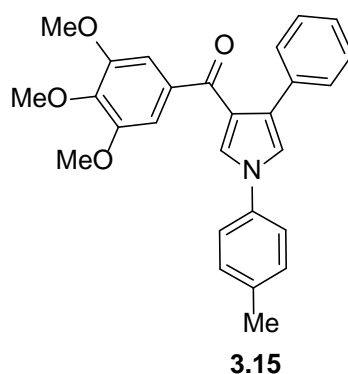
Synthesized as **3.3**, starting from **3.32**²⁶ and **3.42**. Yield 33%, 0.04 g, 0.11 mmol, oil. ¹H NMR (DMSO-d₆, 400 MHz): δ 2.38 (s, 3H), 3.72 (s, 3H), 3.77 (s, 6H), 7.10 (s, 2H), 7.14-7.20 (m, 2H), 7.27 (t, *J* = 8.1 Hz, 2H), 7.36-7.40 (m, 3H), 7.55 (d, *J* = 8.1 Hz, 1H), 7.62 (s, 1H), 7.72 (d, *J* = 4.2 Hz, 1H), 7.92 ppm (d, *J* = 4.1 Hz, 1H). ¹³C NMR (DMSO-d₆): δ 21.40, 56.35, 60.53, 107.42, 117.46, 120.58, 121.09, 123.14, 126.56, 126.81, 127.66, 128.31, 128.71, 129.98, 134.46, 139.14, 139.89, 152.88, 189.52 ppm. IR: ν 1638 cm⁻¹.

(1-(3-Fluorophenyl)-4-phenyl-1H-pyrrol-3-yl)(3,4,5-trimethoxyphenyl) methanone (3.13).



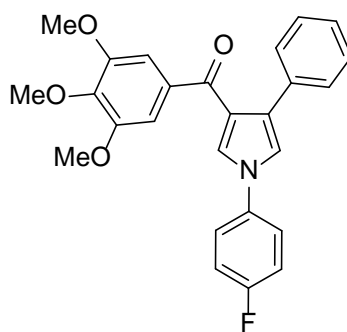
Synthesized as **3.3**, starting from **3.32**²⁶ and **3.43**. Yield 4%, 0.007 g, 0.02 mmol, oil. ¹H NMR (DMSO-d₆, 400 MHz): δ 3.72 (s, 3H), 3.77 (s, 6H), 7.11 (s, 2H), 7.20-7.22 (m, 2H), 7.28 (t, *J* = 8.3 Hz, 2H), 7.37 (d, *J* = 4.2 Hz, 2H), 7.50-7.56 (m, 1H), 7.67 (d, *J* = 8.2 Hz, 1H), 7.76-7.79 (m, 1H), 7.83 (d, *J* = 4.0 Hz, 1H), 8.03 ppm (s, 1H). IR: ν 1640 cm⁻¹.

(4-Phenyl-1-(p-tolyl)-1H-pyrrol-3-yl)(3,4,5-trimethoxyphenyl)methanone (3.15).



Synthesized as **3.3**, starting from **3.32**²⁶ and **3.45**. Yield 15%, 0.03 g, 0.07 mmol, 35-40 °C (from ethanol/*n*-hexane). ¹H NMR (DMSO-d₆, 400 MHz): δ 2.34 (s, 3H), 3.71 (s, 3H), 3.76 (s, 6H), 7.10 (s, 2H), 7.2 (d, *J* = 8.1 Hz, 1H), 7.30 (m, 4H), 7.38 (d, *J* = 4.2 Hz, 2H), 7.65 (d, *J* = 8.2 Hz, 2H), 7.69 (d, *J* = 4.1 Hz, 1H), 7.88 ppm (d, *J* = 4.2 Hz, 1H). IR: ν 1622 cm⁻¹.

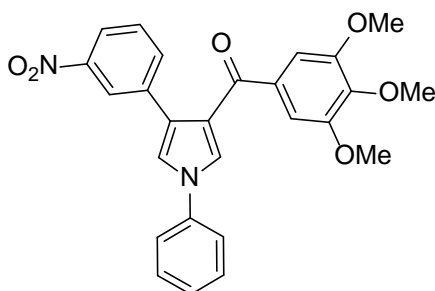
(1-(4-Fluorophenyl)-4-phenyl-1H-pyrrol-3-yl)(3,4,5-trimethoxyphenyl) methanone
(3.16).



3.16

Synthesized as **3.3**, starting from **3.32**²⁶ and **3.46**. Yield 31%, 0.06 g, 0.14 mmol, 55-58 °C (from ethanol/*n*-hexane). ¹H NMR (DMSO-*d*₆, 400 MHz): δ 3.71 (s, 3H), 3.77 (s, 6H), 7.11 (s, 2H), 7.19 (t, *J* = 8.2 Hz, 1H), 7.28 (t, *J* = 4.2 Hz, 2H), 7.36 (t, *J* = 8.1 Hz, 4H), 7.71 (d, *J* = 4.1 Hz, 1H), 7.80-7.84 (m, 2H), 7.92 ppm (d, *J* = 4.2 Hz, 1H). ¹³C NMR (DMSO-*d*₆): δ 56.35, 60.52, 107.38, 109.99, 113.09, 116.71, 117.01, 120.89, 122.63, 122.78, 126.61, 127.16, 127.89, 128.33, 128.71, 134.39, 134.72, 152.87, 189.47 ppm. IR: ν 1630 cm⁻¹.

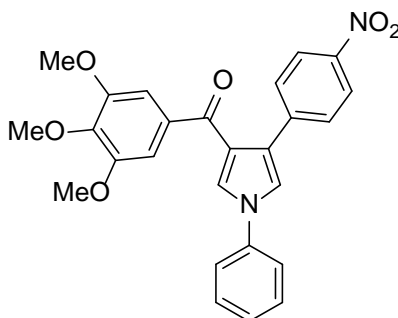
(4-(3-Nitrophenyl)-1-phenyl-1H-pyrrol-3-yl)(3,4,5-trimethoxyphenyl)methanone
(3.47).



3.47

Synthesized as **3.3**, starting from **3.36** and **3.40**. Yield 26%, 0.18 g, 0.39 mmol, oil. ¹H NMR (CDCl₃, 300 MHz): δ 3.85 (s, 6H), 3.89 (s, 3H), 7.13 (s, 2H), 7.27-7.55 (m, 7H), 7.60 (d, *J* = 2.4 Hz, 1H), 7.76-7.79 (m, 1H), 8.06-8.09 (m, 1H), 8.29 ppm (t, *J* = 2.1 Hz, 1H). IR: ν 1637 cm⁻¹.

(4-(4-Nitrophenyl)-1-phenyl-1H-pyrrol-3-yl)(3,4,5-trimethoxyphenyl) methanone
(3.48).

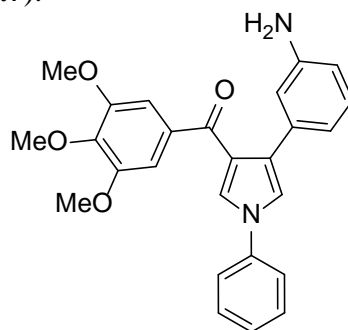


3.48

Synthesized as **3.3**, starting from **3.39** and **3.40**. Yield 72 %, 0.05 g, 0.11 mmol, 110-112 °C (from ethanol/*n*-hexane). ¹H NMR (DMSO-*d*₆, 400 MHz): δ 3.73 (s, 3H), 3.80 (s,

6H), 7.16 (s, 2H), 7.37 (t, $J = 7.4$ Hz, 1H), 7.53 (t, $J = 7.5$ Hz, 2H), 7.67-7.69 (m, 2H), 7.79-7.81 (m, 2H), 8.00-8.04 (m, 2H), 8.16-8.18 ppm (m, 2H). IR: ν 1657 cm^{-1} .

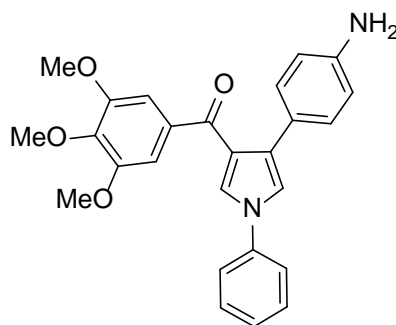
Synthesis of (4-(3-Aminophenyl)-1-phenyl-1H-pyrrol-3-yl)(3,4,5-trimethoxyphenyl)methanone (3.7).



3.7

A mixture of **3.47** (0.06 g, 0.14 mmol) and Pd/C (0.03 g) in methanol (1.1 mL) was stirred at 25 °C under a H_2 stream (1 atm) for 2 h and filtered. Evaporation of the solvent gave a residue that was purified by column chromatography (silica gel, ethyl acetate:*n*-hexane = 4:6 as eluent) to furnish **3.7** (0.02 g, 0.05 mmol, 82%), oil. ^1H NMR (CDCl_3 , 300 MHz): δ 3.11 (br s, disappeared after treatment with D_2O , 2H), 3.81 (s, 6H), 3.88 (s, 3H), 6.53 (d, $J = 5.7$ Hz, 1H), 6.70 (d, $J = 1.2$ Hz, 1H), 6.76 (d, $J = 5.7$ Hz, 1H), 7.04 (t, $J = 5.7$ Hz, 1H), 7.13 (s, 2H), 7.24 (d, $J = 1.8$ Hz, 1H), 7.36 (t, $J = 1.2$ Hz, 1H), 7.44-7.48 (m, 4H), 7.55 ppm (d, $J = 1.8$ Hz, 1H). ^{13}C NMR (CDCl_3): δ 56.26, 60.87, 107.42, 110.06, 114.10, 115.98, 119.65, 120.81, 123.98, 126.34, 127.04, 128.62, 129.11, 129.89, 129.99, 134.45, 135.39, 139.57, 141.71, 152.71, 190.51 ppm. IR: ν 1635 and 2924 cm^{-1} .

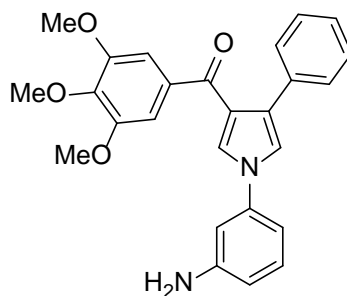
General Procedure for the Preparation of Compounds 3.10, 3.14 and 3.51. Example: (4-(4Aminophenyl)-1-phenyl-1H-pyrrol-3-yl)(3,4,5-trimethoxyphenyl)methanone (3.10).



3.10

A mixture of **3.48** (0.06 g, 0.13 mmol) and tin(II) chloride dihydrate (0.08 g, 0.39 mmol) in ethyl acetate (17.0 mL) was heated at reflux for 6 h, cooled, made basic (pH \approx 8) with a saturated aqueous solution of sodium hydrogen carbonate and filtered. The organic layer was washed with brine, dried and filtered. Evaporation of the solvent gave a residue that was purified by column chromatography (silica gel, ethyl acetate:*n*-hexane = 7:3 as eluent) to furnish **10** (0.03 g, 0.08 mmol, 60%), 65-68 °C (from ethanol/*n*-hexane). ^1H NMR (DMSO-d_6 , 400 MHz): δ 3.71 (s, 3H), 3.75 (s, 6H), 4.98 (br s, disappeared after treatment with D_2O , 2H), 6.46 (d, $J = 8.6$ Hz, 2H), 7.03-7.07 (m, 4H), 7.29-7.31 (m, 1H), 7.50-7.54 (m, 3H), 7.74 (d, $J = 7.6$ Hz, 2H), 7.84 ppm (d, $J = 2.5$ Hz, 1H). IR: ν 1625, 2932 and 3359 cm^{-1} .

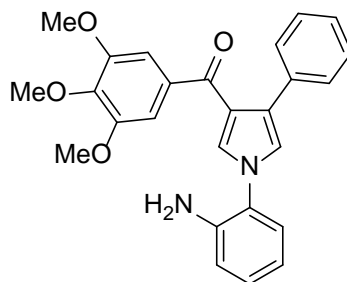
(1-(3-Aminophenyl)-4-phenyl-1H-pyrrol-3-yl)(3,4,5-trimethoxyphenyl) methanone
(3.14).



3.14

Synthesized as **3.10**, starting from **3.50**. Yield 52%, 0.10 g, 0.23 mmol, 170-173 °C (from ethanol/*n*-hexane). ¹H NMR (DMSO-*d*₆, 400 MHz): δ 3.71 (s, 3H), 3.77 (s, 6H), 5.35 (br s, disappeared after treatment with D₂O, 2H), 6.53 (d, *J* = 8.2 Hz, 1H), 6.82 (d, *J* = 8.1 Hz, 2H), 7.09 (s, 2H), 7.13 (d, *J* = 8.2 Hz, 1H), 7.19 (t, *J* = 8.0 Hz, 1H), 7.27 (t, *J* = 8.2 Hz, 2H), 7.36 (d, *J* = 7.5 Hz, 2H), 7.55 (d, *J* = 4.1 Hz, 1H), 7.69 ppm (d, *J* = 4.1 Hz, 1H). IR: ν 1629 and 3412 cm⁻¹.

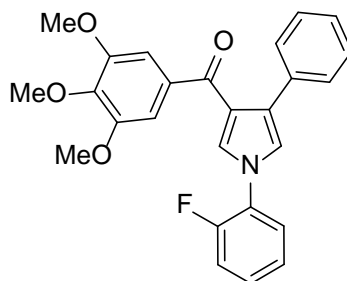
(1-(2-Aminophenyl)-4-phenyl-1H-pyrrol-3-yl)(3,4,5-trimethoxyphenyl) methanone
(3.51).



3.51

Synthesized as **3.10**, starting from **3.49**. Yield 47%, 0.02 g, 0.04 mmol, oil. ¹H NMR (DMSO-*d*₆, 400 MHz): δ 3.71 (s, 3H), 3.79 (s, 6H), 5.22 (br s, disappeared after treatment with D₂O, 2H), 6.66 (t, *J* = 8.1 Hz, 1H), 6.87 (d, *J* = 4.2 Hz, 1H), 7.12 (t, *J* = 8.0 Hz, 1H), 7.17-7.19 (m, 4H), 7.24-7.29 (m, 3H), 7.42-7.44 ppm (m, 3H). IR: ν 1622 and 3371 cm⁻¹.

Synthesis of (1-(2-Fluorophenyl)-4-phenyl-1H-pyrrol-3-yl)(3,4,5-trimethoxyphenyl) methanone (**3.11**).

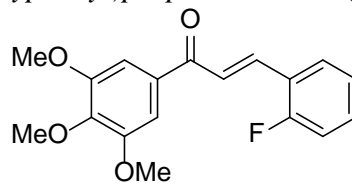


3.11

A mixture of **3.51** (0.04 g, 0.22 mmol) in tetrafluoroboric acid (0.89 mL; 48 wt. % in water) was cooled at 0 °C. Sodium nitrite (0.12 g, 1.73 mmol) was carefully added, and the reaction mixture was stirred in the same condition for 1 h, made basic with a 1N aqueous solution of sodium hydroxide and extracted with ethyl acetate. The organic layer was washed with brine, dried and filtered. Evaporation of the solvent gave a residue that

was purified by column chromatography (silica gel, ethyl acetate:*n*-hexane = 1:1 as eluent) to furnish **3.11** (0.01 g, 0.03 mmol, 13%), 190-195 °C (from ethanol/*n*-hexane). ¹H NMR (DMSO-*d*₆, 400 MHz): δ 3.71 (s, 3H), 3.73 (s, 6H), 7.14 (s, 2H), 7.31 (t, *J* = 7.3 Hz, 2H), 7.38 (t, *J* = 7.1 Hz, 2H), 7.61 (d, *J* = 8.2 Hz, 2H), 7.75 (t, *J* = 8.3 Hz, 1H), 7.93 (t, *J* = 7.2 Hz, 1H), 8.43 (d, *J* = 8.2 Hz, 1H), 8.55 (d, *J* = 8.1 Hz, 1H), 9.00 ppm (s, 1H). IR: ν 1620 cm⁻¹.

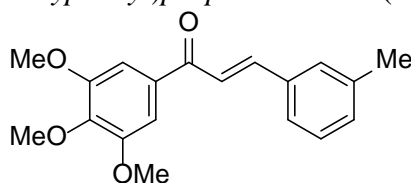
General Procedure for the Preparation of Compounds 3.25-3.31. Example: 3-(2-Fluorophenyl)-1-(3,4,5-trimethoxyphenyl)prop-2-en-1-one (3.25).



3.25

A mixture of **3.17** (1.0 g, 4.76 mmol), **3.18** (0.60 g, 0.50 mL, 4.76 mmol) and sodium hydroxide (0.11 g, 2.77 mmol) in ethanol (19 mL) was stirred at 25 °C for 24 h, diluted with water and extracted with ethyl acetate. The organic layer was washed with brine, dried and filtered. Removal of the solvent gave a residue that was purified by column chromatography (silica gel, ethyl acetate:petroleum ether = 2:8 as eluent) to furnish **3.17** (1.08 g, 3.41 mmol, 72%), mp 115-117 °C (from ethanol/*n*-hexane). ¹H NMR (CDCl₃, 300 MHz): δ 3.95 (s, 9H), 7.11-7.29 (m, 4H), 7.36-7.43 (m, 1H), 7.57-7.68 (m, 2H), 7.90 ppm (d, *J* = 15.9 Hz, 1H). IR: ν 1634 cm⁻¹.

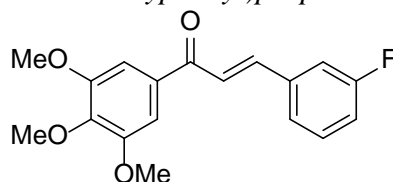
*3-(*m*-Tolyl)-1-(3,4,5-trimethoxyphenyl)prop-2-en-1-one (3.26).*



3.26

Synthesized as **3.25**, starting from **3.17** and **3.19**. Yield 73%, 1.09 g, 3.49 mmol, mp 78-80 °C (from ethanol/*n*-hexane). ¹H NMR (DMSO-*d*₆, 400 MHz): δ 2.41 (s, 3H), 3.95 (s, 9H), 7.23-7.34 (m, 4H), 7.47 (d, *J* = 12.4 Hz, 3H), 7.79 ppm (d, *J* = 15.9 Hz, 1H). IR: ν 1654 cm⁻¹.

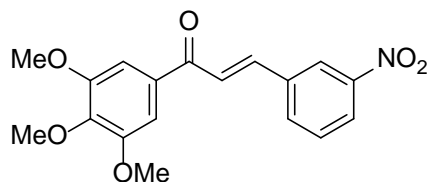
3-(3-Fluorophenyl)-1-(3,4,5-trimethoxyphenyl)prop-2-en-1-one (3.27).



3.27

Synthesized as **3.25**, starting from **3.17** and **3.20**. Yield 40%, 0.18 g, 0.41 mmol, mp 113-115 °C (from ethanol/*n*-hexane). ¹H NMR (CDCl₃, 300 MHz): δ 3.96 (s, 9H), 7.09-7.14 (m, 1H), 7.37-7.51 (m, 6H), 7.77 ppm (d, *J* = 15.6 Hz, 1H). IR: ν 1661 cm⁻¹.

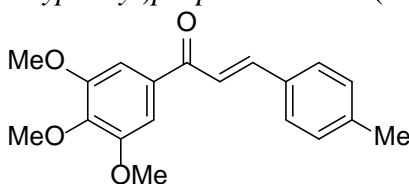
3-(3-Nitrophenyl)-1-(3,4,5-trimethoxyphenyl)prop-2-en-1-one (3.28).



3.28

Synthesized as **3.25**, starting from **3.17** and **3.21**. Yield 59%, 0.96 g, 2.79 mmol, mp 146-148 °C (from ethanol/*n*-hexane). ¹H NMR (CDCl₃, 300 MHz): δ 3.97 (s, 9H), 7.31 (s, 2H), 7.59-7.65 (m, 2H), 7.83-7.94 (m, 2H), 8.25-8.28 (m, 1H), 8.52 ppm (t, *J* = 2.1 Hz, 1H). IR: ν 1721 cm⁻¹.

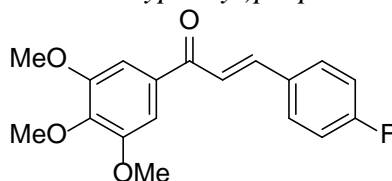
3-(p-Tolyl)-1-(3,4,5-trimethoxyphenyl)prop-2-en-1-one (3.29).



3.29

Synthesized as **3.25**, starting from **3.17** and **3.22**. Yield 71%, 1.05 g, 3.36 mmol, mp 122-124 °C (from ethanol/*n*-hexane), lit. 120-123 °C.³⁰

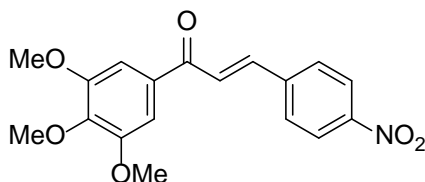
3-(4-Fluorophenyl)-1-(3,4,5-trimethoxyphenyl)prop-2-en-1-one (3.30).



3.30

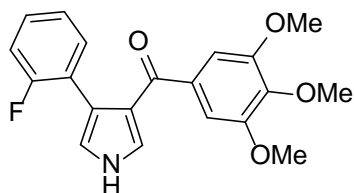
Synthesized as **3.25**, starting from **3.17** and **3.23**. Yield 84%, 1.27 g, 4.0 mmol, mp 120-122 °C (from ethanol/*n*-hexane), lit. 122-125 °C.²¹

3-(4-Nitrophenyl)-1-(3,4,5-trimethoxyphenyl)prop-2-en-1-one (3.31). Synthesized as **3.25**, starting from **3.17** and **3.24**. Yield 89%, 1.46 g, 4.25 mmol, mp 188-190 °C (from ethanol/*n*-hexane), lit. 190-191 °C.³¹ ¹H NMR (DMSO-d₆, 400 MHz): δ 3.77 (s, 3H), 3.90 (s, 6H), 7.46 (s, 2H), 7.82 (d, *J* = 15.6 Hz, 1H), 8.12-8.20 (m, 3H), 8.31 ppm (d, *J* = 8.9 Hz, 2H). IR: ν 1653 cm⁻¹.



3.31

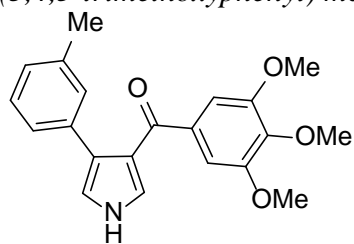
General Procedure for the Preparation of Compounds 3.33-3.39. Example: (4-(2-Fluorophenyl)1H-pyrrol-3-yl)(3,4,5-trimethoxyphenyl) methanone (3.33).



3.33

A mixture of **3.25** (1.08 g, 3.41 mmol) and *p*-toluenesulfonylmethyl isocyanide (0.67 g, 3.43 mmol) in anhydrous methyl sulfoxide/diethyl ether (1:2; 31.5 mL) into a well stirred suspension of sodium hydride (0.61 g, 15.19 mmol; 60% in mineral oil) was added dropwise under an Ar stream. The reaction mixture was stirred at 25 °C for 4 h, diluted with water and extracted with ethyl acetate. The organic layer was washed with brine, dried and filtered. Evaporation of the solvent gave a residue that was purified by column chromatography (silica gel, ethyl acetate:petroleum ether = 4.5:5.5 as eluent) to furnish **3.33** (0.96 g, 2.7 mmol, 79%), mp 193-195 °C (from ethanol/*n*-hexane). ¹H NMR (CDCl₃/CD₃OD: 2/1, 300 MHz): δ 3.85 (s, 9H), 6.93-6.99 (m, 2H), 7.02-7.11 (m, 3H), 7.12-7.17 (m, 1H), 7.27-7.32 (m, 2H), 11.21 ppm (broad s, disappeared after treatment with D₂O). IR: ν 1609 and 3257 cm⁻¹.

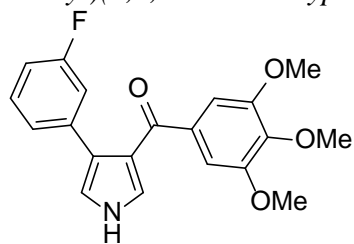
(4-(*m*-Tolyl)-1H-pyrrol-3-yl)(3,4,5-trimethoxyphenyl)methanone (**3.34**).



3.34

Synthesized as **3.33**, starting from **3.26**. Yield 58%, 0.71 g, 2.02 mmol, mp 51-53 °C (from ethanol/*n*-hexane). ¹H NMR (DMSO-*d*₆, 400 MHz): δ 2.24 (s, 3H), 3.79 (s, 6H), 3.86 (s, 3H), 6.84 (s, 1H), 6.97 (s, 1H), 7.06 (s, 2H), 7.11 (d, *J* = 4.0 Hz, 3H), 7.24 (d, *J* = 12.8 Hz, 1H), 9.20 ppm (br s, disappeared after treatment with D₂O, 1H). IR: ν 1579 and 3312 cm⁻¹.

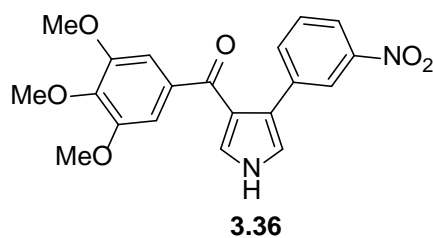
(4-(3-Fluorophenyl)-1H-pyrrol-3-yl)(3,4,5-trimethoxyphenyl)methanone (**3.35**).



3.35

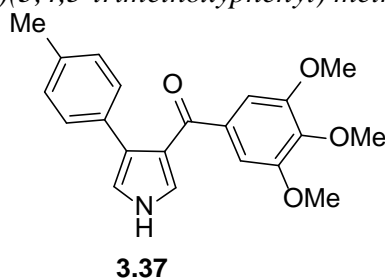
Synthesized as **3.33**, starting from **3.27**. Yield 84%, 0.54 g, 1.6 mmol, mp 192-194 °C (from ethanol/*n*-hexane). ¹H NMR (CDCl₃/CD₃OD: 9/1, 300 MHz): δ 3.83 (s, 6H), 3.87 (s, 3H), 6.83-6.89 (m, 1H), 6.95 (d, *J* = 2.1 Hz, 1H), 7.03-7.24 (m, 5H), 7.31 (d, *J* = 1.8 Hz, 1H), 10.84 ppm (br s, disappeared after treatment with D₂O, 1H). IR: ν 1608 and 3265 cm⁻¹.

(4-(3-Nitrophenyl)-1H-pyrrol-3-yl)(3,4,5-trimethoxyphenyl)methanone (**3.36**).



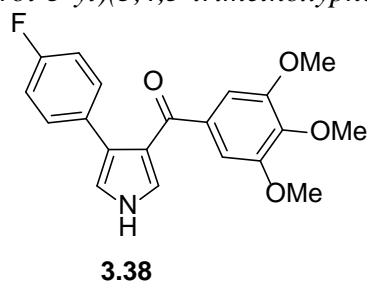
Synthesized as **3.33**, starting from **3.28**. Yield 54%, 0.58 g, 1.51 mmol, mp 74-76 °C (from ethanol/*n*-hexane). ¹H NMR (CDCl₃, 300 MHz): δ 3.85 (s, 6H), 3.89 (s, 3H), 6.98 (t, *J* = 2.1 Hz, 1H), 7.10 (s, 2H), 7.27-7.31 (m, 1H), 7.43 (t, *J* = 7.8 Hz, 1H), 7.71-7.75 (m, 1H), 8.01-8.05 (m, 1H), 8.22 (t, *J* = 2.1 Hz, 1H), 9.40 ppm (br s, disappeared after treatment with D₂O, 1H). IR: ν 1618 and 3308 cm⁻¹.

(4-(p-Tolyl)-1H-pyrrol-3-yl)(3,4,5-trimethoxyphenyl) methanone (3.37).



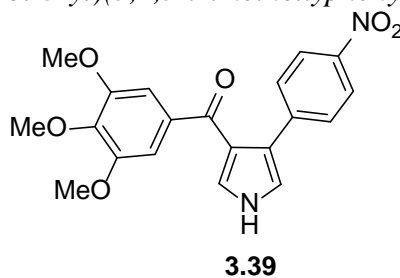
Synthesized as **3.33**, starting from **3.29**. Yield 38%, 0.44 g, 1.25 mmol, mp 165-166 °C (from ethanol/*n*-hexane). ¹H NMR (DMSO-*d*₆, 400 MHz): δ 2.26 (s, 3H), 3.70 (s, 3H), 3.75 (s, 6H), 7.00-7.05 (m, 5H), 7.20 (d, *J* = 8.0 Hz, 2H), 7.33 (d, *J* = 1.6 Hz, 1H), 11.56 ppm (br s, disappeared after treatment with D₂O, 1H). IR: ν 1612 and 3219 cm⁻¹.

(4-(4-Fluorophenyl)-1H-pyrrol-3-yl)(3,4,5-trimethoxyphenyl)methanone (3.38).



Synthesized as **3.33**, starting from **3.30**. Yield 67%, 0.95 g, 2.21 mmol, mp 214-216 °C (from ethanol/*n*-hexane). ¹H NMR (DMSO-*d*₆, 300 MHz): δ 3.72 (s, 3H), 3.78 (s, 6H), 7.03-7.10 (m, 5H), 7.34-7.40 (m, 3H), 11.64 ppm (br s, disappeared after treatment with D₂O, 1H). IR: ν 1611 and 3251 cm⁻¹.

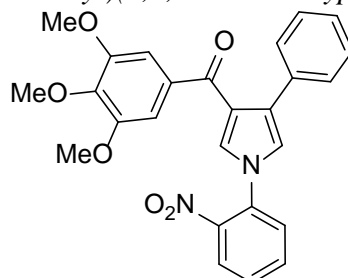
(4-(4-Nitrophenyl)-1H-pyrrol-3-yl)(3,4,5-trimethoxyphenyl)methanone (3.39).



Synthesized as **3.33**, starting from **3.31**. Yield 27%, 0.06 g, 0.16 mmol, mp 175-178 °C (from ethanol/*n*-hexane). ¹H NMR (DMSO-*d*₆, 400 MHz): δ 3.71 (s, 3H), 3.79 (m, 6H),

7.07 (s, 2H), 7.34 (d, $J = 1.9$ Hz, 1H), 7.47 (d, $J = 2.0$ Hz, 1H), 7.59-7.62 (m, 2H), 8.10-8.13 (m, 2H), 11.87 ppm (br s, disappeared after treatment with D₂O, 1H). IR: ν 1634 and 3195 cm⁻¹.

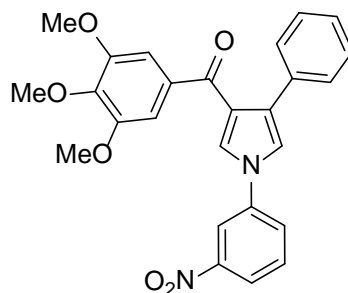
General Procedure for the Preparation of Compounds 49 and 50. Example: (1-(2-Nitrophenyl)-4-phenyl-1H-pyrrol-3-yl)(3,4,5-trimethoxyphenyl) methanone (3.49).



3.49

A mixture of copper(I) bromide (1.41 mg, 0.009 mmol), cesium carbonate (0.64 g, 0.020 mmol) and quinoline-*N*-oxide (2.87 mg, 0.020 mmol) was degassed for 10 min. A solution of **3.32**²⁶ (0.50 g, 1.48 mmol) and **3.41** (0.25 g, 0.99 mmol) in DMSO (1.0 mL) was added, and the resulting suspension was heated at 65 °C for 6 h under an Ar stream. After cooling, the reaction mixture was diluted with water and extracted with ethyl acetate. The organic layer was washed with brine, dried and filtered. Removal of the solvent gave a residue that was purified by column chromatography (silica gel, ethyl acetate:*n*-hexane = 1:1 as eluent) to furnish **3.49** (0.04 g, 0.087 mmol, 9%), mp 150-155 °C (from ethanol/*n*-hexane). ¹H NMR (DMSO-*d*₆, 400 MHz): δ 3.73 (s, 3H), 3.82 (s, 6H), 7.13 (s, 2H), 7.22 (d, $J = 4.1$ Hz, 1H), 7.30 (t, $J = 4.2$ Hz, 2H), 7.39 (m, 3H), 7.61 (s, 1H), 7.71 (t, $J = 8.1$ Hz, 1H), 7.86 (m, 2H), 8.17 ppm (d, $J = 8.2$ Hz, 1H). IR: ν 1632 cm⁻¹.

(1-(3-Nitrophenyl)-4-phenyl-1H-pyrrol-3-yl)(3,4,5-trimethoxyphenyl) methanone (3.50).



3.50

Synthesized as **3.49**, starting from **3.32**²⁶ and **3.44**. Yield 34%, 0.23 g, 0.50 mmol, mp 162-167 °C (from ethanol/*n*-hexane). ¹H NMR (DMSO-*d*₆, 400 MHz): δ 3.72 (s, 3H), 3.78 (s, 6H), 7.14 (s, 2H), 7.21 (t, $J = 8.2$ Hz, 1H), 7.30 (t, $J = 4.1$ Hz, 2H), 7.40 (d, $J = 8.2$ Hz, 2H), 7.80 (t, $J = 8.2$ Hz, 1H), 7.98 (d, $J = 4.1$ Hz, 1H), 8.15-8.19 (m, 2H), 8.29 (d, $J = 8.1$ Hz, 1H), 8.63 ppm (t, $J = 4.2$ Hz, 1H). IR: ν 1638 cm⁻¹.

3.7.2 Molecular Modeling

The ARDAP binding mode was extensively studied by molecular docking into 5 different tubulin crystal structures (PDB codes 1SA0,³² 3N2G,³³ 3HKD,³⁴ 4O2A³⁵ and 4YJ3³⁶). The proposed ARDAP binding mode was nearly identical in all 5 crystal structures. Inspection of the binding mode of **3.3** led to identify a series of pharmacophoric interactions. The 3-trimethoxyphenyl moiety was hydrophobically stabilized by β Leu255

and β Leu248, and this functionality was within bond distance of the thiol group of β Cys241, making polar contact. The 1-phenylpyrrole moiety established Van der Waals contacts with β Lys352, β Asn258 and β Met259, while the 3-phenyl group formed hydrophobic interactions with β Lys254 and β Leu248 (Figure 3.12). The introduction of all substituents summarized in Table 3.1 did not affect the Plants proposed binding mode. All molecular modeling studies were performed on a MacPro dual 2.66GHz Xeon running Ubuntu 14. The tubulin structures were downloaded from the PDB data bank (<http://www.rcsb.org/>). Ligand structures were built with MOE³⁷ and minimized using the MMFF94 forcefield until a RMSD gradient of 0.05 kcal mol⁻¹ Å⁻¹ was reached. The docking simulations were performed using PLANTS;³⁸ figures were generated by Pymol.³⁹

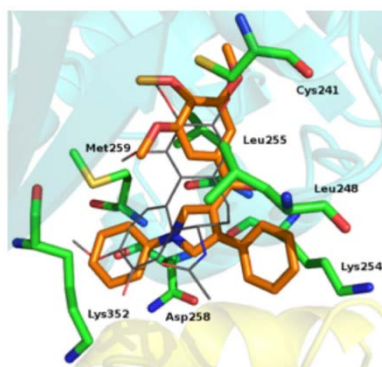


Figure 3.12 Proposed binding mode for compound **3.3** (orange stick for carbon atoms, oxygen in red and nitrogen in blue). Colchicine is shown by gray lines. Residues of β -tubulin involved in interactions with the ligand are shown by green stick for their carbon atoms, with oxygen shown in red, nitrogen in blue and sulfur in yellow. Tubulin is shown as a cartoon (cyan for β -tubulin, yellow for α -tubulin).

3.7.3 Biological assays

Tubulin Assembly. The reaction mixtures contained 0.8 M monosodium glutamate (pH 6.6 with HCl in a 2 M stock solution), 10 μ M tubulin, and varying concentrations of drug. Following a 15 min preincubation at 30 °C, samples were chilled on ice, GTP to 0.4 mM was added, and turbidity development was followed at 350 nm in a temperature controlled recording spectrophotometer for 20 min at 30 °C. Extent of reaction was measured. Full experimental details were previously reported.⁴⁰

[³H]Colchicine Binding Assay. The reaction mixtures contained 1.0 μ M tubulin, 5.0 μ M [³H]colchicine, and 5.0 μ M inhibitor and were incubated 10 min at 37 °C.

Complete details were described previously.⁴¹

Cell Viability Assays. The methodology for the evaluation of the growth of human MCF-7 breast carcinoma, OVCAR-8, and NCI/ADR-RES cells, obtained from the National Cancer Institute drug screening laboratory, was previously described, except that cells were grown for 96 h for IC₅₀ determinations.⁴² KBM5, KU812, and LAMA84 cell lines expressing the imatinib mesylate (IM)-sensitive wild type BCR/ABL were derived from CML patients in blast crisis.¹⁸ These CML cell lines were purchased from ATCC (Rockville, MD) and cultured in RPMI-1640 (Life Technologies, Gaithersburg, MD) containing 10% fetal bovine serum (FBS, Cambrex, Baltimore, MD), 100 Units/mL penicillin, 100 μ g/mL streptomycin, 2 mM L-glutamine (GibcoBRL, Paisley, UK) at 37 °C with a 5% CO₂ atmosphere. KBM5-T315I cells ectopically expressing the IM-resistant T315I mutation of BCR-ABL were also from ATCC and maintained in the presence of IM at 1.0 μ M. Peripheral blood mononuclear cells (PBMCs) were obtained after informed

consent from 2 healthy donors, and purified by standard Ficoll-Hypaque density gradient centrifugation (Amersham Biosciences, Uppsala, Sweden). IM was kindly provided by Novartis (Basel, Switzerland) or synthesized by Dr. Alfonso Zambon (University of Venezia, Italy). Stock solutions of IM at 1 or 10 mM in sterile water were filtered and stored at -20 °C. For the NB4 (acute promyelocytic leukemia), THP-1 (acute monocytic leukemia) and KYSE-150 (esophageal squamous cell carcinoma) lines, cell growth was measured using CellTiter-Fluor (CellTiter-Fluor™, Promega cod. G6082), a nonlytic, single-reagent-addition fluorescence assay that detects the relative number of living cells in samples after experimental manipulation. The CellTiterFluor cell viability assay measures the conserved and constitutive protease activity within live cells and, therefore, acts as a marker for cell viability. NB4, THP-1 and KYSE-1500 cells were seeded in 96 multiwell plates at a density of 3500 cells/well, 2000 cells/well and 1500 cells/well in 50 µL of the appropriate medium, respectively. The compounds were dissolved in 100% DMSO and then were diluted at ten different concentrations, ranging from 0 to 100 µM. All cell lines were maintained at 37 °C in the appropriate culture medium; THP-1 and KYSE-150 cells were treated with test compounds for 48 h and 96 h, the NB4 cell line only for 48 h. At the end of treatment, CellTiter-Fluor reagent was added to the cell culture medium (1:1, v/v) and incubated for at least 90 min at 37 °C. Fluorescence was recorded (excitation wavelength, 360 nm; emission wavelength, 535 nm), and the IC₅₀ was calculated using GraphPad software. Cell viability of HT29, HCT116 and HepG2 cells was determined using the 3-(4,5dimethylthiazol-2-yl)-2,5-diphenyltetrazolium bromide (MTT) colorimetric assay. HT 29 cells were seeded into 24-well plates to a density of 20 × 10³/mL per well. HepG2 and HCT116 cells were seeded into 24-well plates to a density of 15 × 10³/mL per well. After 24 h of growth to allow attachment of cells to the wells, test compounds were added at 5–320 nM. After 48 h of growth and removal of the culture medium, 500 µL/well of PBS containing 500 µM MTT was added. Cell cultures were further incubated at 37 °C for 2 h in the dark. The solutions were then gently aspirated from each well, and the formazan crystals within the cells were dissolved in propan-2-ol and 0.04 N HCl (200 µL). Optical densities were read at 550 nm using a Multiskan Spectrum Thermo Electron Corporation reader. The results were expressed as % relative to vehicle-treated control (0.1% DMSO), and IC₅₀ values were calculated by nonlinear regression analysis (GraphPad Prism statistics software). Experiments were performed in triplicate.

Functional studies. Viable cells were counted in a hemocytometer by trypan blue dye exclusion (Sigma-Aldrich Corp., St. Louis, MO), and morphological changes were monitored under phase contrast microscopy using an inverted Olympus IX51 microscope equipped with a 10X objective.

Proliferation assays. CML cells (104-304/well) were seeded in flat bottom 96 well plates in a volume of 100 µL in supplemented medium. Dilutions of the drugs were added as indicated in the Figure legends and the volume adjusted to 200 µL. Cell-growth was quantified by the MTT assay following the instructions of the manufacturer (Sigma Chemical Co., St. Louis, MO). The IC₅₀ inhibitory drug concentration (producing a 50% decrease in proliferation compared to control) was also calculated.

Cell cycle analysis. Cells were harvested, washed with ice-cold phosphate-buffered saline (PBS, Sigma-Aldrich) and fixed in 70% cold ethanol. Samples were then treated with DNase-free RNase (Boehringer Mannheim, Indianapolis, IN) and stained with 50 µg/mL propidium iodide (Sigma Chemicals). DNA content and distribution of individual cells into different phases of the cell cycle was assessed by FACScan flow cytometry and Cell-quest software (Becton Dickinson, San Jose, CA). The ranges for G₀/G₁, S, G₂/M and sub-G₁ phase cells were established on the basis of the corresponding DNA content

of histograms. At least 10,000 cells per sample were considered in the gate regions used for calculations.

Apoptosis assay. Cells were labeled with annexin V-FITC or Hoechst-3258 (BD-PharMingen, San Diego, CA) and analyzed using flow cytometry and Cell-quest software (Becton Dickinson). Apoptosis was also analyzed by MoFlo® Astrios™ flow-cytometry (Beckman Coulter, Brea, CA, USA), according to the protocol for fluorescein isothiocyanate (FITC), using the Annexin V Apoptosis Detection Kit I (BD Bioscience, Franklin Lakes, NJ, USA). HepG2 cells were seeded at 1×10^4 cells/mL in 60-mm culture plates for 48 h and then treated with medium containing the drug at 160 nM or DMSO for 48 h. Cells were then harvested using trypsin, washed twice with ice-cold PBS and resuspended in 1X binding buffer with 5 μ L annexin V and 5 μ L propidium iodide added. The mixture was incubated for 15 min at room temperature in the dark; 400 μ L of binding buffer was then added, and cells were analyzed immediately by flow cytometry.

Caspase-3 activity measurement. Cells were harvested, washed once with PBS and fixed in 4% paraformaldehyde (Sigma-Aldrich) for 15 min at 4 °C. Fixed cells were then washed with PBS and fixed in 70% cold ethanol overnight at -20 °C. After washing twice in PBS containing 0.1% Tween 20 (Sigma-Aldrich), the cells were incubated for 1 h with phycoerythrin-conjugated antibody against the active form of caspase-3 (Becton Dickinson). Cells were washed to remove unbound antibody, suspended in PBS-0.1% Tween 20 and analyzed using flow cytometry (Becton Dickinson).

Mitochondrial permeability transition detection. Changes in the mitochondrial transmembrane potential (MTP) were detected using a fluorescent cationic dye (MitoCapture Apoptosis Detection Kit, BioVision Inc., Milpitas, CA) that fluoresces differently in healthy vs apoptotic cells. In healthy cells, MitoCapture accumulates and aggregates in the mitochondria, giving off a bright red fluorescence. In apoptotic cells, MitoCapture cannot aggregate in the mitochondria due to the altered mitochondrial transmembrane potential, and, thus, it remains in the cytoplasm in its monomer form, fluorescing green. The fluorescent signals were detected by fluorescence microscopy using the FITC channel for green monomers (Ex/Em = 488/530 + 30 nm) and Cell-quest software (Becton Dickinson).

Indirect Tubulin Immunostaining. Cells were seeded in 8-well chamber slides (Nalge Nunc International, Rockester, NY) and incubated for 2 days at 37 °C with 5% CO₂ before overnight treatment (16 h) with the indicated drugs. Cells were washed once with PBS and then fixed in 4% paraformaldehyde for 15 min at room temperature. Fixed cells were washed with PBS and permeabilized in 100% cold methanol for 1 min. Cells were washed twice in PBS and covered with blocking buffer (1% BSA-1% horse serum in PBS) for 1 h before staining. The primary tubulin antibody (1:300 dilution; BD Transduction Laboratories, Lexington, KY) was visualized with a fluorescent secondary antibody Alexa®-488 conjugated goat anti-mouse IgG-FITC (used 1:300; Molecular Probes, Inc., Eugene, OR). After washing, cells were mounted in VECTASHIELD media (Vector Laboratories, Burlingame, CA) containing 4',6-diamidino-2-phenylindole (DAPI) and observed on a Nikon Eclipse 600 fluorescence microscope with a Nikon DXM 1200 digital camera.

Western immunoblotting. After treatment with the indicated drugs, cells were harvested, washed once in PBS at 4 °C and resuspended in lysis buffer [50 mM Tris-HCl, pH 7.4; 1% Triton X-100; 5 mM EDTA; 150 mM NaCl, 1 mM Na₃VO₄; 1 mM NaF; 1 mM phenylmethylsulfonyl fluoride; and protease inhibitor cocktail (Sigma, P8340) (10 μ M benzamidine-HCl and 10 μ g each of aprotinin, leupeptin and pepstatin A per mL)], followed by incubation on ice for 30 min. Lysates were then clarified by centrifugation at 13,000 x g for 15 min at 4 °C and transferred into fresh reaction tubes. The protein concentration of cell lysates was determined using the BCA protein assay (Pierce,

Rockford, IL), and 25 µg total proteins were separated on 8% sodium dodecyl sulfate polyacrylamide gels. Immunoblotting was performed using an Immobilon-P nitrocellulose membrane (Millipore Corp., Bedford, MA). Primary incubations were 1-3 h. Secondary incubations were for 1 h, and antibodies used were HRP-conjugated anti-mouse or anti-rabbit IgG (Amersham, Arlington Hgts, IL). Proteins were visualized by the Enhanced Chemiluminescence System as recommended by the manufacturer (Amersham). Primary antibodies were as follows: anti-C-terminal β-catenin (immunogenic epitope within the amino acids 560-781) and anti-E-cadherin (clone HECD-1-ICRF) were from BD Transduction Laboratories, Lexington, KY; anti-active N-terminal β-catenin S/Tnonphosphorylated (clone 8E4), anti-phosphotyrosine (clone 4G10), anti-total ABL (clone 8E9) and anti-active ABL (phosphoY245), anti-total cofilin (clone AB3831) and anti-active cofilin (phosphoSer3), anti-p21 WAF1 (clone Ab-3) and anti-PARP (clone 7A10) were from Millipore, Billerica, MA; anti-α-actin antibody was from Santa Cruz Biotechnology Inc., Santa Cruz, CA.

3.8 References

1. NCI. SEER Stat Fact Sheets: Chronic Myeloid Leukemia (CML). <https://seer.cancer.gov/statfacts/html/cmyle.html> (accessed on 24/07/ 2019).
2. Apperley, J. F. Chronic myeloid leukaemia. *Lancet* **2015**, 385, 1447–1459.
3. Kantarjian, H. M.; Deisseroth, A.; Kurzrock, R.; Estrov, Z.; Talpaz, M. Chronic myelogenous leukemia: a concise update. *Blood*. **1993**, 82, 691-703.
4. Savage, D. G.; Szydlo, R. M.; Goldman, J. M. Clinical features at diagnosis in 430 patients with chronic myeloid leukemia seen at a referral centre over a 16-year period. *Br J Haematol*. **1997**, 96, 111-6.
5. Kantarjian, H. M.; Dixon, D.; Keating M. J.; Talpaz, M.; Walters R. S.; McCredie K. B.; et al. Characteristics of accelerated disease in chronic myelogenous leukemia. *Cancer*. **1988**, 61, 1441-6.
6. Savage, D. G.; Szydlo, R. M.; Chase, A.; Apperley, J. F.; Goldman, J. M. Bone marrow transplantation for chronic myeloid leukaemia: the effects of differing criteria for defining chronic phase on probabilities of survival and relapse. *Br J Haematol*. **1997**, 99, 30-5.
7. Sokal, J. E.; Baccarani, M.; Russo, D.; Tura, S. Staging and prognosis in chronic myelogenous leukemia. *Semin Hematol*. **1988**, 25, 49-61.
8. Giles, F. J.; Cortes, J. E.; Kantarjian, H. M.; O'Brien, S. M. Accelerated and blastic phases of chronic myelogenous leukemia. *Hematol. Oncol. Clin. N.* **2004**, 18, 753–774.
9. Daley, G. Q.; Van Etten, R. A.; Baltimore, D. Induction of chronic myelogenous leukemia in mice by the P210bcr/abl gene of the Philadelphia chromosome. *Science* **1990**, 247, 824-30.
10. Kelliher, M. A.; McLaughlin, J.; Witte, O. N., Rosenberg, N. Induction of a chronic myelogenous leukemia-like syndrome in mice with v-abl and BCR/ABL. *Proc Natl Acad Sci U S A* **1990**, 87, 6649-53.
11. Heisterkamp, N.; Jenster, G.; ten Hoeve, J.; Zovich, D.; Pattengale, P. K.; Groffen, J. Acute leukaemia in bcr/abl transgenic mice. *Nature* **1990**, 344, 251-3.
12. Lugo, T. G.; Pendergast, A. M.; Muller, A. J.; Witte, O. N. Tyrosine kinase activity and transformation potency of bcr-abl oncogene products. *Science* **1990**, 247, 1079-82.
13. Yang, B.; Papoian, T. Tyrosine kinase inhibitor (TKI)-induced cardiotoxicity: approaches to narrow the gaps between preclinical safety evaluation and clinical outcome. *J. Appl. Toxicol.* **2012**, 32, 945-951.
14. Cismowski, M. J. Tyrosine Kinase Inhibitors. xPharm: The Comprehensive Pharmacology Reference. **2007**,1-4.

15. Goldman, J. M.; Melo, J. V. Targeting the BCR-ABL tyrosine kinase in chronic myeloid leukemia. *N Engl J Med.* **2001**, 344, 1084-1086.
16. Walz, C.; Sattler, M. Novel targeted therapies to overcome imatinib mesylate resistance in chronic myeloid leukemia (CML). *Crit. Rev. Oncol./Hematol.* **2006**, 57, 145-164.
17. Wei, Y.; Hardling, M.; Olsson, B.; et al. Not all imatinib resistance in CML are BCR-ABL kinase domain mutations. *Ann. Hematol.* **2006**, 85, 841-847.
18. Le Coutre, P.; Tassi, E.; Varella-Garcia, M.; Barni, R.; Mologni, L.; Cabrita, G.; Marchesi, E.; Supino, R.; Gambacorti Passerini, C. Induction of resistance to the Abelson inhibitor STI571 in human leukemic cells through gene amplification. *Blood* **2000**, 95, 1758-1766.
19. Pagnano, K. B.; Bendit, I.; Boquimpani, C.; et al. Bengio, 5 on behalf of Latin American Leukemia Net Lalnet RM. BCR-ABL mutations in chronic myeloid leukemia treated with tyrosine kinase inhibitors and impact on survival. *Cancer Invest.* **2015**, 33, 451-458.
20. Bates, D.; Feris, E. J.; Danilov, A. V.; Eastman, A. Rapid induction of apoptosis in chronic lymphocytic leukemia cells by the microtubule disrupting agent BNC105. *Cancer Biol. Ther.* **2016**, 17, 291-299.
21. Ducki, S.; Rennison, D.; Woo, M.; Kendall, A.; Fournier Dit Chabert, J.; McGown, A. T.; Lawrence, N. J. Combretastatin-like chalcones as inhibitors of microtubule polymerization. Part 1: synthesis and biological evaluation of antivasular activity. *Bioorg. Med. Chem.* **2009**, 17, 7698-7710.
22. Ducki, S.; Forrest, R.; Hadfield, J. A.; Kendall, A.; et al. Potent antimitotic and cell growth inhibitory properties of substituted chalcones. *Bioorg. Med. Chem. Lett.* **1998**, 8, 1051-1056.
23. Cao, R.; Wang, Y.; Huang, N. Discovery of 2-acylaminothiophene-3-carboxamides as multitarget inhibitors for BCR-ABL kinase and microtubules. *J. Chem. Inf. Model.* **2015**, 55, 2435-2442.
24. Rowinsky, E. K.; Donehower, R. C.; Jones, J. J.; Tucker, R. W. Microtubule changes and cytotoxicity in leukemic cell lines treated with taxol. *Cancer Res.* **1988**, 48, 4093-4100.
25. La Regina, G.; Sarkar, T.; Bai, R. et al. New arylthioindoles and related bioisosteres at the sulfur bridging group. 4. Synthesis, tubulin polymerization, cell growth inhibition, and molecular modeling studies. *J. Med. Chem.* **2009**, 52, 7512-7527.
26. La Regina, G.; Bai, R.; Coluccia, A. et al. New pyrrole derivatives with potent tubulin polymerization inhibiting activity as anticancer agents including Hedgehog-dependent cancer. *J. Med. Chem.* **2014**, 57, 6531-6552.
27. La Regina, G.; Bai, R.; Coluccia, A.; Famigliani, V.; Passacantilli, S.; Naccarato, V.; Ortar, G.; Mazzoccoli, C.; Ruggieri, V.; Agriesti, F.; Piccoli, C.; Tataranni, T.; Nalli, M.; Brancale, A.; Vultaggio, S.; Mercurio, C.; Varasi, M.; Saponaro, C.; Sergio, S.; Maffia, M.; Coluccia, A. M. L.; Hamel, E.; Silvestri, R. 3-Aroyl-1,4-diarylpyrroles inhibit chronic myeloid leukemia cell growth through an interaction with tubulin. *ACS Med. Chem. Lett.* **2017**, 8, 521-526.
28. Nguyen, T. L.; McGrath, C.; Hermone, A. R.; Burnett, J. C.; Zaharevitz, D. W.; Day, B. W.; Wipf, P.; Hamel, E.; Gussio, R. A common pharmacophore for a diverse set of colchicine site inhibitors using a structure-based approach. *J. Med. Chem.* **2005**, 48, 6107-6116.
29. La Regina, G.; Bai, R.; Rensen, W. M.; Di Cesare, E.; Coluccia, A.; Piscitelli, F.; Famigliani, V.; Reggio, A.; Nalli, M.; Pelliccia, S.; Da Pozzo, E.; Costa, B.; Granata, I.; Porta, A.; Maresca, B.; Soriani, A.; Iannitto, M. L.; Santoni, A.; Li, J.; Cona, M. M.; Chen, F.; Ni, Y.; Brancale, A.; Dondio, G.; Vultaggio, S.; Varasi, M.; Mercurio, C.; Martini, C.;

Hamel, E.; Lavia, P.; Novellino, E.; Silvestri, R. Toward highly potent cancer agents by modulating the C-2 group of the arylthioindole class of tubulin polymerization inhibitors. *J. Med. Chem.* **2013**, *56*, 123–149.

30. Batovska, D.; Parushev, S.; Slavova, A.; Bankova, V.; Tsvetkova, I.; Ninova, M.; Najdenski, H. Study on the substituents' effects of a series of synthetic chalcones against the yeast *Candida albicans*. *Eur. J. Med. Chem.* **2007**, *42*, 87–92.

31. Edwards, M. L.; Stemerick, D. M.; Sunkara, P. S. Chalcones: a new class of antimitotic agents. *J. Med. Chem.* **1990**, *33*, 1948–1954.

32. Ravelli, R. B.; Gigant, B.; Curmi, P. A.; Jourdain, I.; Lachkar, S.; Sobel, A.; Knossow, M. Insight into tubulin regulation from a complex with colchicine and a stathmin-like domain. *Nature* **2004**, *428*, 198–202.

33. Barbier, P.; Dorleans, A.; Devred, F.; Sanz, L.; Allegro, D.; Alfonso, C.; Knossow, M.; Peyrot, V.; Andreu, J. M. Stathmin and interfacial microtubule inhibitors recognize a naturally curved conformation of tubulin dimers. *J. Biol. Chem.* **2010**, *285*, 31672–31681.

34. Dorleans, A.; Gigant, B.; Ravelli, R. B. G.; Mailliet, P.; Mikol, V.; Knossow, M. Variations in the colchicine-binding domain provide insight into the structural switch of tubulin. *Proc. Natl. Acad. Sci. U. S. A.* **2009**, *106*, 13775–13779.

35. Prota, A. E.; Danel, F.; Bachmann, F.; Bargsten, K.; Buey, R. M.; Pohlmann, J.; Reinelt, S.; Lane, H.; Steinmetz, M. O. The novel microtubule-destabilizing drug BAL27862 binds to the colchicine site of tubulin with distinct effects on microtubule organization. *J. Mol. Biol.* **2014**, *426*, 1848–1860.

36. McNamara, D. E.; Senese, S.; Yeates, T. O.; Torres, J. Z. Structures of potent anticancer compounds bound to tubulin. *Protein Sci.* **2015**, *24*, 1164–1172.

37. Molecular Operating Environment (MOE 2007.09). Chemical Computing Group, Inc. Montreal, Quebec, Canada.

38. Korb, O.; Stutzle, T.; Exner, T. E. PLANTS: Application of ant colony optimization to structure-based drug design. In *Ant Colony Optimization and Swarm Intelligence, Proceedings of the 5th International Workshop, ANTS*; Dorigo, M.; Gambardella, L. M.; Birattari, M.; Martinoli, A.; Poli, R.; Stutzle, T.; Eds. *Lecture Notes in Computer Science*, Series 4150; Springer: Berlin, **2006**; pp 247–258.

39. PyMOL version 1.2r1. DeLano Scientific LLC: SanCarlos, CA.

40. Hamel, E. Evaluation of antimitotic agents by quantitative comparisons of their effects on the polymerization of purified tubulin. *Cell Biochem. Biophys.* **2003**, *38*, 1–21.

41. Verdier-Pinard, P.; Lai, J.-Y.; Yoo, H.-D.; Yu, J.; Marquez, B.; Nagle, D. G.; Nambu, M.; White, J. D.; Falck, J. R.; Gerwick, W. H.; Day, B. W.; Hamel, E. Structure–activity analysis of the interaction of curacin A, the potent colchicine site antimitotic agent, with tubulin and effects of analogs on the growth of MCF-7 breast cancer cells. *Mol. Pharmacol.* **1998**, *35*, 62–76.

42. Ruan, S.; Okcu, M. F.; Pong, R. C.; Andreeff, M.; Levin, V.; Hsieh, J. T.; Zhang, W. Attenuation of WAF1/Cip1 expression by an antisense adenovirus expression vector sensitizes glioblastoma cells to apoptosis induced by chemotherapeutic agents 1,3-bis(2chloroethyl)-1-nitrosourea and cisplatin. *Clin. Cancer Res.* **1999**, *5*, 197–202.

4. *Wnt/β-catenin Pathway in Human Colorectal Cancer (CRC)*

4.1 *Introduction*

Human colorectal cancer (CRC) arises from activating mutations in the Wnt/β-catenin pathway that converge with additional molecular changes to shape tumor development and patient prognosis. Na⁺/H⁺ exchanger 3 regulating factor 1 (NHERF1)/EBP50 is an adaptor molecule that interacts with β-catenin and undergoes successive alterations during the colorectal adenoma-to-carcinoma transition, ranging from loss of normal apical membrane distribution to ectopic cytoplasmic overexpression. NHERF1 depletion in human intestinal epithelial polarized cells induced epithelial-mesenchymal transition, β-catenin nuclear translocation with elevation of Wnt/βcatenin transcriptional targets, and increased cell migration and invasion. Ectopic cytoplasmic NHERF1 expression additionally intensified the transformed phenotype by increasing cell proliferation. The epithelial morphology and reduced cell motility could only be restored by re-expression of NHERF1 specifically at the apical plasma membrane. Alterations in the apical membrane localization of NHERF1 contribute to CRC through the disruption of epithelial morphology.¹ Since physiological or pathological roles of NHERF1 are related to its subcellular localization, targeted approaches aiming at modulating NHERF1 activity, rather than its overall expression, would be preferred to preserve the normal functions of this versatile protein. By far, particular attention has been paid to the NHERF1/PDZ1-domain that governs its membrane recruitment/displacement through a transient phosphorylation switch and to the design and synthesis of novel NHERF1 PDZ1 domain inhibitors.²

4.1.1. *Human Colorectal Cancer (CRC)*

Human colorectal cancer (CRC) is one of the most common type of cancer and the third cause of mortality due to cancer in the United States, besides the second most common cause of cancer death in Europe.^{3,4} It typically evolves from a benign polyp, or adenoma, to malignant carcinoma that starts in the mucosa (*carcinoma in situ*) and spreads through the other layers of the colon. In advanced stages, malignant cells metastasize to the lymph nodes or to distant organs. The ability of CRC cells to invade and metastasize renders the tumors unresectable and resistant to chemotherapy and diminishes abruptly the overall survival rate for patients with metastatic disease to approximately 10% at 5 years.

4.1.2 *Epithelial-Mesenchymal-like Transition (EMT)*

The acquired invasiveness of malignant cells results from the disorganization of epithelial morphology leading to an epithelial-mesenchymal-like transition (EMT).⁵ This process occurs naturally during the embryonic development of some structures and is reactivated in malignant cells of epithelial origin. Essentially, during this event, epithelial cells actively downregulate cell-cell adhesion systems, lose their polarity, and acquire a mesenchymal phenotype with reduced intercellular interactions and increased migratory capacity. This is a key biological process during embryonic development, tissue remodeling, restitution and wound repair; in these cases, in fact, there is a requirement for epithelial cells to escape from the rigid structural constraints provided by the tissue architecture and adopt a phenotype more amenable to cell migration and movement.⁴ The reverse of EMT, known as mesenchymal–epithelial transition (MET), also occurs at various stages of morphogenesis, for example during the formation of the heart and the somites (Figure 4.1).

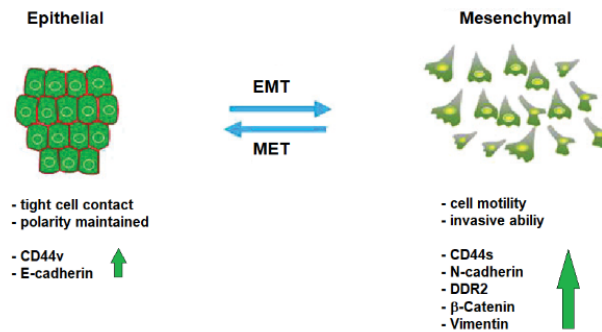


Figure 4.1 EMT and MET. Epithelial cells display tight cell-cell contacts, maintain polarity and are not particularly motile, whereas mesenchymal-like cells are more motile and invasive. Proteins associated with the epithelial-like or the mesenchymal-like states are referred to as biomarkers.

The progression of epithelial-derived tumors (carcinomas) may also involve spatial or temporal occurrences of EMT. Therefore, and not unlike other physiological processes that become coopted by tumor cells, the EMT can be considered a pathological process that contributes to cancer progression, particularly as it relates invasion and metastasis.⁶ In neoplastic cells, EMT is reflected by various degrees of epithelial change, from mild loss of cell polarity to the acquisition of frank mesenchymal/fibroblastic characteristics with increased cell motility.⁷ The main event in EMT is the loss of E-cadherin from adherens junctions, and several pathways have been involved in triggering it.⁸

The Wnt/ β -catenin pathway, for example, can promote EMT through activation of the Slug and Snail transcription factors, which are known to repress the E-cadherin promoter.^{9,10}

4.1.3 Role of E-Cadherin in EMT

The ability of a cell to undergo EMTs correlates with a loss of its ability to recognize with and adhere to its neighbors. One important molecule involved in these events is E-cadherin, a single transmembrane protein that mediates cell-cell adhesion in a strictly Ca^{2+} -dependent manner.⁶ In detail E-cadherin is the prototypic type I cadherin; type I cadherins mediate homophilic interactions by forming adhesive bonds between one or several immunoglobulin (Ig) domains in their extracellular region and connecting to actin microfilaments indirectly via α -catenin and β -catenin in the cytoplasm.¹¹⁻¹³ The intracellular domain of E-cadherin, in fact, is linked to the cytoskeleton through proteins like β -catenin or p120-catenin. These proteins interact with cytoskeletal components and are targets for regulatory interactions which thus modulate cell-cell interactions. The *de novo* production of E-cadherin in normal and transformed mesenchymal cells can induce the formation of stable cell-cell contacts and the development of adherens junctions (Figure 4.2). In epithelial cells, early contacts are also mediated by E-cadherin molecules that cluster into small junctional complexes, which then expand to establish stable adherens junctions and promote the formation of desmosomes.¹⁴⁻¹⁶

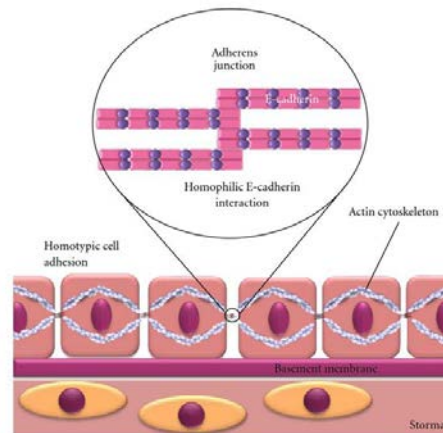


Figure 4.2 Diagrammatic representation of homophilic E-cadherin interaction and homotypic cell adhesion within the epithelium. E-cadherin cis-dimers form transhomodimers with E-cadherin molecules on neighbouring cells to facilitate epithelial integrity.

Another cadherin, N-cadherin, is produced in some carcinoma cells that have lost E-cadherin¹⁷ and, in these cellular contexts, N-cadherin behaves as a weak intercellular adhesion system. Targeted disruption of E-cadherin during tumor progression resulting in decreased intercellular adhesiveness is one of the most common alterations in human cancers.^{18,19} Further, abolishing E-cadherin function in vitro confers invasive properties to non-invasive cells and conversely, introduction of E-cadherin into invasive epithelial cell lines abrogates their invasive potential. In this regard, E-cadherin is considered a broadly acting suppressor of invasion and metastasis, and its functional inactivation represents a critical step in the acquisition of this capability.¹⁹ Not surprisingly, then, loss of E-cadherin expression is a defining characteristic of EMT.²⁰ Although a subset of tumors, including some lobular breast carcinomas and gastric cancers,²¹⁻²⁴ exhibit mutations in the E-cadherin gene, multiple mechanisms contribute to the inactivation of E-cadherin including promoter methylation, phosphorylation and transcriptional repression.¹⁸ Indeed, the discovery that transcriptional repressors of E-cadherin such as Snail, Slug and Twist contribute to invasion and metastasis has strengthened the evidence for the importance of the EMT in carcinoma progression.²⁵⁻²⁷

4.1.4 Transcriptional Repressors of E-cadherin: Snail, Slug and Twist

Slug (SNAI2) and Snail (SNAI1) are master regulatory transcription factors for organogenesis and wound healing that are also involved in the epithelial to mesenchymal transition (EMT) of cancer cells. In particular, Snail (SNAI1) is a zinc-finger transcription factor that belongs to a larger superfamily known as SNAI and participates in cell differentiation and survival.²⁸ Snail's main action mode is by inducing epithelial-to-mesenchymal transition (EMT) by suppression of E-cadherin transcription, which is responsible for cell adhesion and migratory capabilities.²⁹ Snail is sufficient to induce EMTs in tissue culture, and transfection of Snail into epithelial cell lines, such as MDCK, results in their mesenchymalization associated with a downregulation of E-cadherin expression (Figure 4.3).²⁵

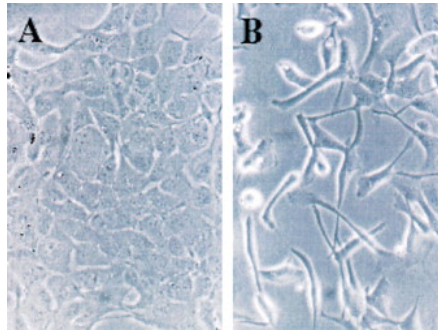


Figure 4.3 Snail Induces EMTs in MDCK Cells. (A) MDCK cells in tissue culture. (B) MDCK cells that express the snail gene constitutively.

Snail repression via silencing RNA (siRNA) results in decreased tumor metastasis and immunosuppression and, in addition, there is an increased T-cell response in the tumor due to suppression of Snail.³⁰ Slug (SNAI2) is another zinc-finger transcription factor crucial for EMTs; it has activities similar to Snail, including E-cadherin transcriptional repression and anti-apoptotic activity, and it plays a crucial role in organogenesis and neuralization.

Slug expression is increased in patients with melanoma, lung, colon and ovarian cancers.³¹ Snail and Slug are linked to tumor progression and invasiveness by their ability to alter E-cadherin and vimentin gene expression;³² Both Snail and Slug are, in fact, direct repressors of E-cadherin and act by binding to the specific E-boxes of E-cadherin's proximal promoter.³³ They have, also, been suggested to be involved in the acquisition of resistance to apoptosis, thereby promoting tumor survival. When Snail was overexpressed in epidermoid cancer cells, E-cadherin expression was lost with a concomitant change in cell morphology to a fibroblastic phenotype and vimentin gene expression was upregulated, indicating that Snail induced an EMT.³⁴ Finally, Twist is another promoter repressor of CDH1 (E-cadherin gene), also involved in tumor progression by silencing E-cadherin expression and EMT induction.^{27,35} Twist is considered as a promoter of the EMT, the key event in the tumoral invasion step. Up-regulation of Twist is associated with malignant transformation of melanoma and T-cell lymphoma.²⁷ It is possibly involved in E-cadherin conversion during EMT.³⁵

4.2 *Wnt/β-catenin Pathway*

Recently, increasing attention has been paid to cellular signal transduction in CRC, especially Wingless–Int (Wnt) pathway which regulates cell growth, differentiation and death in embryogenesis and tumor development, attributing to the presence of an activating mutation of the canonical Wnt signaling pathway in about 90% of all CRCs.³⁶⁻⁴⁰ The Wnt/β-catenin pathway is, in fact, activated in more than 90% of CRCs by mutations in either the APC gene (80%-85%) or the gene encoding β-catenin (5%-10%).⁴¹ Activation of the Wnt signaling pathway is characterized by the accumulation of the crucial transcriptional factor β-catenin in nuclei.⁴² It was reported, in fact, that nuclear β-catenin is detectable in colorectal tumors and its amount is increased from early adenomas to adenocarcinomas.⁴³ In detail, Wnts are powerful regulators of cell proliferation and differentiation, and their signaling pathway involves proteins that directly participate in both gene transcription and cell adhesion. The central player is β-catenin, which is a transcription cofactor with T cell factor/lymphoid enhancer factor TCF/ LEF in the Wnt pathway⁴⁴ and a structural adaptor protein linking cadherins to the actin cytoskeleton in cell-cell adhesion.⁴⁵ In the absence of Wnt signaling, intracellular β-catenin levels are regulated by multiprotein complex encompassing the adenomatous polyposis coli (APC) protein, axin, and glycogen synthase kinase 3β (GSK3β). The complex phosphorylates β-

catenin making it for subsequent ubiquitination and degradation (Figure 4.4 A). In the stimulated cells, Wnt ligands bind to one of the Wnt receptors, coactivating low-density lipoprotein receptor-related proteins (LRP). Binding of Wnts leads to phosphorylation of the cytoplasmic protein Dishevelled (Dsh) and consequently Dsh binds to axin resulting in dissociation of the complex and stabilization of β -catenin (Figure 4.4 B). Intracellular β -catenin accumulation results in its nuclear translocation, nevertheless the molecular mechanism is still unclear. In nuclei, β -catenin works as a cofactor for transcription factors of the T-cell factor/lymphoid enhancing factor (TCF/LEF), modulating the expression of a broad spectrum of target genes (Table 4.1), which affects stemness, proliferation and differentiation.⁴⁶ In 85% familial and sporadic CRCs, the APC gene mutations lead to loss of β -catenin degradation of the complex function and intracellular β -catenin accumulation and translocation, which is the mark of active Wnt signaling.³⁸ Accordingly, constitutive activation of this Wnt- β -catenin-TCF pathway, also called canonical Wnt pathway, is blamed for carcinogenesis in CRC.

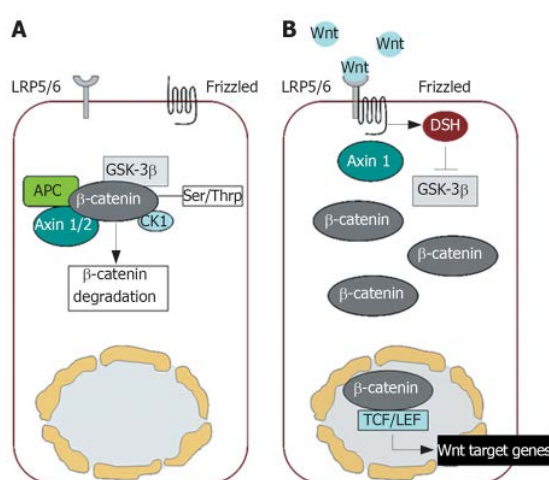


Figure 4.4 Schematic illustration of the canonical Wnt/ β -catenin signaling pathway. A: In the absence of Wnt ligands, destruction complex phosphorylates β -catenin for ubiquitination and proteolytic degradation; B: In the presence of Wnt ligands, formation of destruction complex is not accomplished, resulting in nuclear translocation of β -catenin.⁴⁶

Table 4.1 β -catenin target genes related to cancer.

Function	Function Target gene
Cell proliferation	C-myc; Cyclin D1
Inhibition of apoptosis	MDR1/PGP; COX-2; PPAR δ
Tumor progression	MMPs; uPAR,Upa; CD44; Laminin γ 2; Nr-CAM
Growth factors	c-met; VEGF; WISP-1; BMP-4
Transcription factors	c-jun, fra-1; ITF-2; Id2; AF17
Negative feedback targets	Conductin; Tcf-1; Nkd

4.2.1 Wnt Protein Secretion

Wnt proteins are characterized by a high number of conserved cysteine residues. Although Wnt proteins carry an N-terminal signal peptide and are secreted, they are relatively insoluble. This insolubility has been attributed to a particular protein

modification, cysteine palmitoylation, which is essential for Wnt function.⁴⁷ It was found out that a *Drosophila* gene required in the Wnt-secreting cell, termed *porcupine*, displays homology to acyl-transferases, enzymes that acylate a variety of substrates in the endoplasmic reticulum.⁴⁸ Thus, *porcupine* and its worm homolog *mom-1* are believed to encode the enzyme that is responsible for Wnt palmitoylation.⁴⁹ Recently, it was uncovered in *Drosophila* another conserved gene that is essential for Wnt secretion, named *wntless* (*wls*) and *evenness interrupted* (*evi*), respectively.^{50,51} The gene encodes a seven-pass transmembrane protein that is conserved from worms (*mom-3*) to man (*hWLS*). In the absence of *Wls/evi*, Wnts are retained inside the cell that produces them. The Wntless protein resides primarily in the Golgi apparatus, where it colocalizes and physically interacts with Wnts. A genetic screen in *C. elegans* revealed that the retromer, a multiprotein complex involved in intracellular trafficking and conserved from yeast to man, is also essential for Wnt secretion and for the generation of a Wnt gradient.⁵² An attractive hypothesis is that the retromer complex is involved in recycling a Wnt cargo receptor (such as Wntless) between the default secretory pathway and a compartment dedicated to Wnt secretion (Figure 4.5). Wnt is thought to act as a morphogen (that is, a long-range signal whose activity is concentration dependent).⁵³ However, it is unclear how these long-range gradients are generated. It is conceivable that the palmitoyl moiety constrains movement away from membranes or lipid particles. Thus, Wnts may be tethered to intercellular transport vesicles or lipoprotein particles.⁵⁴

Alternatively, Wnts may be transported by cytonemes, which are long, thin filopodial processes. Additionally, studies in *Drosophila* suggest a role for extracellular heparan sulfate proteoglycans (HSPG) in the transport or stabilization of Wnt proteins. For instance, flies carrying mutations in Dally, a GPI-anchored HSPG, or in genes encoding enzymes that modify HSPGs resemble wingless mutants.⁵⁵

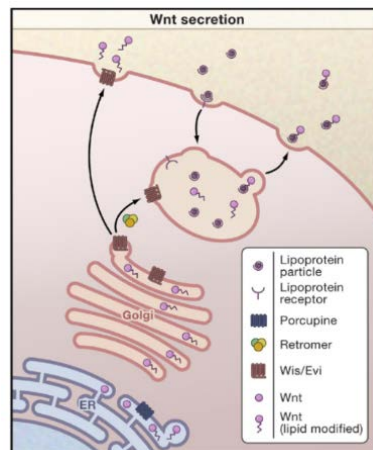


Figure 4.5 Wnt Secretion. To be secreted, Wnt proteins in the endoplasmic reticulum (ER) need to be palmitoylated by the action of Porcupine. Wnt proteins also require Wntless (Wls/Evi) in order to be routed to the outside of the cell. Loading onto lipoprotein particles may occur in a dedicated endo/exocytic compartment. The retromer complex may shuttle Wls between the Golgi and the endo/exocytic compartment.

4.2.2 Wnt Receptors, Agonists, and Antagonists

Wnts bind Frizzled (Fz) proteins, which are seven-pass transmembrane receptors with an extracellular *N*-terminal cysteine-rich domain (CRD; Figure 4.6).

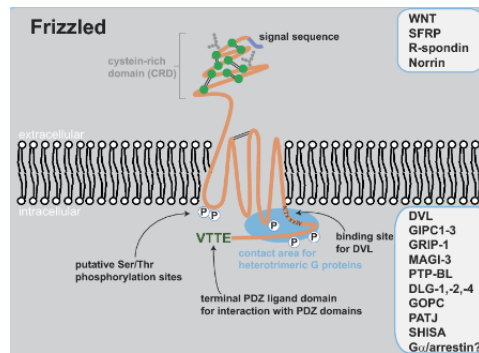


Figure 4.6 Simplified scheme of Frizzled structure and extracellular and intracellular binding partners. Extracellular and intracellular interaction partners are listed in the squares.

The Wnt-Fz interaction appears promiscuous, in that a single Wnt can bind multiple Frizzled proteins and vice versa.⁵⁶ In binding Wnt, Fzs cooperate with a single-pass transmembrane molecule of the LRP family known as Arrow in *Drosophila*⁵⁷ and LRP5 and LRP6 in vertebrates.⁵⁸ The transport of Arrow/LRP5/6 to the cell surface is dependent on a chaperone called Boca in *Drosophila* and Mesd in mice⁵⁹ and consistent with a role of the Boca/Mesd chaperone in the transport of Arrow/LRP5/6 transport, mutations in *Boca* and *Mesd* resemble loss of *Arrow/LRP5/6*. Although it has not been formally demonstrated that Wnt molecules form trimeric complexes with LRP5/6 and Frizzled, surface expression of both receptors is required to initiate the Wnt signal.

Derailed, a transmembrane tyrosine kinase receptor from the RYK subfamily, is an unusual Wnt receptor. *Drosophila* Wnt5 controls axon guidance in the central nervous system. Embryos lacking *Dwnt-5* resemble those lacking Derailed, that is, they generate aberrant neuronal projections across the midline.⁶⁰ Derailed binds DWnt-5 through its extracellular WIF (Wnt inhibitory factor) domain. Signaling events downstream of this alternative Wnt receptor remain unclear. Somewhat unexpectedly, the Derailed kinase domain may be dispensable for signaling, maybe because, unlike the *Drosophila* Ryk homolog Derailed, mammalian Ryk functions as a coreceptor along with Fz.⁶¹ Mammalian Ryk binds Dishevelled to activate the canonical Wnt/ β -catenin signaling pathway. Another tyrosine kinase receptor, *Ror2*, harbors a Wnt binding CRD motif. Wnt5a can engage *Ror2* to inhibit the canonical Wnt signaling pathway, although paradoxically Wnt5a can also activate the canonical pathway by directly engaging Fz4⁶² and Fz5.⁶³ At least two types of proteins that are unrelated to Wnt factors activate the Frizzled/LRP receptors. One of these factors is the cysteine-knot protein Norrin, which is mutated in Norrie disease, a developmental disorder characterized by vascular abnormalities in the eye and blindness. Norrin binds with high affinity to Frizzled-4 and activates the canonical signaling pathway in an LRP5/6-dependent fashion.⁶⁴ Other factors that activate the canonical Wnt signaling pathway are R-spondins, which are thrombospondin domain-containing proteins. Human R-spondin-1 has been found to strongly promote the proliferation of intestinal crypt cells, a process which involves the stabilization of β -catenin.⁶⁵ Indeed, studies in cultured cells demonstrate that R-spondins can physically interact with the extracellular domains of LRP6 and Fzd8 and activate Wnt reporter genes.⁶⁶ The secreted Dickkopf (Dkk) proteins inhibit Wnt signaling by direct binding to LRP5/6.⁶⁷ Through this interaction, Dkk1 crosslinks LRP6 to another class of transmembrane molecules, the Kremens,⁶⁸ thus promoting the internalization and inactivation of LRP6. An unrelated secreted Wnt inhibitor, *Wise*, also acts by binding to LRP,⁶⁹ as does the WISE family member SOST.^{70,71} Soluble Frizzled-Related Proteins (SFRPs) resemble the ligand-binding CRD domain of the Frizzled family of Wnt

receptors.⁷² WIF proteins are secreted molecules with similarity to the extracellular portion of the Derailed/RYK class of transmembrane Wnt receptors.⁷³ SFRPs and WIFs are believed to function as extracellular Wnt inhibitors⁵³ but, depending on context, may also promote signaling by Wnt stabilization or by facilitating Wnt secretion or transport.

Once bound by their cognate ligands, the Fz/LRP coreceptor complex activates the canonical signal-ing pathway (Figure 4.7).

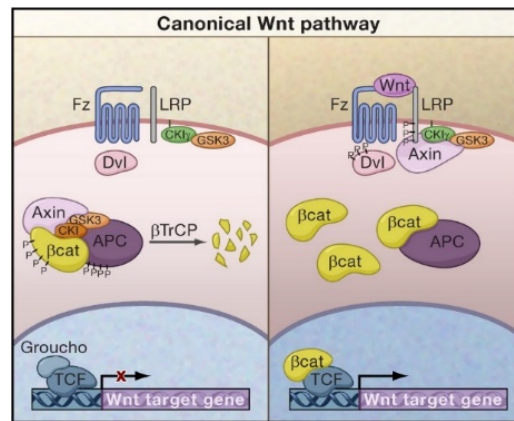


Figure 4.7 Canonical Wnt Signaling. (Left panel) When Wnt receptor complexes are not bound by ligand, the serine/threonine kinases, CK1 and GSK3 α/β , phosphorylate β -catenin. Phosphorylated β -catenin is recognized by the F box/WD repeat protein β -TrCP, a component of a dedicated E3 ubiquitin ligase complex. Following ubiquitination, β -catenin is targeted for rapid de-struction by the proteasome. In the nucleus, the binding of Groucho to TCF (T cell factor) inhibits the transcription of Wnt target genes. (Right panel) Once bound by Wnt, the Frizzled(Fz)/LRP coreceptor complex activates the canonical signaling pathway. Fz interacts with Dsh, a cytoplasmic protein that functions upstream of β -catenin and the kinase GSK3 β . Wnt signaling controls phosphorylation of Dishevelled (Dsh). Wnts are thought to induce the phosphorylation of LRP by GSK3 β and casein kinase I- γ (CK1 γ), thus regulating the docking of Axin. The recruitment of Axin away from the destruction complex leads to the stabilization of β -catenin. In the nucleus, β -catenin displaces Groucho from Tcf/Lef to promote the transcription of Wnt target genes.

Fz can physically interact with Dsh, a cytoplasmic protein that functions upstream of β -catenin and the kinase GSK-3. Wnt signaling controls phosphorylation of Dsh.⁷⁴ However, it remains unclear whether the binding of Wnt to Fz regulates a direct Fz-Dsh interaction, nor is it known how Dsh phosphorylation is controlled or how phosphorylated Dsh functions in Wnt signal transduction. Recent studies have indicated that the coreceptor LRP5/6 interacts with Axin through five phosphorylated PPP(S/T)P repeats in the cytoplasmic tail of LRP.⁷⁵ Wnts are thought to induce the phosphorylation of the cytoplasmic tail of LRP, thus regulating the docking of Axin. GSK3 phosphorylates the PPP(S/T)P motif, whereas casein kinase I- γ (CK1 γ) phosphorylates multiple motifs close to the GSK3 sites. CK1 γ is unique within the CK1 family in that it is anchored in the membrane through C-terminal palmitoylation. Both kinases are essential for signal initiation. It remains presently debated whether Wnt controls GSK3-mediated phosphorylation of LRP5/6⁷⁶ or whether CK1 γ is the kinase regulated by Wnt.⁷⁵ When bound to their respective membrane receptors, Dsh and Axin may cooperatively mediate downstream activation events by heterodimerization through their respective DIX (Dishevelled-Axin) domains.

4.2.3 β -catenin and The Cytoplasmic Destruction Complex

Beta-catenin (β -catenin) is a multifunctional, 90 kD protein that contributes to cell development under normal physiological conditions; it is the central player in the canonical Wnt cascade and its stability is regulated by the destruction complex. The tumor suppressor protein Axin acts as the scaffold of this complex as it directly interacts with all other components: β -catenin, the tumor suppressor protein APC, and the two kinase families (CK1 α , - δ , - ϵ and GSK3 α and - β).⁷⁷ When WNT receptor complexes are not engaged, CK1 and GSK3 α/β sequentially phosphorylate β -catenin at a series of highly conserved Ser/Thr residues near its *N*-terminus (Figure 4.7). Phosphorylated β -catenin is then recognized by the F box/WD repeat protein β -TrCP, a component of a dedicated E3 ubiquitin ligase complex. As a consequence, β -catenin is ubiquitinated and targeted for rapid destruction by the proteasome.⁷⁸ The CK1 and GSK3 kinases perform paradoxical roles in the Wnt pathway; at the level of the LRP coreceptor they act as agonists, whereas in the destruction complex they act as antagonists. Although genetic observations imply an essential role for APC in the destruction complex, there is no consensus on its specific molecular activity. APC has a series of 15 and 20 amino acid repeats with which it interacts with β -catenin. Three Axin-binding motifs are interspersed between these β -catenin-binding motifs. Increasing the expression of Axin in cancer cells that lack APC restores the activity of the destruction complex, implying that APC is only essential when Axin levels are limiting. Quantitatively, Axin indeed appears to be the limiting factor⁷⁹ and may be the key scaffolding molecule that promotes the rapid assembly and disassembly of the destruction complex. Given that CK1, Dsh, β -TrCP, and GSK3 participate in other signaling pathways, low levels of Axin may insulate the Wnt pathway from changes in the abundance or activity of these signaling components. It has been proposed that APC is required for efficient shuttling and loading/unloading of β -catenin onto the cytoplasmic destruction complex. Both APC and Axin can themselves be phosphorylated by their associated kinases, which changes their affinity for other components of the destruction complex. β -catenin plays a second role in simple epithelia, that is, as a component of adherens junctions; it is an essential binding partner for the cytoplasmic tail of various cadherins, such as E-cadherin.⁸⁰ Unlike the signaling pool of β -catenin, the pool that is bound to the adherens junction is highly stable. It is currently unclear whether the adhesive and signaling properties of β -catenin are interconnected. In a likely scenario, newly synthesized β -catenin first saturates the pool that is part of the adhesion junction, which never becomes available for signaling. "Excess," free cytoplasmic β -catenin protein is then efficiently degraded by the APC complex. It is only this second, highly unstable pool that is subject to regulation by Wnt signals. In support of this model, these two functions of β -catenin are separately performed by two different β -catenin homologs in *C. elegans*.⁸¹ Upon receptor activation by WNT ligands, the intrinsic kinase activity of the APC complex for β -catenin is inhibited. It is unclear how this occurs, but it likely involves the Wnt-induced recruitment of Axin to the phosphorylated tail of LRP and/or to Fz-bound Dsh. As a consequence, stable, nonphosphorylated β -catenin accumulates and translocates into the nucleus, where it binds to the *N* terminus of LEF/TCF (lymphoid enhancer factor/T cell factor) transcription factors (Figure 4.8).⁸²

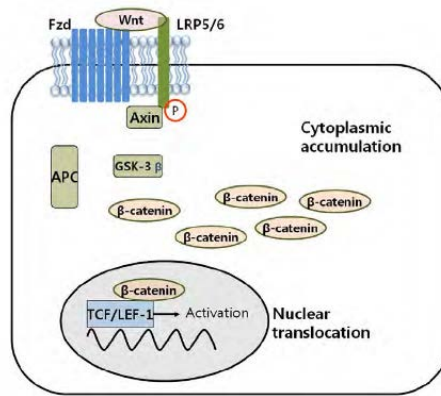


Figure 4.8 Regulation of Wnt/ β -catenin signaling pathway. Upon Wnt signaling, the activity of GSK-3 β is inhibited by Dsh, hence β -catenin is accumulated in the cytoplasm. The accumulated β -catenin can enter the nucleus and activates the target genes such as LEF-1, c-myc and cyclin D1.

It has been suggested that protein phosphatases may regulate β -catenin stability as antagonists of the serine kinases.⁷⁷ For example, heterotrimeric PP2A is required for the elevation of β -catenin levels that is dependent on Wnt.

Moreover, PP2A can bind Axin and APC, suggesting that it might function to dephosphorylate GSK3 substrates. If and how PP2A activity is regulated by Wnt signals remains to be resolved. Crystallographic studies are starting to provide insights into the structure of the destruction complex. The central region of β -catenin (to which most partners bind) was the first component of the pathway to be crystallized. It consists of 12 armadillo repeats, which adopt a superhelical shape with a basic groove running along its length. Subsequently, structural interactions of Axin, APC, E-cadherin, and TCF with β -catenin have been visualized (Figure 4.9).^{83,84} APC, E-cadherin, and TCF bind the central part of the basic groove in a mutually exclusive fashion. Despite very limited conservation of primary sequence in the respective interaction domains, the modes of binding are structurally very similar. Axin utilizes a helix that occupies the groove formed by the third and fourth armadillo repeats of β -catenin. Axin binding precludes the simultaneous interaction with other β -catenin partners in this region. Based on this observation, it is suggested that a key function of APC is to remove phosphorylated β -catenin from the active site of the complex.⁸⁵

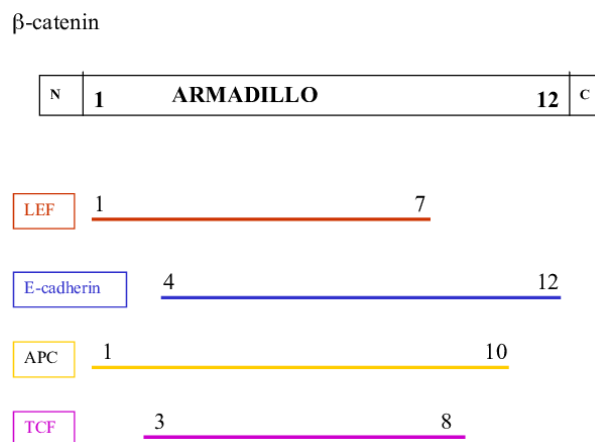


Figure 4.9 Diagram of the twelve armadillo repeats of β -catenin. The β -catenin protein consists of 12 armadillo repeats designated as 1-12. β -Catenin associates with specific proteins within the indicated region of the 12 repeats, in a mutually exclusive manner.

Armadillo repeats 1-7 is designated as the LEF binding region; E-cadherin binds to repeats 4-12; APC binds to repeats 1-10; Tcf binds to repeats 3-8 of the β -catenin protein. Armadillo protein 12 has been shown to be involved in transactivation of Wnt-responsive genes. N, N-terminus; C, Carboxy-terminus; LEF, lymphoid enhancer-binding factor; APC, adenomatous polyposis coli; TCF, T-cell Transcription factor.

4.2.4 Nuclear β -Catenin in CRC

Recently, it has been reported that APC mutations are associated with an accumulation of intracellular β -catenin protein, which leads to loss of control of normal β -catenin signalling.⁸⁶ The Wnt/ β -catenin pathway is activated in more than 90% of CRCs by mutations in either the APC gene (80%-85%) or the gene encoding β -catenin (5%-10%).⁴¹ These mutations interfere with the degradation of cytoplasmic β -catenin, allowing its translocation to the nucleus and the subsequent activation of genes involved in proliferation and EMT. Thus, β -catenin may promote colorectal adenoma formation resulting from the APC mutation. Recapitulating, β -catenin is involved in two major functions: cell adhesion and mediation of the Wingless/Wnt signal transduction pathway.⁸² Signal transduction of β -catenin involves post-translational stabilization and its passage into the nucleus, where it interacts with transcription factors of the T-cell factor or lymphoid enhancer factor (LEF) family to activate target genes regulating cell proliferation and apoptosis (Figure 4.10).⁸⁷

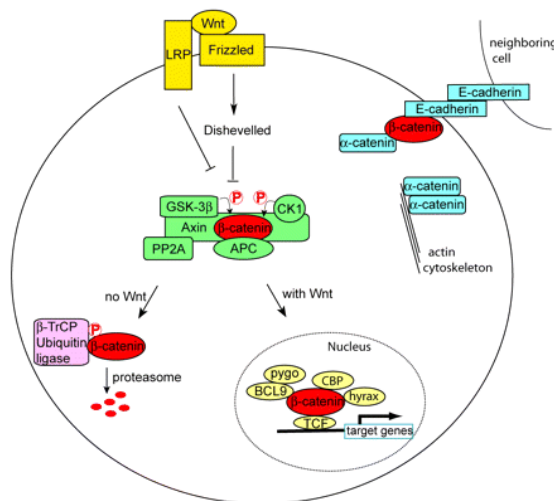


Figure 4.10 Role of β -catenin in cell.

Therefore, the specific localization of β -catenin may influence its oncogenic activity; nuclear β -catenin accumulation may be a valuable biomarker associated with invasion, metastasis and poor prognosis of CRC. However, the pathology of CRC is complex and cannot be fully explained by this central pathway alone.⁴⁶ Modifying influences are present within and outside the Wnt/ β -catenin central pathway, and it is interesting to investigate whether NHERF1/EBP50 (Na^+/H^+ exchanger 3 regulating factor 1; ezrin-radixin-moesin (ERM) binding phosphoprotein 50), an adaptor protein that interacts directly with β -catenin,⁸⁸ plays a role in CRC.

4.3 Role of NHERF1 (Na^+/H^+ exchanger 3 regulating factor 1) in CRC

NHERF1 is a 50-kDa adaptor protein of 358 amino acids carrying two NH_2 -terminal PDZ (postsynaptic density 95/discs large/ zona occludens 1) tandem domains. PDZ1 (11–97 amino acids) and PDZ2 (150–237 amino acids) show 74% identity to each other and bind to specific carboxyl-terminal motifs on target proteins, such as β -catenin and

PTEN, that may have a pivotal role in tumorigenesis. Besides the two tandem PSD-95/Disc-large/ZO-1 (PDZ) domains NHERF1 has a carboxyl (C)-terminal ERM-binding region.^{89,90} NHERF1 associates with β -catenin through its PDZ2 domain⁸⁸ and with ezrin through its ERM-binding region (Figure 4.11).⁸⁹

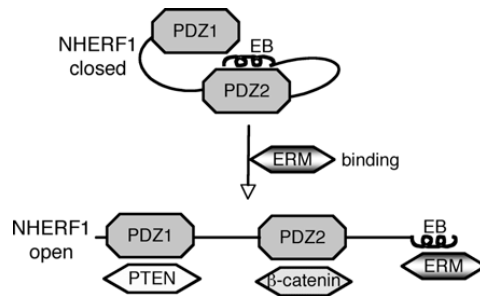


Figure 4.11 Model for NHERF1 complex formation with PDZ ligands. NHERF1 presents a “closed” conformation in which the PDZ2 domain binds to the C-terminal EB region in a “head-to-tail” interaction masking the PDZ domains. Engagement of the EB region by ERM proteins switches NHERF1 to an “open” conformation in which the PDZ domains are unmasked and able to bind PDZ domain ligands, represented here by PTEN and β -catenin.

NHERF1 is localized mainly at the apical plasma membrane (PM) in human epithelial tissues⁹¹ and its inactivation in mice induces ultrastructural abnormalities of the intestinal brush border membrane.^{92,93} Previous studies in mouse embryonic fibroblasts showed that NHERF1 behaves as a tumor suppressor through its effects on β -catenin and PTEN.^{94,95} Hayashi and coworkers found out that alterations in the apical membrane localization of NHERF1 contribute to CRC through the disruption of epithelial morphology; in their study they identify NHERF1 as a new player in CRC progression and support the notion that the expression or subcellular distribution of NHERF1 may be used as diagnostic marker for CRC.¹ In detail, they used intestinal Caco-2 cells to examine the function of NHERF1 in CRC. Caco-2 are unusual for CRC-derived cells in that, despite the presence of Apc and other genetic mutations,⁹⁶ they differentiate to quasi-normal polarized monolayers on reaching confluency in culture.⁹⁷ Importantly, endogenous NHERF1 is expressed in the microvilli at the apical membrane similar to normal intestinal cells, thus providing an *in vitro* cell system for the study of the stage-wise progression of CRC. Loss of NHERF1, as observed in adenoma, induced prominent epithelial morphology alterations manifested as typical EMT-like changes. Previous studies using NHERF1 knockdown in undifferentiated mouse embryonal carcinoma or syncytiotrophoblast cell lines have shown a requirement for NHERF1 only in microvilli morphogenesis.^{98,99} It seems that NHERF1 depletion triggers much more profound morphologic changes in intestinal epithelial cells, thereby implicating NHERF1 more broadly in epithelial morphogenesis. Surprisingly, the morphologic changes induced by NHERF1 depletion in polarized epithelial cells were not reversed by expression of wild-type NHERF1. In this instance, the expression of wild-type NHERF1 after previous depletion of endogenous NHERF1 resulted in cytoplasmic and nuclear localization of the protein and a more aggressive phenotype than the loss of NHERF1 alone. NHERF1 has been reported to interact with β -catenin and to increase β -catenin transcriptional activation in reporter assays.⁸⁸ In NHERF1-depleted cells, they observed a shift of β -catenin to the nucleus that most likely contributed to EMT and the increased invasiveness of cells. However, an extra layer of Wnt/ β -catenin activation may be added after expression of aberrantly localized NHERF1, perhaps by direct interactions with oncogenic β -catenin, and this could explain the increased proliferation and lack of EMT rescue (Figure 4.12).

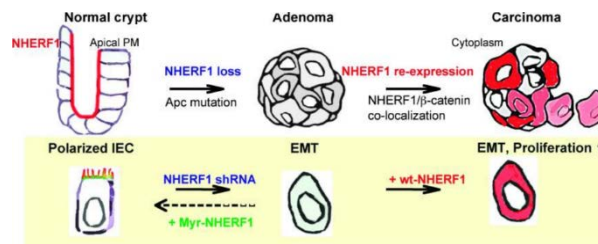


Figure 4.12 Model of the NHERF1 alterations in the progression of CRC and of the molecular interventions in Caco-2 intestinal epithelial cells (IECs) designed to mimic these alterations.

In addition, disruption of the PM localization of NHERF1 could destabilize PM complexes with other NHERF1 ligands and lead to structural abnormalities and increased cell invasiveness and proliferation.¹⁰⁰ For example, NHERF1 interacts with the ERM proteins,⁸⁹ and they have shown that the presence of NHERF1 at the apical PM is required for the proper brush border organization and the localization of the ERM proteins in the same compartment in intestinal epithelial cells *in vivo*.⁹³ Another member of the ERM family, the neurofibromatosis type 2 gene product merlin, interacts with NHERF1 in actin-rich membrane structures, such as ruffles, microvilli, and filopodia,¹⁰¹ and merlin displacement from PM has been linked to inactivation of its tumor suppressor function.^{102,103} Of note is that NHERF1 also interacts with platelet-derived growth factor receptor and epidermal growth factor receptor,^{104, 105} and its removal from the PM enhances the platelet-derived growth factor receptor–dependent signaling and cell motility.⁹⁵ Interestingly, the expression of membrane-targeted Myr-NHERF1 did rescue the EMT induced after depletion of endogenous NHERF1. Moreover, Myr-NHERF1 localized specifically to the apical PM dependent on the presence of the ERM-binding region in NHERF1.

In addition they have found that in polarized opossum kidney cells exogenous NHERF1 localizes at the apical microvilli, and disruption of the ERM-binding region either by truncation or mutation redirects it to the cytoplasm.^{106, 107} All these observations suggest that apically localized NHERF1 is required to maintain epithelial morphology but that it is the interaction with ERM proteins that properly localizes NHERF1 at the apical PM. In conclusion, this study they show how NHERF1 alterations correlate with the progression and enhanced invasiveness of human CRC and implicates NHERF1 as an important regulator of epithelial morphology. However, further studies are necessary to elucidate how the NHERF1 loss from the PM and the cytoplasmic re-expression in CRC occur because these seem to be sequential events correlated with the CRC pathological progression.

4.4 References

1. Hayashi, Y.; Molina, J.R.; Hamilton, S.R.; Georgescu, M.M. NHERF1/EBP50 is a new marker in colorectal cancer. *Neoplasia* **2010**, *12*, 1013-1022.
2. Coluccia, A.; La Regina, G.; Naccarato, V.; Nalli, M.; Orlando, V.; Biagioni, S.; De Angelis, M. L.; Baiocchi, M.; Gautier, C.; Gianni, S.; Di Pastena, F.; Di Magno, L.; Canettieri, G.; Coluccia, A. M. L.; Silvestri, R. Drug Design and Synthesis of First in Class PDZ1 Targeting NHERF1 Inhibitors as Anticancer Agents. *ACS Med. Chem. Lett.* **2019**, *10*, 499–503.
3. Jemal, A.; Siegel, R.; Ward, E.; Hao, Y.; Xu, J.; Murray, T.; Thun, M. J. Cancer statistics, 2008. *CA Cancer J Clin.* **2008**, *58*, 71–96.

4. Bates, R. C.; Pursell, B. M.; Mercurio, A. M. Epithelial-mesenchymal transition and colorectal cancer: gaining insights into tumor progression using LIM 1863 cells. *Cells Tissues Organs*. **2007**, *185*, 29–39.
5. Thiery, J. P. Epithelial-mesenchymal transitions in tumour progression. *Nat Rev Cancer*. **2002**, *2*, 442–454.
6. Arias, A. M. Epithelial mesenchymal interactions in cancer and development. *Cell* **2001**, *105*, 425–31.
7. Klymkowsky, M. W.; Savagner, P. Epithelial-mesenchymal transition: a cancer researcher's conceptual friend and foe. *Am J Pathol* **2009**, *174*, 1588–1593.
8. Schmalhofer, O.; Brabletz, S.; Brabletz, T. E-cadherin, β -catenin, and ZEB1 in malignant progression of cancer. *Cancer Metastasis Rev*. **2009**, *28*, 151–166.
9. Conacci-Sorrell, M.; Simcha, I.; Ben-Yedidia, T.; Blechman, J.; Savagner, P.; Ben-Ze'ev, A. Autoregulation of E-cadherin expression by cadherin-cadherin interactions: the roles of β -catenin signaling, Slug, and MAPK. *J Cell Biol*. **2003**, *163*, 847–857.
10. Yook, J. I.; Li, X. Y.; Ota, I.; Fearon, E. R.; Weiss, S. J. Wnt-dependent regulation of the E-cadherin repressor snail. *J Biol Chem*. **2005**, *280*, 11740–11748.
11. Takeichi, M. Morphogenetic roles of classic cadherins. *Curr. Opin. Cell Biol*. **1995**, *7*, 619–627.
12. Kemler, R. From cadherins to catenins: cytoplasmic protein interactions and regulation of cell adhesion. *Trends Genet*. **1993**, *9*, 317–321.
13. Tepass, U.; Truong, K.; Godt, D.; Ikura, M.; Peifer, M. Cadherins in embryonic and neural morphogenesis. *Nature Rev. Mol. Cell Biol*. **2000**, *1*, 91–100.
14. Adams, C. L.; Nelson, W. J. Cytomechanics of cadherin-mediated cell-cell adhesion. *Curr. Opin. Cell Biol*. **1998**, *10*, 572–577.
15. Kowalczyk, A. P.; Bornslaeger, E. A.; Norvell, S. M.; Palka, H. L.; Green, K. J. Desmosomes: intercellular adhesive junctions specialized for attachment of intermediate filaments. *Int. Rev. Cytol*. **1999**, *185*, 237–302.
16. Garrod, D.; Chidgey, M.; North, A. Desmosomes: differentiation, development, dynamics and disease. *Curr. Opin. Cell Biol*. **1996**, *8*, 670–678.
17. Frixen, U. H. et al. E-cadherin-mediated cell-cell adhesion prevents invasiveness of human carcinoma cells. *J. Cell Biol*. **1991**, *113*, 173–185.
18. Hirohashi, S. Inactivation of the E-cadherin-mediated cell adhesion system in human cancers. *Am J Pathol*. **1998**, *153*, 333–9.
19. Hanahan, D.; Weinberg, R. A. The hallmarks of cancer. *Cell*. **2000**, *100*, 57–70.
20. Thiery, J. P. Epithelial-mesenchymal transitions in tumour progression. *Nature Rev Cancer*. **2002**, *2*, 442–54.
21. Berx, G.; Cleton-Jansen, A. M.; Nollet, F.; de Leeuw, W. J.; van de Vijver, M.; Cornelisse, C.; van Roy, F. E-cadherin is a tumour/invasion suppressor gene mutated in human lobular breast cancers. *EMBO J*. **1995**, *14*, 6107–15.
22. Droufakou, S.; Deshmane, V.; Roylance, R.; Hanby, A.; Tomlinson, I.; Hart, I.R. Multiple ways of silencing E-cadherin gene expression in lobular carcinoma of the breast. *Int J Cancer*. **2001**, *92*, 404–8.
23. Oda, T.; Kanai, Y.; Oyama, T.; Yoshiura, K.; Shimoyama, Y.; Birchmeier, W.; Sugimura, T.; Hirohashi, S. E-cadherin gene mutations in human gastric carcinoma cell lines. *Proc Natl Acad Sci USA*. **1994**, *91*, 1858–62.
24. Becker, K. F.; Atkinson, M. J.; Reich, U.; Becker, I.; Nekarda, H.; Siewert, J. R.; Hofler, H. E-cadherin gene mutations provide clues to diffuse type gastric carcinomas. *Cancer Res*. **1994**, 3845–52.
25. Cano, A.; Perez-Moreno, M. A.; Rodrigo, I.; Locascio, A.; Blanco, M. J.; del Barrio, M. G.; Portillo, F.; Nieto, M. A. The transcription factor snail controls the

- epithelial-mesenchymal transitions by repressing E-cadherin expression. *Nat Cell Biol.* **2000**, *2*, 76-83. 23.
26. Batlle, E.; Sancho, E.; Franci, C.; Dominguez, D.; Monfar, M.; Baulida, J.; Garcia De Herreros, A. The transcription factor Snail is a repressor of E-cadherin gene expression in epithelial tumour cells. *Nat Cell Biol.* **2000**, *2*, 84-9.
27. Yang, J.; Mani, S. A.; Donaher, J. L.; Ramaswamy, S.; Itzykson, R. A.; Come, C.; Savagner, P.; Gitelman, I.; Richardson, A.; Weinberg, R. A. Twist, a master regulator of morphogenesis, plays an essential role in tumor metastasis. *Cell.* **2004**, *117*, 927-39.
28. Nieto, M.A. The snail superfamily of zinc-finger transcription factors. *Nat. Rev. Mol. Cel. Biol.* **2002**, *3*, 155-166.
29. Bolos, V.; Peinado, H.; Perez-Moreno, M. A.; Fraga, M. F.; Esteller, M.; Cano A. The transcription factor Slug represses E-cadherin expression and induces epithelial to mesenchymal transitions: a comparison with Snail and E47 repressors. *J. Cell Sci.*, **2003**, *116*, 499-511.
30. Kudo-Saito, C.; Shirako, H.; Takeuchi, T.; Kawakami, Y. Cancer metastasis is accelerated through immunosuppression during Snail-induced EMT of cancer cells. *Cancer Cell.* **2009**, *15*, 195-206.
31. Elloul, S.; Elstrand, M. B.; Nesland, J. M.; Trope, C. G.; Kvalheim, G.; Goldberg, I.; Reich, R.; Davidson B. Snail, Slug, and Smad-interacting protein 1 as novel parameters of disease aggressiveness in metastatic ovarian and breast carcinoma. *Cancer.* **2005**, *103*, 1631-1643.
32. Come, C.; Arnoux, V.; Bibeau, F.; Savagner P. Roles of the transcription factors snail and slug during mammary morphogenesis and breast carcinoma progression. *J. Mammary Gland Biol. Neoplasia.* **2004**, *9*, 183-193.
33. Seki, K.; Fujimori, T.; Savagner, P.; Hata, A.; Aikawa, T.; Ogata, N.; Nabeshima, Y.; Kaechoong, L. Mouse Snail family transcription repressors regulate chondrocyte, extracellular matrix, type II collagen, and aggrecan. *J. Biol. Chem.* **2003**, *278*, 41862-41870.
34. Yokoyama, K.; Kamata, N.; Fujimoto, R.; Tsutsumi, S.; Tomonari, M.; Taki, M.; Hosokawa, H.; Nagayama, M. Increased invasion and matrix metalloproteinase-2 expression by Snail-induced mesenchymal transition in squamous cell carcinomas. *Int. J. Oncol.* **2003**, *22*, 891-898.
35. Vernon, A. E.; La Bonne, C. Tumor metastasis: A new Twist on epithelial mesenchymal transitions. *Curr Biol.* **2004**, *14*, 719-721.
36. Miller, J. R.; Hocking, A. M.; Brown, J. D.; Moon, R. T. Mechanism and function of signal transduction by the Wnt/beta-catenin and Wnt/Ca²⁺ pathways. *Oncogene.* **1999**, *18*, 7860-7872.
37. Polakis, P. Wnt signaling and cancer. *Genes Dev.* **2000**, *14*, 1837-1851.
38. Giles, R. H.; van Es, J. H.; Clevers, H. Caught up in a Wnt storm: Wnt signaling in cancer. *Biochim Biophys Acta.* **2003**, *1653*, 1-24.
39. Taipale, J.; Beachy, P. A. The Hedgehog and Wnt signalling pathways in cancer. *Nature.* **2001**, *411*, 349-354.
40. Bienz, M.; Clevers, H. Linking colorectal cancer to Wnt signaling. *Cell.* **2000**, *103*, 311-320.
41. Vogelstein, B.; Kinzler, K. W. Cancer genes and the pathways they control. *Nat Med.* **2004**, *10*, 789-799.
42. Wong, N. A.; Pignatelli, M. Beta-catenin--a linchpin in colorectal carcinogenesis? *Am J Pathol.* **2002**, *160*, 389-401.
43. Brabletz, T.; Herrmann, K.; Jung, A.; Faller, G.; Kirchner, T. Expression of nuclear beta-catenin and c-myc is correlated with tumor size but not with proliferative activity of colorectal adenomas. *Am J Pathol.* **2000**, *156*, 865-870.

44. Cadigan, K. M.; Nusse, R. Wnt signaling: a common theme in animal development. *Genes Dev.* **1997**, *11*, 3286-305.
45. Jamora, C.; Fuchs, E. Intercellular adhesion, signalling and the cytoskeleton. *Nat Cell Biol.* **2002**, *4*, 101-8.
46. Huang, D.; Du, X. Crosstalk between tumor cells and microenvironment via Wnt pathway in colorectal cancer dissemination. *World J Gastroenterol.* **2008**, *14*, 1823-7.
47. Willert, K.; Brown, J. D.; Danenberg, E.; Duncan, A. W.; Weissman, I. L.; Reya, T.; Yates, J. R.; Nusse, R. Wnt proteins are lipid-modified and can act as stem cell growth factors. *Nature.* **2003**, *423*, 448-452.
48. Hofmann, K. A superfamily of membrane-bound O-acyltransferases with implications for wnt signaling. *Trends Biochem. Sci.* **2000**, *25*, 111-112.
49. Zhai, L.; Chaturvedi, D.; Cumberledge, S. Drosophila wnt-1 undergoes a hydrophobic modification and is targeted to lipid rafts, a process that requires porcupine. *J. Biol. Chem.* **2004**, *279*, 33220-33222.
50. Banziger, C.; Soldini, D.; Schutt, C.; Zipperlen, P.; Hausmann, G.; Basler, K. Wntless, a conserved membrane protein dedicated to the secretion of wnt proteins from signaling cells. *Cell.* **2006**, *125*, 509-522.
51. Bartscherer, K.; Pelte, N.; Ingelfinger, D.; Boutros, M. Secretion of wnt ligands requires evi, a conserved transmembrane protein. *Cell.* **2006**, *125*, 523-533.
52. Coudreuse, D. Y.; Roel, G.; Betist, M. C.; Destree, O.; Korswagen, H. C. Wnt gradient formation requires retromer function in Wnt-producing cells. *Science.* **2006**, *312*, 921-924.
53. Logan, C. Y.; Nusse, R. The Wnt signaling pathway in development and disease. *Annu. Rev. Cell Dev. Biol.* **2004**, *20*, 781-810.
54. Panakova, D.; Sprong, H.; Marois, E.; Thiele, C.; Eaton, S. Lipoprotein particles are required for Hedgehog and Wingless signaling. *Nature.* **2005**, *435*, 58-65.
55. Lin, X. Functions of heparan sulfate proteoglycans in cell signaling during development. *Development.* **2004**, *131*, 6009-6021.
56. Bhanot, P.; Brink, M.; Samos, C. H.; Hsieh, J. C.; Wang, Y.; Macke, J. P.; Andrew, D.; Nathans, J.; Nusse, R. A new member of the frizzled family from Drosophila functions as a Wingless receptor. *Nature.* **1996**, *382*, 225-230.
57. Wehrli, M.; Dougan, S. T.; Caldwell, K.; O'Keefe, L.; Schwartz, S.; Vaizel-Ohayon, D.; Schejter, E.; Tomlinson, A.; DiNardo, S. Arrow encodes an LDL-receptor-related protein essential for Wingless signaling. *Nature.* **2000**, *407*, 527-530.
58. Pinson, K. I.; Brennan, J.; Monkley, S.; Avery, B. J.; Skarnes, W. C. An LDL-receptor-related protein mediates Wnt signaling in mice. *Nature.* **2000**, *407*, 535-538.
59. Culi, J.; Mann, R. S. Boca, an endoplasmic reticulum protein required for wingless signaling and trafficking of LDL receptor family members in Drosophila. *Cell.* **2003**, *112*, 343-354.
60. Yoshikawa, S.; McKinnon, R. D.; Kokel, M.; Thomas, J. B. Wnt-mediated axon guidance via the Drosophila Derailed receptor. *Nature.* **2003**, *422*, 583-588.
61. Lu, W.; Yamamoto, V.; Ortega, B.; Baltimore, D. Mammalian Ryk is a Wnt coreceptor required for stimulation of neurite outgrowth. *Cell.* **2004**, *119*, 97-108.
62. Mikels, A. J.; Nusse, R. Purified Wnt5a protein activates or inhibits beta-catenin-TCF signaling depending on receptor context. *PLoS Biol.* **2006**, *4*, 115.
63. He, X.; Saint-Jeannet, J. P.; Wang, Y.; Nathans, J.; Dawid, I.; Varmus, H. A member of the Frizzled protein family mediating axis induction by Wnt-5A. *Science.* **1997**, *275*, 1652-1654.
64. Xu, Q.; Wang, Y.; Dabdoub, A.; Smallwood, P. M.; Williams, J.; Woods, C.; Kelley, M. W.; Jiang, L.; Tasman, W.; Zhang, K.; Nathans, J. Vascular development in

the retina and inner ear: control by Norrin and Frizzled-4, a high-affinity ligand-receptor pair. *Cell*. **2004**, *116*, 883-895.

65. Kim, K. A.; Kakitani, M.; Zhao, J.; Oshima, T.; Tang, T.; Binnerts, M.; Liu, Y.; Boyle, B.; Park, E.; Emtage, P.; Funk, W. D.; Tomizuka, K. Mitogenic influence of human R-spondin1 on the intestinal epithelium. *Science*. **2005**, *309*, 1256-1259.

66. Nam, J. S.; Turcotte, T. J.; Smith, P. F.; Choi, S.; Yoon, J. K. Mouse Cristin/R-spondin family proteins are novel ligands for the frizzled 8 and LRP6 receptors and activate beta-catenin-dependent gene expression. *J. Biol. Chem.* **2006**, *281*, 13247-13257.

67. Glinka, A.; Wu, W.; Delius, H.; Monaghan, A. P.; Blumenstock, C.; Niehrs, C. Dickkopf-1 is a member of a new family of secreted proteins and functions in head induction. *Nature*. **1998**, *391*, 357-362.

68. Mao, B.; Wu, W.; Davidson, G.; Marhold, J.; Li, M.; Mechler, B. M.; Delius, H.; Hoppe, D.; Stannek, P.; Walter, C.; Glinka, A.; Niehrs, C. Kremen proteins are Dickkopf receptors that regulate Wnt/beta-catenin signaling. *Nature*. **2002**, *417*, 664-667.

69. Itasaki, N.; Jones, C. M.; Mercurio, S.; Rowe, A.; Domingos, P. M.; Smith, J. C.; Krumlauf, R. Wise, a context-dependent activator and inhibitor of Wnt signaling. *Development*. **2003**, *130*, 4295-4305.

70. Li, X.; Zhang, Y.; Kang, H.; Liu, W.; Liu, P.; Zhang, J.; Harris, S. E.; Wu, D. Sclerostin binds to LRP5/6 and antagonizes canonical Wnt signaling. *J. Biol. Chem.* **2005**, *280*, 19883-19887.

71. Semenov, M.; Tamai, K.; He, X. SOST is a ligand for LRP5/LRP6 and a Wnt signaling inhibitor. *J. Biol. Chem.* **2005**, *280*, 26770-26775.

72. Hoang, B.; Moos Jr., M.; Vukicevic, S.; Luyten, F. P. Primary structure and tissue distribution of FRZB, a novel protein related to *Drosophila* frizzled, suggest a role in skeletal morphogenesis. *J. Biol. Chem.* **1996**, *271*, 26131-26137.

73. Hsieh, J. C.; Kodjabachian, L.; Rebbert, M. L.; Rattner, A.; Smallwood, P. M.; Samos, C. H.; Nusse, R.; Dawid, I. B.; Nathans, J. A new secreted protein that binds to Wnt proteins and inhibits their activities. *Nature*. **1999**, *398*, 431-436.

74. Wallingford, J. B.; Habas, R. The developmental biology of Dishevelled: an enigmatic protein governing cell fate and cell polarity. *Development*. **2005**, *132*, 4421-4436.

75. Davidson, G.; Wu, W.; Shen, J.; Bilic, J.; Fenger, U.; Stannek, P.; Glinka, A.; Niehrs, C. Casein kinase 1 gamma couples Wnt receptor activation to cytoplasmic signal transduction. *Nature*. **2005**, *438*, 867-872.

76. Zeng, X.; Tamai, K.; Doble, B.; Li, S.; Huang, H.; Habas, R.; Okamura, H.; Woodgett, J.; He, X. A dual-kinase mechanism for Wnt co-receptor phosphorylation and activation. *Nature*. **2005**, *438*, 873-877.

77. Price, M. A. CKI, there's more than one: casein kinase I family members in Wnt and Hedgehog signaling. *Genes Dev.* **2006**, *20*, 399-410.

78. Aberle, H.; Bauer, A.; Stappert, J.; Kispert, A.; Kemler, R. Beta-catenin is a target for the ubiquitin-proteasome pathway. *EMBO J.* **1997**, *16*, 3797-3804.

79. Lee, E.; Salic, A.; Kruger, R.; Heinrich, R.; Kirschner, M. W. The roles of APC and Axin derived from experimental and theoretical analysis of the Wnt pathway. *PLoS Biol.* **2003**, *1*, 10.

80. Peifer, M.; McCrea, P. D.; Green, K. J.; Wieschaus, E.; Gumbiner, B. M. The vertebrate adhesive junction proteins beta-catenin and plakoglobin and the *Drosophila* segment polarity gene armadillo form a multigene family with similar properties. *J. Cell Biol.* **1992**, *118*, 681-691.

81. Korswagen, R.; Herman, M.; Clevers, H. Distinct beta-catenins mediate adhesion and signaling functions in *C. elegans*. *Nature* **2000**, *406*, 527-532.

82. Behrens, J.; von Kries, J. P.; Kuhl, M.; Bruhn, L.; Wedlich, D.; Grosschedl, R.; Birchmeier, W. Functional interaction of beta-catenin with the transcription factor LEF-1. *Nature* **1996**, *382*, 638-642.
83. Choi, H. J.; Huber, A. H.; Weis, W. I. Thermodynamics of beta-catenin-ligand interactions: the roles of the N- and C-terminal tails in modulating binding affinity. *J. Biol. Chem.* **2006**, *281*, 1027-1038.
84. Murali, A. K.; Norris, J. S. The Role of E-Cadherin-Catenin Complex in Prostate Cancer Progression. *Adv. Prostate Cancer*. **2013**, *26*.
85. Spink, K. E.; Polakis, P.; Weis, W. I. Structural basis of the Axin-adenomatous polyposis coli interaction. *EMBO J.* **2000**, *19*, 2270-2279.
86. Munemitsu, S.; Albert, I.; Souza, B.; Rubinfeld, B.; Polakis, P. Regulation of intracellular β -catenin levels by the adenomatous polyposis coli (APC) tumor suppressor protein. *Proc Natl Acad Sci USA* **1995**, *92*, 3046-3050.
87. Korinek, V.; Barker, N.; Morin, P. J.; van Wichen, D.; de Weger, R.; Kinzler, K. W.; Vogelstein, B.; Clevers, H. Constitutive transcriptional activation by a β -catenin/Tcf complex in APC2/2 colon carcinoma. *Science* **1997**, *275*, 1784-1787.
88. Shibata, T.; Chuma, M.; Kokubu, A.; Sakamoto, M.; Hirohashi, S. EBP50, a β -catenin-associating protein, enhances Wnt signaling and is overexpressed in hepatocellular carcinoma. *Hepatology* **2003**, *38*, 178-186.
89. Reczek, D.; Berryman, M.; Bretscher, A. Identification of EBP50: A PDZ-containing phosphoprotein that associates with members of the ezrin-radixin-moesin family. *J Cell Biol* **1997**, *139*, 169-179.
90. Weinman, E. J.; Steplock, D.; Tate, K.; Hall, R. A.; Spurney, R. F.; Shenolikar, S. Structure-function of recombinant Na/H exchanger regulatory factor (NHE-RF). *J Clin Invest* **1998**, *101*, 2199-2206.
91. Stemmer-Rachamimov, A. O.; Wiederhold, T.; Nielsen, G. P.; James, M.; Pinney-Michalowski, D.; Roy, J. E.; Cohen, W. A.; Ramesh, V.; Louis, D. NHE-RF, a merlin-interacting protein, is primarily expressed in luminal epithelia, proliferative endometrium, and estrogen receptor-positive breast carcinomas. *Am J Pathol* **2001**, *158*, 57-62.
92. Broere, N.; Chen, M.; Cinar, A.; Singh, A. K.; Hillesheim, J.; Riederer, B.; Lunnemann, M.; Rottinghaus, I.; Krabbenhoft, A.; Engelhardt, R.; Rausch, B.; Weinman, E. J.; Donowitz, M.; Hubbard, A.; Kocher, O.; de Jonge, H. R.; Hogema, B. M.; Seidler, U. Defective jejunal and colonic salt absorption and altered Na⁺/H⁺ exchanger 3 (NHE3) activity in NHE regulatory factor 1 (NHERF1) adaptor protein-deficient mice. *Pflugers Arch* **2009**, *457*, 1079-1091.
93. Morales, F. C.; Takahashi, Y.; Kreimann, E. L.; Georgescu, M. M. Ezrin-radixin-moesin (ERM)-binding phosphoprotein 50 organizes ERM proteins at the apical membrane of polarized epithelia. *Proc Natl Acad Sci USA* **2004**, *101*, 17705-17710.
94. Kreimann, E. L.; Morales, F. C.; de Orbeta-Cruz, J.; Takahashi, Y.; Adams, H.; Liu, T. J.; McCrea, P. D.; Georgescu, M. M. Cortical stabilization of β -catenin contributes to NHERF1/EBP50 tumor suppressor function. *Oncogene* **2007**, *26*, 5290-5299.
95. Takahashi, Y.; Morales, F. C.; Kreimann, E. L.; Georgescu, M. M. PTEN tumor suppressor associates with NHERF proteins to attenuate PDGF receptor signaling. *EMBO J* **2006**, *25*, 910-920.
96. Gayet, J.; Zhou, X. P.; Duval, A.; Rolland, S.; Hoang, J. M.; Cottu, P.; Hamelin, R. Extensive characterization of genetic alterations in a series of human colorectal cancer cell lines. *Oncogene* **2001**, *20*, 5025-5032.
97. Simon-Assmann, P.; Turck, N.; Sidhoum-Jenny, M.; Gradwohl, G.; Kedinger, M. In vitro models of intestinal epithelial cell differentiation. *Cell Biol Toxicol* **2007**, *23*, 241-256.

98. Chiba, H.; Sakai, N.; Murata, M.; Osanai, M.; Ninomiya, T.; Kojima, T.; Sawada, N. The nuclear receptor hepatocyte nuclear factor 4 α acts as a morphogen to induce the formation of microvilli. *J Cell Biol* **2006**, *175*, 971–980.
99. Hanono, A.; Garbett, D.; Reczek, D.; Chambers, D. N.; Bretscher, A. EPI64 regulates microvillar subdomains and structure. *J Cell Biol* **2006**, *175*, 803–813.
100. Georgescu, M. M.; Morales, F. C.; Molina, J. R.; Hayashi, Y. Roles of NHERF1/EBP50 in cancer. *Curr Mol Med* **2008**, *8*, 459–468.
101. Murthy, A.; Gonzalez-Agosti, C.; Cordero, E.; Pinney, D.; Candia, C.; Solomon, F.; Gusella, J.; Ramesh, V. NHE-RF, a regulatory cofactor for Na⁺-H⁺ exchange, is a common interactor for merlin and ERM (MERM) proteins. *J Biol Chem* **1998**, *273*, 1273–1276.
102. Curto, M.; McClatchey, A. I. Nf 2/Merlin: a coordinator of receptor signalling and intercellular contact. *Br J Cancer* **2008**, *98*, 256–262.
103. Morales, F. C.; Molina, J. R.; Hayashi, Y.; Georgescu, M. M. Overexpression of ezrin inactivates NF2 tumor suppressor in glioblastoma. *Neuro Oncol* **2010**, *12*, 528–539.
104. Lazar, C. S.; Cresson, C. M.; Lauffenburger, D. A.; Gill, G. N. The Na⁺/H⁺ exchanger regulatory factor stabilizes epidermal growth factor receptors at the cell surface. *Mol Biol Cell* **2004**, *15*, 5470–5480.
105. Maudsley, S.; Zamah, A. M.; Rahman, N.; Blitzer, J. T.; Luttrell, L. M.; Lefkowitz, R. J.; Hall, R. A. Platelet-derived growth factor receptor association with Na(+)/H(+) exchanger regulatory factor potentiates receptor activity. *Mol Cell Biol* **2000**, *20*, 8352–8363.
106. Morales, F. C.; Takahashi, Y.; Momin, S.; Adams, H.; Chen, X.; Georgescu, M. M. NHERF1/EBP50 head-to-tail intramolecular interaction masks association with PDZ domain ligands. *Mol Cell Biol* **2007**, *27*, 2527–2537.
107. Hernando, N.; Deliot, N.; Gisler, S. M.; Lederer, E.; Weinman, E. J.; Biber, J.; Murer, H. PDZ-domain interactions and apical expression of type IIa Na/P(i) cotransporters. *Proc Natl Acad Sci USA* **2002**, *99*, 11957–11962.
108. Cardone, R. A.; Bellizzi, A.; Busco, G.; Weinman, E. J.; Dell’Aquila, M. E.; Casavola, V.; Azzariti, A.; Mangia, A.; Paradiso, A.; Reshkin, S. J. The NHERF1 PDZ2 domain regulates PKA-RhoA-p38-mediated NHE1 activation and invasion in breast tumor cells. *Mol Biol Cell* **2007**, *18*, 1768–1780.
109. Mangia, A.; Chiriatti, A.; Bellizzi, A.; Malfettone, A.; Stea, B.; Zito, F. A.; Reshkin, S. J.; Simone, G.; Paradiso, A. Biological role of NHERF1 protein expression in breast cancer. *Histopathology* **2009**, *55*, 600–608.
110. Song, J.; Bai, J.; Yang, W.; Gabrielson, E. W.; Chan, D. W.; Zhang, Z. Expression and clinicopathological significance of oestrogen-responsive ezrinradixin-moesin-binding phosphoprotein 50 in breast cancer. *Histopathology* **2007**, *51*, 40–53.

5. *NHERF1-Mediated Survival of CRC Cells After β -Catenin Knockdown*

5.1 *Introduction*

As illustrated in the previous chapter, nuclear activated β -catenin caused by Wnt-pathway mutations is the earliest driving event in hereditary (10%) and sporadic (90%) human colorectal cancers (CRC).¹ Deletion of the tumor suppressor adenomatous polyposis coli (APC) (>80%) or ‘gain-of-function’ mutations in GSK3 β -target residues in β -catenin gene (5–10%) increase the nuclear import of β -catenin with ensuing aberrant activation of TCF/LEF (T-cell factor/lymphoid enhanced factor) transcriptional factors. Activating mutations of KRAS and BRAF genes are detected in up to 60% of CRC, not long after APC or β -catenin mutations, and contribute to enforce the oncogenic signaling of β -catenin also conveying an invasive and metastatic behavior in cancer cells.² Despite its causative role in CRC, however, β -catenin remains an elusive therapeutic target. Targeting of β -catenin by small hairpin RNAs (shRNAs) or pharmacological inhibitors reduces the growth of established CRC xenografts in vivo without affecting the viability of malignant cells.^{3,4} CRC cells harboring inducible β -catenin shRNAs undergo cell cycle arrest, differentiate into polarized epithelial cells but rapidly resume their proliferative potential when relieved from β -catenin inhibition in vitro.^{5,6} Thus, from a biological and therapeutic perspective, a better characterization of the signaling outcome of β -catenin knockdown could provide new molecular events tied to survival control in CRC tumorigenesis that could be potentially used in combination therapy to improve the efficacy of Wnt-targeted approaches at early disease stages.

Recent data earmark NHERF1 as a tumor suppressor upstream of Wnt/ β -catenin-driven intestinal tumorigenesis in vivo.⁷ The complete lack of NHERF1 expression, either by shRNA knockdown in CRC cells or by gene knockout (NHERF1^{-/-}) in ApcMin/+ mutant mice that develop multiple intestinal adenomas, was reported to increase tumor growth and the transactivating effects of β -catenin.⁷ These data have relatively explained the heterogeneous pattern of NHERF1 observed in primary CRC,⁸⁻¹⁰ where membranous expression of NHERF1 is usually lost in dysplastic adenomas, and either absent or low/ectopically re-expressed through the cytoplasm and nuclei in approximately half of differentiated adenocarcinomas.^{11,12} Little is known about molecular mechanisms governing the early loss-of-NHERF1 expression in CRC and, in particular, the impact of oncogenic β -catenin remains unexploited.

5.2 *Objective of the Study*

In collaboration with Saponaro’s group we decided to explore a double β -catenin/NHERF1-inhibitory strategy as a fruitful approach to augment apoptotic death of CRC cells refractory to Wnt-targeted agents.¹³ In detail, using CRC cells harboring different Wnt/ β -catenin pathway mutations and low-NHERF1-levels at baseline, we show that genetic or pharmacological knockdown of β -catenin is sufficient to increase NHERF1 as a major driver of a cytoprotective autophagic response. As a Ph.D. student of Prof. R. Silvestri’s research group, I participated to the synthesis and characterization of compound **5.1** (see Experimental Section, 5.5.12) that was proved to be a novel NHERF1/ PDZ1-domain ligand antagonist with a promising therapeutic value.

5.3 *Results and Discussion*

5.3.1 *β -catenin represses NHERF1 expression by associating with TCF4*

An integrated doxycycline (Dox)-inducible shRNA vector was used to silence β -catenin in two human cell lines that recapitulate the earliest events implicated in CRC (Ls174T have mutated β -catenin/ KRAS genes and DLD-1 have mutated APC/KRAS genes) in order to investigate the impact of β -catenin on NHERF1 expression. β -catenin was successfully silenced in sh β -catenin stably transfected Ls174T and DLD-1 cells

(below named Ls174Tsh β -Cat and DLD1sh β -Cat) cultured with Dox (+Dox) compared with untreated cells (-Dox) or a mock clone expressing a negative control shRNA (shCtr) (Figure 5.1 A, B). Both CRC cell lines expressed low-steady-state levels of NHERF1 (Figure 5.1 B, C), while its mRNA transcript and protein levels was gradually increased in sh β -Cat-depleted CRC cells maintained under Dox (+Dox), achieving a peak of induction upon complete β -catenin knockdown (Figure 5.1 B, C).

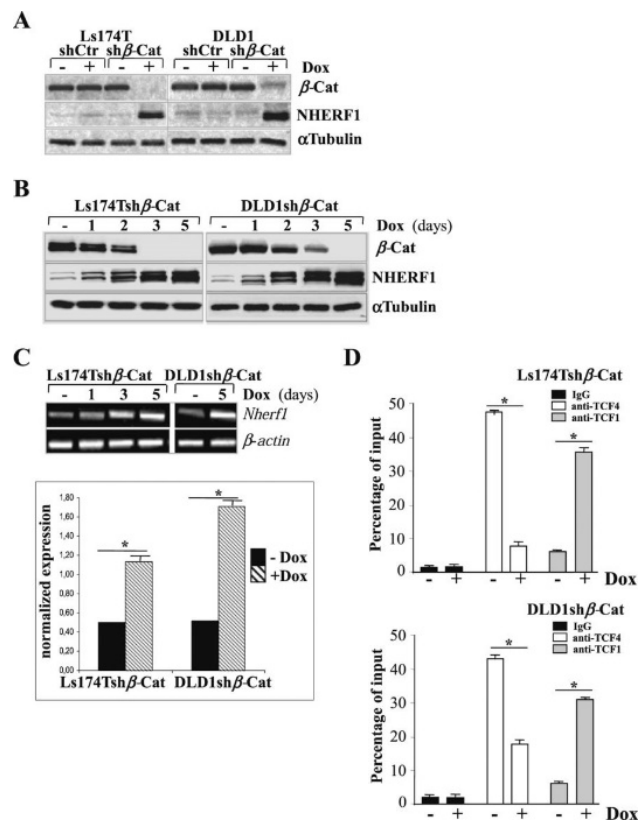


Figure 5.1 β -catenin represses NHERF1 expression through associating with TCF4. A: Ls174T and DLD1 cells stably transfected with a doxycycline (Dox)-inducible small hairpin (sh)RNA for β -catenin (sh β -Cat) or a scramble shRNA (shCtr) as control were cultured without (-) or with (+) Dox for 5 days. Total cell lysates were then probed for β -catenin (β -Cat) and NHERF1 protein amounts. Tubulin served as a loading control. B: Ls174Tsh β -Cat and DLD1sh β -Cat cells expressing a Dox-inducible shRNA for β -catenin were cultured without (-) or with (+) Dox for 1, 2, 3, or 5 days and then assessed by western blotting as indicated. C: an equal amount of RNA (1 μ g) of Ls174Tsh β -Cat and DLD1sh β -Cat cells cultured in the absence (-) or presence of Dox at the indicated time points, was analyzed by RT-PCR for assessing *nherf1* and β -actin mRNA levels. The normalized *nherf1* expression versus β -actin mRNA at day 5 was quantified by using Image J analysis software for Windows. Data from three independent experiments were presented as means \pm SEM (* p <0.05). D: ChIP of TCF1 and TCF4 in the *Nherf1* promoter region in Ls174Tsh β -Cat and DLD1sh β -Cat cells cultured in the absence (-) or presence of Dox (+) for 5 days. qPCR was performed to quantify ChIP assay results. Enrichment was quantified relative to input controls. An anti-IgG antibody was used as a negative control. Results are represented as the average \pm SD of three independent experiments (* p < 0.01).¹³

By using a ChIP assays it was possible to determine whether β -catenin regulates NHERF1 via recruiting key transcriptional mediators of the Wnt pathway like TCF1, also

called transcription factor 7 (TCF7), and TCF4 also called transcription factor 7-like 2 (TCF7L2), both of which involved in CRC carcinogenesis.^{1,2} It appeared evident that the knockdown of β -catenin strikingly reduced the binding of TCF4 with the Nherf1 promoter, while promoting the association with TCF1 in both CRC cell lines (Figure 5.1 D). The intracellular distribution of NHERF1 and β -catenin in Ls174Tsh β -Cat cells was then evaluated by laser scanning confocal microscopy (Figure 5.2 A). β -catenin was nearly undetectable in Dox-treated cells correlating with a more pronounced ectopic staining of NHERF1 compared with the Dox-untreated control samples (Figure 5.2 A). Similar results were obtained by testing DLD1sh β -Cat cells (data not shown), which were also subjected to cell fractionation experiments to assess changes on NHERF1 subcellular compartmentalization during β -catenin knockdown (Figure 5.2 B). A fraction of cortical β -catenin was evident in Dox-untreated CRC cells ($-$ Dox), although it was predominantly accumulated in the cytosolic and nuclear fractions, in line with an oncogenic β -catenin/TCF-transcriptional activation. Following Dox-exposure ($+$ Dox), β -catenin remained evident only in the nuclear extracts with ensuing increased cytoplasmic/nuclear NHERF1 levels vs Dox-untreated ($-$ Dox) cells.

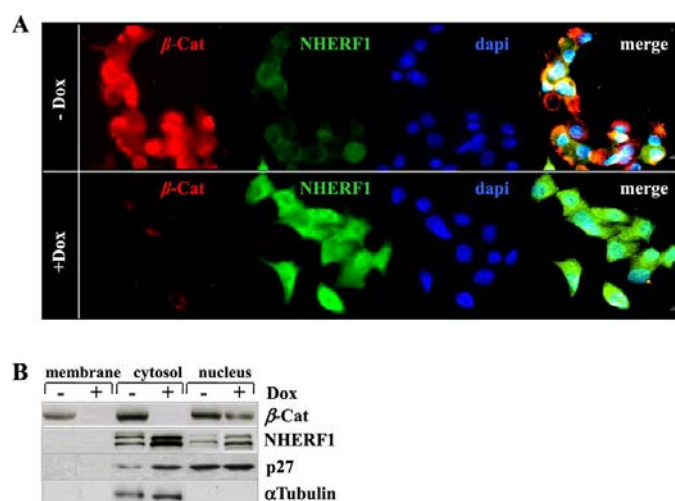


Figure 5.2 Ectopic cytoplasmic and nuclear overexpression of NHERF1 in β -catenin-depleted CRC adenocarcinoma cells. A: Ls174Tsh β -Cat were cultured in the absence or presence of Dox ($-$ Dox/ $+$ Dox) for 5 days, stained with primary antibodies for β -catenin (β -Cat) or NHERF1 and visualized with a fluorescent IgG-TRITC (for β -Cat) or IgG-FITC (for NHERF1) secondary antibodies by laser scanning confocal microscopy. DNA was stained with 4',6-diamidino-2-phenylindole (DAPI). A merge of the two fluorescence signals and DAPI staining is also shown (Magnification, $\times 60$). Each confocal image is representative of three independent experiments. B: DLD1sh β -Cat cells were cultured in the absence or presence of 2 μ g/mL of Dox ($-$ Dox/ $+$ Dox) for 5 days and then fractionated to obtain purified extracts from either membrane, cytosol, and nucleus of cells. Equal amounts of each cell extract (100 μ g) were separated by SDS-PAGE and probed with the indicated antibodies.¹³

NHERF1 was significantly upregulated in Ls174Tsh β -Cat cells treated with FH535 (5.1) and pyvinium pamoate (5.2), two unrelated drugs that have been reported to block β -catenin signaling via different mechanisms (Figures 5.3 and 5.4).

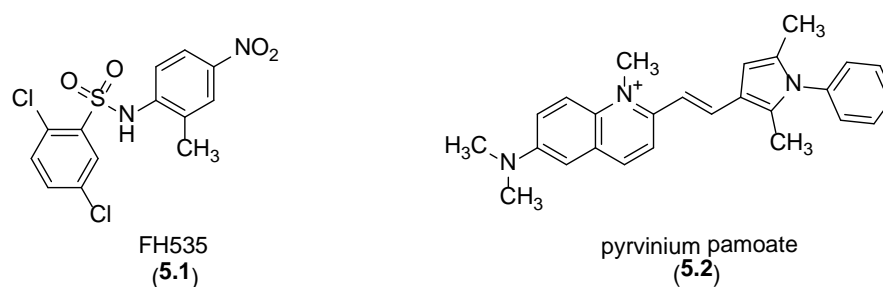


Figure 5.3 Structures of FH535 (5.1) and pyrvinium pamoate (5.2)

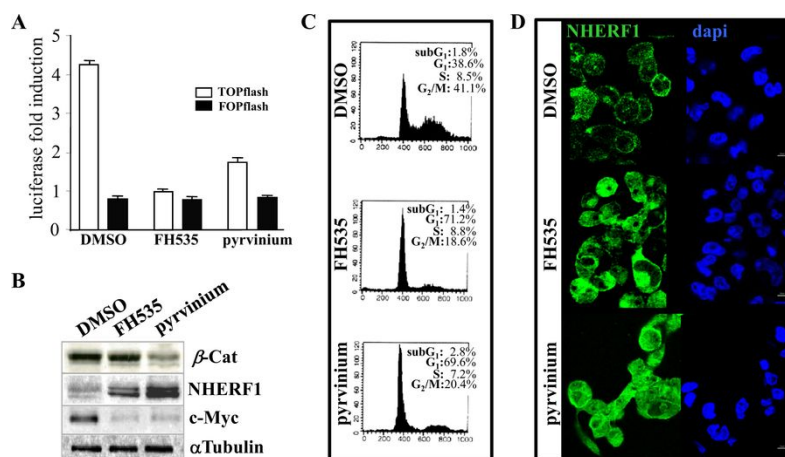


Figure 5.4 Small molecule inhibitors of β -catenin promote NHERF1 overexpression and mislocalization in CRC cells. **A**: Subconfluent Ls174Tsh β -Cat were co-transfected with the luciferase reporter constructs TOPflash or FOPflash. At 24h after transfection, cells were treated with vehicle alone (DMSO), FH535 (1 μ M) or pyrvinium pamoate (150nM) for additional 72h. Luciferase activity was expressed as fold activation compared with carrier control cells. Values represent means \pm SD of three representative experiments. **B**: After 4 days of treatment with DMSO, FH535 (1 μ M) or pyrvinium pamoate (150 nM), total cell lysates were probed for β -catenin (β -Cat), c-Myc and NHERF1 expression. Tubulin served as a loading control. **C**: Ls174Tsh β -Cat cells exposed for 4 days to DMSO, FH535 (1 μ M) or pyrvinium pamoate (150 nM) were analyzed by propidium iodide-staining and flow cytometric analysis for assaying cell cycle distribution. A representative dot plot of three replicate experiments shows the percentages of cells into different phases of the cell cycle for each indicated treatment. **D**: Each confocal image is representative of three independent immunofluorescence analyses of NHERF1 by a rabbit polyclonal antibody visualized with a fluorescent IgG-FITC secondary antibody for the indicated treatments (left panels). DAPI staining (right panels) is also shown (Magnification, $\times 60$).¹³

FH535 (5.1) is a sulfonamide-based compound that suppresses β -catenin/TCF-mediated transcription without affecting β -catenin levels;¹⁷ while pyrvinium (5.2) is an anthelmintic drug that promotes β -catenin degradation via activation of CK1 α (casein kinase1 α).¹⁸ Both drugs reduced transcription from the β -catenin/TCF-responsive reporter plasmid TOPflash (Figure 5.4 A) and expression of cMyc, a β -catenin transcriptional target that promotes cell proliferation (Figure 5.4 B). The two drugs induced CRC cell cycle arrest without significant apoptosis (Figure 5.4 C)^{5,6} and increased low-endogenous NHERF1 levels, as well as its ectopic cytoplasmic/nuclear subcellular distribution, although at a higher extent in pyrvinium (5.2) vs FH535 (5.1)-treated cells (Figure 5.4 D).

All together these data unveils a new oncogenic role for β -catenin in CRC through very early NHERF1 suppression at the transcriptional level via TCF4 directly

5.3.2 CRC Apoptosis after Genetic Targeting of β -catenin and NHERF1

Knockdown of β -catenin promoted cell differentiation coupled to a prominent vacuolization in Dox-treated (+Dox) Ls174Tsh β -Cat and DLD1sh β -Cat cells vs their untreated counterparts (-Dox) (Figure 5.5 A).^{5,6} Similarly to pharmacological targeting of β -catenin (Figure 5.3), genetic depletion of β -catenin was sufficient to cause cell cycle arrest (Figure 5.5 B, C, left panels) sustaining an adaptive autophagic response, as judged by staining for monodansylcadaverine (MDC) used as a hallmark of autophagic vacuoles (Figure 5.5 B, C, right panels). As shown in Figure 5.5 D, heightened endogenous levels of NHERF1 in settings of viable β -catenin-depleted CRC cells also correlated with hyperphosphorylated ERK1/2 (pERK1/2) and increased levels of the cell cycle inhibitor p27, as well as of key endocytosis/autophagy regulators, such as the microtubule associated protein light chain 3 (LC3), Beclin-1 (BECN1), Cathepsin D, the regulatory VIG1 subunit of the vacuolar ATPase (V-ATPase), the small GTPase Rab7 and its effector RILP.^{19,20} The accumulation of LC3-II, Beclin-1, and Cathepsin D isoforms were specific molecular makers of autophagy predicted based on morphological parameters (Figure 5.5 A).

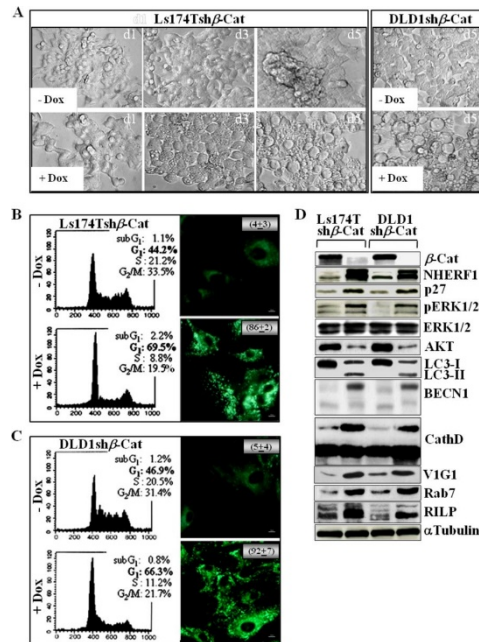


Figure 5.5 β -catenin-silenced CRC cells show a unique protein profile centred around autophagy and energy metabolism. Ls174T and DLD1 cells expressing a doxycycline (Dox)-inducible shRNA for β -catenin (Ls174Tsh β -Cat and DLD1sh β -Cat) were cultured without or with 2 μ g/mL of Dox (-Dox/+Dox) for 1, 3, or 5 days. A: A representative image of cells from one of the six fields captured from each well by using a camera attached to an inverted Olympus IX51 microscope is shown. B: After 5 days of treatment without or with doxycycline (-Dox/+Dox), Ls174Tsh β -Cat cells were analyzed by propidium iodide-staining and flow cytometric analysis for assaying cell cycle distribution. A representative dot plot of three replicate experiments shows the percentages of cells into different phases of the cell cycle for each indicated treatment (left panels). Under the same experimental conditions, Ls174Tsh β -Cat cells were analyzed for the presence of MDC-positive autophagosomes, distinct dot-like structures trapped in acidic, membrane-rich organelles distributed in the cytoplasm or localizing in the perinuclear regions of CRC cells (Magnification, $\times 60$). The numbers indicate the

percentage of autophagy induction for each treatment condition. C: After 5 days of treatment without or with doxycycline (-Dox/+Dox), cell cycle distribution of DLD1sh β -Cat cells was analyzed by propidium iodide-staining and flow cytometric analysis. A representative plot of three replicate experiments shows the percentages of cells into different phases of the cell cycle for each indicated treatment (left panels). DLD1sh β -Cat cells were analyzed for the presence of MDC-positive autophagosomes, as previously reported for Ls174Tsh β -Cat cells (Magnification, $\times 60$). The numbers indicate the percentage of autophagy induction for each treatment condition. D: Total cell lysates from Ls174Tsh β -Cat and DLD1sh β -Cat cultured without (-) or with (+) Dox for 5 days were assessed by western blotting with the indicated antibodies.¹³

These findings were corroborated by an unbiased broad proteomic characterization indicating that 1161 proteins were differentially expressed in Ls174Tsh β -Cat cells cultured with or without doxycycline (\pm Dox) (Figure 5.6). The heat-map generated by Perseus segregated samples into two separated branches characterized respectively by 464 proteins upregulated (Cluster 1) and 697 proteins downregulated (Cluster 2) in β -catenin-depleted cells. Each protein cluster was also enriched with specific signaling cascades based on KEGG (Kyoto Encyclopedia of Genes and Genomes) pathway analysis using STRING software (Table 5.1). These proteins were statistically categorized by STRING (false discovery rate $\leq 1.31e-05$) showing that Cluster 1 was enriched with proteins involved in the assembling of actin cytoskeleton and adherens junctions, fatty acid degradation, phagosome/lysosome maturation, autophagy, and endocytosis. Conversely, downregulated proteins into the Cluster 2 were involved in the regulation of spliceosome, RNA transport and ribosome biogenesis. This proteomic profiling corroborated the molecular changes reported in Figure 5.5 D, earmarking differences into our dataset in terms of energy metabolism, actin filament-based processes and especially autophagic/endocytic processes.

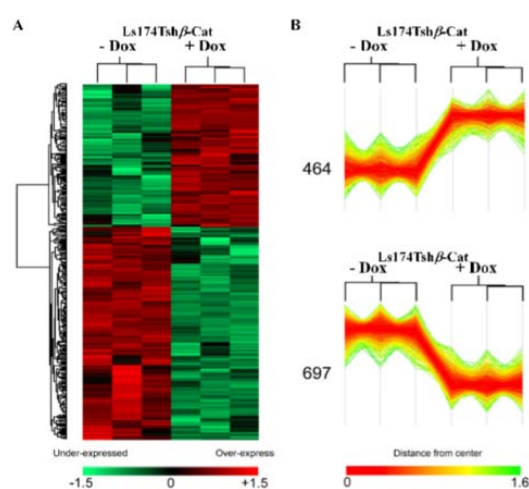


Figure 5.6 LC-MS/MS analysis of β -Catenin depleted CRC cells. A: Ls174Tsh β -Cat cells were cultured in the absence or presence of Dox (-Dox; n = 3 / +Dox; n = 3) for 5 days and analysed for the identification of differentially expressed proteins. Heat map of proteins with different regulation profiles as determined after label free quantification highlighting the presence of 2 main protein clusters. Hierarchical clustering of proteins was performed in Perseus on logarithmized intensities after z-score normalization of the data, using Euclidean distances. In each cluster, proteins down-regulated are presented in green, and proteins up-regulated are shown in red. B; Two main clusters extracted from A.

The windows contain the expression profiles of the proteins within clusters. The number of differentially expressed proteins in each cluster is also depicted.¹³

Table 5.1 The principle KEGG pathways of the upregulated and downregulated genes.

	Category	Pathway ID	Pathway description	Count in gene set	False discovery rate
Up-regulated	KEGG_PATHWAY	01100	Metabolic pathways	80	4.79e-17
	KEGG_PATHWAY	04810	Regulation of actin cytoskeleton	24	8.5e-09
	KEGG_PATHWAY	05132	Salmonella infection	15	3.03e-08
	KEGG_PATHWAY	04145	Phagosome	19	3.45e-08
	KEGG_PATHWAY	04721	Synaptic vesicle cycle	13	3.6e-08
	KEGG_PATHWAY	05110	Vibrio cholerae infection	12	4.97e-08
	KEGG_PATHWAY	04142	Lysosome	17	6.65e-08
	KEGG_PATHWAY	04144	Endocytosis	20	5.05e-07
	KEGG_PATHWAY	05130	Pathogenic Escherichia coli infection	11	5.54e-07
	KEGG_PATHWAY	00071	Fatty acid degradation	10	7.72e-07
	KEGG_PATHWAY	04530	Tight junction	17	7.72e-07
	Down-regulated	KEGG_PATHWAY	03040	Spliceosome	50
KEGG_PATHWAY		03013	RNA transport	40	1.06e-22
KEGG_PATHWAY		03008	Ribosome biogenesis in eukaryotes	27	1.68e-19
KEGG_PATHWAY		03010	Ribosome	34	1.68e-19
KEGG_PATHWAY		01100	Metabolic pathways	96	1.2e-14

A high confidence (0.700) was set as the threshold to define significant differences.¹³

The next challenge was to investigate whether NHERF1 could play a role in modulating ERK1/2 and Rab7 expression upon β -catenin depletion (Figure 5.7). To this end, Ls174Tsh β -Cat or DLD1sh β -Cat cells were transiently transfected with NHERF1 targeted shRNAs (shNHERF1) or scramble shRNAs as control (shCtr) and then cultured with or without Dox (\pm Dox) to modulate concomitantly stable si β -catenin expression. As shown in Figure 5.7 A, NHERF1 knockdown alone did not alter overall phospho-ERK1/2, Beclin-1 (BECN1), Rab7, and PARP protein levels at baseline, while combined targeting of NHERF1 and β -catenin annulled the hyper-activation of ERK1/2 and the accumulation of the autophagy markers Beclin-1 (BECN1) and Rab7 elicited by single- β -catenin depletion (Figure 5.7 A, 5.5 D). Such molecular changes were consistent with a massive apoptotic death occurrence in Dox-treated Ls174Tsh β -Cat/shNHERF1 (75 \pm 6%) and DLD1sh β -Cat/shNHERF1 (82 \pm 8%) cells, compared with <5% in controls (sh β -Cat/siCtr+Dox or sh β -Cat/shNHERF1–Dox) (Figure 5.7 B, C), as further confirmed by the cleavage of PARP (Figure 5.7 A) and Caspase-3 activity (Figure 5.7 D). A modest increase of β -catenin protein amounts was also evident in sh β -Cat/shNHERF1 maintained with or without Dox for 4 days (Figure 5.7 A), in keeping with additive affects that NHERF1 knockdown extents on β -catenin stabilization reported by others.⁷ Moreover, NHERF1 knockdown alone conferred a moderate clonogenic advantage to Dox-untreated Ls174Tsh β -Cat or DLD1sh β -Cat cells (Figures 5.8 A and B) which showed a more sprouted/invasive phenotype when cultured in sub-confluent monolayers (Figure 5.7 B)

or in soft agar (Figures 5.8 C). Collectively, these data indicate that combining NHERF1 inhibition in settings of β -catenin-silenced CRC cells, in which NHERF1 is highly/ectopically re-expressed, is mandatory to promote an autophagy-to-apoptosis switch in CRC cells refractory to single- β -catenin targeting.

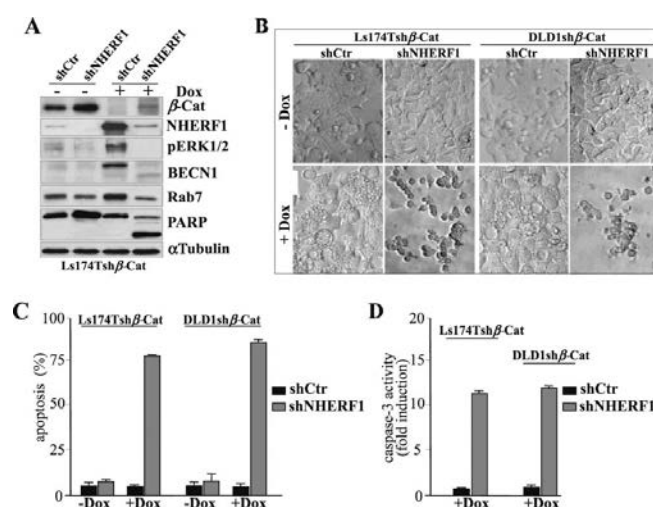


Figure 5.7 Combined shRNA-mediated downregulation of β -catenin and NHERF1-induces apoptosis in human CRC cells. Subconfluent Ls174T cells stably harboring a doxycycline (Dox)-inducible shRNA for β -catenin (Ls174Tsh β -Cat) were further transiently transfected with 200 nM of NHERF1 targeted shRNAs (shNHERF1) or scramble shRNAs as control (shCTR). **A**: Total protein extracts from double sh β Cat/shCTR or sh β -Cat/shNHERF1 expressing cells cultured without (-) or with (+) Dox for 5 days to simultaneously induce shRNAs for β -catenin were assessed by western blotting with the indicated antibodies. **B**: A representative image of Dox-treated (+Dox) or untreated shCTR or shNHERF1 expressing Ls174Tsh β -Cat or DLD1sh β -Cat cells from one of the six fields captured from each well by using a camera attached to an inverted Olympus IX51 microscope is shown. **C**: Ls174Tsh β -Cat or DLD1sh β -Cat cells expressing a scramble control shCTR or specific shRNAs for NHERF1 (shNHERF1) were cultured without (-) or with (+) Dox for 5 days and then labeled by Annexin V/PI (propidium iodide) staining for apoptosis evaluation by flow cytometry. Values represent the mean \pm SD of three independent experiments. **D**: Caspase-3 activity was also measured and data reported as fold induction over vehicle-treated control samples.¹³

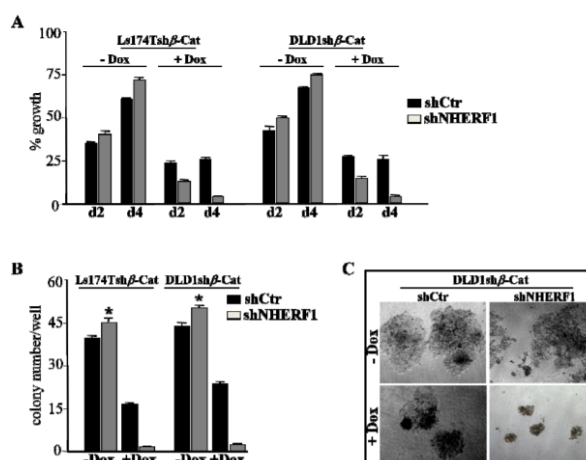


Figure 5.8 NHERF1 shRNA-knockdown confers a moderate growth advantage to CRC cells and promotes a sprouted/invasive phenotype. Subconfluent Ls174T or DLD1

cells stably harbouring a doxycycline (Dox)- inducible shRNA for β -Catenin (Ls174Tsh β -Cat or DLD1sh β -Cat) were further transiently transfected with 250 nM of NHERF1 targeted shRNAs (shNHERF1) or scramble shRNAs as control (shCtr). A: Proliferation assays of Ls174Tsh β -Cat or DLD1sh β -Cat transfected with the indicated shRNA and cultured in the absence or presence of Dox (-Dox/+Dox) for 2 and 4 days. Data were expressed as % of growth inhibition. B: Number of colonies formed in soft agar by Ls174Tsh β -Cat or DLD1sh β -Cat transfected with the indicated shRNA and cultured in the absence or presence of Dox (-Dox/+Dox) for 14 days. The values are presented as mean + SD of three independent experiments (*= P < 0.05). C: A representative cell colony image was captured for the indicted treatment condition by using a camera attached to an inverted Olympus IX51 microscope.¹³

5.3.3 Synthesis of a novel NHERF1/PDZ1-domain antagonist that synergizes with β -catenin inhibitors in promoting CRC apoptosis

The canonical inactivating binding motifs for the NHERF1 PDZ1-domain have been predicted in previous studies focused on small molecule ligands of the PDZ1-domain of NHERF1 to prevent its ectopic cytoplasmic/nuclear mislocalization and oncogenic function;²¹⁻²³ they are four D/E- (S/T)-X-(L/V/I/M) residues that are commonly contained at the C-terminal of its specific ligands, such as DSLL for the β 2-adrenergic receptor (β 2-AR) or ETWM for the parathyroid hormone receptor (PTHr).²⁴ Based on these premises, we evaluated the conformational flexibility of NHERF1 PDZ1-DSLL and PDZ1-ETWM peptide complexes by molecular dynamics (MD) simulations to draw a consensus pharmacophore model.^{25,26} An in-house library of 6000 compounds was screened using the pharmacophore model leading to the selection of compound **5.3** as the only one of six lowest-energy derivatives with remarkable cytotoxicity in vitro (Figure 5.9). Therefore, I participated to the synthesis of a large amount of compound **5.3**, namely 3-benzyl-5-chloro-N-(4-(hydroxymethyl)phenyl)-1*H*-indole-2-carboxamide; its chemical structure is depicted in Figure 5.9 A. The analysis of the binding mode of **5.3** led us to identify a series of residues involved in the interactions at the NHERF1 PDZ1 domain (Figure 5.9 B). Specifically: (i) a key Pi-cation interaction between the R80 guanidine and the benzyl group at position 3 of the indole of **5.3**; (ii) hydrophobic contacts between the 2-(4-hydroxymethyl)benzoyl moiety and F27 and I79 of the PDZ1, and between the indole nucleus and V76; (iii) two H-bonds with L27 backbone. To address the inhibitory effect of **5.3**, we resorted to test the effect of this molecule on NHERF1/PDZ1 domain in vitro. A construct encoding for NHERF1 PDZ1 was expressed and challenged with a dansylated peptide corresponding to the C-terminal sequence of β 2-AR (DNDSLL). In order to measure binding, a fluorescent pseudowild type was produced by replacing Tyr38 of PDZ1 with a Trp. Binding was then measured by Forster Resonance energy transfer between the fluorescent donor (Trp) and acceptor (Dansyl). Binding experiments were performed in the presence and in the absence of a constant concentration of **5.3** (Figure 5.9 C). It is evident, that, while the PDZ1 is capable to bind the C-terminal sequence of β 2-AR with an affinity of about 10 μ M, binding is essentially abolished in the presence of **5.3**.

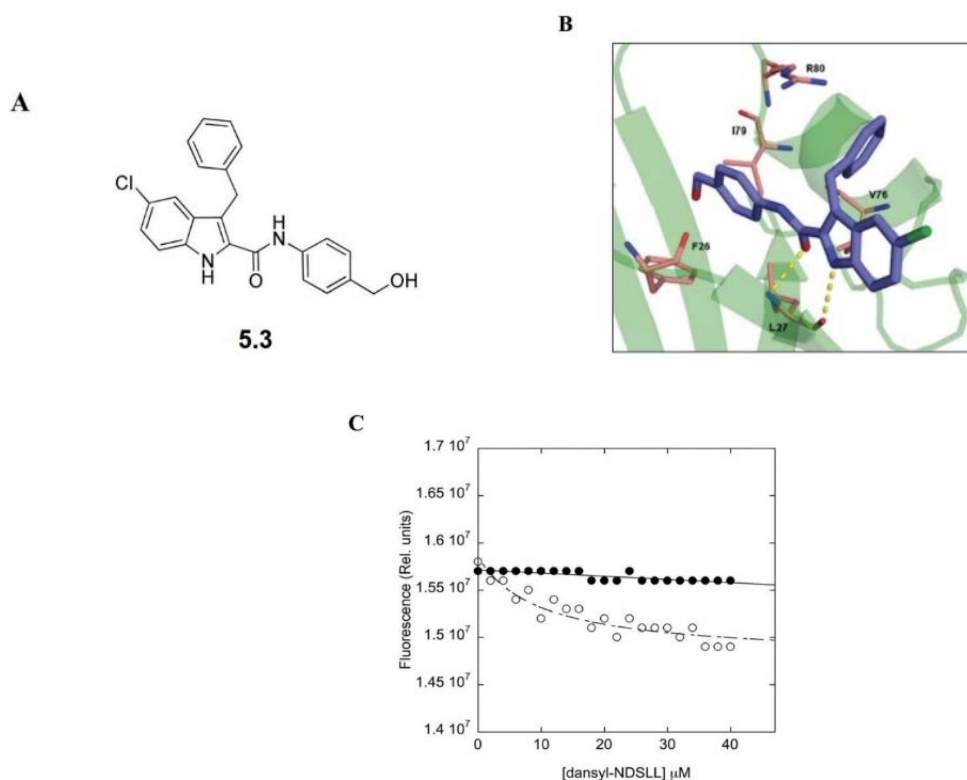


Figure 5.9 Compound **5.3** is a new PDZ1-domain antagonist of NHERF1. A: chemical structure of **5.3**. B: Proposed binding mode for **5.3** (purple) to the NHERF1 PDZ1 domain that is depicted as green cartoon. Residues involved in interactions were reported as pink stick. H-bonds were shown as yellow dot lines. C: Binding of PDZ1 NHERF1 Y38W to the ligand Dansyl-NDSLL in the presence (filled circles) and in the absence (open circles) of 5 mM **5.3**. Fluorescence data were recorded in the presence of 50 mM Na phosphate, pH 7.2, 300 mM NaCl, 5 mM DTT, 20% DMSO, at 25 °C. Lines are the best fit to a hyperbolic binding transition. It is evident that binding between PDZ1 NHERF1 Y38W to the ligand Dansyl-NDSLL is abolished in the presence of **5.3**.¹³

This finding confirms that this compound is a specific inhibitor of NHERF1/PDZ1 domain. To evaluate the growth inhibitory effects of **5.3**, Ls174Tsh β -Cat, or DLD1sh β -Cat cells were exposed to escalating doses (0.1–100 μ M) of the compound in the presence or absence of Dox for 4 days and then analyzed by MTT assays. As shown in Figure 5.10 A, the half maximal inhibitory concentration (IC₅₀) for **5.3** in Dox-untreated Ls174Tsh β -Cat or DLD1sh β -Cat cells expressing low levels of NHERF1 was 52 \pm 6 μ M and 65 \pm 11 μ M, respectively. Conversely, the equivalent IC₅₀ value of **5.3** was reduced to 8 \pm 2 μ M in Ls174Tsh β -Cat cells and 11 \pm 5 μ M in DLD1sh β -Cat cells maintained under concomitant Dox exposure. Our mechanistic investigations suggest that the enhanced cytotoxic effects of **5.3** against Dox-treated CRC cells can be explained by inhibition of a NHERF1-mediated survival response restricted to cells that silence β -catenin (Figure 5.7). Moreover, **5.3** used as single agent did not substantially affect the survival, proliferation rate and clonogenic potential of sh β -Cat transfected CRC cells (Figure 5.10 B, C). On the contrary, the combined use of 10 μ M **5.3** and Dox increased the proportion of apoptotic cells in the sub-G1 peak of the cell cycle compared with single-Dox exposure (86.6 vs 5.4%) (Figure 5.10 C), by also impairing the clonogenicity of β -catenin depleted cells (Figure 5.10 D). Interestingly, **5.3** alone did not confer any proliferative advantage to CRC cells compared with shRNA-based NHERF1 knockdown (Figure 5.8), while promoting the outgrowth of more cohesive cell colonies in soft agar (Figure 5.10 D).

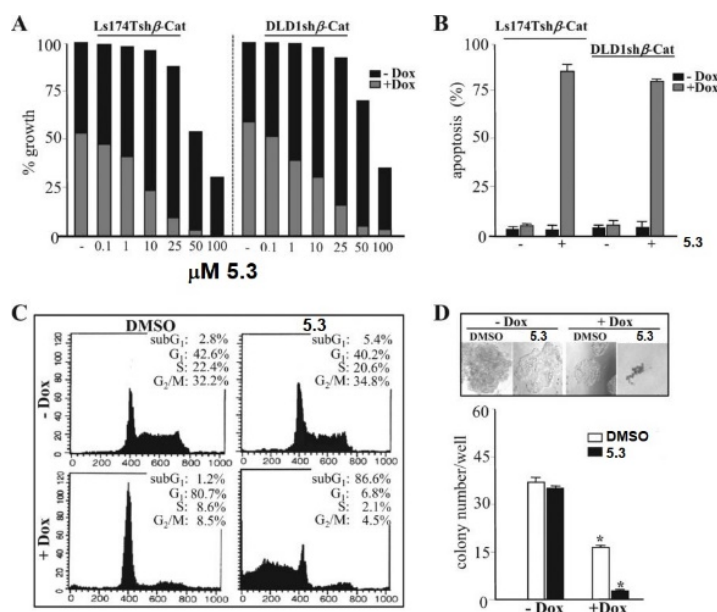


Figure 5.10 Compound **5.3** synergizes with shRNA-mediated silencing of β -catenin in promoting CRC cell death. **A:** Proliferation assays of Ls174Tsh β Cat or DLD1sh β -Cat cells exposed to increasing concentrations of **5.3** (range 0.1–100 μ M) or vehicle alone (–) in the absence or concomitant presence of Dox (–Dox/+Dox) for 5 days. Data were expressed as % of growth inhibition. **B:** Ls174Tsh β -Cat or DLD1sh β Cat cells were treated with 10 μ M **5.3** in the absence or presence of Dox (–Dox/+Dox) for 5 days and then labelled by Annexin V-PE for apoptosis evaluation by flow cytometry. Values represent the mean \pm SD of three independent experiments. **C:** Ls174Tsh β -Cat or DLD1sh β -Cat cells were treated with 10 μ M **5.3** (+) or DMSO as vehicle control (–) in the absence or concomitant presence of Dox (–Dox/+Dox) for 5 days and then analyzed by propidium iodide staining and flow cytometric analysis for assaying cell cycle distribution. A representative dot plot of three replicate experiments shows the percentages of cells into different phases of the cell cycle for each indicated treatment. **D:** Number of Ls174Tsh β -Cat or DLD1sh β -Cat colonies formed in soft agar containing DMSO or 10 μ M **5.3** after 14 days. The values are presented as mean \pm SD of three independent experiments (* $P < 0.05$). A representative cell colony image was captured for the indicated treatment condition by using a camera attached to an inverted Olympus IX51 microscope.¹³

Confocal immunofluorescence and cell fractionation analysis revealed that **5.3** markedly prevented the nuclear import of NHERF1 in CRC cells cultured in the absence or presence of Dox restoring its physiological membranous localization (Figure 5.11 A, B). Moreover, **5.3** did not change NHERF1 levels whilst it had stabilizing effects on the overall β -catenin protein content regardless of Dox treatment (Figure 5.11 B, C). To further exploit this issue, DLD1sh β -Cat cells were prior exposed to **5.3** and/or Dox for 3 days, then labeled with [³⁵S]-methionine and chased with complete non-radioactive medium for additional 4 or 8 h to analyze metabolic stability of β -catenin by pull-down assays (Figure 5.12). Compound **5.3** delayed the protein degradation rate of β -catenin, as judged by densitometric analysis (expressing the intensity of the labeled β -catenin bands as a percentage of the value at time 0) indicating that the estimated half-life of β -catenin was longer than 8 h in **5.3**-treated samples over DMSO control samples (–). The occurrence of apoptotic cell death in Ls174sh β -Cat cells exposed to Dox and **5.3** (Figure 5.10) was further confirmed by the cleavage of PARP and reduced phospho-ERK1/2, Beclin-1 (BECN1) and the Rab-effector RILP protein levels compared to cells exposed to

single-Dox treatment (i.e., only β -catenin silenced). Moreover, the **5.3**-mediated targeting of NHERF1 did not affect the overall Rab7 expression neither at baseline or during β -catenin knockdown (Dox setting), in contrast to what herein reported for shRNA-mediated NHERF1 knockdown (Figures 5.11 C and 5.5 A). We finally tried to recapitulate our previous findings by the use of **5.3** and small-molecule inhibitors of β catenin (Figure 5.13). We show here that **5.3** synergized with β -catenin inhibitors FH535 (**5.1**) and pyrvinium pamoate (**5.2**) in triggering massive apoptosis of Ls174T and DLD1 colon cancer cells (Figure 5.13 A, B), thereby preventing persistent ERK1/2 phospho-activation mediated by single- β -catenin targeting (Figure 5.13 C).

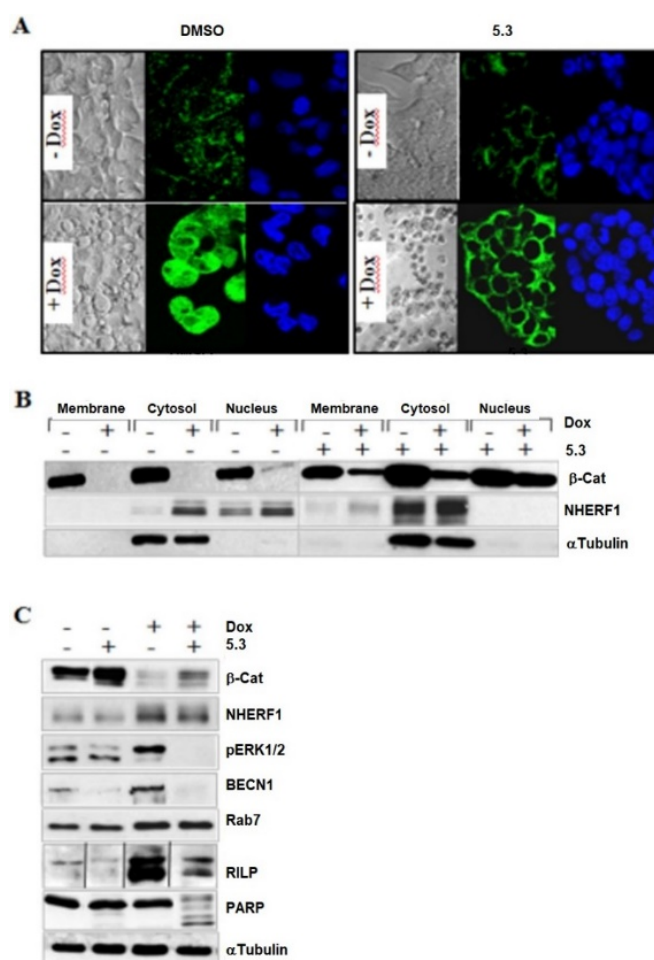


Figure 5.11 Compound **5.3** prevents nuclear import of NHERF1 and sh β catenin-mediated accumulation of phospho-ERK1/2 and RILP in CRC cells. **A**: DLD1sh β -Cat cells treated with 10 μ M **5.3** or DMSO in the absence or concomitant presence of Dox (-Dox/+Dox) for 5 days were stained using an anti-NHERF1 rabbit polyclonal primary antibody followed by an IgGFITC secondary antibody and DAPI staining for each indicated treatment. Each confocal image is representative of three independent immunofluorescence experiments (Magnification, $\times 60$). **B**: Ls174Tsh β -Cat cells were treated with 10 μ M **5.3** or DMSO in the absence or concomitant presence of 2 μ g/mL of Dox (-Dox/ +Dox) for 5 days and then fractionated to obtain purified extracts from either membrane, cytosol, and nucleus of cells. Equal amounts of each cell extract (100 μ g) were separated by SDS-PAGE and probed with the indicated antibodies. **C**: Ls174Tsh β -Cat cells were exposed to 10 μ M **5.3** in the absence or concomitant presence of 2 μ g/mL of Dox (-Dox/ +Dox) for 5 days and total lysates were then analyzed by western blotting with the indicated antibodies.¹³

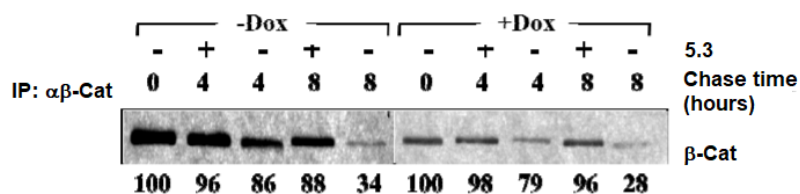


Figure 5.12 Compound **5.3** delays the protein degradation rate of β -catenin. Subconfluent DLD1Tsh β -Cat cells treated with 10 μ M **5.3** in the absence or concomitant presence of 2 μ g/mL of Dox (-Dox/+Dox) for 3 days were then labeled with [³⁵S]-methionine and chased with complete non-radioactive medium for additional 4 or 8 h. Cells were then lysed and immunoprecipitated for β -Catenin. The results were analyzed by densitometry and expressed as a percentage of the intensity value at time 0 for cells cultured without or with Dox (-Dox/+Dox), respectively.¹³

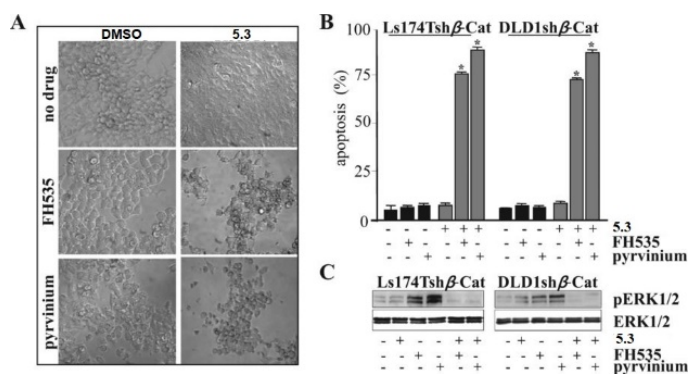


Figure 5.13 Compound **5.3** induces CRC cell death when combined to pharmacological inhibitors of β -catenin. A: Ls174Tsh β -Cat cells were treated with 10 μ M **5.3** as single agent or in combination with FH535 (1 μ M) or pyrvinium pamoate (150 nM) for 4 days and a representative image of one of the six fields captured from each well by using a camera attached to an inverted Olympus IX51 microscope is shown. B: Ls174Tsh β -Cat or DLD1sh β -Cat cells treated with 10 μ M **5.3** alone or in combination with FH535 (1 μ M) or Pyrvinium pamoate (150 nM) for 4 days were then labelled by Annexin V/propidium iodide staining for apoptosis evaluation by flow cytometry. Values represent the mean \pm SD of three independent experiments (*P < 0.003). C: Total lysates from Ls174Tsh β -Cat or DLD1sh β -Cat cells treated with 10 μ M **5.3** alone or in combination with FH535 (1 μ M) or Pyrvinium pamoate (150 nM) for 4 days were analyzed by western blotting with the indicated antibodies.¹³

5.4 Conclusions

The PDZ-scaffold protein NHERF1 is over-expressed in breast and colon carcinomas,^{11,12,14} associated significantly with aggressive histological grade and poor prognosis.²⁷⁻³¹

By physically tethering several cancer-related proteins, such as β -catenin,⁷ the tyrosine-kinase receptors PDGFR (platelet-derived growth factor receptor)³² and EGFR (epidermal growth factor receptor),³³ some Wnt-ligand engaged receptors of the Frizzled (FZD) family,³⁴ the tumor suppressor phosphatases PTEN (phosphatase and tensin homolog)³⁵ or PHLPP (PH leucine-rich repeat protein phosphatase),³⁶ NHERF1 engages in various functional complexes promoting specific phenotypic outcomes in cancer progression and metastatic organotropism.^{12,27,31} However, NHERF1 is early lost and weakly re-expressed

during the adenoma-toadenocarcinoma transition,^{7,11,27,35} thus playing potential antinomic roles as tumor suppressor, when it maintains a proper membrane localization, or tumor promoter when its expression is lost or mislocalized in the cytoplasm and nucleus.^{6,8} Regarding CRC, a recent study stated the tumor suppressor activity of NHERF1.^{6,7} NHERF1 depletion exacerbated the transformed phenotype in vitro and in vivo, thereby increasing nuclear β -catenin signaling.⁷ Here we showed that mRNA transcript and protein levels of NHERF1 expression are negatively regulated by oncogenic β -catenin signaling in CRC cell lines harboring different Wnt/ β -catenin pathway mutations. Moreover, ChIP assays demonstrated that nuclear activated β -catenin can regulate NHERF1 via TCF4 directly, while the interaction between TCF1 and the *nherf1* promoter increases upon β -catenin knockdown.¹³ These findings provide novel insight into the β -catenin/TCF-dependent mechanisms of CRC carcinogenesis, suggesting that the relative amounts of β -catenin and those of different TCFs may ultimately dictate or relieve a default repression of *nherf1* gene, in keeping with the notion that TCFs function as powerful transcriptional activators or repressors.³⁷

NHERF1 expression is known to be negatively regulated by histone deacetylases,³⁸ and was correlated with increasing levels of HIF1 α (hypoxia-inducible factor 1 α)^{27, 31} that competes with TCF4 for direct binding to β -catenin under hypoxia.³⁹ Thus, it seems conceivable that either epigenetic changes and/or microenvironment cues may further integrate different molecular factors, within or outside the central Wnt/ β -catenin cascade, to modulate NHERF1 expression, as well as the phenotypic heterogeneity observed in primary human CRC.^{7,10} Here we disclosed, maybe for the first time, NHERF1 as a major survival driver in settings of β -catenin depleted CRC cells which adopt a cytostatic viable phenotype and a unique proteomic signature centred around autophagy and energy metabolism processes (i.e., ribosome biogenesis, spliceosome and RNA transport, oxidative stress and fatty acid degradation). Accordingly, recent evidence earmark NHERF1 as an autophagy regulator in breast cancers via its influence on the ubiquitin-dependent degradation of BECN1, a critical component of the autophagic core lipid kinase complex.⁴⁰ Moreover, NHERF1 was recently implicated in the oxidative stress response regulation in liver cancer cells via the recruitment of the MAPK-activated protein kinase 2 (MK2) that belongs to the stress-induced p38 MAPK pathway.⁴¹ Genetic or pharmacological targeting of NHERF1 was sufficient to prime an 'autophagy-to-apoptosis switch' that strikingly impacted the fate of CRC cells during β -catenin knockdown. These data were remarkably consistent across two human CRC cell lines harboring different Wnt/ β -catenin pathway mutations in APC/KRAS or β -catenin/KRAS genes, thus excluding any clonal effects. Mechanistically, combined targeting of NHERF1 and β -catenin triggered the activation of Caspase-3 and the cleavage of PARP also abrogating the hyper-activation of ERK1/2, the accumulation of autophagy-related proteins like Beclin-1 (BECN1), Rab7 or its effector RILP elicited by single β -catenin knockdown. These molecular changes may relatively explain why a double β -catenin/NHERF1-inhibitory strategy may be a fruitful mechanism-based strategy to augment apoptotic death of CRC cells refractory to Wnt/ β -catenin-targeted therapeutics.^{3,5,6} However, as physiological or pathological roles of NHERF1 strictly depend on its subcellular localization, targeted approaches aiming at modulating NHERF1 activity, rather than its overall expression, would be preferred to preserve the normal functions of this versatile protein. By far, particular attention has been paid to the NHERF1/ PDZ1-domain that governs its membrane recruitment/displacement through a transient phosphorylation switch.²¹⁻²³

By using a rational virtual screening, we validated compound **5.3** as a novel NHERF1/PDZ1 ligand that abrogates its nuclear entry exhibiting a remarkable cytotoxicity on β -catenin-depleted CRC cells which highly reexpress NHERF1. Although,

further studies will exploit the safety profile of **5.3** in vivo, understanding that β -catenin signaling negatively regulates NHERF1 in CRC tumorigenesis will trigger the refinement of Wnt-targeted approaches to overcome the therapeutic resistance occurring at early disease stages.

5.5 Experimental Section

5.5.1 Cells Cultures and Reagents

Colorectal cancer (CRC) cell lines Ls174T and DLD-1 were purchased from the American Type Culture Collection (Manassas, VA, USA) and routinely assessed to check their identity.⁴² Cells were stably transfected with Doxycycline hyclate (Dox)-inducible short hairpin RNA (shRNA) for β -catenin (Ls174Tsh β -Cat and DLD1sh β -Cat) or a scramble control shRNA (shCtr), as previously described.^{3,42} To obtain NHERF1 downregulation, Ls174Tsh β Cat and DLD1sh β -Cat were transfected with 250 nM of NHERF1 shRNA (shNHERF1) or a scramble control shRNA (shCtr) (sc-156113) (Santa Cruz Biotechnology, CA, USA), according to the manufacturer's instructions. FH535 (**5.1**) (Calbiochem, San Diego, CA) and pyrvinium pamoate (**5.2**) (Sigma-Aldrich) were resuspended in dimethylsulfoxide (DMSO, Sigma-Aldrich).

5.5.2 RT-PCR

Total RNA of Ls174Tsh β -Cat and DLD1sh β -Cat cells was isolated using Trizol reagent (Invitrogen, Carlsbad, CA). The Nherf1 mRNA levels were determined using an RTPCR kit (New England Biolabs, Beverly, MA) and the following primers: forward 5'-CCCAGTGGCTATGGCTTCAA-3' and reverse 5'-GAAGTCTAGGATGGGGTCGG-3'. The primers for β -actin were: forward 5'-CCACGGCTGCTTCCAGCTCC-3' and reverse 5'-GGAGGGCCGACTCGTCAT-3'. The relative Nherf1 mRNA abundance versus β -actin mRNA was quantified by Image J analysis.

5.5.3 Chromatin immunoprecipitation (ChIP) assay

A CHIP-KIP, including an anti-TCF4 antibody, a mouse IgG control and Gapdh promoter primers was from Millipore (#17-10109). An anti-TCF1 antibody (clone 7H3) was also from Millipore. TCF-associated DNA immunoprecipitates were verified by qPCR using SYBR Green Mix (TaKaRa) and Nherf1 promoter primers as follows: Nherf1 5'-CCTCCGTCTTAATTCTCGAG-3' (forward) and 5'-CCTTCACCTTCACAAACAAT-3' (reverse). Data are reported as percent input of each IP sample relative to input chromatin for each amplicon and ChIP sample.

5.5.4 Immunofluorescence Staining

Cells were assayed using an anti-NHERF1 (1:500; ThermoFisher, Rockford, IL) or β -catenin primary antibody (1:500; BD Transduction Laboratories, Lexington, KY) followed by Alexa Fluor 488-conjugated goat anti-rabbit IgG-FITC or a goat anti-rabbit IgG-TRITC (1:1000; Molecular Probes, Inc., Eugene, OR) secondary antibodies, and then analyzed using a confocal laser scanning microscope (LSM 710, Zeiss, Germany), equipped with a 60 oilimmersion objective and a spatial resolution of 200 nm in x-y and 100 nm in z.

5.5.5 Staining of Monodansylcadaverine (MDC)-labeled Vacuoles

Cells were stained with 0.05 mM MDC in PBS at 37 °C for 10 min, washed and assayed by fluorescence microscope (Nikon Eclipse TE300, Japan). Images were captured using Image Pro-plus software.

5.5.6 Cell Proliferation and Apoptosis Assays

Cells (10^5 – 50^5 cells/well) were treated with serial dilutions of compound **5.3** or DMSO in the absence (–Dox) or presence (+Dox) of Dox in a volume of 200 μ l.

Cell growth was quantified by MTT (3-[4,5-dimethylthiazol-2-yl]-2,5-diphenyl Tetrazolium bromide) (Sigma-Aldrich) according to manufacturer's recommendations. For apoptosis assays, the cells were stained with Annexin V-PE (BD-PharMingen, San Diego, CA) or Caspase-Glo assay kit (Promega) and analyzed by flow cytometry.

5.5.7 Luciferase Reporter Assays, Flow Cytometry, and Soft Agar Clonogenic Analysis
Cells were analyzed as previously described.⁴²

5.5.8 Subcellular Fractionation Assays

Cells were collected in the subcellular fractionation buffer (SF buffer): 250 mM sucrose, 20 mM HEPES (pH 7.4), 10 mM KCl, 1.5 mM MgCl₂, 1 mM EDTA and EGTA, to which 1 mM DTT and protease/phosphatase inhibitors (1 mM PMSF; 5 mM NaF and 1 mM Na₃VO₄) were added at time of use. Lysates were then put on a tube roller (30–50 r.p.m.) at 4 °C for 30 min and centrifuged at 720 \times g at 4 °C for 5 min. Pellet was washed with 500 μ l of SF buffer, centrifuged at 720 \times g at 4 °C for 10 min, and dissolved for 15 min in nuclear lysis buffer (NL buffer): 50 mM Tris-HCl (pH 8), 150 mM NaCl, 1% NP-40, 0.5% sodium deoxycholate, 0.1% SDS, to which 10% glycerol and protease/phosphatase inhibitors were added at time of use. To obtain cytosolic fraction, the supernatant was centrifuged at 10,000 \times g at 4 °C for 10 min and ultracentrifuged at 100,000 \times g at 4 °C for 1 h. To obtain the membrane fraction, the ultracentrifuged pellet was washed with SF buffer and ultracentrifuged at 100,000 \times g at 4 °C for 1 h. Last pellet was dissolved in NL buffer and sonicated on ice.

5.5.9 Pulse-Chase Analysis, Immunoprecipitation, and Western Blotting

Cells were assayed as previously described.⁴² Primary antibodies were as follows: total β -catenin was from BD Transduction Laboratories, total NHERF1 from ThermoFisher, total c-Myc, cyclin D1, p27, Rab7, RILP, V1G1, Cathepsin D, and α -Tubulin were from Santa Cruz Biotechnology Inc. (Santa Cruz, CA), total and phosphorylated pERK1/2 (pThr202/Tyr204) MAPK, total AKT, LC3, Beclin-1 (BECN1), and PARP were from Millipore.

5.5.10 Sample Preparation and Mass Spectrometry Evaluation

Quantity of 20 μ g of whole-protein extracts prepared using Illustra TriplePrep kit (GE Healthcare) were diluted 10-fold in 8 M urea in 0.1 M Tris-HCl, pH 8.5, filtered into the Microcon Ultracel YM-30 devices (Millipore), and centrifuged at 14,000 \times g for 15 min. Samples were then further diluted in 8 M urea, centrifuged again, reduced in 10 mM DTT for 30 min, and then alkylated in 50 mM IAM for 20 min. After four washes (2 in 8 M urea and 2 in 50 mM NH₄HCO₃), trypsin solution was added in an enzyme-to-protein ratio of 1:100 w/w, and samples were maintained at 37 °C for 16 h. Peptides were centrifuged and acidified by trifluoroacetic acid, desalted-concentrated on C-18 ZipTip (Millipore), dried under vacuum and then resuspended in 20 μ l of ACN/H₂O (FA 0.1%) (2:98, v/v).

Separation was obtained using an EASY-nLC 1000 UPLC (Thermo Scientific) through 75 mm \times 2 cm pre-column with nanoViper fittings (Acclaim pepMap 100, C18, 2 μ m, Thermo Scientific) and 50 mm ID \times 150 mm analytical column with nanoViper fittings (Acclaim PepMap RSLC, C18, 2 μ m, Thermo Scientific). Elution was carried out over 120 min by using a 2-h gradient of ACN. The Q-Exactive instrument (Thermo Scientific) was set up to a spray voltage of 1.6 kV and the survey scans were taken at 70,000 FWHM (at m/z 400) resolving power in positive ion mode with a scan range from 300 to 1600 m/z.

5.5.11 Database Searching and Bioinformatics Analysis

Q-Exactive spectra were processed using the MaxQuant proteomics software (version 1.5.3.8) and matched using the Andromeda algorithm.⁴³ Trypsin was used as enzyme with two missed cleavages allowed. N-terminal acetylation and methionine oxidation were variable modifications, while carbamidomethylation of cysteines was a fixed modification. An initial mass spectra accuracy of 6 p.p.m. was selected, and the MS/MS tolerance was 20 p.p.m. for the HCD data with a false discovery rate of 1% for peptides and proteins identification. The MaxLFQ algorithm was used for assessing relative, label-free quantification of the proteins.⁴⁴

5.5.12 Chemical Synthesis of Compound 5.3

Derivative **5.3**, namely 3-benzyl-5-chloro-N-(4-(hydroxymethyl)phenyl)-1*H*-indole-2-carboxamide, was synthesized by coupling reaction of 3-benzyl-5-chloro-1*H*-indole-2-carboxylic acid with protected (4-(hydroxymethyl)aniline in the presence of PyBOP reagent and triethylamine in DMF. The product was deprotected by reaction with tetrabutylammonium fluoride solution (1 M in anhydrous THF).

5.5.13 Virtual Screening Studies

The NHERF1 PDZ1 domain was retrieved from the Protein Data Bank, under the PDB accession code 21GQ4 and the substrates (DSLL and ETVM) were drawn by Maestro (Schrödinger Release 2016-4: Maestro, Schrödinger, LLC, New York, NY, 2016) and analysed by molecular dynamics with Amber 12.⁴⁵ The minimized structure was solvated in a periodic octahedron simulation box using TIP3P water molecules, providing a minimum of 10 Å of water between the protein surface and any periodic box edge. Following minimization, the entire system was heated to 298 K (20 ps), and the simulation was conducted at 298 K with constant pressure, periodic boundary condition and shake bond length condition (ntc = 2). Trajectories analysis were carried out by the cpptraj modules.²⁵ This led to 5 structures for each complex which were used to draw a consensus pharmacophore model by Phase.²⁶ An in-house library of about 6000 compounds were docked into the binding site of each structures by Plants.⁴⁶ Structures fitting the pharmacophore queries were selected for biological evaluation. Picture was depicted by Pymol (PyMOL version 1.2r1. DeLanoScientificLLC:SanCarlos, CA).

5.5.14 In Vitro Binding Studies

A NHERF1 PDZ1 subcloned in pETG41 plasmid was kindly obtained from Dr. Nicolas Wolff (Pasteur Institute, Paris, France). A site-directed mutagenesis by Quickchange Lighting mutagenesis kit was confirmed by DNA sequencing. A dansylated peptide relative to the C-terminal portion of the β 2-adrenergic receptor, D-NDSLL, was from JPT Peptide Technologies (Berlin, Germany) and purified using HPLC. Equilibrium binding experiments were carried out in the presence of 50 mM Na phosphate buffer, pH 7.2, 300 mM NaCl at 25 °C by monitoring fluorescence upon exciting the sample at 280 nm and measuring emission on a Fluoromax single-photon spectrofluorometer (Jobin-Yvon, NJ, USA).⁴⁷

5.5.15 Statistical Analysis

Data are reported as the mean \pm SEM. Significance levels were determined with the Student's t-test. Proteomic statistical analysis was performed with the Perseus software (version 1.5.2.4). Multiple-samples tests were performed using ANOVA test by using a false discovery rate threshold of 0.05 and preserving grouping in randomization. Hierarchical clustering of proteins was performed in Perseus on logarithmized intensities

after z-score normalization of the data, using Euclidean distances. Gene Ontology (GO) and Kyoto Encyclopedia of Genes and Genomes (KEGG) analysis of our protein dataset was performed by STRING version 10 (<http://string-db.org>) (Nucleic Acids Res 2015; 43(Database issue):D447-52. doi: 10.1093/nar/gku1003).

5.6 References

1. Frattini, M.; Balestra, D.; Suardi, S.; Oggionni, M.; Alberici, P.; Radice, P.; Costa, A.; Daidone, M. G.; Leo, E.; Pilotti, S.; Bertario, L.; Pierotti, M. A. Different genetic features associated with colon and rectal carcinogenesis. *Cancer Res.* **2004**, *10*, 4015–21.
2. Janssen, K. P.; Alberici, P.; Fsihi, H.; Gaspar, C.; Breukel, C.; Franken, P.; Rosty, C.; Abal, M.; El Marjou, F.; Smits, R.; Louvard, D.; Fodde, R.; Robine, S. APC and oncogenic KRAS are synergistic in enhancing Wnt signaling in intestinal tumor formation and progression. *Gastroenterology.* **2006**, *131*, 1096–109.
3. Mologni, L.; Brussolo, S.; Ceccon, M.; Gambacorti-Passerini, C. Synergistic effects of combined Wnt/KRAS inhibition in colorectal cancer cells. *PLoS ONE.* **2012**, *7*, e51449.
4. Song, L.; Li, Y.; He, B.; Gong, Y. Development of small molecule targeting the Wnt signaling pathway in cancer stem cells for the treatment of colorectal cancer. *Clin Colorectal Cancer.* **2015**, *14*, 133–45.
5. van de Wetering, M.; Oving, I.; Muncan, V.; Pon Fong, M. T.; Brantjes, H.; van Leenen, D.; Holstege, F. C. P.; Brummelkamp, T. R.; Agami, R.; Clevers, H. Specific inhibition of gene expression using a stably integrated, inducible small-interfering-RNA vector. *EMBO Rep.* **2003**, *4*, 609–15.
6. Verma, U. N.; Surabhi, R. M.; Schmaltieg, A.; Becerra, C.; Gaynor, R. B. Small interfering RNAs directed against beta-catenin inhibit the in vitro and in vivo growth of colon cancer cells. *Clin Cancer Res.* **2003**, *9*, 1291–1300.
7. Georgescu, M. M.; Gagea, M.; Cote, G. NHERF1/EBP50 suppresses Wnt- β -catenin pathway-driven intestinal neoplasia. *Neoplasia.* **2016**, *18*, 512–23.
8. Georgescu, M. M.; Morales, F. C.; Molina, J. R.; Hayashi, Y. Roles of NHERF1/EBP50 in cancer. *Curr Mol Med.* **2008**, *8*, 459–68.
9. Hayashi, Y.; Molina, J. R.; Hamilton, S. R.; Georgescu, M. M. NHERF1/EBP50 is a new marker in colorectal cancer. *Neoplasia.* **2010**, *22*, 1013–22.
10. Georgescu, M. M.; Cote, G.; Agarwal, N. K.; White, C. L. NHERF1/EBP50 controls morphogenesis of 3D colonic glands by stabilizing PTEN and ezrin-radixin-moesin proteins at the apical membrane. *Neoplasia.* **2014**, *16*, 365–74.
11. Mangia, A.; Saponaro, C.; Malfettone, A.; Bisceglie, D.; Bellizzi, A.; Asselti, M.; Popescu, O.; Reshkin, S. J.; Paradiso, A.; Simone, G. Involvement of nuclear NHERF1 in colorectal cancer progression. *Oncol Rep.* **2012**, *28*, 889–94.
12. Saponaro, C.; Malfettone, A.; Dell’Endice, T. S.; Brunetti, A. E.; Achimas-Cadariu, P.; Paradiso, A.; Mangia, A. The prognostic role of the Na⁺/H⁺ exchanger regulatory factor 1 (NHERF1) protein in cancer. *Cancer Biomark.* **2014**, *14*, 177–84.
13. Saponaro, C.; Sergio, S.; Coluccia, A.; De Luca, M.; La Regina, G.; Mologni, L.; Famigliani, V.; Naccarato, V.; Bonetti, D.; Gautier, C.; Gianni, S.; Vergara, D.; Salzet, M.; Fournier, I.; Bucci, C.; Silvestri, R.; Gambacorti Passerini, C.; Maffia, M.; Coluccia, A. M. L. β -Catenin knockdown promotes NHERF1-mediated survival of colorectal cancer cells: implications for a double-targeted therapy. *Oncogene* **2018**, *37*, 3301–3316.
14. Yang, M.; Zhong, W. W.; Srivastava, N.; Slavin, A.; Yang, J.; Hoey, T.; An, S. G protein-coupled lysophosphatidic acid receptors stimulate proliferation of colon cancer cells through the beta-catenin pathway. *Proc Natl Acad Sci USA.* **2005**, *102*, 6027–32.
15. Ilyas, M.; Tomlinson, I. P.; Rowan, A.; Pignatelli, M.; Bodmer, W. F. Beta-catenin mutations in cell lines established from human colorectal cancers. *Proc Natl Acad Sci USA.* **1997**, *94*, 10330–34.

16. Gayet, J.; Zhou, X. P.; Duval, A.; Rolland, S.; Hoang, J. M.; Cottu, P.; Hamelin, R. Extensive characterization of genetic alterations in a series of human colorectal cancer cell lines. *Oncogene*. **2001**, *20*, 5025–32.
17. Handeli, S.; Simon, J. A. A small-molecule inhibitor of Tcf/betacatenin signaling down-regulates PPARgamma and PPARdelta activities. *Mol Cancer Ther*. **2008**, *7*, 521–29.
18. Thorne, C. A.; Hanson, A. J.; Schneider, J.; Tahinci, E.; Orton, D.; Cselenyi, C. S. Small molecule inhibition of Wnt signaling through activation of casein kinase 1alpha. *Nat Chem Biol*. **2010**, *6*, 829–36.
19. Cantalupo, G.; Alifano, P.; Roberti, V.; Bruni, C. B.; Bucci, C. Rabinteracting lysosomal protein (RILP): the Rab7 effector required for transport to lysosomes. *EMBO J*. **2001**, *20*, 683–93.
20. De Luca, M.; Cogli, L.; Progida, C.; Nisi, V.; Pascolutti, R.; Sigismund, S.; Di Fiore, P. P.; Bucci, C. RILP regulates vacuolar ATPase through interaction with the V1G1 subunit. *J Cell Sci*. **2014**, *127*, 2697–708.
21. Mayasundari, A.; Ferreira, A. M.; He, L.; Mahindroo, M.; Bashford, D.; Fuji, N. Rational design of the first small-molecule antagonists of NHERF1/EBP50 PDZ domains. *Bioorg Med Chem Lett*. **2008**, *18*, 942–45.
22. Du, G.; Gu, Y.; Hao, C.; Yuang, Z.; He, J.; Jiang, W. G.; Cheng, S. The cellular distribution of Na⁺/H⁺ exchanger regulatory factor 1 is determined by the PDZ-I domain and regulates the malignant progression of breast cancer. *Oncotarget*. **2016**, *7*, 29440–53.
23. Fitzpatrick, J. M.; Pellegrini, M.; Cushing, P. R.; Mierke, D. F. Small molecule inhibition of Na⁽⁺⁾/H⁽⁺⁾ exchange regulatory factor 1 and parathyroid hormone 1 receptor interaction. *Biochemistry*. **2014**, *53*, 5916–22.
24. Mamonova, T.; Kunikova, M.; Friedman, P. A. Structural basis for NHERF1 PDZ domain binding. *Biochemistry*. **2012**, *51*, 3110–20.
25. Roe, D. R.; Cheatham, T. E. PTRAJ and CPPTRAJ: Software for processing and analysis of molecular dynamics trajectory data. *J Chem Theory Comput*. **2013**, *9*, 3084–95.
26. Dixon, S. L.; Smondyrev, A. M.; Rao, N. S. PHASE: a novel approach to pharmacophore modeling and 3D database searching. *Chem Biol Drug Des*. **2006**, *67*, 370–72.
27. Cardone, R. A.; Bellizzi, A.; Busco, G.; Weinman, E. J.; Dell'Aquila, M. E.; Casavola, V.; Azzariti, A.; Mangia, A.; Paradiso, A.; Reshkin, S. J. The NHERF1 PDZ2 domain regulates PKARhoA-p38-mediated NHE1 activation and invasion in breast tumor cells. *Mol Biol Cell*. **2007**, *18*, 1768–80.
28. Song, G. J.; Leslie, K. L.; Barrick, S.; Mamonova, T.; Fitzpatrick, J. M.; Drombosky, K. W.; Peyser, N.; Wang, B.; Pellegrini, M.; Bauer, P. M.; Friedman, P. E.; Mierke, D. F.; Bisello, A. Phosphorylation of ezrin-radixin-moesin-binding phosphoprotein 50 (EBP50) by Akt promotes stability and mitogenic function of S-phase kinase-associated protein-2 (Skp2). *J Biol Chem*. **2015**, *290*, 2879–87.
29. Bellizzi, A.; Mangia, A.; Malfettone, A.; Cardone, R. A.; Simone, G.; Reshkin, S. J.; Paradiso, A. Na⁺/H⁺ exchanger regulatory factor 1 expression levels in blood and tissue predict breast tumour clinical behaviour. *Histopathology*. **2011**, *58*, 1086–95.
30. Karn, T.; Pusztai, L.; Holtrich, U.; Iwamoto, T.; Shiang, C. Y.; Schmidt, M.; Muller, V.; Solbach, C.; Gaetje, R.; Hanker, L.; Ahr, A.; Liedtke, C.; Ruckhaberle, E.; Kaufmann, M.; Rody, A. Homogeneous datasets of triple negative breast cancers enable the identification of novel prognostic and predictive signatures. *PLoS ONE*. **2011**, *6*, e28403.
31. Malfettone, A.; Silvestris, N.; Paradiso, A.; Mattioli, E.; Simone, G.; Mangia, A. Overexpression of nuclear NHERF1 in advanced colorectal cancer: association with

hypoxic microenvironment and tumor invasive phenotype. *Exp Mol Pathol.* **2012**, *92*, 296–303.

32. Maudsley, S.; Zamah, A. M.; Rahman, N.; Blitzer, J. T.; Luttrell, L. M.; Lefkowitz, R. J.; Hall, R. A. Platelet-derived growth factor receptor association with Na(+)/H(+) exchanger regulatory factor potentiates receptor activity. *Mol Cell Biol.* **2000**, *20*, 8352–63.

33. Lazar, C. S.; Cresson, C. M.; Lauffenburger, D. A.; Gill, G. N. The Na⁺/H⁺ exchanger regulatory factor stabilizes epidermal growth factor receptors at the cell surface. *Mol Biol Cell.* **2004**, *15*, 5470–78.

34. Wheeler, D. S.; Barrick, S. R.; Grubisha, M. J.; Brufsky, A. M.; Friedman, P. A.; Romero, G. Direct interaction between NHERF1 and Frizzled regulates β -catenin signaling. *Oncogene.* **2011**, *30*, 32–42.

35. Takahashi, Y.; Morales, F. C.; Kreimann, E. L.; Georgescu, M. M. PTEN tumor suppressor associates with NHERF proteins to attenuate PDGF receptor signaling. *EMBO J.* **2006**, *25*, 910–20.

36. Molina, J. R.; Agarwal, N. K.; Morales, F. C.; Hayashi, Y.; Aldape, K. D.; Cote, G.; Georgescu, M. M. PTEN, NHERF1 and PHLPP form a tumor suppressor network that is disabled in glioblastoma. *Oncogene.* **2012**, *31*, 1264–67.

37. Blauwkamp, T. A.; Chang, M. V.; Cadigan, K. M. Novel TCF-binding sites specify transcriptional repression by Wnt signalling. *EMBO J.* **2008**, *27*, 1436–46.

38. Schroeder, T. M.; Nair, A. K.; Staggs, R.; Lamblin, A. F.; Westendorf, J. J. Gene profile analysis of osteoblast genes differentially regulated by histone deacetylase inhibitors. *BMC Genom.* **2007**, *8*, 362.

39. Kaidi, A.; Williams, A. C.; Paraskeva, C. Interaction between β -catenin and HIF-1 promotes cellular adaptation to hypoxia. *Nat Cell Biol.* **2007**, *9*, 210–7.

40. Liu, H.; Ma, Y.; He, H. W.; Wang, J.P.; Jiang, J. D.; Shao, R. G. SLC9A3R1 stimulates autophagy via BECN1 stabilization in breast cancer cells. *Autophagy.* **2015**, *11*, 2323–34.

41. Nguyen Ho-Boulidoires, T. H.; Clapéron, A.; Mergey, M.; Wendum, D.; Desbois-Mouthon, C.; Tahraoui, S.; Fartoux, L.; Chettouh, H.; Merabtene, F.; Scatton, O.; Gaestel, M.; Praz, F.; Housset, C.; Fouassier, L. Mitogen-activated protein kinase-activated protein kinase 2 mediates resistance to hydrogen peroxide-induced oxidative stress in human hepatobiliary cancer cells. *Free Radic Biol Med.* **2015**, *89*, 34–46.

42. Coluccia, A. M.; Benati, D.; Dekhil, H.; De Filippo, A.; Lan, C.; Gambacorti Passerini, C. SKI-606 decreases growth and motility of colorectal cancer cells by preventing pp60(c-Src)-dependent tyrosine phosphorylation of β -catenin and its nuclear signalling. *Cancer Res.* **2006**, *66*, 2279–86.

43. Cox, J.; Neuhauser, N.; Michalski, A.; Scheltema, R. A.; Olsen, J. V.; Mann, M. Andromeda: a peptide search engine integrated into the MaxQuant environment. *J Proteome Res.* **2011**, *10*, 1794–805.

44. Cox, J.; Hein, M. Y.; Luber, C. A.; Paron, I.; Nagaraj, N.; Mann, M. Accurate proteome-wide label-free quantification by delayed normalization and maximal peptide ratio extraction, termed MaxLFQ. *Mol Cell Proteom.* **2014**, *13*, 2513–26. 45. Case, D. A.; Darden, T. A.; Cheatham, T. E.; Simmerling, C. L.; Wang, J.; Duke, R. E., et al. AMBER 12. San Francisco: University of California; **2012**.

46. Korb, O.; Stützle, T.; Exner, T. E. An ant colony optimization approach to flexible protein-ligand docking. *Swarm Intell.* **2007**, *1*, 115–34.

47. Ivarsson, Y.; Travaglini-Allocatelli, C.; Jemth, P.; Malatesta, F.; Brunori, M.; Gianni, S. An on-pathway intermediate in the folding of a PDZ domain. *J Biol Chem.* **2007**, *282*, 8568–72.

6. Synthesis of Novel NHERF1 PDZ1 Domain Inhibitors as Anticancer Agents

6.1 Introduction

NHERF1 (Na⁺/H⁺ exchanger 3 regulating factor 1) is a member of the PSD-95/Discs-large/Zo-1 (PDZ) family of proteins.¹ This integral membrane adaptor protein of 358 amino acids contains two *N*-terminal PDZ (postsynaptic density 95/discs large/ zona occludens 1) tandem domains and one *C*-terminal Ezrin/ Radixin/Moesin/Merlin-binding domain (EBD) that attaches to the cytoskeleton.¹ PDZ1 (11–97 amino acids) and PDZ2 (150–237 amino acids) show 74% identity to each other and bind to specific carboxyl-terminal motifs on target proteins, such as β -catenin and PTEN, that may have a pivotal role in tumorigenesis. Oncogenic activity of NHERF1 depends on its subcellular localization.^{2,3} While a loss of its physiologic membranous expression usually occurs in early dysplastic human adenomas, especially those of colon and breast, NHERF1 is progressively re-expressed throughout the cytoplasm and nuclei in highly invasive/metastatic carcinomas. Recent evidence also earmarked NHERF1 as a major driver of a cytoprotective autophagic response elicited by therapeutic inhibition of the Wnt/ β Catenin signaling cascade, which triggers colorectal cancers (CRC).⁴ In recent studies the attention has been focused on a combined β -catenin/NHERF1-inhibitory strategy as a fruitful approach to augment apoptotic death of CRC cells refractory to currently available Wnt-targeted agents, particularly at early stages of the disease and on the design and synthesis of small-molecule ligands of the PDZ1-domain of NHERF1 able to prevent its ectopic cytoplasmic/nuclear mislocalization and oncogenic function.⁵⁻⁷ As reported in the previous chapter, these studies predicted the canonical inactivating binding motif for the NHERF1 PDZ1-domain on four D/E-(S/T)-X-(L/V/I/ M) residues that are commonly contained at the C-terminal of its specific ligands, such as DSLL for the β 2-adrenergic receptor (β 2-AR) or ETWM for the parathyroid hormone receptor (PTHrR).⁸

6.1.1 Molecular Dynamics (MD) Simulations of the PDZ1- β 2-AR and PDZ1-PTH1R Complexes

The crystal structure of the PDZ1- β 2-AR C-terminal peptide is available at the protein data bank (PDB code 1GQ4).⁹ The complex was fixed by cutting the chimeric covalent bond between PDZ1 and the substrate (-NDSLL) and submitted to molecular dynamics (MD) simulations to obtain reasonable binding conformations. MD of the complex PDZ1-PTH1R Cterminal peptide (WETVM) was also performed (Figures 6.1 and 6.2).

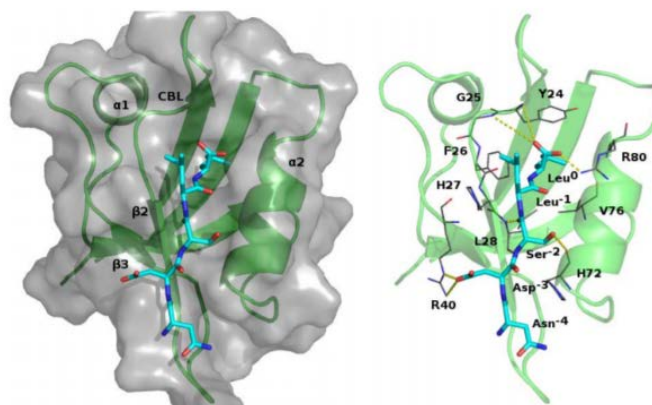


Figure 6.1 Molecular dynamics (MD) simulations of the PDZ1- β 2-AR complex. Left panel: Structure of the NHERF1 PDZ1 domain with -NDSLL (β 2-AR). Surface (gray) and cartoon (green) β -strands β 1 and β 2, helices α 1 and α 2 and CBL (t-COOH binding pocket) are labeled. Right panel: Closed view of the residues involved in the binding of the -NDSLL substrate, H-bonds are reported as yellow dot lines.¹²

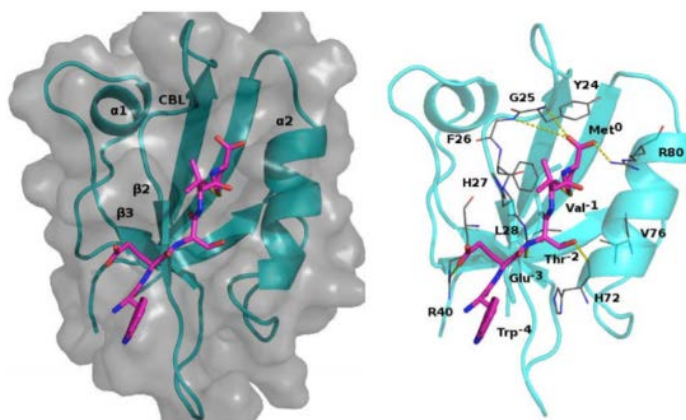


Figure 6.2 Molecular dynamics (MD) simulations of the PDZ1-PTH1R complex. Left panel: Structure of the NHERF1 PDZ1 domain with -WETVM (PTH1R). Surface (gray) and cartoon (cyan) β -strands β 1 and β 2, helices α 1 and α 2 and CBL (t-COOH binding pocket) are labeled. Right panel: Closed view of the residues involved in the binding of the -WETVM substrate, H-bonds are reported as yellow dot lines.¹²

The main interactions between the PDZ1 and the β 2-AR substrate observed at the crystal structures were retained during the simulation. Indeed, the Leu⁰ side chain formed hydrophobic interactions with Tyr24, Gly25, Phe26 residues, furthermore the Leu⁰ terminal carboxyl moiety was involved in H-bonds with Arg80 side chain and Tyr24 and Gly25 backbone (t-COOH binding pocket); the Leu-1 formed hydrophobic contact with His27; the Ser-2 residue made two H-bonds, one between the backbone oxygen atom and the Leu28 backbone and one between side chain oxygen atom and His72 backbone both with a rate of formation of 100%; the Asp-3 formed an H-bond with His27 (50% of stability during the simulation) and a salt bridge with Arg40; the Asp-3 and Asn-4 backbone formed hydrophobic contacts with Leu28, Val76 and His72. (Figure 6.1). Similar behavior was observed also for the PDZ1-ETVM simulation (Figure 6.2). The reported substrates binding was consistent with the crystal structure and with the biochemical data.^{10,11} Trajectory analyses showed that the systems were stable during a simulation time of 50 ns, with an average PDZ1 C α RMSD of 1.66 and 1.73 Å for PDZ1-NDSLL-COOH and PDZ1-WETVM-COOH, respectively. The trajectories were clustered by the RMSDs of the binding site residues, giving five clusters for the two studied complexes, each containing representative structures.

6.1.2 Objective of the Study

The obtained 10 structures guided the design of a pharmacophore model (Figure 6.3) that was used to filter out an in-house training set of about 6000 compounds. One out of six selected compounds showed significant NHERF1 inhibition.⁴

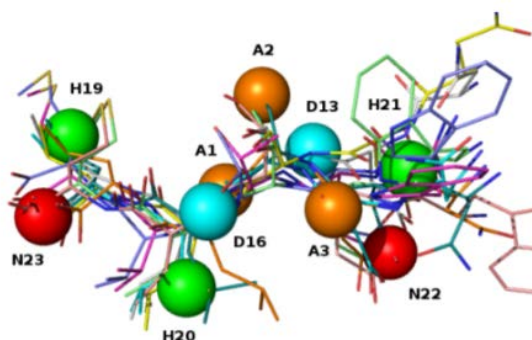
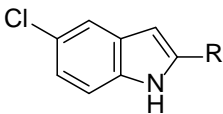
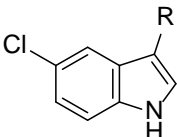
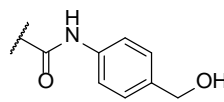
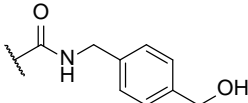
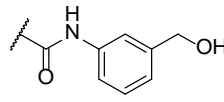
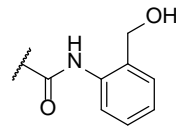
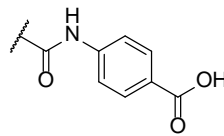
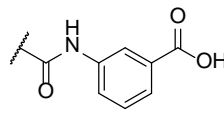
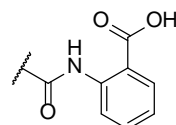
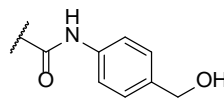
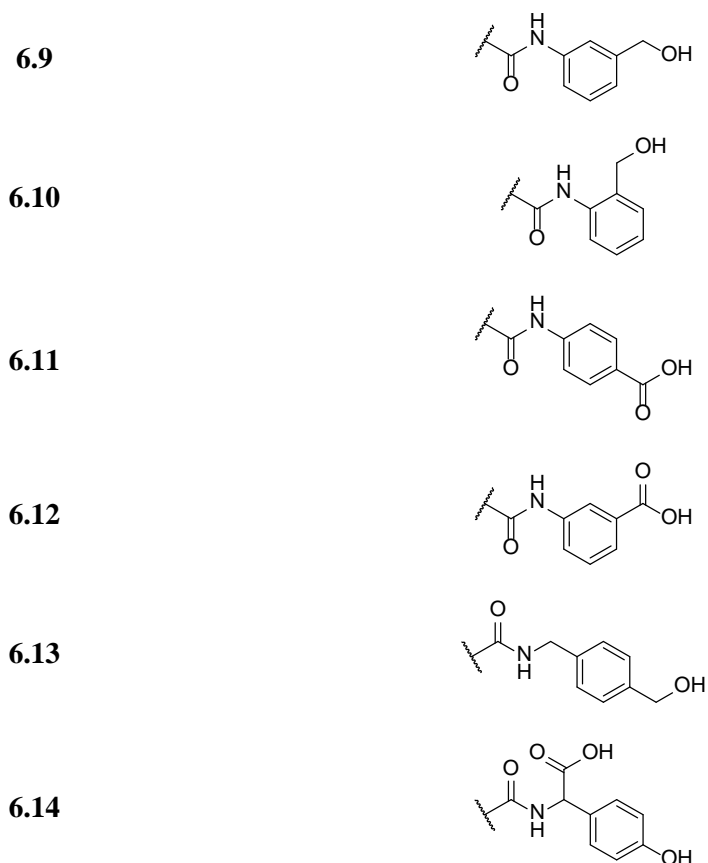


Figure 6.3 Pharmacophore model. The hydrogen bond acceptor (A1, A2 and A3), hydrogen bond donor (D16, D13), hydrophobic (H19, H20 and H21) and negative point (N22 and N23) chemical features were generated based on the most stable interaction points identified by the molecular dynamics trajectories analyses.

As a Ph.D. student of Prof. R. Silvestri's research group, I participated to the synthesis and characterization of new NHERF1 inhibitors **2.1–2.14** (Table 6.1)¹². In preliminary docking studies, these compounds matched the requirements of the pharmacophore model, in particular, the interactions at the t-COOH binding pocket.¹³

Table 6.1 Structure of Compounds **6.1–6.14**

Compd	R
6.1–6.7	
6.8–6.14	
6.1	
6.2	
6.3	
6.4	
6.5	
6.6	
6.7	
6.8	



6.2 Chemistry

Compounds **6.1–6.14** were synthesized starting from 5-chloro-1*H*-indole-2-carboxylic acid (**6.18**) or its 3-isomer **6.19** as illustrated in Scheme 6.1.

In detail, the acids were transformed into the corresponding acyl chlorides with thionyl chloride and coupled with an appropriate aminobenzoate in dichloromethane in the presence of pyridine to afford carboxamides **6.20–6.24**.

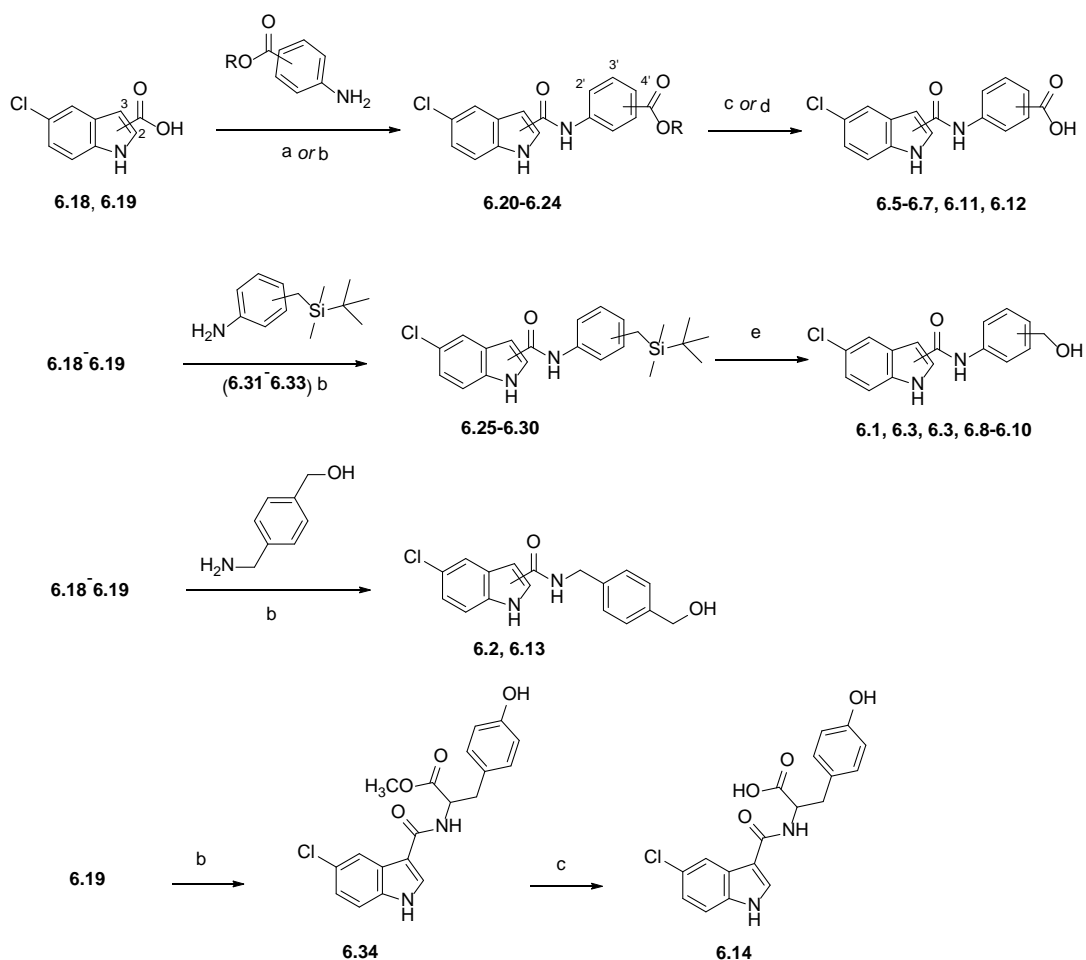
Hydrolysis of the ester functionality of **6.20–6.24** was performed with lithium hydroxide monohydrate in tetrahydrofuran (**6.5** and **6.6**) or with 3*N* sodium hydroxide in ethanol at 25 °C (**6.7**, **6.11**, and **6.12**). Alcohol derivatives **6.1**, **6.3**, **6.4**, and **6.8–6.10** were obtained by tetrabutylammonium fluoride cleavage in tetrahydrofuran at 25 °C of the corresponding tertbutyldimethylsilyl derivatives **6.25–6.30**.

The latter compounds were prepared by reaction of **6.18** or **6.19** with tertbutyldimethylsilyloxymethylanilines **6.31–6.33**.

Carboxamides **6.2**, **6.13**, **6.25–6.30**, and **6.34** were synthesized from the corresponding anilines in the presence of tripyrrolidinophosphonium hexafluorophosphate (PyBOP) and triethylamine in DMF at 25 °C.

Compound **6.14** was obtained after hydrolysis with lithium hydroxide of the intermediate methyl tyrosinate **6.34**.¹²

Scheme 6.1 Synthesis of Compounds **6.1–6.14**^a



6.1-6.14: see Table 6.1; **6.18:** 2-COOH; **6.19:** 3-COOH; position of substituents: **6.20, 6.25:** 2,4'; **6.21,6.26:** 2,3'; **6.22, 6.27:** 2,2'; **6.28:** 3,4'; **6.23, 6.29:** 3,3'; **6.24, 6.30:** 3,2'; **6.31, 4:** **6.32,** 3; **6.33,** 2. ^aReagents and reaction conditions: (a) (i) SOCl₂, 50 °C, 2 h; (ii) aminobenzoate, pyridine, DCM, 25 °C, overnight; (b) PyBOP, Et₃N, DMF, 25 °C, 12 h; (c) LiOH, THF/H₂O, 25 °C, overnight; (d) 3N NaOH, EtOH, 80 °C, 2 h; (e) TBAF, THF, 25 °C, 3 h.

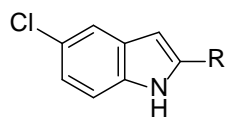
6.3 Results and Discussion

6.3.1 Inhibition of NHERF1

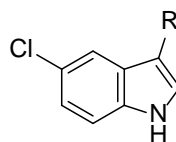
The ability of newly synthesized compounds **6.1-6.14** to inhibit NHERF1 was assessed in Ls174T CRC cells harboring a doxycycline hyclate (Dox)-inducible small hairpin RNA (shRNA) for β-catenin (Ls174Tshβ-Cat) (Table 6.2).

These CRC cells exhibited low/undetectable NHERF1 levels at the baseline (i.e., in the absence of Dox), while they markedly increase the expression of the protein as well as a NHERF1-mediated survival response under Dox treatment.⁴

Table 6.2 Structure and Activity of Compounds **6.1-6.14** in Ls174TshβCat Cells Expressing Low (-DOX) or High (+DOX) Levels of the Protein Target NHERF1^a

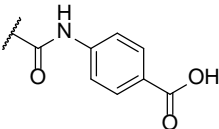
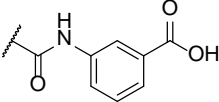
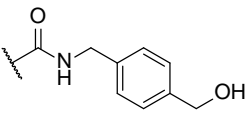
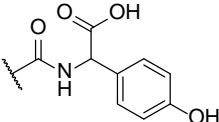


6.1-6.7



6.8-6.14

Cpd	R	Ls174Tsh IC ₅₀ (μM)		
		-Dox	+Dox	Δ
6.1		62 ± 4	24 ± 4	38
6.2		66 ± 2	25 ± 2	41
6.3		65 ± 2	24 ± 5	41
6.4		62 ± 2	22 ± 3	40
6.5		74 ± 6	12 ± 4	62
6.6		66 ± 4	25 ± 2	41
6.7		64 ± 8	22 ± 6	42
6.8		86 ± 24	55 ± 21	31
6.9		82 ± 4	8 ± 4	74
6.10		84 ± 4	5 ± 2	79

6.11		65 ± 6	22 ± 2	43
6.12		66 ± 2	25 ± 2	41
6.13		85 ± 2	10 ± 2	75
6.14		68 ± 4	25 ± 2	43

^aLs174T cells stably transfected with Dox-inducible shRNA for β -catenin (Ls174Tsh β -Cat) were cultured without or with 2 μ g/mL of Dox (-Dox/+Dox) for 1, 3, or 5 days.¹²

The relative activity of derivatives **6.1–6.14** can be explained by Δ values obtained by subtracting the IC₅₀ values of the Ls174Tsh β -Cat cells cultured in the presence or in the absence of Dox. Indeed, NHERF1/PDZ-1 ligand inhibitors are expected to exert their growth-inhibitory effects only on β -catenin-depleted CRC cells, which highly re-expressed the protein target NHERF1, thus showing the highest Δ values with regard to Dox-untreated cells. Exploring the results of the biological activity showed in Table 6.2 is evident that the introduction of a methylene spacer between the 2-carboxamide function and the phenyl group of **6.1** (-Dox IC₅₀ = 62 μ M; +Dox IC₅₀ = 24 μ M) to afford **6.4** gave a slight improvement of activity; while the displacement of the hydroxymethyl group of **6.1** from para position to meta- (**6.3**) or ortho-positions (**6.4**) only minimally affected the difference (Δ) of activity between the two cell lines. The introduction of a carboxylic acid function in **6.5** (-Dox IC₅₀ = 74 μ M; +Dox IC₅₀ = 12 μ M) in place of the hydroxymethyl of **6.1** improved the Δ value from 38 to 62, while the corresponding meta (**6.6**) or ortho (**6.7**) carboxylic acids gave similar results for **6.2–6.4**. We synthesized the corresponding analogues **6.8–6.14** at position 3 of the indole nucleus. Derivatives **6.9** (-Dox IC₅₀ = 82 μ M; +Dox IC₅₀ = 8 μ M) and **6.10** (-Dox IC₅₀ = 84 μ M; +Dox IC₅₀ = 5 μ M) bearing the hydroxymethyl at positions meta and ortho (Δ of 74 and 79, respectively) were superior to the para analogue **6.7** as well as to the carboxylic acids **6.11** and **6.12**. The 3-indolecarboxamide **6.13** (-Dox IC₅₀ = 85 μ M; +Dox IC₅₀ = 10 μ M) yielded a good Δ value of 75 that was 1.8-fold superior to the isomeric derivative **6.1**. In general derivatives **6.5**, **6.9**, **6.10**, and **6.13** exhibited a remarkable cytotoxicity and the highest Δ values on Ls174Tsh β -Cat, which highly re-express the specific protein target NHERF1.¹²

6.3.2 Molecular Modeling

The indole NH and the carboxamide oxygen formed H-bonds with the Leu27 backbone. Hydrophobic contacts were observed between the phenyl ring and Tyr24, Phe26, and Ile78 as well as between the indole ring and Val75 and Val76. The carboxylic group of derivatives **6.5–6.7** formed polar contacts with the Arg80 (Figure 6.4, left panel).

Derivatives **6.8–6.14** showed binding modes with different patterns in H-bonding. In comparing the alcohol **6.9** and its corresponding carboxylic acid **6.12**, the indole NH formed an H-bond with the His72 backbone, the amide oxygen atom formed an H-bond with the His27 side chain, the indole ring established hydrophobic contacts with Leu28

and Val75, the phenyl ring arranged hydrophobic contacts with Tyr24 and Phe26, and a π -cation interaction with the guanidine moiety of Arg80 occurred. The alcohol and the carboxyl moieties were involved in H-bond/polar contact with the terminal COOH binding pocket (Figure 6.4, right panel).¹²

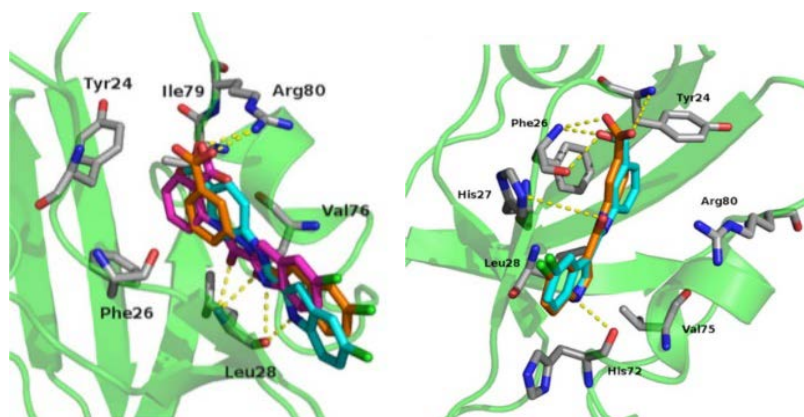


Figure 6.4 Proposed binding modes. Left panel: derivatives **6.5** (cyan), **6.6** (orange), and **6.7** (magenta). Right panel: derivatives **6.9** (cyan) and **6.12** (orange). Residues involved in interactions are reported as stick. PDZ1 is reported as cartoon (green). The H-bonds are depicted as yellow dotted lines.¹²

6.3.3 Binding to NHERF1 PDZ1

The binding of the most potent compounds **6.9**, **6.10**, and **6.13** to NHERF1 PDZ1 was assessed by means of a dansylated peptide corresponding to the C-terminal sequence of β 2-AR (DNDSL) using a fluorescent pseudowild type produced by replacing Tyr38 of PDZ1 with a Trp.¹³ The presence of a constant concentration of **6.9**, **6.10**, or **6.13** abolished the binding C-terminal sequence of β 2-AR with an affinity of about 10 μ M, thus validating these compounds as specific inhibitors of the NHERF1/PDZ1 domain (Figure 6.5).¹²

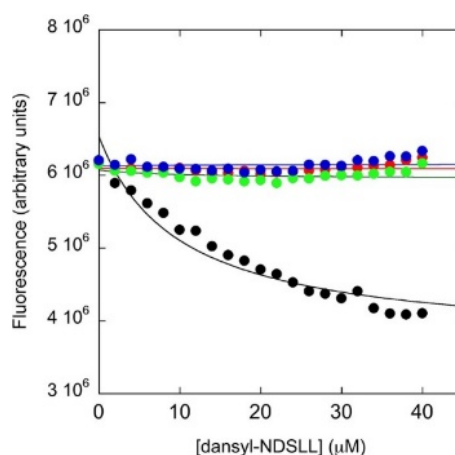
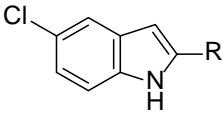
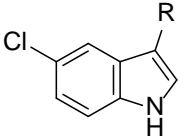
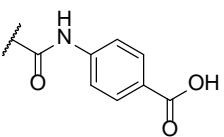
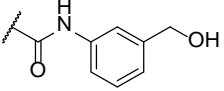
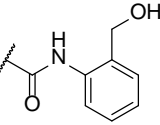
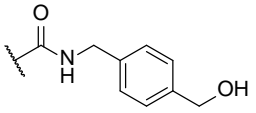


Figure 6.5 Binding of PDZ1 NHERF1 Y38W to the ligand dansyl-NDSL in the presence (black circles) and in the absence of 5 μ M of **6.9** (green), **6.10** (red), or **6.13** (blue). Fluorescence data were recorded in the presence of 50 mM Na phosphate pH 7.2, 300 mM NaCl, 5 mM DTT, 20% DMSO, at 25 $^{\circ}$ C. Lines are the best fit to a hyperbolic binding transition. The binding between PDZ1 NHERF1 Y38W to the ligand dansyl-NDSL was abolished in the presence of **6.9**, **6.10**, or **6.13**.¹²

6.3.4 Cell Growth Inhibition of DLD-1, SW480, and SW620 Cell Lines

Compounds **6.5**, **6.9**, **6.10**, and **6.13** that exhibited the highest Δ values as inhibitors of Ls174Tsh β -Cat cells were also tested in three CRC cell lines, such as DLD-1, SW480, and SW620. It is known that NHERF1 is expressed at detectable baseline levels in SW480 and SW620 but not in DLD-1 cells.⁴ This relatively explains why DLD-1 cells showed the highest IC₅₀ values compared to SW480 and SW620 cells (Table 6.3) at micromolar concentrations quite similar to those previously obtained in Dox-untreated Ls174Tsh β -Cat cells (Table 6.2).

Table 6.3 Cell Growth Inhibition of DLD-1, SW480, and SW620 Cell Lines by Compounds **6.5**, **6.9**, **6.10**, and **6.13**^a

Cpd	R	IC ₅₀ (μ M)		
		DLD-1	SW480	SW620
				
				
		6.1-6.7	6.8-6.14	
6.5		68 \pm 1	17 \pm 1	22 \pm 1
6.9		82 \pm 2	13 \pm 1	27 \pm 1
6.10		85 \pm 2	15 \pm 1	30 \pm 1
6.13		84 \pm 2	16 \pm 1	31 \pm 1

^aCytotoxic concentrations for the indicated cell lines. Experiments were performed in triplicate and repeated at least twice.

In the previous chapter is illustrated how compound **5.3**, 3-benzyl-5-chloro-*N*-(4-(hydroxymethyl)phenyl)-1*H*-indole-2-carboxamide, a NHERF1 PDZ1 inhibitor with -Dox IC₅₀ = 52 μ M and +Dox IC₅₀ = 8 μ M synergized *N*-(2-methyl-4-nitrophenyl)-2,5-dichlorobenzenesulfonamide (FH535, **5.1**) and the pyrvinium pamoate (**5.2**), inhibitor of β -catenin-dependent transcription, in triggering massive apoptosis of Ls174T and DLD1 CRC cells, thereby preventing persistent ERK1/2 phospho-activation mediated by single β -Catenin targeting.^{4,14,15} We therefore speculated the potential benefit of a synergic activity of NHERF1 PDZ1 and β -catenin inhibitors in CRC therapy by comparing the compound with the highest Δ value within this series (**6.10**) and **5.3**,⁴ with two β -Catenin inhibitors, FH535 (**5.1**)¹⁶ and **6.15** (Figure 6.6).

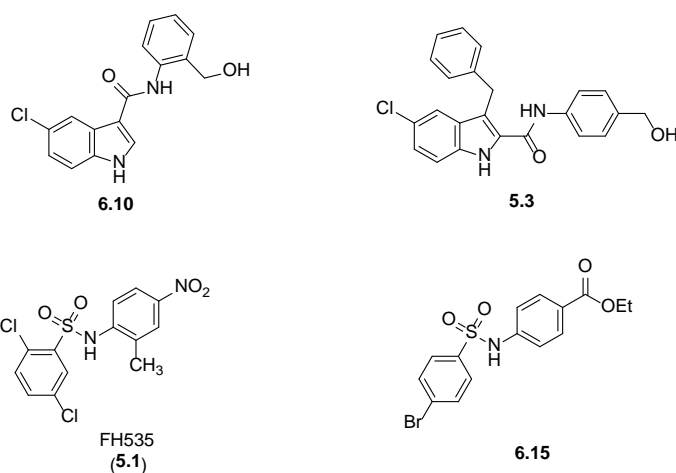


Figure 6.6 Structures of compounds **6.10**, **5.3**, **5.1**, **6.15**.

6.3.5 Inhibition of the Wnt Pathway

The effect of increasing concentrations of **6.15** on the Wnt signaling pathway was tested by performing Wnt reporter assays in 293T cells. TOPFlash (TOP) reporter plasmid, containing eight repeats of TCF/LEF binding site or FOPFlash (FOP) plasmid, where the TFC/LEF binding sites were mutated as negative control were transfected.¹⁷ The Wnt pathway was activated using the GSK3beta inhibitor LiCl. Derivative **6.15** was found to be able to inhibit the activity of the TOP reporter, with an IC_{50} of 14.1 μ M (Figure 6.7), but failed to prevent the activity of FOP reporter, indicating the specificity of the inhibition of the Wnt pathway.¹²

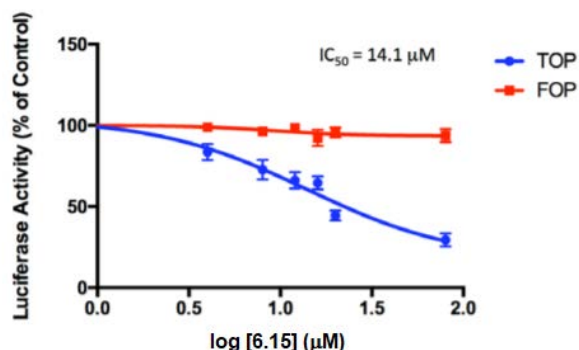


Figure 6.7 Compound **6.15** specifically inhibits Wnt signaling. Cells were transfected with TOP or FOP plasmids and treated with the GSK3beta inhibitor 50 mM LiCl and the indicated amount of **6.15** for 24 h. At the end of the incubation, luciferase activity was determined. IC_{50} concentration was 14.1 μ M. Results are expressed as % of luciferase activity compared to DMSO control and are represented as means \pm S.E. (error bars) of three independent experiments, each performed in triplicate.¹²

Indeed, a 1:1 combination of a NHERF1 inhibitor with a β -catenin inhibitor significantly improved the growth inhibition of all CRC cells. All combinations were superior to each single tested compound in DLD-1 and SW480 cells. Compound combinations **6.10** + **6.15**, **5.3** + **5.1**, and **5.3** + **6.15** inhibited the SW480 cells at submicromolar concentrations, and the most potent combination was **5.3** + **6.15**. Combinations **6.10** + **6.15** and **5.3** + **6.15** showed the higher effectiveness, and **5.3** + **6.15** was the most potent with IC_{50} values of 0.1 and 0.5 μ M (Table 6.4).¹²

Table 6.4 Synergistic Cell Growth Inhibition of SW480 and SW620 Cell Lines by Compounds **6.10**, **6.15**, **5.1**, **5.3**^{a,b}

compd	inhibitor	IC ₅₀ (μM)		
		DLD-1	SW480	SW620
6.10	NHERF1	85 ± 2	15 ± 1	30 ± 1
5.3	NHERF1	65 ± 11	8 ± 1	13 ± 2
5.1	β-Cat	28 ± 5	10 ± 2	19 ± 1
6.15	β-Cat	21 ± 2	8 ± 2	17 ± 1
6.10 + 5.1	NHERF1	0.8 ± 2	3.0 ± 2	22 ± 2
6.10 + 6.15	NHERF1	0.1 ± 2	0.3 ± 2	12 ± 2
5.3 + 5.1	NHERF1	0.5 ± 3	0.9 ± 2	18 ± 1
5.3 + 6.15	NHERF1	0.1 ± 2	0.1 ± 2	0.5 ± 2

^aCytotoxic concentrations for the indicated cell lines. Experiments were performed in triplicate repeated at least twice. ^bCompound combinations were in a 1:1 ratio.¹²

6.3.6 Inhibition of Cancer Stem Cells

The identification of targeted drugs active on cancer stem cells (CSCs) may give hope of full tumor eradication since they have proved to be selectively resistant to chemotherapies. Preliminary screening of two APC-mutated CSCs indicated that their sensitivity to compounds **6.10** and **6.15** was broadly comparable to that of standard cell lines (Table 6.5). Analysis on a wider panel of CSCs is ongoing in order to verify a possible role of different mutational profiles of individual CSCs on drug sensitivity.¹²

Table 6.5 Cell Growth Inhibition of CSC13 and CSC8 Cancer Stem Cell Lines by Compounds **6.10** and **6.15**^a

compd	inhibitor	IC ₅₀ (μM)	
		CSC13	CSC8
6.10	NHERF1	12 ± 1	8 ± 1
6.15	β-Cat	22 ± 2	13 ± 2

^aCytotoxic concentrations for the indicated CSCs. Experiments were performed in triplicate repeated at least twice.¹²

6.4 Conclusions

The physiological or pathological activity of NHERF1 depends on its subcellular localization targeted, this means that approaches aiming at modulating NHERF1 activity, rather than its overall expression, would be preferred to preserve its normal functions. By far, particular attention has been paid to the NHERF1/PDZ1-domain that governs its membrane recruitment/displacement through a transient phosphorylation switch. We herein characterized novel NHERF1 PDZ1 domain inhibitors with therapeutic value when used in combination with antagonists of β-catenin. This double-targeted strategy shows potential to augment apoptotic death of CRC cells refractory to currently available Wnt targeted agents, particularly at early stages of the disease.¹²

6.5 Experimental Section

6.5.1 Molecular Modeling Studies

All molecular modelling studies were performed on a MacPro dual 2.66 GHz Xeon running Ubuntu 14 LTS. The images in the manuscript were created with PyMOL.¹⁸ The PDZ1 structures were downloaded from the PDB, pdb code 1GQ4.¹⁰ Hydrogen atoms were added to the protein, using Maestro protein preparation wizard¹⁹ and minimized, keeping all the heavy atoms fixed until a rmsd gradient of 0.05 kcal/(mol·Å) was reached. Molecular dynamics was performed with the AMBER 12 suite.²⁰ The substrates were parametrized by Leap of Amber, the -WETVM substrate was modelled by single point mutation starting from the co-crystallized substrate -NDSLL coordinates. The structure was solvated in a periodic octahedron simulation box using TIP3P water molecules, providing a minimum of 10 Å of water between the protein surface and any periodic box edge. Ions were added to neutralize the charge of the total system. The water molecules and ions were energyminimized keeping the coordinates of the protein-ligand complex fixed (1000 cycle), and then the whole system was minimized (5000 cycle). Following minimization, the entire system was heated to 298 K (20 ps). The production (50 ns) simulation was conducted at 298 K with constant pressure and periodic boundary condition. Shake bond length condition was used (ntc = 2).

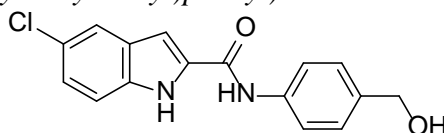
Production was carried out on GeForce gtx780 gpu. Trajectories analysis and the clustering analyses were carried out by cpptraj program.²¹ The RMSD cut off for the clustering was set to 1.5 Å to obtain 5 clusters for each of the studied trajectories. Then for each cluster was computed a representative structure as the closest (RMSD) structure to the average structure of the cluster. Ligand structures were built with Maestro and minimized using the MMFF94x force field until a rmsd gradient of 0.05 kcal/(mol·Å) was reached. The trajectories were centered on the substrate (image command).²¹ The counter ions and the water molecules were stripped by means of the cpptraj module.²¹ The RMSD, RMSF together with the H-bonds and the hydrophobic contacts (rate of formation and distances) were evaluated by cpptraj module.²¹ The trajectories were visually inspected by Chimera 1.12.²² The docking simulations were performed using PLANTS.²³ A binding lattice of 12 Å radius was setted using all default settings. The receptor structures were obtained by cpptraj as the representative structure of the most populated cluster. The pharmacophore model was obtained by Phase.²⁴ The pharmacophore features were fixed at the most stable interaction points identified by the molecular dynamics trajectories analyses. The polar features had a tolerance of 2Å while the hydrophobic features had a tolerance of 2.5Å. The in house library (6000 derivatives) was docked at the representative structure for the studied complex. All the proposed binding conformations (10 per molecule) were filtered out by the pharmacophore model and the best 100 were visual inspected. The visual inspection was carried out by Maestro GUI¹⁹ and the intermolecular interactions were highlighted by the ligand interactions module.¹⁹

6.5.2 Chemical Synthesis

All reagents and solvents were handled according to the material safety data sheet of the supplier and were used as purchased without further purification. 5-Chloro-1*H*-indole-2-carboxylic acid (**6.18**) and 5-chloro-1*H*-indole-3-carboxylic acid (**6.19**) were commercially available. Organic solutions were dried over anhydrous sodium sulphate. Evaporation of solvents was carried out on a Büchi Rotavapor R-210 equipped with a Büchi V-850 vacuum controller and a Büchi V-700 vacuum pump. Column chromatography was performed on columns packed with silica gel from Macherey-Nagel (70–230 mesh). Silica gel thin layer chromatography (TLC) cards from Macherey-Nagel (silica gel precoated aluminum cards with fluorescent indicator visualizable at 254 nm) were used for TLC. Developed plates were visualized with a Spectroline ENF 260C/FE UV apparatus. Melting points (mp) were determined on a Stuart Scientific SMP1 apparatus and are uncorrected. Infrared (IR) spectra were recorded on a PerkinElmer

Spectrum 100 FT-IR spectrophotometer equipped with a universal attenuated total reflectance accessory and IR data acquired and processed by PerkinElmer Spectrum 10.03.00.0069 software. Band position and absorption ranges are given in cm^{-1} . Proton nuclear magnetic resonance (^1H NMR) spectra were recorded with a Varian Mercury (300 MHz) or a Bruker Avance (400 MHz) spectrometer in the indicated solvent, and the corresponding fid files were processed by MestreLab Research SL MestreReNova 6.2.1-769 software. Chemical shifts are expressed in δ units (ppm) from tetramethylsilane. Mass spectra were recorded on a Bruker Daltonics MicroTOF LC/MS mass spectrometer equipped with a positive ion ESI source. Compound purity was checked by high pressure liquid chromatography (HPLC). Purity of tested compounds was found to be $>95\%$. The HPLC system used (Thermo Fisher Scientific Inc. Dionex UltiMate 3000) consisted of an SR-3000 solvent rack, a LPG-3400SD quaternary analytical pump, a TCC-3000SD column compartment, a DAD-3000 diode array detector, and an analytical manual injection valve with a 20 μL loop. Samples were dissolved in acetonitrile (1 mg/mL). HPLC analysis was performed by using a Thermo Fisher Scientific Inc. Acclaim 120 C18 column (5 μm , 4.6 mm x 250 mm) at 25 ± 1 $^\circ\text{C}$ with an appropriate solvent gradient (acetonitrile/water), flow rate of 1.0 mL/min and signal detector at 206, 230, 254 and 365 nm. Chromatographic data were acquired and processed by Thermo Fisher Scientific Inc. Chromeleon 6.80 SR15 Build 4656 software.

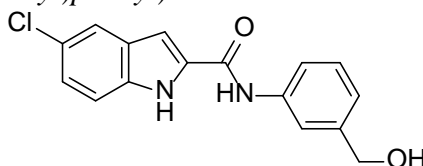
General Procedure for the Preparation of Compounds 6.1, 6.3, 6.4 and 6.8-6.10.
Example: 5-Chloro-N-(4-(hydroxymethyl)phenyl)-1H-indole-2-carboxamide (6.1).



6.1

To a mixture of **6.25** (0.03 g, 0.07 mmol), in anhydrous tetrahydrofuran (5 mL) was added tetrabutylammonium fluoride hydrate (TBAF) (0.1 mL, 0.1 mmol). The reaction mixture was stirred at 25 $^\circ\text{C}$ for 3 h, then 1N HCl was added up to pH 5 and the mixture was extracted with ethyl acetate. The organic layer was washed with brine, dried and filtered. Evaporation of the solvent gave a residue that was purified by column chromatography (silica gel, n-hexane:ethyl acetate = 2:3) to furnish **6.1** (0.015 g, 70%), mp 270-272 $^\circ\text{C}$ (from ethanol). Spectral data were in agreement with Lit.²⁵

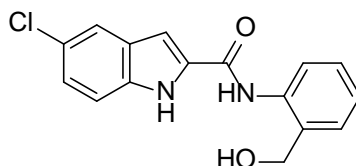
5-Chloro-N-(3-(hydroxymethyl)phenyl)-1H-indole-2-carboxamide (6.3).



6.3

Synthesized as **6.1** starting from **6.26**. Yield 100%, 0.055 g, mp 219-222 $^\circ\text{C}$ (from ethanol). ^1H NMR (DMSO- d_6 , 300 MHz): δ 4.50 (d, $J = 5.5$ Hz, 2H), 5.24 (t, $J = 5.7$ Hz, 1H), 7.04 (d, $J = 7.8$ Hz, 1H), 7.19-7.22 (m, 1H), 7.30 (t, $J = 7.8$ Hz, 1H), 7.42-7.48 (m, 2H), 7.69-7.75 (m, 3H), 10.27 (s, disappeared after treatment with D_2O , 1H), 11.92 ppm (br s, disappeared after treatment with D_2O , 1H). IR: ν 1619 and 3325 cm^{-1} .

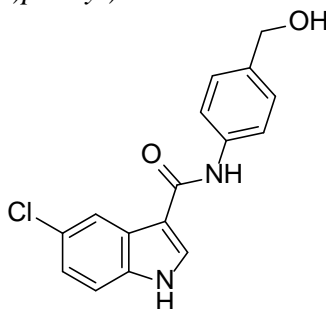
5-Chloro-N-(2-(hydroxymethyl)phenyl)-1H-indole-2-carboxamide (6.4).



6.4

Synthesized as **6.1** starting from **6.27**. Yield 100%, 0.048 g, mp 185-188 °C (from ethanol). ¹H NMR (DMSO-d₆, 300 MHz): δ 4.61 (d, *J* = 5.2 Hz, 2H), 5.65 (t, *J* = 4.9 Hz, 1H), 7.18-7.23 (m, 3H), 7.29-7.31 (m, 1H), 7.42-7.47 (m, 2H), 7.72-7.76 (m, 2H), 10.21 (s, disappeared after treatment with D₂O, 1H), 12.02 ppm (br s, disappeared after treatment with D₂O, 1H). IR: ν 1656 and 3262 cm⁻¹.

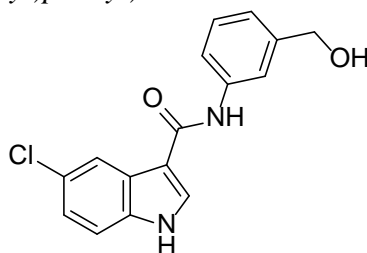
5-Chloro-N-(4-(hydroxymethyl)phenyl)-1H-indole-3-carboxamide (6.8).



6.8

Synthesized as **6.1** starting from **6.28**. Yield 100%, 0.007 g, mp 210-213 °C (from ethanol). ¹H NMR (DMSO-d₆, 300 MHz): δ 4.43-4.45 (m, 2H), 5.08-5.11 (m, 1H), 7.16-7.19 (m, 1H), 7.24-7.26 (m, 2H), 7.46-7.50 (m, 1H), 7.67- 7.69 (m, 2H), 8.16-8.17 (m, 1H), 8.34-8.35 (m, 1H), 9.73 (s, disappeared after treatment with D₂O, 1H), 11.92 ppm (br s, disappeared after treatment with D₂O, 1H). IR: ν 1642 and 2922 cm⁻¹.

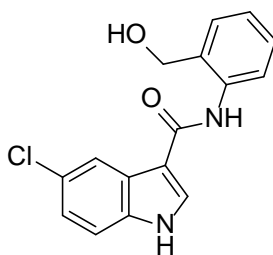
5-Chloro-N-(3-(hydroxymethyl)phenyl)-1H-indole-3-carboxamide (6.9).



6.9

Synthesized as **6.1** starting from **6.29**. Yield 82%, 0.02 g, mp 169-172 °C (from ethanol). ¹H NMR (DMSO-d₆, 300 MHz): δ 4.48 (d, *J* = 5.4 Hz, 2H), 5.21 (t, *J* = 6 Hz, 1H), 6.97 (d, *J* = 7.8 Hz, 1H), 7.16-7.27 (m, 2H), 7.48 (d, *J* = 8.6 Hz, 1H), 7.64. (d, *J* = 8.3 Hz, 1H), 7.72 (s, 1H), 8.17 (s, 1H), 8.37 (s, 1H), 9.76 (s, disappeared after treatment with D₂O, 1H), 11.91 ppm (br s, disappeared after treatment with D₂O, 1H). IR: ν 1727 and 3319 cm⁻¹.

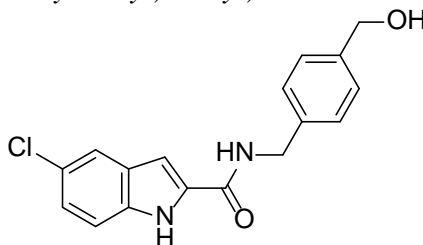
5-Chloro-N-(2-(hydroxymethyl)phenyl)-1H-indole-3-carboxamide (6.10).



6.10

Synthesized as **6.1** starting from **6.30**. Yield 52%, 0.02 g, mp 150-153 °C (from ethanol). ¹H NMR (DMSO-d₆, 300 MHz): δ 4.59 (s, 2H), 5.57 (s, 1H), 7.11-7.17 (m, 1H), 7.20-7.29 (m, 2H), 7.40 (d, *J* = 7.9 Hz, 1H), 7.50 (d, *J* = 8.8 Hz, 1H), 7.72 (d, *J* = 7.4 Hz, 1H), 8.12-8.16 (m, 2H), 9.65 (s, disappeared after treatment with D₂O, 1H), 11.98 ppm (br s, disappeared after treatment with D₂O, 1H). IR: ν 1613 and 3235 cm⁻¹.

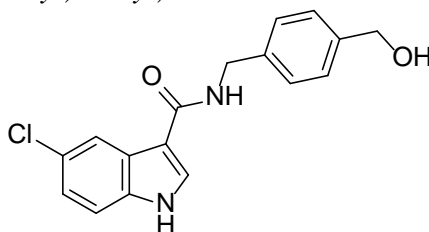
General Procedure for the Preparation of Compounds 6.2, 6.13, 6.21 and 6.25-6.30.
 Example: 5-Chloro-*N*-(4-(hydroxymethyl)benzyl)-1*H*-indole-2-carboxamide (**6.2**).



6.2

To a mixture of **6.18** (0.1 g, 0.50 mmol), 4-(aminomethyl)phenylmethanol (0.1 g, 0.75 mmol), triethylamine (0.1 mL, 0.75 mmol) in anhydrous *N,N*-dimethylformamide (5 mL) was added (benzotriazol-1-yloxy) tripyrrolidinophosphonium hexafluorophosphate (PyBOP) (0.16 g, 0.50 mmol). The reaction mixture was stirred at 25 °C for 12 h, then 1*N* HCl was added up to pH 5 and the mixture was extracted with ethyl acetate. The organic layer was washed with brine, dried and filtered. Evaporation of the solvent gave a residue that was purified by column chromatography (silica gel, *n*-hexane:ethyl acetate = 1:1) to furnish **6.2** (0.02 g, 13%), mp 210-213 °C (from ethanol). ¹H NMR (DMSO-d₆, 400 MHz): δ 4.48 (t, *J* = 8.0 Hz, 4H), 5.16 (t, *J* = 5.7 Hz, 1H), 7.16 (s, 1H), 7.18 (dd, *J* = 2.0 and 8.7 Hz, 1H), 7.26-7.30 (m, 4H), 7.43 (d, *J* = 8.7 Hz, 1H), 7.70 (d, *J* = 2.0 Hz, 1H), 9.12 (t, *J* = 6.0 Hz, 1H), 11.84 ppm (br s, disappeared after treatment with D₂O, 1H). IR: ν 1648 and 3261 cm⁻¹.

5-Chloro-*N*-(4-(hydroxymethyl)benzyl)-1*H*-indole-3-carboxamide (**6.13**).

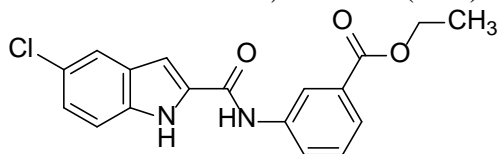


6.13

Synthesized as **6.2** starting from **6.19**. Yield 8%, 0.012 g, mp 212-215 °C (from ethanol). ¹H NMR (DMSO-d₆, 300 MHz): δ 4.43- 4.50 (m, 4H), 5.13 (t, *J* = 5.6 Hz, 1H), 7.14 (dd, *J* = 2.0 and 8.6 Hz, 1H), 7.23-7.28 (m, 4H), 7.44 (d, *J* = 8.5 Hz, 1H), 8.12-8.14

(m, 2H), 8.49-8.53 (m, 1H), 11.74 ppm (br s, disappeared after treatment with D₂O, 1H). IR: ν 1591 and 3380 cm⁻¹.

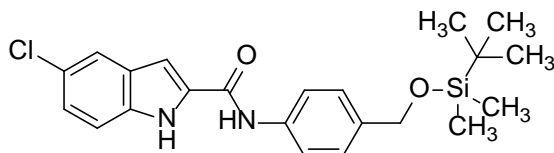
Ethyl 3-(5-chloro-1H-indole-2-carboxamido)benzoate (6.21).



6.21

Synthesized as **6.2** starting from **6.18** and ethyl 3-aminobenzoate. Yield 54%, 0.07 g, mp 268-270 °C (from ethanol). ¹H NMR (DMSO-d₆, 300 MHz): δ 1.32 (t, *J* = 7.1 Hz, 3H), 4.32 (q, *J* = 7.1 Hz, 2H), 7.22 (dd, *J* = 2.0 and 8.7 Hz, 1H), 7.44- 7.54 (m, 3H), 7.69 (d, *J* = 7.2 Hz, 1H), 7.77 (d, *J* = 1.7 Hz, 1H), 8.10-8.14 (m, 1H), 8.42 (s, 1H), 10.51 (s, 1H), 11.99 ppm (br s, disappeared after treatment with D₂O, 1H). IR: ν 1719 and 3270 cm⁻¹.

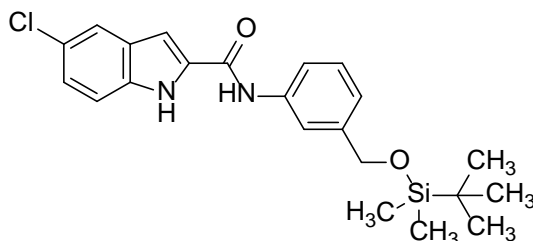
N-(4-(((tert-Butyldimethylsilyl)oxy)methyl)phenyl)-5-chloro-1H-indole-2-carboxamide (6.25).



6.25

Synthesized as **6.2** starting from **6.18** and **6.32**. Yield 18%, 0.03 g, mp 238-240 °C (from ethanol). ¹H NMR (DMSO-d₆, 300 MHz): δ 0.07 (s, 6H), 0.89 (s, 9H), 4.67 (s, 2H), 7.20 (dd, *J* = 2.0 and 8.8 Hz, 1H), 7.28 (d, *J* = 8.7 Hz, 3H), 7.38 (s, 1H), 7.45 (d, *J* = 8.8 Hz, 1H), 7.73-7.75 (m, 3H), 10.27 (s, 1H), 11.94 ppm (br s, disappeared after treatment with D₂O, 1H). IR: ν 1655 and 3286 cm⁻¹.

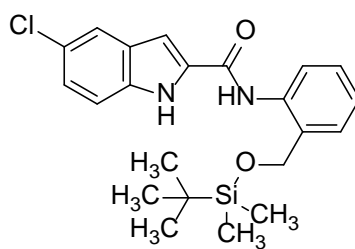
N-(3-(((tert-Butyldimethylsilyl)oxy)methyl)phenyl)-5-chloro-1H-indole-2-carboxamide (6.26).



6.26

Synthesized as **6.2** starting from **6.18** and **6.33**. Yield 30%, 0.07 g, mp 227-230 °C (from ethanol). ¹H NMR (DMSO-d₆, 300 MHz): δ 0.09 (s, 6H), 0.90 (s, 9H), 4.70 (s, 2H), 7.01-7.03 (m, 1H), 7.20 (dd, *J* = 1.8 and 8.9 Hz, 1H), 7.31 (t, *J* = 7.83 Hz, 1H), 7.43 (t, *J* = 8.9 Hz, 2H), 7.63-7.66 (m, 1H), 7.76-7.81 (m, 2H), 10.29 (s, 1H), 11.95 ppm (br s, disappeared after treatment with D₂O, 1H). IR: ν 1662 and 3292 cm⁻¹.

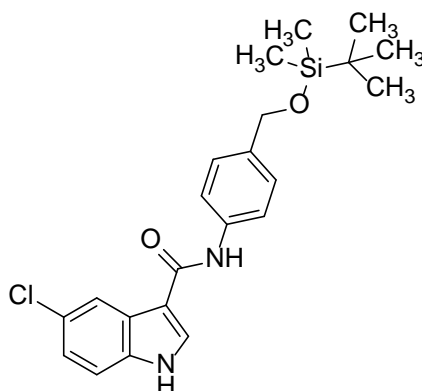
N-(2-(((tert-Butyldimethylsilyl)oxy)methyl)phenyl)-5-chloro-1H-indole-2-carboxamide (6.27).



6.27

Synthesized as **6.2** starting from **6.18** and **6.34**. Yield 17%, 0.056 g, mp 195-197 °C (from ethanol). ¹H NMR (DMSO-d₆, 300 MHz): δ 0.02 (s, 6H), 0.85 (s, 9H), 4.76 (s, 2H), 7.19-7.34 (m, 4H), 7.42-7.52 (m, 3H), 7.72-7.74 (m, 1H), 9.99 (s, 1H), 11.99 ppm (br s, disappeared after treatment with D₂O, 1H). IR: ν 1657 and 3274 cm⁻¹.

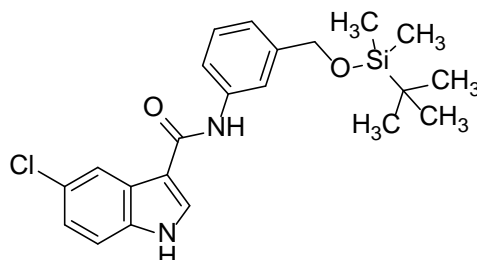
N-(4-(((*tert*-Butyldimethylsilyl)oxy)methyl)phenyl)-5-chloro-1H-indole-3-carboxamide (**6.28**).



6.28

Synthesized as **6.2** starting from **6.19** and **6.32**. Yield 7%, 0.007 g, mp 203-205 °C (from ethanol). ¹H NMR (DMSO-d₆, 300 MHz): δ 0.06 (s, 6H), 0.89 (s, 9H), 4.65 (s, 2H), 7.16-7.26 (m, 3H), 7.48 (d, *J* = 8.6 Hz, 1H), 7.69 (d, *J* = 8.4 Hz, 2H), 8.16 (d, *J* = 2.1 Hz, 1H), 8.34 (s, 1H), 9.74 (s, 1H), 11.88 ppm (br s, disappeared after treatment with D₂O, 1H). IR: ν 1642 and 2927 cm⁻¹.

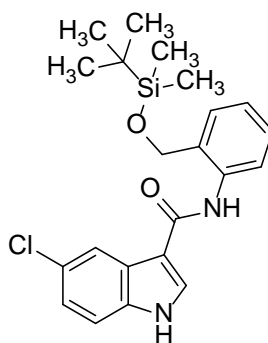
N-(3-(((*tert*-Butyldimethylsilyl)oxy)methyl)phenyl)-5-chloro-1H-indole-3-carboxamide (**6.29**).



6.29

Synthesized as **6.2** starting from **6.19** and **6.33**. Yield 17%, 0.035 g, mp 210-212 °C (from ethanol). ¹H NMR (DMSO-d₆, 300 MHz): δ 0.09 (s, 6H), 0.90 (s, 9H), 4.69 (s, 2H), 6.97-6.99 (m, 1H), 7.17-7.20 (m, 1H), 7.27 (t, *J* = 7.7 Hz, 1H), 7.48 (d, *J* = 8.6 Hz, 1H), 7.60-7.65 (m, 1H), 7.72 (s, 1H), 8.15-8.16 (m, 1H), 8.35 (s, 1H), 9.76 (s, 1H), 11.84 ppm (br s, disappeared after treatment with D₂O, 1H). IR: ν 1642 and 2952 cm⁻¹.

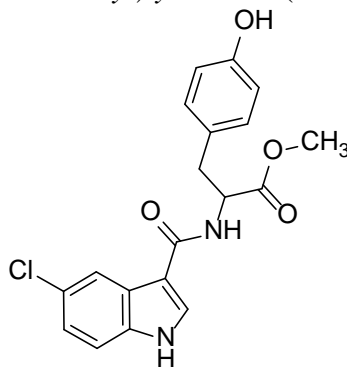
N-(2-(((*tert*-Butyldimethylsilyl)oxy)methyl)phenyl)-5-chloro-1*H*-indole-3-carboxamide (**6.30**).



6.30

Synthesized as **6.2** starting from **6.19** and **6.34**. Yield 22%, 0.045 g, mp 168-170 °C (from ethanol). ¹H NMR (DMSO-*d*₆, 300 MHz): δ 0.01 (s, 6H), 0.83 (s, 9H), 4.76 (s, 2H), 7.17-7.30 (m, 3H), 7.43-7.55 (m, 3H), 8.06-8.19 (m, 2H), 9.43 (s, 1H), 11.98 ppm (br s, disappeared after treatment with D₂O, 1H). IR: ν 1644 and 3266 cm⁻¹.

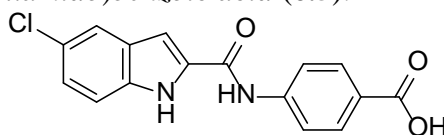
Methyl (5-chloro-1*H*-indole-3-carbonyl)tyrosinate (**6.34**).



6.34

Synthesized as **6.2** starting from **6.19** and methyl tyrosinate. Yield 18%, 0.033 g, mp 192-195 °C (from ethanol). ¹H NMR (DMSO-*d*₆, 300 MHz): 2.93-3.04 (m, 2H), 3.61 (s, 3H), 4.52-4.59 (m, 1H), 6.64 (d, *J* = 8.4 Hz, 2H), 7.08 (d, *J* = 8.4 Hz, 2H), 7.13-7.16 (m, 1H), 7.44 (d, *J* = 8.7 Hz, 1H), 8.02 (d, *J* = 2.1 Hz, 1H), 8.16 (s, 1H), 8.28 (d, *J* = 7.7 Hz, 1H), 9.22 (s, 1H), 11.78 ppm (br s, disappeared after treatment with D₂O, 1H). IR: ν 1722 and 3287 cm⁻¹.

*General Procedure for the Preparation of Compounds 6.5, 6.6 and 6.14. Example: 4-(5-Chloro-1*H*-indole-2-carboxamido)benzoic acid (6.5).*

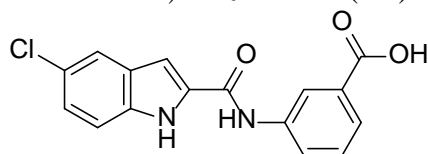


6.5

A mixture of **6.20** (0.082 g, 0.50 mmol) and lithium hydroxide monohydrate (0.032g, 0.76 mmol) in tetrahydrofuran (9.25 mL) and water (9.25 mL) was stirred at 25 °C overnight. The reaction mixture was made acid with 1N HCl and extracted with ethyl acetate. The organic layer was washed with brine, dried and filtered. Evaporation of the solvent gave **6.5** (0.06 g, yield 76%), mp >300 °C (from ethanol). ¹H NMR (DMSO-*d*₆,

300 MHz): δ 7.22 (dd, $J = 1.7$ and 8.8 Hz, 1H), 7.47 (d, $J = 8.8$, 2H), 7.78 (d, $J = 1.7$ Hz, 1H), 7.90-7.93 (m, 4H), 10.54 (s, 1H), 11.99 (s, 1H), 12.72 ppm (br s, disappeared after treatment with D₂O, 1H). IR: ν 1669 and 3413 cm⁻¹.

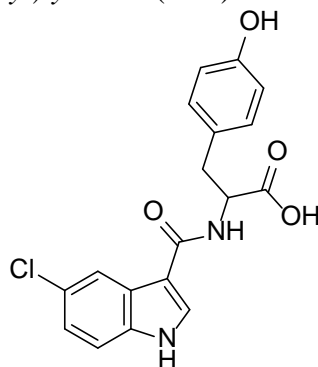
3-(5-Chloro-1H-indole-2-carboxamido)benzoic acid (6.6).



6.6

Synthesized as **6.5** starting from **6.22**. Yield 54%, 0.042 g, mp 268-270 °C (from ethanol). ¹H NMR (DMSO-d₆, 300 MHz): δ 7.23-7.35 (m, 4H), 7.67-7.72 (m, 3H), 8.06-8.09 (m, 1H), 8.44-8.47 (m, 1H), 8.55 (s, disappeared after treatment with D₂O, 1H), 11.34 ppm (br s, disappeared after treatment with D₂O, 1H). IR: ν 1667 and 3282 cm⁻¹.

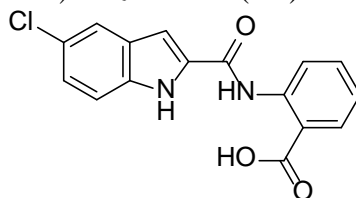
(5-Chloro-1H-indole-3-carbonyl)tyrosine (6.14).



6.14

Synthesized as **6.5** starting from **6.34**. Yield 66%, 0.019 g, mp 222-224 °C (from ethanol). ¹H NMR (DMSO-d₆, 300 MHz): δ 2.85-3.07 (m, 2H), 4.47-4.54 (m, 1H), 6.62-6.65 (m, 2H), 7.08-7.16 (m, 3H), 7.43-7.46 (m, 1H), 8.03 (s, 1H), 8.11-8.16 (m, 2H), 9.19 (s, 1H), 11.77 ppm (br s, disappeared after treatment with D₂O, 1H). IR: ν 1717 and 2963 cm⁻¹.

General Procedure for the Preparation of Compounds 6.7, 6.11 and 6.12. Example: 2-(5-Chloro-1H-indole-2-carboxamido)benzoic acid (6.7).

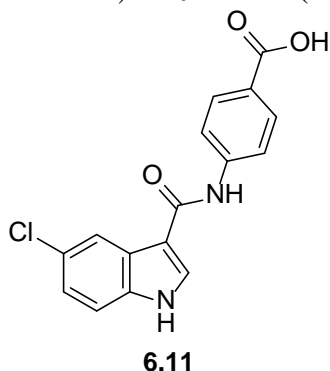


6.7

A mixture of **6.22** (0.042 g, 0.12 mmol), 3N sodium hydroxide (0.6 mL) and ethanol (1 mL) was stirred at 80 °C for 2 h. The reaction mixture was made acid with 1N HCl and extracted with ethyl acetate. The organic layer was washed with brine, dried and filtered. Evaporation of the solvent gave a residue that was triturated with n-hexane under vacuum filtration to furnish **6.7** (0.03 g, yield 78%), mp 253-255 °C (from ethanol). ¹H NMR (DMSO-d₆, 300 MHz): δ 7.10-7.15 (m, 1H), 7.21-7.24 (m, 1H), 7.53 (d, $J = 8.6$ Hz, 1H),

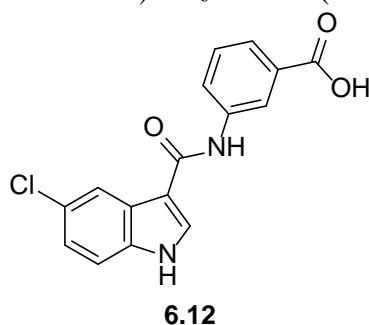
7.58-7.63 (m, 1H), 8.01- 8.08 (m, 2H), 8.18 (d, $J = 8.5$ Hz, 1H), 8.69 (d, $J = 8.5$ Hz, 1H), 11.93 (s, 1H), 12.05 ppm (br s, disappeared after treatment with D₂O, 1H). IR: ν 1653 and 3278 cm⁻¹.

4-(5-Chloro-1H-indole-3-carboxamido)benzoic acid (6.11).



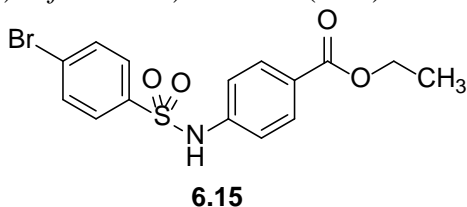
Synthesized as **6.7** starting from **6.23**. Yield 52%, 0.015 g, mp >300 °C (from ethanol). ¹H NMR (DMSO-d₆, 300 MHz): δ 7.20 (dd, $J = 2.1$ and 8.6 Hz, 1H), 7.50 (d, $J = 8.6$ Hz, 1H), 7.85-7.92 (m, 4H), 8.17 (d, $J = 1.8$ Hz, 1H), 8.41 (d, $J = 2.6$ Hz, 1H), 10.06 (s, 1H), 12.02 ppm (br s, disappeared after treatment with D₂O, 1H). IR: ν 1655 and 3279 cm⁻¹.

3-(5-Chloro-1H-indole-3-carboxamido)benzoic acid (6.12).



Synthesized as **6.7** starting from **6.24**. Yield 91%, 0.025 g, mp 273-275 °C (from ethanol). ¹H NMR (DMSO-d₆, 300 MHz): δ 7.17-7.21 (m, 1H), 7.40-7.51 (m, 2H), 7.59-7.62 (m, 1H), 8.00-8.05 (m, 1H), 8.18 (s, 1H), 8.35-8.40 (m, 2H), 9.96 (s, 1H), 11.97 ppm (br s, disappeared after treatment with D₂O, 1H). IR: ν 1698 and 3167 cm⁻¹.

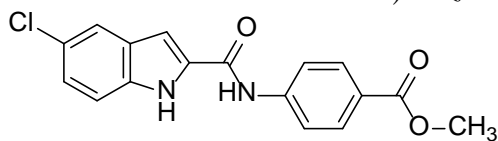
Ethyl 4-((4-bromophenyl)sulfonamido)benzoate (6.15).



To a mixture of ethyl 4-aminobenzoate (0.65 g, 3.9 mmol) in anhydrous pyridine (13 mL) was added 4-bromobenzenesulfonyl chloride (1.0 g, 3.9 mmol). The mixture was stirred at 80 °C for 1 h, then 1N HCl was added up to pH 5 and the reaction mixture was extracted with ethyl acetate. The organic layer was separated, washed with 3N HCl and then with brine, dried and filtered. Evaporation of the solvent gave a residue that was purified²⁴ by column chromatography (silica gel, n-hexane:ethyl acetate = 1:1) to furnish **6.15** (1.5 g, 99%), mp 184-185 °C (from ethanol). ¹H NMR (DMSO-d₆, 300 MHz): δ 1.25 (t, $J = 5.3$ Hz, 3H), 4.23 (q, $J = 5.3$ Hz, 2H), 7.19 (d, $J = 6.5$ Hz, 2H), 7.71 (d, $J = 6.6$ Hz,

2H), 7.77-7.83 (m, 4H), 10.90 ppm (s, disappeared after treatment with D₂O, 1H). IR: ν 1686 and 3198 cm⁻¹.

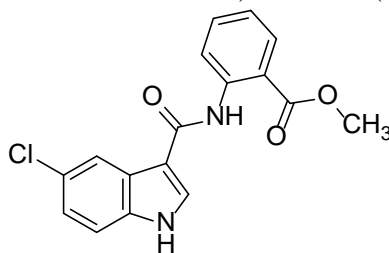
General Procedure for the Preparation of Compounds 6.20, 6.22, 6.23 and 6.24.
Example: Methyl 4-(5-chloro-1H-indole-2-carboxamido)benzoate (6.20).



6.20

A mixture of **6.18** (0.20 g, 1.0 mmol) and thionyl chloride (2 mL) was stirred for 2 h at 50 °C. Excess of thionyl chloride was evaporated in vacuo to obtain the corresponding carbonyl chloride. The latter was added dropwise to a solution of methyl 4-aminobenzoate (0.20 g, 1.3 mmol) in pyridine (2.66 mL) and dichloromethane (1 mL). The reaction was stirred at 25 °C overnight. The mixture was treated with 1N HCl up to pH 5 and extracted with ethyl acetate. The organic layer was washed with brine, dried and filtered. Evaporation of the solvent gave a residue that was purified by column chromatography (silica gel, n-hexane:ethyl acetate = 3:2) to furnish **6.20** (0.10 g, 30%), mp 272-275 °C (from ethanol). ¹H NMR (DMSO-d₆, 300 MHz): δ 3.83 (s, 3H), 7.21-7.24 (m, 1H), 7.46-7.48 (m, 2H), 7.79-7.80 (m, 1H), 7.96 (m, 4H), 10.58 (s, 1H), 12.01 ppm (br s, disappeared after treatment with D₂O, 1H). IR: ν 1732 and 3262 cm⁻¹.

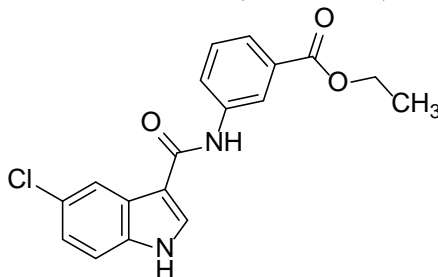
Methyl 2-(5-chloro-1H-indole-3-carboxamido)benzoate (6.22).



6.22

Synthesized as **6.20** starting from **6.18** and methyl 2-aminobenzoate. Yield 49%, 0.042 g, mp 224-226 °C (from ethanol). ¹H NMR (DMSO-d₆, 300 MHz): δ 3.89 (s, 3H), 7.14-7.24 (m, 2H), 7.53 (d, *J* = 8.7 Hz, 1H), 7.61-7.67 (m, 1H), 7.98 (dd, *J* = 1.3 and 8.0 Hz, 1H), 8.13-8.16 (m, 2H), 8.56 (d, *J* = 8.2 Hz, 1H), 11.23 (s, 1H), 11.99 ppm (br s, disappeared after treatment with D₂O, 1H). IR: ν 1649 and 3254 cm⁻¹.

Ethyl 3-(5-chloro-1H-indole-3-carboxamido)benzoate (6.23).

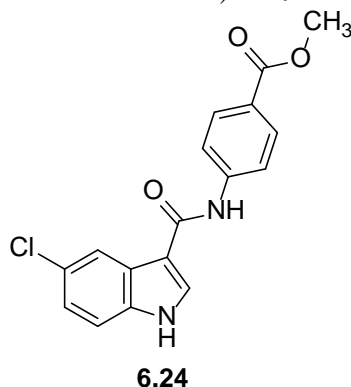


6.23

Synthesized as **6.20** starting from **6.19** and ethyl 3-aminobenzoate. Yield 18%, 0.060 g, mp 195-198 °C (from ethanol). ¹H NMR (DMSO-d₆, 300 MHz): δ 1.33 (t, *J* = 7.1 Hz, 3H), 4.32 (q, *J* = 7.1 Hz, 2H), 7.19 (dd, *J* = 2.0 and 8.6 Hz, 1H), 7.44-7.51 (m, 2H), 7.63 (d, *J* = 7.7 Hz, 1H), 8.07-8.10 (m, 1H), 8.18 (d, *J* = 1.8 Hz, 1H), 8.38 (d, *J* = 9.4 Hz, 2H),

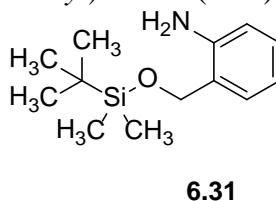
10.00 (s, 1H), 11.93 ppm (br s, disappeared after treatment with D₂O, 1H). IR: ν 1719 and 3168 cm⁻¹.

Methyl 4-(5-chloro-1H-indole-3-carboxamido)benzoate (6.24).



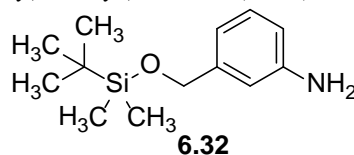
Synthesized as **6.20** starting from **6.19** and methyl 4-aminobenzoate. Yield 12%, 0.019 g, mp 260-265 °C (from ethanol). ¹H NMR (DMSO-d₆, 300 MHz): δ 3.81 (s, 3H), 7.20 (d, J = 8.8 Hz, 1H), 7.50 (d, J = 8.8 Hz, 1H), 7.89-7.95 (m, 4H), 8.16 (s, 1H), 8.41 (s, 1H), 10.10 (s, 1H), 12.04 ppm (br s, disappeared after treatment with D₂O, 1H). IR: ν 1734 and 3262 cm⁻¹.

2-(((tert-Butyldimethylsilyl)oxy)methyl)aniline (6.31).



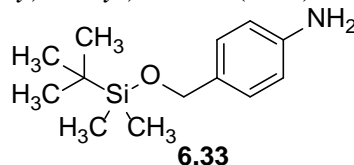
It was prepared according to Lit.²⁶

3-(((tert-Butyldimethylsilyl)oxy)methyl)aniline (6.32).



It was prepared according to Lit.²⁷

4-(((tert-Butyldimethylsilyl)oxy)methyl)aniline (6.33).



It was prepared according to Lit.²⁸

6.5.3 NHERF1 PDZ1 Binding Studies

A NHERF1 PDZ1 subcloned in pETG41 plasmid was kindly obtained from Dr. Nicolas Wolff (Pasteur Institute, Paris, France). To monitor binding by fluorescence, a Trp residue was inserted at position 38 by replacing a Tyr residues using a Quickchange Lighting mutagenesis kit. A dansylated peptide mimicking the C-terminal portion of the β 2 adrenergic receptor, D-NDSL, was purchased from JPT Peptide Technologies (Berlin, Germany) and purified using HPLC. Equilibrium binding experiments were carried out in

the presence of 50 mM Na phosphate buffer, pH 7.2, 300 mM NaCl at 25°C by monitoring fluorescence upon exciting the sample at 280 nm and measuring emission on a Fluoromax single photon spectrofluorometer (Jobin-Yvon, NJ, USA).²⁹

6.5.4 *Wnt Reporter Assay*

293T cells were plated at 20% confluence in 60 mm cell culture dishes and transfected with 2.5 µL/µg DNA of Dreamfect Gold Transfection Reagent (#DG80500, OZ Biosciences) and 2 µg of TOPFlash reporter plasmid containing 8 repeats of TCF/LEF binding sites or 2 µg of FOPFlash reporter vector, containing the mutated TCF/LEF binding sites.³⁰ TK-Renilla and empty pCDNA3.1 vectors were co-transfected in all experimental points to normalize transfection efficiency and to reach the total amount of 4 µg DNA/dish, respectively. After overnight transfection, cells were harvested and plated in 24 well multi-well plates at 20% confluence. After 24 h, cells were starved in medium containing Opti-MEM (#31985070, Thermo Fisher Scientific), FBS 0.5%, Pen/Strep 1%, NaPyr 1%, NeAA 1% for 8 h. After incubation, 50 mM LiCl or DMSO were added to starvation medium for 24 h, together with the indicated amounts of compound.

After treatment, cells were lysed and luciferase assay was performed as previously described.³¹ Dose-response curves were generated by non-linear regression using Graphpad Prism software.

6.5.5 *Cell Cultures*

Colorectal cancer (CRC) cell lines Ls174T and DLD-1 were purchased from American Type Culture Collection (Manassas, VA, USA) and routinely assessed to check their identity.³² Cells were stably transfected with Doxycycline hyclate (Dox)-inducible short hairpin RNA (shRNA) for β-Catenin (Ls174Tshβ-Cat) or a scramble control shRNA (shCtr), as previously described.^{32,33}

Human colon cancer SW480 and SW620 and human urinary bladder cancer T24 cell lines were grown in Dulbecco's Modified Eagle Medium (DMEM) supplemented with 10% fetal bovine serum (FBS), 1% L-glutamine, and antibiotics. The human neuroblastoma cell lines SKNBE and SKNBE(2c)³⁴ was cultured in RPMI-1640 medium complemented with 10% FBS, 1% penicillin/Streptomycin and 1% L-Glutamine (Sigma-Aldrich). All culture were maintained at 37 °C in a 5% CO₂ atmosphere. Cancer Stem cells (CSCs) were generated from individual patients as previously reported,³⁵ and cultured using an optimized medium (CSC medium, see below) in ultra-low attachment tissue culture flasks (Corning Costar, Cambridge, MA), in humidified atmosphere at 37 °C, and 5% CO₂ as previously reported.³⁶

6.5.6 *Determination of the IC₅₀ by MTT Assay*

Cell viability was evaluated by colorimetric MTT assay.³⁷ Briefly, cells (5x10³ cells/well) were seeded in 96-well microculture plates. Cells were then exposed to increasing concentrations of different compounds (range 0-60 µM) for 72 h. At the end of the treatment, media were removed and incubated at 37 °C in the dark for 3 h in phosphate buffered saline (PBS) containing 0.5 mg/mL of 3-(4,5-dimethylthiazol-2-yl)-2,5-diphenyl tetrazolium bromide (MTT) (Sigma-Aldrich). Culture media were then replaced with 150 µL acidic isopropanol (0.04 N HCl in absolute isopropanol) and 1% v/v Triton X-100 to dissolve formazan crystals.

Absorbance at 560 nm was then measured using a microplate spectrophotometer (Glomax-Multi+ Detection System, Promega). The cell growth inhibition rate of different drugs was calculated utilizing the following formula: inhibition rate (%) = [OD sample/OD control]x100. The IC₅₀ of a drug has been determined by constructing a doseresponse curve inhibition with GraphPad Prism 5.

6.5.7 CSC Inhibition Assay

CSC viability upon treatment with inhibitors was determined by CellTiter-Glo luminescent cell viability assay (Promega, Madison, WI, <http://www.promega.ca>) according to the manufacturer's directions. Briefly, CSCs (5×10^3 per well) were dissociated with TrypLE Express (Thermo Fisher Scientific), seeded in 96-well plates (6 replicates per experimental point) in CSC medium, and incubated in a humidified atmosphere at 37 °C, 5% CO₂. Drugs were added 24 h after cell plating, and Luminescence was detected after 72 h, with a DTX880 multimode microplate reader (Beckman Coulter, Brea, CA).

6.6 References

1. Weinman, E. J.; Steplock, D.; Tate, K.; Hall, R. A.; Spurney, R. F.; Shenolikar, S. Structure-function of recombinant Na/H exchanger regulatory factor (NHE-RF). *J Clin Invest.* **1998**, *101*, 2199–206.
2. Vaquero, J.; Nguyen Ho-Bouidoires, T. H.; Claperon, A.; Fouassier, L. Role of the PDZ scaffold protein NHERF1/EBP50 in cancer biology: from signaling regulation to clinical relevance. *Oncogene* **2017**, *36*, 3067–3079.
3. Georgescu, M. M.; Morales, F. C.; Molina, J. R.; Hayashi, Y. Roles of NHERF1/EBP50 in cancer. *Curr. Mol. Med.* **2008**, *8*, 459–468.
4. Saponaro, C.; Sergio, S.; Coluccia, A.; De Luca, M.; La Regina, G.; Mologni, L.; Famiglioni, V.; Naccarato, V.; Bonetti, D.; Gautier, C.; Gianni, S.; Vergara, D.; Salzet, M.; Fournier, I.; Bucci, C.; Silvestri, R.; Gambacorti Passerini, C.; Maffia, M.; Coluccia, A. M. L. AML. β -Catenin knockdown promotes NHERF1-mediated survival of colorectal cancer cells: implications for a double-targeted therapy. *Oncogene* **2018**, *37*, 3301–3316.
5. Mayasundari, A.; Ferreira, A. M.; He, L.; Mahindroo, M.; Bashford, D.; Fujii, N. Rational design of the first small-molecule antagonists of NHERF1/EBP50 PDZ domains. *Bioorg. Med. Chem. Lett.* **2008**, *18*, 942–945.
6. Du, G.; Gu, Y.; Hao, C.; Yuan, Z.; He, J.; Jiang, W. G.; Cheng, S. The cellular distribution of Na⁺/H⁺ exchanger regulatory factor 1 is determined by the PDZ-I domain and regulates the malignant progression of breast cancer. *Oncotarget* **2016**, *7*, 29440–29453.
7. Fitzpatrick, J. M.; Pellegrini, M.; Cushing, P. R.; Mierke, D. F. Small molecule inhibition of Na⁺/H⁺ exchange regulatory factor 1 and parathyroid hormone 1 receptor interaction. *Biochemistry* **2014**, *53*, 5916–5922.
8. Mamonova, T.; Kurnikova, M.; Friedman, P. A. Structural basis for NHERF1 PDZ domain binding. *Biochemistry* **2012**, *51*, 3110–3120.
9. Karthikeyan, S.; Leung, T.; Ladas, J. A. A. Structural determinants of the Na⁺/H⁺ exchanger regulatory factor interaction with the beta 2 adrenergic and platelet-derived growth factor receptors. *J. Biol. Chem.* **2002**, *277*, 18973–18987.
10. Karthikeyan, S.; Leung, T.; Ladas, J. A. A. Structural Determinants of the Na⁺/H⁺ Exchanger Regulatory Factor Interaction with the Beta 2 Adrenergic and Platelet-Derived Growth Factor Receptors. *J. Biol. Chem.* **2002**, *277*, 18973–18987.
11. Mamonova, T.; Kurnikova, M.; Friedman, P. A. Structural basis for NHERF1 PDZ domain binding. *Biochemistry* **2012**, *51*, 31110–31210.
12. Coluccia, A.; La Regina, G.; Naccarato, V.; Nalli, M.; Orlando, V.; Biagioni, S.; De Angelis, M. L.; Baiocchi, M.; Gautier, C.; Gianni, S.; Di Pastena, F.; Di Magno, L.; Canettieri, G.; Coluccia, A. M. L.; Romano S. Drug Design and Synthesis of First in Class PDZ1 Targeting NHERF1 Inhibitors as Anticancer Agents. *ACS Med. Chem. Lett.* **2019**, *10*, 499–503.

13. Gianni, S.; Engström, A.; Larsson, M.; Calosci, N.; Malatesta, F.; Eklund, L.; Ngang, C. C.; Travaglini-Allocatelli, C.; Jemth, P. The kinetics of PDZ domain-ligand interactions and implications for the binding mechanism. *J. Biol. Chem.* **2005**, *280*, 34805–34812.
14. Handeli, S.; Simon, J. A. A small-molecule inhibitor of Tcf/ beta-catenin signaling down-regulates PPAR γ and PPAR δ activities. *Mol. Cancer Ther.* **2008**, *7*, 521–529.
15. Thorne, C. A.; Hanson, A. J.; Schneider, J.; Tahinci, E.; Orton, D.; Cselenyi, C. S.; Jernigan, K. K.; Meyers, K. C.; Hang, B. I.; Waterson, A. G.; Kim, K.; Melancon, B.; Ghidu, V. P.; Sulikowski, G. A.; La Fleur, B.; Salic, A.; Lee, L. A.; Miller, D. M., III; Lee, E. Small-molecule inhibition of Wnt signaling through activation of casein kinase 1 α . *Nat. Chem. Biol.* **2010**, *6*, 829–836.
16. Chen, Y.; Rao, X.; Huang, K.; Jiang, X.; Wang, H.; Teng, L. FH535 inhibits proliferation and motility of colon cancer cells by targeting Wnt/ β -catenin signaling pathway. *J. Cancer* **2017**, *8*, 3142–3153.
17. Veeman, M. T.; Slusarski, D. C.; Kaykas, A.; Louie, S. H.; Moon, R. T. Zebrafish prickle, a modulator of noncanonical Wnt/Fz signaling, regulates gastrulation movements. *Curr. Biol.* **2003**, *13*, 680–685.
18. PyMOL version 1.2r1. DeLano Scientific LLC: San Carlos, CA.
19. Sastry, G. M.; Adzhigirey, M.; Day, T.; Annabhimoju, R.; Sherman, W. Protein and ligand preparation: Parameters, protocols, and influence on virtual screening enrichments. *J. Comput. Aid. Mol. Des.* **2013**, *27*, 221–234.
20. Case, D. A.; Cheatham, T. E. 3rd; Darden, T.; Gohlke, H.; Luo, R.; Merz, K. M. Jr.; Onufriev, A.; Simmerling, C.; Wang, B.; Woods, R. J. The Amber biomolecular simulation programs. *J. Comp. Chem.* **2005**, *26*, 1668–1688.
21. Roe, D. B.; Cheatham, T. E. PTRAJ and CPPTRAJ: Software for Processing and Analysis of Molecular Dynamics Trajectory Data. *J. Chem. Theory Comput.* **2013**, *9*, 3084–3095.
22. Pettersen, E. F.; Goddard, T. D.; Huang, C. C.; Couch, G. S.; Greenblatt, D. M.; Meng, E. C.; Ferrin, T. E. UCSF Chimera—a visualization system for exploratory research and analysis. *J. Comput. Chem.* **2004**, *13*, 1605–1612.
23. Korb, O.; Stützel, T.; Exner, T. E. Empirical scoring functions for advanced protein-ligand docking with PLANTS. *J. Chem. Inf. Model.* **2009**, *49*, 84–96.
24. Dixon, S. L.; Smondyrev, A. M.; Rao, S. N., PHASE: A Novel Approach to Pharmacophore Modeling and 3D Database Searching. *Chem. Biol. Drug Des.* **2006**, *67*, 370–372
25. Onda, K.; Suzuki, T.; Shiraki, R.; Yonetoku, Y.; Negoro, K.; Momose, K.; Katayama, N.; Orita, M.; Yamaguchi, T.; Ohta, M.; Tsukamoto, S. Synthesis of 5-chloro-N-aryl-1H-indole-2-carboxamide derivatives as inhibitors of human liver glycogen phosphorylase a. *Bioorg. Med. Chem.* **2008**, *16*, 5452–5464.
26. Borthwick, J. A.; Ancellin, N.; Bertrand, S. M.; Bingham, R. P.; Carter, P. S.; Chung, C.-W.; Churcher, I.; Dodic, N.; Fournier, C.; Francis, P. L.; Hobbs, A.; Jamieson, C.; Pickett, S. D.; Smith, S. E.; Somers, D. O'N.; Spitzfaden, C.; Suckling, C. J.; Young, R. J. Structurally diverse mitochondrial branched chain aminotransferase (BCATm) leads with varying binding modes identified by fragment screening. *J. Med. Chem.* **2016**, *59*, 2452–2467.
27. Adeyemi, C. M.; Isaacs, M.; Mnkandhla, D.; Klein, R.; Hoppe, H. C.; Krause, R. W. M.; Lobb, K. A.; Kaye, P. T. Synthesis and anti-parasitic activity of C-benzylated (N-arylcarbamoyl)alkylphosphonate esters. *Tetrahedron* **2017**, *73*, 1661–1667.
28. Haynes, K. M.; Abdali, N.; Jhawar, V.; Zgurskaya, H. I.; Parks, J. M.; Green, A. T.; Baudry, J.; Rybenkov, V. V.; Smith, J. C.; Walker, J. K. Identification and structure-

activity relationships of novel compounds that potentiate the activities of antibiotics in *Escherichia coli*. *J. Med. Chem.* **2017**, *60*, 6205–6219.

29. Ivarsson, Y.; Travaglini-Allocatelli, C.; Jemth P.; Malatesta, F.; Brunori, M.; Gianni, S. An onpathway intermediate in the folding of a PDZ domain. *J. Biol. Chem.* **2007**, *282*, 8568–8572.

30. Veeman, M. T.; Slusarski, D. C.; Kaykas, A.; Louie, S. H.; Moon, R. T. Zebrafish prickie, a modulator of noncanonical Wnt/Fz signaling, regulates gastrulation movements. *Curr. Biol.* **2003**, *13*, 680–685.

31. D'Amico, D.; Antonucci, L.; Di Magno, L.; Coni, S.; Sdruscia, G.; Macone, A.; Miele, E.; Infante, P.; Di Marcotullio, L.; De Smaele, E.; Ferretti, E.; Ciapponi, L.; Giangaspero, F.; Yates, J. R., 3rd; Agostinelli, E.; Cardinali, B.; Screpanti, I.; Gulino, A. Canettieri G. Noncanonical Hedgehog/AMPK-mediated control of polyamine metabolism supports neuronal and medulloblastoma cell growth. *Develop. Cell* **2015**, *35*, 21–35.

32. Coluccia, A. M.; Benati, D.; Dekhil, H.; De Filippo, A.; Lan, C.; Gambacorti Passerini C. SKI-606 decreases growth and motility of colorectal cancer cells by preventing pp60(c-Src) dependent tyrosine phosphorylation of β -catenin and its nuclear signalling. *Cancer Res.* **2006**, *66*, 2279–2286.

33. Mologni, L.; Brussolo, S.; Ceccon, M.; Gambacorti-Passerini C. Synergistic effects of combined Wnt/KRAS inhibition in colorectal cancer cells. *PLoS One* **2012**, *7*, e51449.

34. Ciccarone, V.; Spengler, B. A.; Meyers, M. B.; Biedler, J. L.; Ross, R. A. Phenotypic diversification in human neuroblastoma cells: expression of distinct neural crest lineages. *Cancer Res.* **1989**, *49*, 219–225.

35. De Angelis, M. L.; Zeuner, A.; Policicchio, E.; Russo, G.; Bruselles, A.; Signore, M.; Vitale, S.; De Luca, G.; Pillozzi, E.; Boe, A.; Stassi, G.; Ricci-Vitiani, L.; Amoreo, C. A.; Pagliuca, A.; Francescangeli, F.; Tartaglia, M.; De Maria, R.; Baiocchi, M. Cancer stem cell-based models of colorectal cancer reveal molecular determinants of therapy resistance. *Stem Cells Transl. Med.* **2016**, *5*, 511–523.

36. De Angelis, M. L.; De Maria, R.; Baiocchi, M. How to assess drug resistance in cancer stem cells. *Methods Mol. Biol.* **2018**, *1692*, 107–115.

37. Mosmann, T. Rapid colorimetric assay for cellular growth and survival: application to proliferation and cytotoxicity assays. *J. Imm. Meth.* **1983**, *65*, 55–63.

Other Collaborations

7. New Inhibitors of RNA-dependent RNA Polymerase (RdRp) of Norovirus

7.1 Introduction

Foodborne viruses include human norovirus (HuNoV), hepatitis A and E viruses, sapovirus, rotavirus, adenovirus and poliovirus. Among these, HuNoV has long been considered the most prominent cause of illness¹, causing more than 90% of nonbacterial acute gastroenteritis² and over 200,000 global deaths each year. There are a small number of HuNoV antiviral candidates in preclinical development; the majority of these target the viral RNA-dependent RNA polymerase (RdRp) that is the key enzyme responsible for transcription and replication of the viral genome.

7.1.1 Norovirus RNA-dependent RNA polymerase (RdRp)

Noroviruses belong to the Caliciviridae family of single-stranded positive-sense RNA viruses. The genus Norovirus includes seven genogroups (GI-GVII), of which GI, GII and GIV infect humans. Human noroviruses are responsible for widespread outbreaks of acute gastroenteritis and represent one of the most common causes of foodborne illness. No vaccine or antiviral treatment options are available for norovirus infection.

The RNA-dependent RNA polymerase (RdRp) of noroviruses is a key enzyme responsible for transcription and replication of the viral genome. The RdRp can be described as a partially closed right hand, with fingers, thumb, and palm subdomains (Figure 7.1 A and B). The fingers and the thumb subdomains interact to close the hand structure (Figure 7.1 B), forming a channel where the single-stranded template RNA can thread into the polymerase. The template channel merges with the central channel where the 3' end of template RNA and the nascent RNA exit (Figure 7.1 C). At the confluence of the template and central channel is the NTP channel where NTPs enter. Lining the channels are highly conserved residues organized into motifs A through G, which interact with the template, the nascent RNA, and the NTPs for RNA synthesis. The active site lies at the convergence of the template channel and the NTP channel and contains aspartate residues that coordinate divalent metals to promote nucleotide polymerization (Figure 7.1).³

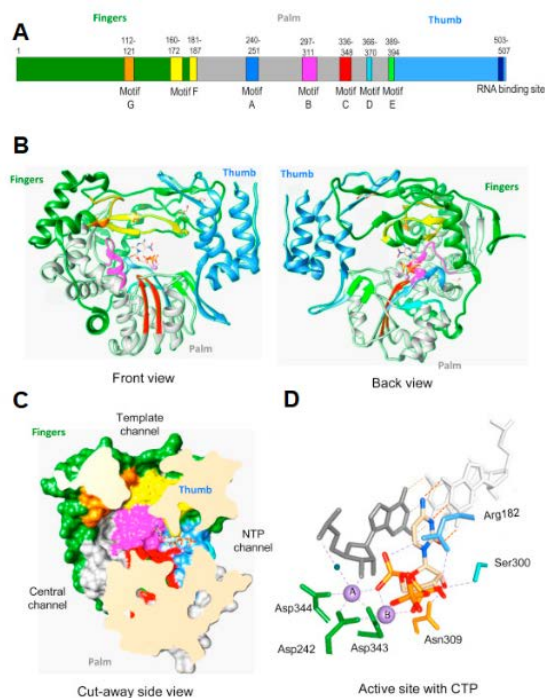


Figure 7.1 Structure of Norovirus Polymerase. (A) Schematic of the HuNoV NS7 protein. The fingers, palm and thumb subdomains are colored green, grey and cornflower blue. The motifs are highlighted in distinct colors and the numbers above the motifs denote the amino acid residues that encode the motifs. The structures are based on the structure of the HuNoV complex complexed to the ternary complex and associated with CTP (pdb: 3BSN). (B) Ribbon structures of the NS7 protein. The subdomains are colored green, grey and Motifs A through F are in, respectively, light blue, magenta, grey, and cornflower blue. The motifs and their colors are: A: blue, B: magenta, C: red, D: sky blue, E: green. The front and back views are rotated by 180 °C. (C) A cut-away view of the HuNoV RdRp that illustrates the locations of the template channel, the central channel, and the NTP channel. The locations of motifs are colored as in panel C. (D) Recognition of CTP in the HuNoV ternary complex. Divalent metals, manganese that are coordinated by the active site aspartates are in purple. A water molecule that is used to H-bond to the template RNA is shown as a blue sphere. Only the side chains of amino acids that recognize the CTP are shown.³

7.1.2 RdRp-Targeted Antivirals

RdRp-targeted antivirals fall into two classes; nucleoside analogues (NAs) and non-nucleoside inhibitors (NNIs). NA prodrugs can be phosphorylated after cellular uptake, then incorporated into the growing viral nucleic acid chain by the RdRp. These antivirals work by competing with incoming nucleoside triphosphates (NTPs) to cause either chain termination, or lethal mutagenesis of the progeny virus. NAs have proven successful in the treatment of several viral infections including hepatitis B virus, hepatitis C virus (HCV), herpesviruses and human immunodeficiency virus (HIV). However, due to their mode of action, they frequently result in off-target side effects, and no NAs have yet reached clinical trials for norovirus treatment. Unlike NAs, NNIs generally bind to allosteric pockets on the viral polymerase to prevent conformational changes necessary for transcription. NNIs have been clinically approved for treating HIV and HCV infections, however, while several potential norovirus NNIs have been identified in pre-clinical studies, none are in clinical trials for the treatment of human norovirus infections. Amongst these pre-clinical candidates is the anthelmintic drug suramin (**7.1**) (Figure 7.2), which demonstrated potent in vitro inhibitory activity against the human norovirus RdRp in enzymatic assays with an IC₅₀ of 27.0 nM. Similarly, the suramin derivative, pyridoxal-5'-phosphate-6-(2'-naphthylazo-6'-nitro-4',8'-disulfonate) tetrasodium salt (PPNDS, **7.2**) (Figure 7.3), has also been shown to inhibit human norovirus RdRp activity in vitro, with an IC₅₀ of 0.45 µM. Recently, PPNDS was reported to exhibit broad-spectrum antiviral activity against other calicivirus RdRps.

However, neither of these compounds are likely to be suitable for the treatment of human norovirus infections, as both suramin (**7.1**) and PPNDS (**7.2**) display poor cell membrane permeability, suramin (**7.1**) induces severe side-effects, and PPNDS (**7.2**) is known to have non-specific, off-target activity.⁴

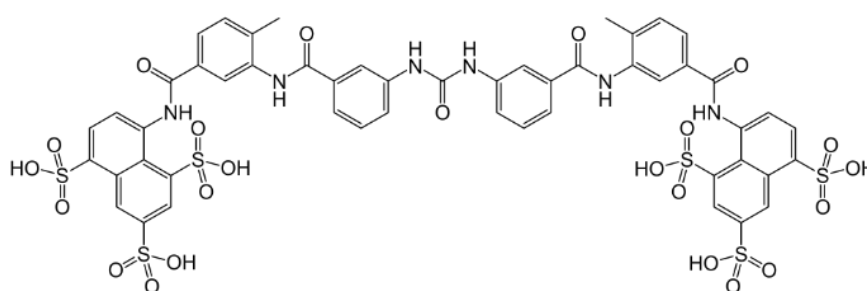


Figure 7.2 Structure of Suramin (7.1)

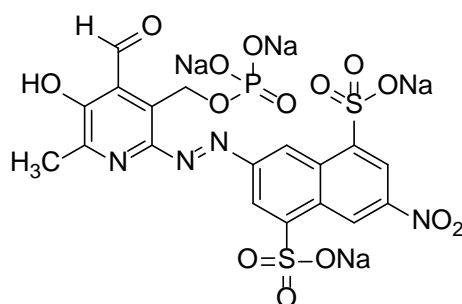


Figure 7.3 Structure of PPNDS (7.2)

7.2 Objective of the Study

Prof. Andrea Brancale and co-workers at Cardiff University, (UK) performed a virtual screening of commercially available drug-like compounds on the suramin and PPNDS binding-sites of the HuNoV RdRp; two molecules were found to have an interesting RdRp inhibitory activity and were selected for a structure-activity relationship study that led to the synthesis of 34 new chemical derivatives.

During the 3-months period I spent at Cardiff University, as a PhD visitor student, under the supervision of Prof. Brancale at the School of Pharmacy and Pharmaceutical Sciences of Cardiff University, I participated to the synthesis of these new inhibitors of the RNA-dependent RNA polymerase of Norovirus. In addition, I had the opportunity to participate to the biological evaluation of the newly prepared compounds at Cardiff School of Biosciences (Sir Martin Evans Building, Museum Ave, Cardiff); in particular we examined the new derivatives for inhibition of HuNoV RdRp activity using PicoGreen Assay and the results were then confirmed by GelShift Assay (chemical structures and biological data are confidential and not shown).

7.3 Results and Discussion

A virtual screening evaluation of commercially available, drug-like compounds (~300,000) was performed on the suramin and PPNDS binding-sites of the human norovirus RdRp. These two RdRp inhibitors occupy two different sites, A and B, situated in the NTP access pathway located between the fingers and thumb domains, and overlap each other in the central part of the protein. Two molecules were found to have an interesting RdRp inhibitory activity and were selected for a SAR study that led to the synthesis of 34 new chemical derivatives.

These newly synthesized compounds were examined for inhibition of human norovirus RdRp activity using PicoGreen assay and Gel Shift assay. In the PicoGreen assay compounds were tested at 100 μM ; 50 μM ; 25 μM ; 10 μM ; 1 μM ; 0.1 μM in order to obtain a dose-response curve. Eight candidates demonstrated dose-dependent RdRp inhibition (IC_{50} s in the 9.0 to 36.0 μM range) which was confirmed using a gel-shift RdRp assay at fixed concentration of 100 μM .

7.4 Experimental Section

7.4.1 Chemistry

All solvents and reagents were used as obtained from commercial sources unless otherwise indicated. All reactions were performed under a nitrogen atmosphere. ^1H and ^{13}C NMR spectra were recorded with a Bruker Avance DPX500 spectrometer operating at 500 MHz for ^1H and 125 MHz for ^{13}C , with Me_4Si as internal standard.

Deuterated chloroform was used as the solvent for NMR experiments, unless otherwise stated. ¹H chemical shifts values (δ) are referenced to the residual non-deuterated components of the NMR solvents ($\delta = 7.26$ ppm for CHCl₃, etc.). The ¹³C chemical shifts (δ) are referenced to CDCl₃ (central peak, $\delta = 77.0$ ppm). TLC was performed on silica gel 60 F254 plastic sheets. Column chromatography was performed using silica gel 60A (35–75 mesh, Fisher) or on an Isolera Biotage system. Purity of prepared compounds was determined by HPLC-UV analysis (Thermo HPLC connected with UV detector).

All compounds tested in biological assays were >95% pure.

The purity of all final compounds was determined to be >95% by HPLC using the eluents water (eluent A), acetonitrile (eluent B), at the following conditions: Varian Pursuit, 150 mm \times 4.6 mm, 5.0 μ m, 1.0 mL/min, gradient 30 min 10% \rightarrow 100% eluent B in eluent A (method 1). Purity of intermediates was >90%, unless otherwise stated.

7.4.2 PicoGreen Assay

Polymerase activity was measured by monitoring the formation of double-stranded RNA (dsRNA) from a single-stranded homopolymeric template, poly(C), using the fluorescent dye PicoGreen (Life Technologies, Carlsbad, CA, USA).⁵

RdRp assays were performed in 96-well plates, and each reaction mixture contained 400 ng enzyme, 0.23 mM GTP, 10 ng/ μ l poly(C) RNA, 2.5 mM MnCl₂, 5 mM dithiothreitol (DTT), 0.01% bovine serum albumin (BSA), and 0.005% Tween 20 in 20 mM Tris-HCl, pH 7.5, with a final volume of 50 μ l. Reactions were run for 10 min at 30 °C and terminated with 17.5 mM EDTA. On completion of the RdRp reaction, contents were transferred into black 96-well microplates (Sigma-Aldrich), and 165 μ L of the commercially available fluorescent dye PicoGreen (Invitrogen; 1:680 [vol/vol] diluted in TE buffer, pH 7.5) was added to a final volume of 225 μ L. The mixture was covered from light, incubated for 5 min, and the fluorescence intensity measured on a POLARstar Omega microplate reader (BMG Labtech, Ortenberg, Germany) at excitation and emission wavelengths of 485 nm and 520 nm, respectively. A separate control reaction with heat-inactivated RdRp was used to quantify background fluorescence.

Compounds were tested at different concentrations (100 μ M; 50 μ M; 25 μ M; 10 μ M; 1 μ M; 0.1 μ M) in order to have a dose-response curve; PPNDS and DMSO (100 μ M; 50 μ M; 25 μ M; 10 μ M; 1 μ M; 0.1 μ M) were used as positive and negative controls. Each experiment was performed in triplicate.

For each compound the background fluorescence was measured beforehand at 100 μ M; 50 μ M; 25 μ M; 10 μ M; 1 μ M; 0.1 μ M and was detracted to final fluorescence results. GraphPad Prism V6.05 (La Jolla, CA, USA) was used to plot the IC₅₀ values.

7.4.3 Gel Shift Assay

Polyacrylamide gel-based assays were used to examine the RdRp activity.⁶ The RNA template PE44-NoV was designed to direct primer extension activity through a stable hairpin at the 3' end. Each reaction mixture contained 1 μ M RNA PE44-NoV, 400 ng norovirus Sydney 2012 RdRp, 0.4 mM rGTP, 5 mM dithiothreitol (DTT), 2.5 mM MnCl₂, 1 unit Ribolock and 20 mM Tris-HCl in a 25 μ l final volume. Reaction mixtures were incubated for 6 h at 30 °C in the presence of test compounds or the compound vehicle DMSO (0.5% [vol/vol]). PE44 products were run in 15% denaturing polyacrylamide gels containing 7 M urea (Bio-Rad, Hercules, CA). Gels were stained with SYBR green II (Invitrogen) and visualized on a Gel Doc molecular imager (Bio-Rad). Compounds were tested at 100 μ M and No RdRp, DMSO 0.5% and PPNDS were used as controls.

7.5 References

1. Cliver, D.O. Virus transmission via food, an IFT status summary. *Food technology*. **1997**, *51*, 71–78.
2. Mead, P.S.; Slutsker, L.; Dietz, V.; McCaig, L.F.; Bresee, J.S. Food-related illness and death in the United States. *Emerg. Infect. Dis.* **1999**, *5*, 607–25.
3. Deval, J.; Jin, Z.; Chuang, Y.; Kao, C. Structure(s), function(s), and inhibition of the RNA-dependent RNA polymerase of noroviruses. *Virus Research*. **2017**, *234*, 21–33.
4. Ferla, F.; Natalie E. Netzler, N.; Ferla, S.; Veronese, S.; Tuipulotu, D.; Guccione, S.; Brancale, A.; Peter A. White, P.; Bassetto, M. In silico screening for human norovirus antivirals reveals a novel non-nucleoside inhibitor of the viral polymerase. *Nature*. **2018**, *8*, 4129.
5. Eltahla, A.; Lim, K.; Eden, J.; Kelly, A.; Mackenzie, J.; White, P. Nonnucleoside inhibitors of norovirus RNA polymerase: scaffolds for rational drug design. *Antimicrob. Agents Chemoter.* **2014**, *58*, 3115–23.
6. Eltahla, A.; Tay, E.; Douglas, M. W.; White, P. A. Cross-genotypic examination of hepatitis C virus polymerase inhibitors reveals a novel mechanism of action for thumb binders. *Antimicrob. Agents Chemoter.* **2014**, *58*, 7215–7224.

General Conclusions

During the Ph.D. program, my research activity has been focused on the discovery of small molecules with therapeutic activity, through modern methods of organic synthesis. In this context, I have been primarily involved in the development of anticancer agents that target tubulin and microtubules and NHERF1 PDZ1 domain. I conducted my research activity at the Department of Drug Chemistry and Technologies of “Sapienza” University in Rome, in the Laboratory of Prof. Romano Silvestri. The passion for research prompted me to move abroad and work for three months at Cardiff University (UK); in particular, I had the opportunity to work on the synthesis of new inhibitors of Norovirus RNA-dependent RNA polymerase (RdRp) at the Welsh School of Pharmacy in the laboratory of Prof. Andrea Brancale and, additionally, I was involved in the biological evaluation of these newly synthesized compounds at the School of Biosciences of Cardiff University. Furthermore, I had the opportunity to be part of Prof. A. Brancale’s group meetings and present my research goals and results. The research activities conducted during my Ph.D. work resulted in the publication of five peer reviewed research articles (with additional manuscripts that are in preparation):

1. Coluccia A.; La Regina G.; Naccarato V.; Nalli M.; Orlando V.; Biagioni S.; De Angelis ML.; Baiocchi M.; Gautier C.; Gianni S.; Di Pastena F.; Di Magno L.; Canettieri G.; Coluccia A.M.L.; Silvestri R. Drug Design and Synthesis of First in Class PDZ1 Targeting NHERF1 Inhibitors as Anticancer Agents. *ACS Med. Chem. Lett.* **2019**, *10* (4), 499–503.

2. La Regina, G.; Coluccia, A.; Naccarato, V.; Silvestri, R. Towards modern anticancer agents that interact with tubulin. *Eur J Pharm Sci.* **2019**, *131*, 58–68.

3. La Regina, G.; Bai, R.; Coluccia, A.; Naccarato, V.; Famiglioni, V.; Nalli, M.; Masci, D.; Verrico, A.; Rovella, P.; Mazzoccoli, C.; Da Pozzo, E.; Cavallini, C.; Martini, C.; Vultaggio, S.; Dondio, G.; Varasi, M.; Mercurio, C.; Hamel, E.; Lavia, P.; Silvestri, R. New 6- and 7-heterocyclyl-1*H*-indole derivatives as potent tubulin assembly and cancer cell growth inhibitors. *Eur. J. Med. Chem.* **2018**, *152*, 283–297.

4. Saponaro, C.; Sergio, S.; Coluccia, A.; De Luca, M.; La Regina, G.; Mologni, L.; Famiglioni, V.; Naccarato, V.; Bonetti, D.; Gautier, C.; Gianni, S.; Vergara, D.; Salzet, M.; Fournier, I.; Bucci, C.; Silvestri, R.; Gambacorti Passerini, C.; Maffia, M.; Coluccia, A. M. L. β -catenin knockdown promotes NHERF1-mediated survival of colorectal cancer cells: implications for a double-targeted therapy. *Oncogene* **2018**, *37*, 3301–3316.

5. La Regina, G.; Bai, R.; Coluccia, A.; Famiglioni, V.; Passacantilli, S.; Naccarato, V.; Ortar, G.; Mazzoccoli, C.; Ruggieri, V.; Agriesti, F.; Piccoli, C.; Tataranni, T.; Nalli, M.; Brancale, A.; Vultaggio, S.; Mercurio, C.; Varasi, M.; Saponaro, C.; Sergio, S.; Maffia, M.; Coluccia, A. M. L.; Hamel, E.; Silvestri, R. 3-Aroyl-1,4-diarylpyrroles inhibit chronic myeloid leukemia cell growth through an interaction with tubulin. *ACS Med. Chem. Lett.* **2017**, *8*, 521–526.

As well as three poster or oral presentations:

1. Naccarato V., La Regina G., Coluccia A., Silvestri R. *New NHERF1 PDZ1 Domain Inhibitors as Anticancer Agents*. Poster Presentation. 3rd International Scientific Retreat, June, 12-15th, 2019, Rome (Italy).

2. Valentina Naccarato, Giuseppe La Regina, Antonio Coluccia, Addolorata Maria Luce Coluccia, Hernest Hamel, Romano Silvestri. *New pyrrole inhibitors of chronic myeloid leukemia cell growth*. Poster Presentation. XXVI Congresso Nazionale della Società Chimica Italiana, Programma del XXVI Congresso Nazionale della Società Chimica Italiana, FAR PO40, September 10-14th, 2017, Paestum, Italy.

3. Valentina Naccarato, La Regina Giuseppe, Coluccia Antonio, Marianna Nalli, Hamel Ernest, Silvestri Romano. *New Indole Derivatives as Potent Inhibitors of Tubulin Polymerization and Cancer Cell Growth*. Oral Presentation. Second Workshop on Research, July, 12th, 2018, Rome, Italy.

In conclusion, I believe that the Ph.D. experience has given me the opportunity to improve my scientific competence and knowledge as a student of the “Istituto Pasteur Italia – Fondazione Cenci Bolognetti”, also training undergraduate students, working in different research groups and participating to scientific meetings, seminars and conferences.

Acknowledgements

My Ph.D. work was funded by the Istituto Pasteur Italia-Fondazione Cenci Bolognetti. I am grateful to all the Ph.D. program teaching board.

I am very thankful to my supervisor Prof. Romano Silvestri for the invaluable advice and suggestions during the entire Ph.D. experience and to Prof. Giuseppe La Regina who introduced me to the medicinal chemistry world since I was an undergraduate student and for his long-term support. I am profoundly grateful to Prof. Andrea Brancale and his research group for giving me the opportunity to work for three months at Cardiff University and for introducing me to the biology world; the work we conducted and the experience abroad represent important achievements that significantly enriched not only my career but my life in general.

I also thank my colleagues from the Ph.D. program and the colleagues from Sapienza and all my friends and family who have always believed in me, encouraging and supporting my professional career.